Flame and smoke characterization in reduced gravity for enhanced spacecraft safety

Yutao Li

THÈSE DE DOCTORAT

SORBONNE UNIVERSITÉ

Spécialité: Mécanique

École Doctorale de Sciences Mécaniques, Acoustique, Electronique et Robotique de Paris (ED 391)

Présentée par

Yutao LI

Pour obtenir le grade de

DOCTEUR DE SORBONNE UNIVERSITÉ

Caractérisation des flammes et des fumées en gravité réduite pour le renforcement de la sécurité des modules spatiaux

---

Flame and smoke characterization in reduced gravity for enhanced spacecraft safety

---

Dirigée par

Guillaume Legros et Jose Torero

à l'Institut Jean le Rond ∂'Alembert

Soutenance prévue le 06 December 2022 devant le jury composé de

Mme. Sandra Olson	Rapporteur
M. Yuji Nakamura	Rapporteur
M. Fabien Halter	Examinateur
M. Stéphane Zaleski	Examinateur
M. Augustin Guibaud	Invité
M. Guillaume Legros	Directeur de thèse
M. Jose Torero	Co-directeur de thèse

Acknowledgements

I am sincerely grateful to all the people I met during my thesis.

First of all, I would like to thank my supervisor, Guillaume Legros. During these three years, we encountered various difficulties, but you always managed to be behind me with great support. And I have learned a lot from you, not only in academic terms. I am sure that all this will be beneficial for my whole life. I am also grateful to my co-supervisor Jose Torero. It was a pleasure to have you take the time out of your busy schedule to give me advice, and your advice is always brief and concise, which has been a great benefit to me. I would also like to thank Augustin Guibaud, who has been giving me valuable guidance since my master's internship, thus saving me from many, many detours. You were always able to put yourself in the other person's shoes. When I lacked confidence, you gave me the confidence to do my best. You have always been my best role model.

I would also like to thank everyone on Tech Team. For me, Jean Marie Citerne is simply superhuman. Every time I had a problem with the experiments, you were able to solve it perfectly. I was always amazed by the solutions you came up with. Of course, I also enjoyed the "French lessons" you gave me. I learned a lot of new and unique French words and phrases from you. Thanks to Hugo Dutilleul and Jérôme Bonnety, I always get a lot of inspiration from you, especially when we "traiter les dossiers" or "sciencer" together.

I had the pleasure to work with two very talented students, Samson Boubli and Antoine Bordino. Thanks to your efficient work, we have been able to achieve so many results and I hope that the time spent in the lab will be unforgettable for you as well.

As a foreigner who was completely ignorant of the French administrative system, I was lucky to have a lot of help from our lab managers. Especially Evelyne Mignon and Celia, all the travel tasks could not have been done so well without you. Especially Evelyne Mignon and Célia Sakho, without you, all the missions could not have been accomplished so well.

I must also thank Centre National d'Etudes Spatiales (CNES) for supporting the DIAMONDS project by giving me the opportunity to experience the reduced gravity experiments and providing a platform to work with different teams. Speaking of reduced gravity experiments, they were certainly able to run smoothly without the support of the entire staff of NoveSpace.

This Ph.D. has been a great opportunity to collaborate and learn from different teams in different fields. Jean-Louis Consalvi, I really enjoyed working with you and I especially appreciated that you sacrificed your New Year's Day and weekends to fight for the deadline of PROCI. Alain Coimbra, you and I started our thesis almost at the same time and have similar topics, and I was very lucky that we could discuss each other when we had issues. The team of Lille, Serge Bourbigot, Johan Sarazin and Pierre Bachelet, you are always full of energy (especially after a little sleep during the day) and efficient, and the time spent with you on the missions of the parabolic flight was so memorable. Thanks also to Jean-Baptiste Renard, the addition of LOAC is very meaningful for the practical application of fire detection. Certainly, I have to thank the Japanese team, Osamu Fujita, Masashi Nagachi, and Yusuke Konno, for your excellent work and timely feedback to make the

difficult partial gravity mission in Germany a success and the excellent publications afterward. Also, thanks to Thomas Seon, it was a pleasure to discuss with you, and opened up many new ideas with your inspiration.
Definitely, I have to thank the members of the jury: Yuji Nakamura and Sandra Olson, who carefully revised my manuscript and gave practical advice so that I could better prepare for my defense. Fabien Halter, who made my research objectives clearer each year. Stephane Zaleski, who conducted my defense perfectly and gave me honest advice about my future carrier.
Besides, there are many Ph.D. students who struggled with me and gave me a lot of help. In Saint Cyr, Marcellin Perceau, Renaud Jalain and Théo Benkovic, in addition to working together, those times when we traveled together were so memorable. First of all, I would like to thank the members of office 512: Ghita Ben el barguia, Sagar Pal, Adrien Rohfritsch and Mandeep Saini, who were as warm and welcoming as the temperature of the office ((it is the hottest office in the whole institute). Also, Sarah Vincent, Mahshid Sharifi, Lucas Prouvost and Samy Lakhal in office 502, who shared the stress of last year of our thesis (well, even though Samy was not in the last year of thesis, but you got to experience the ambiance in advance). The other office I need to mention is office 405, where I often pass by to disturb Quentin Baudis and Patricia Vernier, and I always request them to take a break with me.
Whenever I encountered a setback, I was able to forget about it once I was with our special team in Paris: Le Menu (slogan: C-F-Q-C-S). Especially, thanks to the founder of the team, my roommate, Hector Amino, for working with me when we were at home, and supporting each other during our thesis. Additionally, Xinhui Huang (BuBu) and Weikang Zeng (Kangkang) have provided me with a lot of help and advice in life (Pubg, Brawstar, Overcook, etc).
Finally, I must thank my parents and family. Although I was not able to see you during my thesis due to various reasons and I also missed a lot of major events, you still have always supported me, cared for me, and given me unlimited confidence. You made me fearless because I do know where I should go back to when I feel vulnerable.

Abstract

This PhD thesis is dedicated to the study of non-premixed flame spread with a specific attention paid to detection and mitigation in a reduced gravity environment. These works intend to contribute to an enhanced fire safety of spacecraft. To this end, an existing rig that enables experiments in parabolic flights has been further equipped at Institut Jean Le Rond d'Alembert. With this setup, cylindrical samples can be ignited and the subsequent flame spread documented in a reduced gravity environment. Within the spread, the surrounding laminar oxidizer flow is finely controlled, the inlet oxygen content, pressure, and flow velocity being especially adjustable.

Fire detection is one of the priorities of spacecraft fire safety. It especially relies on the identification of soot particles. As a result, the lack of understanding of the soot morphology in microgravity affects the accuracy of fire detection. In this context, a novel soot sampling technique using electric fields is developed and successfully applied for the first time in microgravity to a flame spreading over cylindrical electric wire. The sampled soot particles are analyzed under Transmission Electron Microscope (TEM). With the developed TEM image analysis tools, soot particle projected area, radius of gyration, fractal dimension, and primary particle size are extracted. Then, the influence of gravity is investigated and evidenced on the evolution of these morphological properties within the flame.

The lack of data on flame spread in partial gravity is also an imminent challenge to fire safety for upcoming deep space exploration. Experiments on flame spread over cylindrical samples are performed for the first time at Lunar and Martian gravity. The characteristics of flame spread are analyzed under different oxidizer flow conditions and different configurations of samples. Varying gravity and oxygen content, the extinction limits of the different sample configurations are identified and the flame spread rates are extracted. At high gravity (Mars gravity and normal gravity), droplet leakage affects the extinction limit of wire samples with lower thermal conductivity metallic cores. At the same time, it also impacts the flame spread mechanism. In particular, at Martian gravity, a cyclic flame spread is unveiled and its original mechanism is analyzed.

Fire prevention has always been the key concern of spacecraft firefighting strategies, where the flammability of materials largely limits the choice of materials. Drawing on the experience of ground-based fire prevention, the enhancement of materials' performances with flame retardants may overcome the limitations imposed by material flammability. Cylindrical samples loaded with flame retardants are investigated in microgravity. Two flame retardants with different expansion mechanisms are considered, i.e., Expanded Graphite (EG) and Ammonium polyphosphate/Pentaerythritol (AP). The observed results are then reported and compared with those obtained with different flame retardant loads under normal gravity, for a given ambient pressure and flow rate, with variations in oxygen content. At normal gravity, increasing the flame retardant load increases the extinction limit and slows down the flame spread rate. In contrast, results in microgravity show no detectable improvement in extinction limits for the range of flame retardant loads studied, while the benefit of reduced flame spread rates is not evident. In addition, the

increase in flame retardant loads under microgravity resulted in smoke emissions. This observation was more pronounced for EG loaded samples. These conflicting effects of adding AP and EG on fire safety in microgravity are not evident in normal gravity, requiring careful integration of flame retardants within the context of space exploration.
The results obtained in this study provide useful information and new insights for fire detection and prevention in microgravity, while the experimental data in partial gravity might serve as a database for future fire safety design in space exploration.

Keywords: microgravity, partial gravity, fire safety, flame spread, soot sampling, flame retardant.

Résumé

Les travaux présentés dans le présent mémoire de thèse sont dédiés à l'étude de la propagation de flamme non-prémélangée dans un environnement à gravité réduite, une attention particulière étant prêtée à la détection et la mitigation. Ces travaux entendent contribuer à l'amélioration de la sécurité-incendie des habitacles spatiaux. À cette fin, un dispositif existant qui permet les expérimentations en vols paraboliques a été équipé de nouveaux diagnotics à l'Institut Jean Le Rond d'Alembert. Ainsi, des échantillons cylindriques peuvent être enflammés et la propagation de flamme qui s'ensuit étudiée dans un environnement à gravité réduite. L'écoulement laminaire oxydant alimentant la flamme non-prémlénagée est contrôlé en terme de teneur en oxygène, de pression ambiante et de vitesse d'écoulement.

La détection d'incendie est l'une des priorités des efforts actuellement produits pour sécuriser les habitacles spatiaux. Cette détection repose tout particulièrement sur l'identi-fication des particules de suie. Le manque évident de connaissances sur la morphologie des particules de suie formées en microgravité affecte la précision de la détection des incendies. Dans ce contexte, une technique originale de prélèvement des particules de suie utilisant un champ électrique est développée et réalisée avec succès pour la première fois en microgravité au cours d'une propagation de flamme établie sur un échantillon cylindrique. Les particules de suie prélevées sont analysées au microscope électronique à transmission (TEM). Grâce aux outils d'analyse d'images TEM développés, la surface projetée des particules de suie, la distribution de rayon de giration, les dimensions fractales et les tailles des particules primaires sont extraites. L'effet de la gravité peut alors être étudié et illustré avec l'évolution de ces propriétés morphologiques dans la flamme.

Dans le cadre de l'exploration de l'espace lointain, des expériences sur la propagation de flamme sur fil électrique ont également pu être réalisées pour la première fois à gravité lunaire et martienne. Les caractéristiques de la propagation de la flamme sont analysées sous différentes conditions d'écoulement oxydant et différentes configurations de fils électriques. En variant le niveau gravitationnel et la teneur en oxygène, les limites d'extinction des différentes configurations d'échantillons sont identifiées et les vitesses de propagation de la flamme extraites. À gravité élevée (ici gravité martienne et gravité normale), le suintement de gouttelettes en amont de la flamme affecte la limite d'extinction, ce tout particulièrement pour des échantillons à coeur métallique de faible conductivité thermique. Dans le même temps, ce suintement a également un impact sur le mécanisme de propagation de la flamme. En particulier, à gravité martienne, une propagation cyclique de la flamme est découverte et les mécanismes qui la pilote analysés.

Dans l'optique d'une prévention accrue des incendies dans les modules spatiaux, des échantillons cylindriques chargés de retardateurs de flamme sont étudiés en microgravité et à gravité normale, ce pour une teneur en oxygène variable. Deux types de retardateurs de flamme présentant des mécanismes d'expansion différents sont considérés, à savoir le graphite expansé (EG) et le polyphosphate d'ammonium/pentaérythritol (AP). En micropesanteur, l'augmentation de la charge de retardateur n'améliore pas de façon détectable la limite d'extinction tandis que la réduction de la

vitesse de propagation de la flamme n'est pas aussi évidente qu'à gravité normale pour la gamme de charges de retardateur de flamme étudiée. En outre, l'augmentation des charges de retardateur de flamme en micropesanteur a provoqué des émissions de fumée. Ces effets contrariants de l'ajout de retardateur de flamme sur la sécurité-incendie en micropesanteur ne sont pas évidents à gravité normale. Ces observations originales imposent une intégration prudente des retardateurs de flamme dans le contexte de l'exploration spatiale.
Les résultats obtenus dans cette étude fournissent des informations utiles et de nouvelles perspectives pour la détection et la prévention des incendies en micropesanteur, tandis que les données expérimentales en gravité partielle pourront servir de base de données pour la conception future de la sécurité-incendie dans l'exploration spatiale.

Mots-clefs: micropesanteur, gravité partielle, sécurité-incendie, propagation de flamme non-prémélangée, suies, prélèvement, retardateur de flamme.

Contents

Nomenclature

α_g	Average thermal diffusivity in the gas phase
β	Parameter identified using the power law relating pyrolysis mass flow rate to oxygen content
β_d	Length-to-width aspect ratio of the contact line
β_T	Thermal expansion coefficient
δ_s	Thickness of the material
$\dot{q}_g$	Heat loss from the droplet to the surrounding gas by convection
$\dot{q}_s$	Conduction heat through the solid within the condensed phase
$\dot{Q}_{c,fl}$	Conductive heat flux from the flame to the LDPE
$\dot{Q}_{c,s}$	Conductive heat flux from the metallic core to the LDPE
η	Non-Newtonian viscosity
γ	Surface tension
λ	Wavelength
λ_s	Thermal conductivity
μ_{air}	Dynamic viscosity of the forced flow
μ_p	Dynamic viscosity of the LDPE
ν	Kinematic viscosity
$\dot{\gamma}$	Shear rate
$\dot{m}''_F$	Local pyrolysis rate of the solid fuel
$\dot{m}_F$	Overall pyrolysis rate
$\dot{q}''_f$	Heat flux from the flame to the sample surface
ρ	Density
ρ_g	Density of the gas
τ_{ch}	Characteristic time of the first-order reaction related to fuel and oxygen
τ_c	Characteristic time that the flame requires to catch up with the droplet
τ_{exp}	Time that the droplet needs to travel in one cycle

τ_r	Residence time of the gas mixture in the flow
θ_{Adv}	Advancing contact angle
θ_{Rec}	Receding contact angle
A	Cross-section area
a	Box size applied to the box counting method
A_c	Contact area of the droplet with the wire
A_g	Pre-exponential factor
Bo	Bond number
c	Specific heat
d	Distance traveled by the droplet in one cycle
D_f	Fractal dimension of an aggregate
d_{pp}	Diameter of the primary particle
Da	Damköhler number
E_α	Activation energy
F_τ	Viscous force
F_{ad}	Adhesion force
$F_{buoyancy}$	Buoyancy force
F_D	Drag force
g	Gravitational acceleration
Gr	Grashof number
h_d	Droplet height
k	Numerical constant depended on the shape of the droplet
k_g	Gas-phase heat conductivity
L	Characteristic length of objective
L_b	Length at which the combustible coating is completely consumed at the end of the experiment
l_c	Capillary length
L_f	Visible flame length
L_g	Gas-phase preheat length
l_h	Characteristic length of preheating zone
$N(a)$	Number of boxes need to recover the aggregate
P	Pressure

P_p Perimeter of molten LDPE droplet

R Universal gas constant

r_d Droplet radius

r_a Mass center of an aggregate

R_g Gyration radius

r_i Coordinates of mass element in an aggregate

r_s Radius of solid fuel

r_w Radius of the electric wire

Re Reynolds number

Ri Richardson number

S_g Surface of the droplet in contact with the gas

T Temperature of the objective

T_p Pyrolysis temperature of LDPE

T_∞ Ambient temperature

$T_{d,max}$ Maximum surface droplet temperature

T_{fl} Flame temperature

$t_{res,s}$ Characteristic flow time scale for the soot production process

U' Incoming flow velocity relative to flame spread rate

U Flow velocity

U_∞ Flow velocity included the buoyant flow velocity and the forced flow velocity

$U_{buoyancy}$ Flow rate due to buoyancy

U_{fl} Characteristic forced convective velocity of the flame

V_d Droplet volume

V_f Flame spread rate

V_g Opposed-flow velocity

w_d Droplet width

$x_{Flame,front}$ Leading edge of the flame (flame front position)

$x_{Flame,tail}$ Trailing edge of the flame

x_{O_2} Oxygen content

$x_{PE,front}$ Leading edge of the molten LDPE (droplet front position)

$x_{PE,tail}$ Trailing edge of the molten LDPE

x_p Primary particle size parameter for the approximation application on the optical technique

Y_F mass fraction of the fuel

Y_O mass fraction of the oxygen

Introduction

For a few years, space exploration has seen more development than ever before. Today, the transition from Low Earth Orbit (LEO) exploration to Deep Space exploration is underway. The construction of lunar bases and the exploration of Mars are on the planning [1, 2]. Spacecraft safety is a prerequisite for the success of these space exploration missions, where fire safety has been identified as a key factor for long-distance manned missions [3].

Manned spaceflight fire safety has been refined continuously since the Apollo I accident in 1967 [4]. An accidental fire can jeopardize the missions and even pose a threat to the health and life safety of astronauts in the worst-case scenarios. Timely post-accident assessment and improved understanding of combustion fundamentals in microgravity have helped refine the fire protection systems that are included in today's spacecraft. Chapter 1 will evaluate the lack of fire protection strategies based on past fire incidents and existing fire protection equipment. Then, it will examine previous key data to identify relevant experiments that need to be complemented.

The transition of development from LEO to Deep Space raises challenges for present fire safety strategies, as it increases the duration of human stay in space and the distance to the Earth. The primary question regarding fire safety during the journey to a remote destination (such as Moon and Mars) is how to identify whether a fire has broken out. To answer this question, usually spacecraft are equipped with flame detection systems inside. These detection systems are developed based on detectors designed on the ground [5, 6]. These fire detectors developed rely heavily on the optical detection of soot particles, which are present in smoke. To properly detect fires, it is important to understand how the optical properties of these particles are affected in reduced gravity conditions [7]. For this purpose, the present Ph.D. thesis introduces a novel technique for soot sampling within non-premixed flame spread using electric fields. This is described in detail in Chapter 2. As a representative illustration of the targeted spread, an opposed-flow flame spread over a Low Density PolyEthylene (LDPE) coated electric wire in microgravity is shown in Fig. 1 (a). After triggering the electric field, as in Fig. 1 (b), it can be noticed that the flame bends to the right due to the electric field. During the process from Fig. 1 (a) to Fig. 1 (b), soot particles are carried on a brass plate due to ionic forces (the shadow of the plate can be seen on the right edge of the frame in Fig. 1 (b)). Then, the analysis of the morphological characteristics of the collected soot will be presented.

Exploration missions could be carried out on the Moon or Mars if all goes well. Unfortunately, the issue of fire safety remains. To make matters worse there are very few experimental data at these partial gravity levels. Therefore, experiments need to be extended to different gravity levels. Figures 1 (c) and (d) show the flame spread over a LDPE coated electric wire under Lunar (0.16 g_0) and Martian (0.38 g_0) gravity [1]. It can be noticed that there is a difference with the flame spread in microgravity (Fig. 1 (a)). The flame appears more stretched and becomes brighter with the increase in gravity. The molten LDPE upstream of the flame drips and even leaks due to the increase in gravity. These show that the flame spread mechanisms are affected by gravity. Chapter 3 describes

[1] where $g_0 = 9.81 m/s^2$

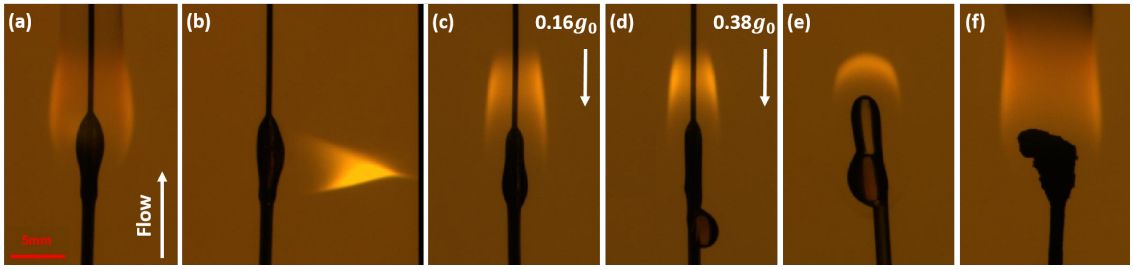

Figure 1: Backlighted frames imaging an opposed-flow flame spread over cylindrical samples in reduced gravity. The surrounding flow conditions are: oxygen content of 21%, pressure of 101.3 kPa, and flow velocity of 150 mm/s. (a) Flame spread over a LDPE coated electric wire in microgravity. (b) Same flame as (a) under electric field during soot sampling. (c) and (d) Flame spread over a LDPE coated electric wire in Lunar and Martian gravity levels, respectively. (e) Flame spread over a cylindrical LDPE sample (without any metallic core) in microgravity. (f) Flame spread over a flame retardant (Expanded Graphite (EG)) loaded LDPE sample in microgravity.

the flame spread behavior under different flow conditions in Lunar and Martian gravity to provide a relevant database for the fire safety of the corresponding exploration programs.

In addition to the gravity factor, the difference in the configuration of the samples also has an effect on the flame spread. Therefore, cylindrical LDPE samples without metallic wire cores were subjected to experiments in microgravity. From Fig. 1 (e), it is found that twin molten LDPE droplets appeared upstream of the flame. These twin droplets are continuously fused and then separated during the spreading process. Comparison with Fig. 1 (a) shows that the presence of a metallic core stabilizes the flame spread. Although removing the metallic core from the sample interrupts the stability of flame spread, it is more convenient for subsequent theoretical modeling. The differences between these two configurations of flame spread are described in detail in Chapter 4. Furthermore, an idea to enhance the material performance in fire safety is introduced. Drawing on the experience of fire protection on the ground, loading the material with a flame retardant material may enable the suppression of the flame spread. Therefore, cylindrical samples loaded with flame retardants (e.g., Fig. 1 (f)) were subjected to experiments in microgravity. The associated flame spread characteristics (e.g., extinction limit, flame spread rate, and soot emission) are presented in the same Chapter.

Overall, the present PhD thesis takes the fire safety of spacecraft as its driving theme, focusing on fire detection and mitigation by analyzing the characteristics of flames and soot. In the end, Chapter 5 will propose future investigations into the above mentioned research directions.

1 Fire safety in reduced gravity

Contents

This chapter focuses on past fire incidents and future exploration needs, together with the related research on fire safety as a background to guide experimental expectations and attempts in this thesis.

Thus, Section 1.1 describes past fire safety failures and analyzes possible shortcomings of present fire safety equipment and strategies based on existing conditions. Furthermore, through future space exploration programs, specific fire safety improvements are proposed. Section 1.2 then summarizes the related present-day academic knowledge, identifies some issues related to combustion fundamentals, and outlines the directions for the expected improvements. Section 1.3 presents the relevant experimental scenarios based on the summary of Section 1.2, and provides an overview and brief analysis of the corresponding experiments.

1.1 Fire safety failures in spacecraft

No matter on Earth or in space, the presence of oxygen, fuel, and heat sources yields the risk of fire. Once prevention is neglected, fires are likely to occur. To avoid fire hazards, it is essential to intervene in the interaction between these three factors and to set fire prevention regulations to reduce the possibility of fire. In addition, it is important to think about how to control the growth and spread of fires once they occur, while implementing mitigation and cleanup measures through effective regulations.

The three elements mentioned above are required to sustain human life on board the spacecraft. Therefore, it is difficult to avoid the danger of fire in a spacecraft with a closed environment. Besides, the ambient environment inside the spacecraft can be thoroughly monitored and controlled. Depending on the needs of the mission, the applied ambient conditions could be different from the sea level on Earth with a pressure of 101.3kPa and an oxygen/nitrogen ratio of 21/79%. The

difference in environmental conditions may change not only the potential for ignition, but also the severity of the fire due to its influence on flame spread rate and smoke production. Moreover, the selection of materials needs to satisfy the relevant functionalities, therefore many materials are not replaceable. With this factor in mind, many combustible materials can be present in spacecraft for high technology equipment, such as polyethylene for radiation shielding [8]. At the same time, instruments for space experiments or daily items needed for the comfort of a long-term mission increase the probability of flammable materials [9]. The multiple electrical systems required to supply power to the various modules and to perform related operations can provide the heat source for ignition. Meanwhile, the unusual overheating challenges faced with reduced natural convection increase the probability of fire in spacecraft [10].
With an understanding of what triggers a fire, it is also helpful to know what the consequences could be. Conceivably, in the enclosed environment of a spacecraft, the consequences of a fire can be dramatic. Far from Earth and with limited resources, damage from a fire could be irreversible. Especially in the case of damage to critical components of the spacecraft, the crew has to interrupt the mission to face the life-threatening situation caused by the damaged modules.
In the last few decades, a well-developed system dedicated to fire detection, mitigation, and cleanup after fires has been developed and tested in normal gravity. However, differences in mass and heat transfer due to reduced natural buoyancy have led to uncertainties in this system in the space environment. In this Section, these uncertainties will be revealed by the ensuing analysis of past fire incidents, which will then be combined with the existing fire protection systems of present-day spacecraft and future space exploration programs to define the corresponding fire safety system shortcomings.

1.1.1 Past incidents and shortcomings

Fire safety protocols have been regularly updated since the first human entry into space in 1961, by learning from the occurred fire incidents, conducting related research and tests, and keeping upgrade the new fire detection and mitigation equipment. Twelve identified fire events that occurred during this period are listed by Guibaud et al. [4] chronologically as shown in Fig. 1.1. The cause, detection, mitigation, and post-event consequences of these incidents are presented in Tab. 1.1. The details of the incidents are described in detail in Ref. [4]. Following is an analysis of these fire incidents from prevention, detection, mitigation, and cleanup aspects to identify the corresponding shortcomings.

A brief description of past fire incidents

From Tab. 1.1, the causes of fire are inseparable from the electrical devices as heat sources. Yet the exploration of space could not be done without electrical components. Three of the twelve fire accidents developed to life-threatening levels. The Command and Service Module (CSM) was damaged in Apollo 1 in 1967 and Apollo 13 in 1970, and the incident in Apollo 1 even cost three astronauts. Although the Mir accident in 1997 only destroyed the canister and displaced electrical cables, the flames that grew to one meter long inside the module still posed a threat to the crew's lives. The other nine fires did not reach the same level of severity, but still had a high possibility of causing damage to the instruments and affecting the mission's progress. For example, two incidents in Salyut-VI resulted in the loss of scientific equipment and four control panels, and two other incidents in Space Shuttle resulted in atmospheric contamination and damage to the canister, respectively. In order to improve the firefighting strategy, the focus needs to be on understanding

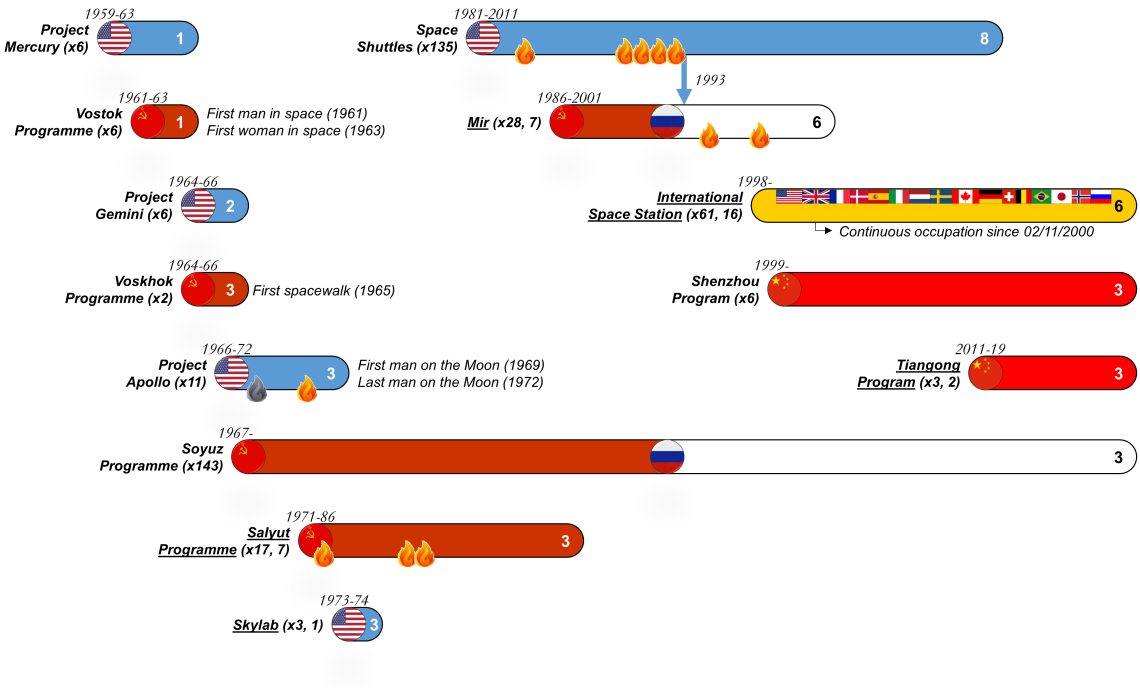

Figure 1.1: Manned Space Exploration as of 2021. Underlined names indicate space stations; the number in brackets, preceded by a '×' symbol is the number of missions executed; the number of space stations, or modules assembled in space in the case of Mir and the ISS, is then specified; fire symbols mark the events listed in Tab. 1. The blue arrow shows the beginning of the Shuttle-Mir Program. Reproduced from Guibaud (2022) [4].

not only the causes and consequences of the incidents, but also the shortcomings of the specific firefighting strategies and operations.

Prevention

Whether the flame can be ignited is directly related to the atmosphere inside the module and the flammability of the materials.
In 1967, the incident in Apollo 1 gave a dramatic lesson. Although this incident did not occur in orbit, the cause of the fire was related to the module atmosphere design strategy of space exploration. During this period of the American space program, the module environment was designed to utilize pure oxygen atmospheric conditions. This is not only beneficial to the astronauts' subsequent spacewalk preparation procedures due to the high oxygen and low-pressure strategy, but also reduces weight and facilitates engineering control with the reduction of gas types. However, the higher oxygen content makes materials that are not flammable under usual conditions easier to ignite and subsequent flames more prone to spread [11]. The exact cause of the fire remains uncertain [12], but electrical wires and piping carrying combustible and corrosive coolants are considered the most likely source of ignition. The importance of the material selection and atmosphere settings was clarified through this incident. To determine the safety range of conditions for material use, the limiting oxygen index (LOI) then helps to identify the minimum oxygen volume fraction of the ambient atmosphere required for a material to sustain combustion in the environment considered. If the oxygen content used exceeds the LOI of the selected material it will increase the chance of fire and the rate of flame spread and growth. After the incident, more

Year	Spacecraft	Ignition source (* presumed)	Smoke/flames	Detection	Mitigation	Significant consequences
1967	Apollo 1	*wiring, *flammable coolant	flames	visual	no	Destruction of the CSM, death of three astronauts
1970	Apollo 13	*short circuit	flames	visual, instruments	no	Destruction of the CSM
1971	Salyut-I	fan mechanical failure	smoke	odour	power off	none
1977	Salyut-VI	*electrical	smoke	visual	power off	loss of scientific equipment
1978	Salyut-VI	*electrical	smoke	visual	water extinguisher	4 control panels lost: 1 to the fire, 3 to water
1983	Space Shuttle	wire fuse	smoke	odour	power off	none
1989	Space Shuttle	short circuit	smoke	visual, instruments	power off	none
1990	Space Shuttle	resistor overeating	smoke	odour	power off	none
1991	Space Shuttle	fan mechanical failure	smoke	odour	power off	contaminated atmosphere
1992	Space Shuttle	electronic failure	smoke	odour	power off	none
1994	Mir	failed cooling of the cloth filter	flames	visual	power off, quenched with jumpsuit	damaged canister
1997	Mir	*oxygen canister contamination	heavy smoke, flames	instruments	complete burn out	

Table 1.1: Summary of documented fire and smoke incidents in spacecraft. Reproduced from Guibaud (2022) [4].

than 100 full-scale simulated fire growth tests were conducted on the ground to find materials suitable for use in an oxygen-enriched environment and to understand where a fire could ignite and spread inside the redesigned spacecraft [13]. However, it is not realistic to find materials that are non-flammable in a pure oxygen environment while satisfying the relevant functional requirements.

In 1970, the Apollo 13 incident was assumed to have been caused by a short circuit that ignited the Teflon insulation used to coat the electrical wires in the oxygen canister, which was also in a pure oxygen atmosphere. This accident mainly demonstrated that besides material testing simply, the combination of heat and fuel should also be the main danger. In cases where both heat and fuel cannot be safely separated, it is critical to reduce the use of flammable materials in the presence of potential ignition sources and to improve ground testing procedures.

In contrast with the aforementioned American space program, Soviet spacecraft and space stations featured a standard sea-level atmosphere with 21% oxygen and 79% nitrogen at 101.3 kPa (14.7 psia) [14]. Under such atmosphere conditions, the flame spread rate and flame growth would be slower than in pure oxygen ones, thus limiting the potential consequences of accidental fires. One thing that should not be overlooked, however, is that oxygen in the module is produced by non-regenerative potassium peroxide cartridges, where this oxygen production process may lead to localized peaks of 40% oxygen content in the module, well above the LOI of most materials on board [15].

In 1974 NASA Handbook 8060.1A was formalized [16], which was a major new shift in fire safety strategy because it defined the flammability standards for space material testing. This NHB, again derived from aircraft regulatory requirements, provides a framework to control the various risks associated with each payload and its combinations [17]. To address the fire risk, the NHB indicated flammability, odor, and off-gassing requirements and testing procedures for materials in an environment that supports combustion. This procedure was further updated in 1998 and to date specifies that materials used in the habitable and non-habitable portions of the spacecraft must be tested for flammability, off-gassing, reactivity in an aggressive environment, and arc tracking of electrical wires under normal gravity [18].

Throughout these incidents, it is very difficult to completely avoid fires because of objective needs. Therefore, in addition to understanding the impact of atmosphere settings and material flammability on fire, it is also important to have strategies and measures in place once a fire has occurred.

Detection

The first question about firefighting in the module is how to identify whether a fire has occurred, and this question is related to fire detection. The fire detection system has been improved with the development of space exploration. Excluding the three fire incidents that threatened the crew's lives, all of the remaining nine fire incidents were detected by the visual or odor senses of the crew. In the early stages of space exploration, the crew was able to respond relatively quickly to fires because of the small space inside the module.

In the Salyut I and Salyut VI space stations, with volumes of 100 and 90 m^3, respectively, fire detection relied on a carbon dioxide analyzer. It was believed that a rapid increase in carbon dioxide levels could reveal unnoticed fires [19]. However, according to three accidents that occurred on these two space stations, the crew noticed the smell of burning or saw smoke before the alarm went off. Indeed, in the absence of natural buoyancy, the products of combustion flow away from the fire relatively slowly as forced convection and diffusion become the dominant transport mechanisms. This also leads to the possibility that the fire may grow to a larger size before it is detected. Reducing

the detection threshold may allow detectors to be more sensitive to combustion products, however, the odds of false alarms would increase at the same time [20].
Space Shuttle was equipped with a fire detection system built from ionized smoke sensors [21, 22], with nine of the sensors on board the orbiter and six in the space laboratory to optimize the response time in the absence of natural convection. However, none of the five accidents that occurred were able to trigger the detection system. At the same time, 14 false alarms or built-in test failures were reported on board the Shuttle [23]. Mir was also equipped with a fire detection system based on optical smoke detectors [24]. In the 1994 incident, it was the crew who identified the fire when they saw smoke. In the 1997 incident, the fire alarm was activated only after the crew noticed it.
The reason for the poor accuracy of the alarms stems from the lack of knowledge about the characteristics of fires in low gravity. Without accurate knowledge of the size distribution of particles released during a fire event, sensors rely on gross assumptions about particle size to distinguish between smoke and ordinary dust particles thereby increasing the potential for false alarms.

Mitigation

In case an emergency is realized, appropriate and prompt treatment is very crucial. The incident on Apollo 1, which took place in a very short time, engulfed the crew in the fire before they could react. Regarding the Apollo 13 incident, the astronauts were able to communicate with the ground crew and decide on the appropriate countermeasures in time, resulting in an excellent rescue operation by escaping to Earth via the lunar module. However, both accidents occurred too quickly and the crew did not have the time to take appropriate measures to mitigate the fire.
From the remaining incidents, it is evident that the majority of fire mitigation is through power shutdown. The layout of the spacecraft is complex, and power shutdown can block the continuous supply of heat sources as much as possible until the exact location of the fire source is determined. This is indeed an effective technique before the fire has progressed enough for a spontaneous combustion situation. Yet once the fire has progressed to the point that combustion can be maintained by its own heat supply, this method will not work. In this case, the crew must intervene at the fire source, usually by using a fire extinguisher.
The use of fire extinguishers in spacecraft requires great care because it is likely to cause damage to the instruments inside the spacecraft due to the enclosed environment full of electrical appliances. In the 1977 incident on Salyut VI, Georgy Grechko suspected that the use of water-based fire extinguishers might damage the electronics [25], and therefore put out the flames by hand. His suspicion was confirmed by the incident that occurred in the same spacecraft in 1978. This incident produced heavy white-blue smoke that spread rapidly to the station [26], and the astronauts used extinguishers and tried to mitigate the smoke release, but the four surrounding control panels were shorted out during this process. Another incident in which fire extinguishers were used was in Mir in 1997. The crew wanted to use a portable fire extinguisher to release a water-based foam solution expanded by Halon 1301 [27, 28] to extinguish the fire. However, when the water-based foam passed through the flames, it produced hot vapors and increased smoke production. Finally, the astronauts changed their strategy and sprayed the foam on the surrounding walls to cool them down and prevent further fire development. This unexpected situation made the entire fire mitigation process more difficult.
Extinguishers can be found to have unexpected effects when used in reduced gravity environments. This needs to be avoided by further testing on the designed extinguishers in the appropriate environment. In addition, the astronauts should be trained to use the fire extinguishers in a way that avoids damage to the electrical devices as much as possible.

Cleanup

Smoke produced during fire events is also a threat that cannot be ignored. Large amounts of smoke in confined spaces can increase the stress of the crew and the produced smoke blocks their vision, which can be a significant obstacle to accident treatment [29]. This was noted in the incidents of Salyut VI in 1978 and Mir in 1997.
Another point is that these smokes can be harmful to the human body. Although astronauts wear protective masks during fires to avoid inhaling toxic gases, the smoke remains in the enclosed module after the fire has occurred. For example, after an accident in Mir in 1997, while the smoke was filtered by the Environmental Control and Life Support System (ECLSS), the lack of air assessment capabilities resulted in the need for the crew to wear masks continuously and undergo repeated lung and blood checks for the following 48 hours [30].
Hence, for the health of the crew and the sustainability of the module, it is essential to build up an effective post-disaster cleaning procedure and provide appropriate cleaning equipment.

1.1.2 Present fire safety strategies

Present active manned space exploration programs have not reported any major fire incidents. This can be mainly attributed to the continuous updating of fire safety protocols and the corresponding low-gravity experiments that complement the fundamentals. In particular, the International Space Station (ISS) is the largest manned station ever constructed and continues to be in service more than two decades later. The shortcomings in fire safety protocols revealed by past fire incidents have been refined in the current fire safety strategies used on the ISS. The following describes the improvements in current fire safety strategies compared to those of the past, and thus identifies the parts that need to be strengthened.
The atmosphere used on the ISS is a mixture of 21% oxygen and 79% nitrogen, and the pressure inside is 101.3 kPa (14.7 psia). Since the atmosphere is similar to that on Earth at sea level, the astronauts can adapt easily. From a fire safety perspective, materials are less likely to ignite and flames grow and spread more slowly than in an oxygen-rich atmosphere. The constituting spacecraft are always tested according to the regulations in the NHB, which was revised in 1998 [18]. As mentioned previously, these tests cover the type of material (sheet, paint, insulated wire, etc.) in different atmospheric conditions, including flammability, flame spread, visible smoke release rate, and other aspects. Different atmospheric conditions are needed for testing because the extreme conditions in the International Space Station (ISS) can reach 23.9% oxygen content [31]. Some parts of the ISS also experience an atmosphere with reduced nitrogen levels for the preparation of the extravehicular activities, where the oxygen content can attain 32% [32]. In addition, in order to provide a more reliable test, the materials are processed into the original components (real size, shape, and structure) in their operational state and placed in the actual or simulated environment for fire characterization experiments. Overall, the idea of the measures taken is to use non-flammable materials or to use the materials with a slow flame spread rate in case they are flammable in the designed atmosphere. Then, the flammable materials should be separated by non-flammable materials, thus cutting off the flame propagation pathway effectively in case of fire. Moreover, the flammable materials are covered with non-flammable materials, so that they cannot catch fire. Furthermore, the overall design and layout minimize and isolate the path of flame propagation. This strict regulation was specified extending the relevance of the test results obtained

in normal gravity to the actual reduced gravity situation in the spacecraft. Realizing that different gravities may lead to different results for the tests, experiments in microgravity complemented the corresponding results and could report some lower LOIs that would occur at flow rates lower than those induced by natural convection [33]. This increases the concern about the possibility of a fire occurring in the spacecraft. Meanwhile, as materials specifically designed to withstand thermal degradation under normal gravity can be less effective in the absence of buoyant flow, minor wire degradation events similar to those experienced on the Space Shuttle were still observed on the ISS [34, 35]. Because the gap in knowledge about flammability and flame spread in reduced gravity situations has not been fully addressed, academic experiments in microgravity are still in progress to design and validate methods for inferring fire safety in the absence of buoyant flow from data obtained in normal gravity [36].

For fire detection, different modules of the space station have different detection strategies and equipment. The Russian orbital segment has 10 optical sensors and 13 ionization detectors. This large number of detectors is designed to prevent false alarms caused by dust, and the master alarm is triggered only in the case of multiple detector alarms. Furthermore, the modeling of airflow in the segment can be used to locate the source of the fire [37]. In contrast, the American, Japanese, and European modules rely on 17 optical sensors. Such sensors include a 2-channel laser diode, one channel sensing forward scattered light (30 degrees) while the other one is a zero-degree masking system to measure the attenuation of the laser beam. This system is designed to alarm based on the magnitude of the scattered light signal with reference to the beam intensity. It provides a certain level of dust discrimination based on the frequency analysis of the scattered light signal [38]. These sensors are primarily located next to the ventilation inlet grids to force air through them, and additional sensors are installed on different systems and payload racks to help the crew locate the source of smoke [39]. Where smoke detectors cannot be equipped, additional data monitoring is performed to track anomalous temperature peaks in the gas phase [28]. If there is a suspicion of air pollution, the ISS is equipped with six handheld Compound Specific Analyzers to identify the combustion products. The crew can then monitor atmospheric levels of carbon monoxide, hydrogen chloride, and hydrogen cyanide [40] and perform periodic checks on the power rack to detect any slow-burning fires. If threshold levels are exceeded, the crew is instructed to wear emergency masks to supply pure oxygen in case of smoke build-up. In the presence of visible flames, they wear masks that filter ambient air to avoid providing additional oxygen to the flames. For post-fire cleanup, this monitoring of the atmosphere also helps in the continuous tracking of air contamination so that the crew knows when the environment has reached a level that is not harmful to humans. However, the lack of knowledge and data on smoke generated in microgravity still leads to false alarms that interfere with astronaut life in space and mission performance. To improve the accuracy of fire detection, research is still ongoing on the production and morphology of smoke particles from the pyrolysis process and formed within flames in microgravity [41].

Mitigation equipment is also equipped in the International Space Station. Four types of fire extinguishers are available, for use in different situations. The Russian segment is equipped with OKP-1 spraying 0.8 L of foam agent pressurized by nitrogen with a pressure of 10.0 MPa. The foam can be delivered in less than 30 seconds to effectively mitigate fires on the appliances of the module [39]. This type of extinguisher is inefficient in the case of fire on clothes. Therefore, in this case, an extinguisher supplemented by a 2.5 L water-based ОСП-4 is to be used. This extinguisher can switch between foam or jet to provide adapted levels of humidity for different fire situations [42]. For the American, Japanese, and European modules, CO_2 portable extinguishers are used, which contain 2.7 kg of gas compressed at 58 atm and can be discharged within 45 seconds. This type of extinguisher would be the first choice in the case of fire in the rack to avoid damage to electrical equipment. However, in the Russian cabin, this extinguisher is forbidden to use due to

the presence of the primary CO_2 removal system Vozdukh [43]. Another type of fire extinguisher is a water-based extinguisher that produces a deionized water mist for about 50 seconds, producing droplets with a characteristic diameter lower than 100 μm to avoid the risk of electric shock to the crew in case of discharge on the electrical equipment. As with the previous spacecraft, flow and electrical shutdown are available to mitigate the supply of oxygen and heat. Depressurization is also possible once the affected modules are isolated. This set of equipment is designed to be flexible in different situations of a fire event and thus prevent further damage to the space station caused by fire extinguishers. Yet, this requires that the astronauts have sufficient training to be able to accurately decide which fire extinguisher should be applied in an emergency for fire mitigation. According to past experience, the difference in gravity environment may still bring unexpected situations. Therefore, practical tests of fire extinguishers in microgravity are necessary. This is also the critical knowledge that is lacking at present.
The above analysis of the present fire safety protocols from all aspects shows that there is a great improvement compared to the past. However, it is undeniable that potential fire safety hazards still exist because of the lack of knowledge about microgravity. Therefore, the relevant microgravity experiments are still ongoing and the research progress and some of the related results will be analyzed in detail in Section 1.2.

1.1.3 Additional deep space exploration challenges

Space exploration will not end in Low-Earth Orbit. Programs to establish a lunar settlement and send people to Mars indicate that the focus of space exploration today is moving from LEO to deep space exploration. The discussion above shows that the current fire safety protocols are focused on LEO programs. This change in space exploration emphasis increases the challenges and uncertainties for fire safety. This is mainly reflected in the poor understanding of lunar (0.16 g_0) and martian (0.38 g_0) gravity, which is between normal gravity and microgravity. In addition, the current technology solutions on the ISS are not designed for long-distance missions.

Lack of gravity fundamentals

Throughout the evolution of the fire safety protocol, its improvement relies on the continuous complement of knowledge related to microgravity. This implies that the knowledge of flame spread in partial gravity needs to be extended to develop reasonable fire safety strategies in the corresponding gravity. Fortunately, there have been no fire incidents in partial gravity, but the potential fire threat still remains because the difference in gravity is likely to affect material flammability, flame spread rate, smoke generation, fire detection, fire mitigation, and post-disaster cleanup. Unfortunately, partial gravity exhibits even sparser data than microgravity, which makes associated fire strategies more difficult to develop.
Partial gravity can be achieved by performing drop tower experiments using a centrifuge apparatus. Three solid fuels (Ultem® 1000, Nomex® HT90-40, and Mylar® G or Melinex® 515) were tested for their flammability in lunar and martian gravity and compared to normal gravity [44, 45]. Remarkably, all three materials could be ignited in lunar gravity at an oxygen content lower than in normal gravity. This reveals that the fire risk rating of the materials might change in partial gravity and calls into question the application of NASA's standard normal gravity test to partial gravity situations. Partial gravity experiments can also be performed in parabolic flight. The experiments regarding the upward and downward flame spread over a solid fuel have been conducted at

gravity levels from 0.05-0.6 g_0 including lunar and martian gravity levels. These studies have shown that downward flame spread peaks in close proximity to martian conditions, while upward flame spread increases linearly with increasing gravity [46, 47]. These unexpected tendencies show that more experiments are needed to understand whether flammability, flame spread rates, smoke production, and other fire-related hazards are positively or negatively altered in partial gravity fields.

Impact of increased space exploration range

Any lunar or martian deep space program now envisaged leads to conditions that are greater in range than any mission performed so far, which further reflects the importance of the fundamental scientific aspects. Any lunar or martian deep space programs now envisaged are greater in range than any mission performed so far, which further reflects the importance of the fundamental scientific aspects. With current propulsion technology, a one-way trip to Mars would take about six months, and it might take an additional 500 days on the Mars surface to wait for an ideal planetary alignment before flying back. Similarly, although the journey to the Moon is only a few days, a permanent lunar settlement could essentially last for many years. The expansion of exploration will affect fire safety strategies from different aspects.

Regarding the design of the atmosphere, the exploration vehicle will likely use a low-pressure atmosphere. The aim is to reduce the unavoidable leakage rate [48], reduce the structural load on the hull, and carry more weight. In addition, this will reduce the pre-breathing time before the ground-based extra-vehicular activity (EVA). The current atmosphere considered for the Gateway vehicle operating in microgravity conditions is 26.5% oxygen / 73.5% nitrogen mixture at 70 kPa (10.2 psia), while the inner volume of the lunar lander is expected to have a higher (34%) oxygen content at a lower pressure of 56.5 kPa (8.2 psia) [49]. For the Chinese manned lunar exploration program during the circumlunar flight and lunar settlement, the atmospheric configuration that will be used is 36% oxygen content at 58 kPa (8.4 psia) [50]. This increase in oxygen content puts additional pressure on fire safety. At oxygen levels above 30%, a wider range of materials will continue to burn to unacceptable levels. In addition, even though low pressure usually leads to lower flame spread rates, it also means reduced air cooling and increased risk of thermal runaway of electrical equipment.

In addition, because of the increased functional requirements, the material needs will become more demanding. However, the effect of partial gravity on the material flammability and also the atmosphere design in the module will hinder the choice of non-metallic materials. For example, long-term exposure to radiation requires stronger radiation shielding, which otherwise puts the crew in serious danger [51]. Since the radiation shielding materials used today are usually non-metallic, the nature and configuration of large shielding and covering elements must be evaluated very carefully from a fire safety perspective to avoid creating a significant fire hazard [52]. For smoke detection, the weak buoyancy caused by partial gravity can lead to different particle morphology from pyrolysis or flames, thus affecting the accuracy of detection. In addition, compared to microgravity, the increase of buoyancy in partial gravity may make the flow field inside the chamber more complex making it more difficult to locate the occurrence of fire. Besides, the increased mission distance and duration then require a higher level of self-sustainability in firefighting strategies. Current fire safety protocols rely heavily on emergency resupply and the ability to escape the station via the Soyuz spacecraft. This means that if an accident occurs and emergency equipment is depleted, the crew will be unprepared for the next accident.

1.2 Investigating fire in reduced gravity

The fundamental theory of combustion in microgravity or partial gravity is essential for the improvement of spacecraft fire safety. While the first Section focuses on the practical aspects of space fire safety, the following Section discusses the progress of scientific research. In this way, it will be possible to identify where the fundamental theory of combustion can be improved and to give reasonable suggestions for future fire safety in space exploration.

1.2.1 Reduced gravity facilities

The most direct approach to study fire safety in space is to conduct experiments in a low-gravity environment and observe combustion. Current facilities that can achieve a low-gravity environment and conduct experiments are drop towers, aircraft, sounding rockets, satellites, and spacecraft [53]. Three of these are ground-based facilities that provide free-fall or semi-free-fall conditions where gravity is counteracted by acceleration, thus achieving reduced gravity conditions. Each facility, including satellites and spacecraft, has different capabilities and characteristics that must be understood prior to conducting the associated experiments so that it can be determined which facility is the most appropriate.

Drop towers

The principle of the drop tower to achieve microgravity is to drop the experimental setup on a tall shaft. The existing drop towers can provide short-term experimental times ranging from 2.2 to 5.2 seconds, as determined by their height [54]. During this time, it can provide stable microgravity acceleration levels between 10^{-5} and 10^{-6} g_0, very close to the spacecraft features. In addition, the drop tower can accommodate large experiment packages with hardware weighing between 100 and 2100 kg, thus allowing the installation of important diagnostic systems. Moreover, compared to other facilities, it can perform a large number of experiments in a short period. The only drawback of this platform is the short microgravity duration, which in most cases is not enough for the flame to reach a steady state. Therefore, the scope of studies is limited to certain materials and combustible phenomena.
Regarding fire safety in space exploration, most studies have reported on flame propagation under quiescent or opposite forced flow. The characteristic time to establish a stable flame under such conditions can be achieved by using thermally thin fuels. Unless using extremely thin fuels or very low-density fuels, it is difficult to achieve stable flame spread experiments in drop towers [55]. It is also worth mentioning that partial gravity experiments can be performed using a centrifuge in a drop tower. As mentioned in the previous Section, Ferkul and Olson [44] and Olson and Ferkul [45] measured the LOCs of flame spread on solid materials in a partial gravity environment.

Aircraft

Aircraft can achieve microgravity or partial gravity environment through parabolic flight. As an illustration of the microgravity period obtained aboard the French airplane, each parabola starts at a horizontal altitude of 6,000 m. The pilot then steers the aircraft upward to 7,500 m. The aircraft will continue to rise with a positive 47° inclination to 8500 m and enter the microgravity phase. Then

the aircraft returns back to 7,500 m with a negative 47° inclination, and the microgravity phase ends. Finally, the aircraft will descend to a horizontal altitude of about 6000 m and will be ready for the next parabola. In most cases, the duration of the microgravity phase is about 20 to 25 seconds. The inclination of the aircraft is constantly changing during the trajectory to balance the air drag with the low level of engine thrust. The rigid-body acceleration of the experiment located in the fuselage away from the effective center of gravity constitutes an inherent microgravity inaccuracy of the platform [55]. Another major challenge is that the g-jitter effect due to the vibration of the aircraft during the parabola may have a negative impact on the results [46]. The accuracy of gravity level is $5x10^{-2}$ g_0. A standard parabolic flight campaign consists of three flight days with long flights of 3-4 hours each, containing 31 parabolas. After five parabolas, a 4-8 minute pause allows scientists to quickly analyze the experiment run and change parameters or experiment settings. Such a flight protocol makes the experiment more flexible than in unmanned facilities. This platform provides a longer microgravity time than any drop tower, and parts of the conditions can lead to flames that can reach a steady spread rate. Under this constraint, most of the relevant fire safety studies on flame spread have focused on opposed-flow conditions or stationary conditions.
Partial gravity conditions can also be attained with parabolic flight. Similar to the process of achieving microgravity, the gravity level of the aircraft can be controlled by reducing the inclination to reach lunar gravity or martian gravity. This allows the aircraft to have a longer duration in partial gravity than in microgravity conditions. The inclination angles for achieving lunar and Martian gravity are 42 and 38 degrees, respectively, and have low gravity durations of about 24 and 33 seconds. The first combustion experiments in partial gravity were performed by Sacksteder and T'ien [46] via a parabolic flight in order to observe the flame spread in a downward and upward configuration on thin cellulose tissue.

Sounding rockets

The last microgravity ground-based facility to be described is the sounding rocket. They consist of three main components, namely a single or two-stage solid fuel propulsion system, a service system (rate control, telemetry module, recovery system), and a scientific payload (the part that carries the instruments for the experiments). Sounding rockets are suborbital launch vehicles, which means that they do not enter orbit around the Earth. They can reach a peak altitude of more than 400 km. The rocket follows a parabolic trajectory from launch to landing. It provides a low-gravity environment for 6 to 13 minutes which is longer than the previously described facilities. Moreover, the accuracy of gravity level can attain 10^{-4} g_0 [56]. In addition, it can carry 150-480 kg of experiments, but the payload must be submitted to a critical gravity (10-40 g_0) during takeoff and landing [57], which raises a challenge for the durability and recovery of the experiment. Such long durations and high microgravity accuracy cannot be frequently achieved for logistical and cost reasons. This leads to questions about the reproducibility of the experiments performed. From a research perspective, longer microgravity durations contribute to the observation of stable flame spread. Studies on this platform have focused on the observation of proposed flame spread and concurrent-flow flame spread [58, 59].

Recoverable satellites

Free-flight satellites without crews also enable microgravity experiments. The satellite is launched into low Earth orbit up to 500 km above the Earth and can provide microgravity levels of 10^{-5}

g_0. Having a longer microgravity time compared to other ground-based facilities, its operating time can be up to tens of days [60]. Although the operating hours in microgravity are increased, it is less maneuverable since the experiment's setup cannot be modified once it has been sent. Moreover, the experiment preparation and data recovery times are longer than in the aforementioned ground-based facilities. So far, the experimental data on combustion is less than all other facilities [61]. The Chinese Academy of Sciences (CAS) conducted combustion experiments using the recoverable satellite ShiJian (SJ). They benefit from the long microgravity experiment duration to perform experiments that are difficult to achieve in ground-based facilities. Kong et al. conducted experiments on overloaded wire insulation and observed its ignition and combustion characteristics [62]. In addition, Wang et al. performed experiments on opposed-flow flame spread over thick solid material [63] and also smoldering experiments [64].

Space station

Conducting research on fire safety for space exploration at the space station is undoubtedly logical because this platform has ideal experiment duration and gravity level. From the facilities described previously, it can be found that there is a strong correlation between the level of gravity and the distance from the Earth. Skylab rotates between 434 km (perigee) and 442 km (apogee) above sea level, while Mir's perigee is 354 km and apogee is 374 km. Chinese space stations, meanwhile, operate between 375 and 391 kilometers above ground. The ISS is currently operating between 408 and 410 km, an orbit that can be considered perfectly circular given its 6,787 km radius. At 400 km above the Earth's surface, there is some residual atmospheric drag that slows down the spacecraft and decays its orbit [65]. To maintain the spacecraft's orbit and apparent weightlessness, corrective measures are required from time to time on the space station. The gravity level on the space station is 10^{-5} g_0. At this accuracy level, the microgravity level is actually set by parasitic phenomena such as instantaneous impulsive accelerations propagating through the spacecraft structure and vibrations of the equipment [66]. However, the acceleration caused by some single events may not be negligible, and it can cause instantaneous acceleration levels of about 10^{-3} g_0 [67].
Overall, the space station still provides the best environment for conducting scientific experiments on combustion. Yet factors such as weight, size, safety, and crew manipulation still pose some limitations to the experiments. To address these limitations as much as possible, an international experimental team deployed a series of experiments in a resupply cargo vehicle named Cygnus [68]. After supplying the ISS, this resupply cargo vehicle flies in the last few orbits before entering the atmosphere. During this period, combustion experiments are performed and data are downlinked before Cygnus is destroyed. Such microgravity facilities provided a series of real scale fire experiments to investigate the effects of microgravity on flame characteristics.

1.2.2 Laminar diffusion flame configuration

Knowing the different ways to achieve a microgravity environment, the question that arises is what configuration of flame would be relevant to the study. A simple configuration in microgravity can facilitate the subsequent development of theoretical models and numerical simulations to support the interpretation of the effects caused by microgravity. From an experimental point of view, it is also important to simplify the complexity of the experiment as much as possible to make it easier to perform experiments in different microgravity facilities and to optimize the reproducibility of the experiment. This Section describes the laminar diffusion flame and explains the importance of

this configuration for the current research context.

Diffusion flame

Fuel and oxidizer are two indispensable elements in a combustion system. Depending on their distribution before ignition, they can be divided into premixed flames and diffusion (non-premixed) ones [69]. As the name implies, a premixed flame means that the fuel and oxidizer are mixed in advance at a molecular scale before combustion takes place. This configuration is involved in applications such as jet flames on flame stands, rocket and automotive engine combustion, and the development of deflagrations and blast waves in jet fields. In addition, the mixture ratio of fuel and oxidizer is controllable and can be modified according to the needs of the application [70].
In the case of diffusion flame, the fuel and oxidizer are separated before being ignited [71]. If the subsequent mixing between them is not fast enough before the chemical reaction starts, then the mixing and reaction will occur only in the thin reaction zone that separates them. Thus, the structure of such a non-premixed flame consists of three zones, with the reaction zone separating the fuel-rich zone from the oxidant-rich zone [72]. This reaction zone usually forms a continuous surface called a flame sheet. Combustion can continue as long as the fuel and oxidizer diffuse into the reaction zone where the temperature remains sufficiently high. This configuration is relevant for many practical applications, including power production, ground transportation, aircraft and spacecraft propulsion, industrial furnaces, and fire safety for ground and spacecraft, among others [55].
Fire can generally be classified as a diffusion flame. When combustible materials such as liquid fuels, wood materials, plastics, etc. are heated, they undergo thermal degradation and produce gaseous fuels. This gaseous fuel then diffuses into the air and mixes with oxygen where combustion occurs due to the heat. Most fires take place in this situation, where the fuel and oxidizer are initially separated. Hence, diffusion flame is of interest to the study of fire safety.

Laminar flame

Whether premixed flame or diffusion flame, a flame can be classified as turbulent or laminar depending on the characteristics of the fuel and oxidizer flows [73]. This can be defined by the Reynolds numbers of the flow as follows:

$$Re = \frac{U L}{\nu} \tag{1.1}$$

where U is the flow velocity, L is the characteristic length of objective, and ν is the kinematic viscosity.
On Earth, most practical flames are turbulent. However, it is usually very difficult to study turbulent flames directly in detail because the instability and distortion of turbulent flames limit the interpretation of flame reactions and transport processes [74]. Moreover, this poses a challenge to the reproducibility of experiments. Therefore, laminar flames are often used as a more tractable flame configuration to further study processes associated with turbulent flames since the gas phase processes in known laminar and actual turbulent flames are similar. These similarities can be used to perform a simplified analysis of turbulent flames [75]. Hence, a proper understanding of laminar flame is a prerequisite for a better interpretation of more complex turbulent flames.
Besides, it is worth mentioning the effect of gravity on laminar and turbulent flows. At normal

gravity, it seems that it is difficult to achieve laminar flames that can ignore the effect of gravity. Before discussing their relationship, it is important to focus on the effects of gravity on different transports, and some simple phenomenological considerations can help quantify their impact. The first is the relationship between gravity and molecular transport, which can be expressed in terms of the Grashof number:

$$Gr = (\frac{\triangle \rho}{\rho})\frac{gL^3}{\nu^2} \tag{1.2}$$

where $\triangle\rho$ and ρ are the characteristic density difference and mean density of the process respectively, g is the gravitational acceleration, L is a characteristic length scale of process and ν is the kinematic viscosity. If the effect of gravity is to be ignored so that a diffusion-dominated flame is obtained, then the Grashof number has to be $Gr < O(10^{-1})$ [76]. For a flame, $\triangle\rho/\rho \sim 1$ can be assumed according to the experimental observation. The viscosity of air under atmospheric conditions is $\nu \sim 10^{-5} m^2 \cdot s^{-1}$. Then, after Eq.(1.2), to form a flame under normal gravity that can ignore the effect of gravity, the size of the flame needs to be :

$$L < O(100\mu m) \tag{1.3}$$

Obviously, from an experimental point of view, it is very impractical to obtain a flame size of this scale. Although such a flame can be obtained, it is difficult for experimental observation and measurement. Therefore, it is unrealistic to obtain a diffusion-dominated flame at normal gravity. On the other hand, convective transport also plays a very important role in the flame. The relationship between gravity and convective transport can be described by the Richardson number:

$$Ri = (\frac{\triangle \rho}{\rho})\frac{g\,L}{U_{fl}^2} \tag{1.4}$$

where U_{fl} is a characteristic forced convective velocity of the flame. To achieve a situation where gravity can be neglected and to obtain a force convection dominated flame, Richardson number has to be $Ri < O(10^{-1})$ [77]. It can be found that increasing the forced flow rate can relatively reduce the effect of gravity. However, it can be noted that this will increase the value of the Reynolds number and is not likely to lead to a laminar flame. Actually, the Reynolds number can be obtained by the ratio of Gr and Ri as follows:

$$Re = (\frac{Gr}{Ri})^{1/2} \tag{1.5}$$

For example, a flame with a typical length of 10 mm at normal gravity is discussed. If this flame is required to be dominated by the forced motion in front of the buoyant motion, it means that the Richardson number is $Ri < O(10-1)$. In this case, from Eq.(1.2), the Grashof number can be obtained as $Gr \sim 10^5$. Meanwhile, its Reynolds number is $Re > 10^2$. This value is greater than the Stokes flow regime ($Re < 1$) while also exceeding the range of laminar flow considerations [78]. Hence, at normal gravity, it is very difficult to realize laminar flame without the influence of gravity, which means that there is no alternative to performing experiments in microgravity.

1.2.3 Opposed-flow flame spread over a solid fuel

The study of laminar diffusion flame can be based on different types of fuels. From the fire safety point of view, based on past fire incidents in space exploration as discussed in Section 1.1.1, there is a high probability of flame spreading over solid fuels. And most of the combustible materials in spacecraft are in solid form. Therefore, the understanding of solid combustion is essential.

In addition, practical fires usually have spreading characteristics. Once their characteristics are well understood, measures can be implemented accordingly. For example, for a material that is already burning, the flame will continue along the fresh fuel. If the heat transfer from the flame to the fresh fuel can be suppressed, the flame will self-extinguish due to the lack of continuous fuel supply. The corresponding strategy to inhibit its propagation requires knowledge of the spreading mechanism. At the same time, this also coincides with the basic idea of the standard flammability test, after all, the non-flammable material implies that the flame cannot spread continuously over its surface. Therefore, the understanding of the spreading mechanism can also reveal the reason why the material is flammable or non-flammable, which will give a clearer idea of the material selection. Hence, mastering the flame spread mechanism in microgravity is critical to specify fire safety standards in spacecraft.
Flame spread is not the only concern in fire safety. There is also another form of flameless combustion spread known as smoldering, which is a slow, relatively low-temperature, flameless combustion [79]. The difference between smoldering and flame spread is that smoldering occurs on the surface of a solid rather than in the gas phase. Smoldering is a surface phenomenon, but in the case of porous fuels, it can spread to their interior. Although the combustion characteristics of smoldering are weaker compared to flame spread, it is still a significant fire hazard [80]. Smoldering releases toxic gases with a higher yield than a flame spread and leaves a large solid combustion residue [81]. The emitted gases are flammable and may subsequently ignite in the gas phase, thus triggering a transition to flame spread [82]. Therefore, this is also an important research aspect for fire safety improvement [83, 84]. However, due to its slow propagation characteristics, it takes a relatively long time to reach a steady state. Thus, it is difficult to conduct microgravity experiments in ground-based facilities, resulting in fewer experimental data in microgravity. Because of its specificity, this phenomenon is not investigated in this thesis. The following discussion will focus on the mechanisms of flame spread and the effects of microgravity.

General description of flame spread in two dimensions

Most flame spread on solid fuels takes place at the surface and is two-dimensional. Diffusion flame spread over solid fuels requires preheating of the neighboring colder virgin fuel. As the flame approaches, the virgin fuel gradually warms up to its pyrolysis temperature (typically 500-700 K) and starts to produce gaseous fuel [55]. According to the nature of the solid fuel, the type of pyrolyzed fuel can be different. In addition, the pyrolysis process undergoes a temperature gradient depending on the distance of the material from the heat source, resulting in different pyrolyzed fuels produced [85]. The pyrolyzed fuels are mixed with air or other types of oxidizers, then a combustible mixture is formed. The flame acts as a heat source and thus ignites the combustible mixture, which drives the flame onward to the colder virgin fuel.
Three different zones can be discriminated within the flame spread mechanism, i.e. the stabilization zone, the pyrolysis zone, and the preheating zone. Each of these three zones experiences different dominating phenomena with specific characteristics. The stabilization zone is the first location where the reaction between the oxidizer and the pyrolyzed fuel takes place. The pyrolysis zone is the region where the solid fuel starts to pyrolyze and the pyrolyzed fuel is released. The preheat zone is the region where the solid fuel has been heated by the flame but has not yet reached the temperature at which the pyrolyzed fuel can be produced. The location of these zones is different depending on the configuration of the flame spread.
In a usual way, flame spread over a solid can be classified based on the direction of flame spread and the direction of oxidizer flow. The two different spread configurations are presented by a flame spread over a thin solid in Fig. 1.2. Their typical examples are presented in the figure, which

is helpful to discuss the mechanisms in both configurations. Opposed-flow flame spread (Fig. 1.2 (a)) is when the flame spreads in the opposite direction of the oxidizer flow, with the flame located above the fuel, and then the hot product from the flame naturally convects away from the unburned surface. In contrast, concurrent-flow flame spread (Fig. 1.2 (b)) is when the flame spreads in the same direction as the oxidizer flow, and the hot product from the flame is convected along the unburned surface. From the examples in Fig. 1.2 where the gravity direction is parallel to the solid fuel, the oxidizer flow can be governed by the difference in pressure (forced flow) or by the difference in density between the ambient and the flame in the gravity field (buoyant flow). Thus, on Earth, upward and downward propagation of pure buoyant flow or propagation of mixed buoyant and forced flow can be observed. However, in microgravity, the flow direction of the oxidizer is determined purely by the forced flow.

Figure 1.2 also shows the positions of the three different zones mentioned above in two different

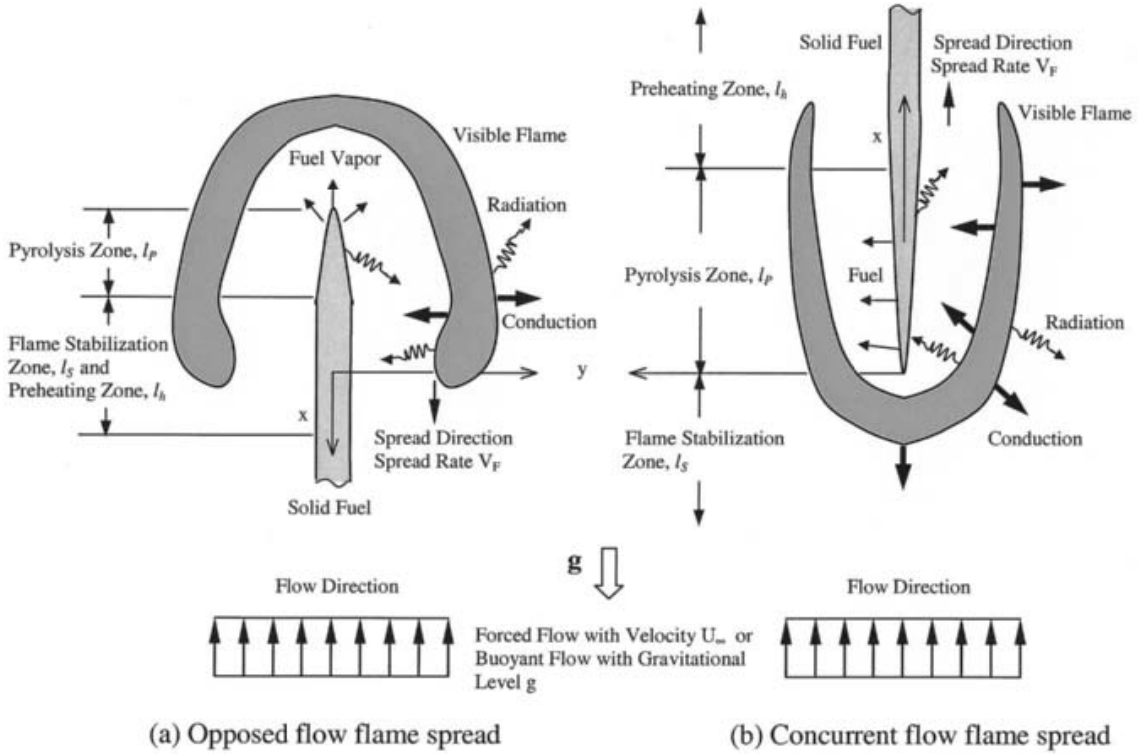

Figure 1.2: Two dimensional schematics of flame spread over a thin solid fuel in opposed-flow (a) and concurrent-flow (b) configurations. Reproduced from T'ien et al. (2001) [86].

flame spread configurations. For both configurations, the stabilization zone is located in the upstream region. These zones are affected by the flow velocity. In buoyant or high-speed flow, the volume covered by the stabilization zone is almost negligible, while the pyrolysis and preheating zones cover most of the volume around the flame. At low velocity flow, as occurs in microgravity, the size of the stable stabilization zone enlarges, while the pyrolysis length and the preheat length decrease [55].

To some extent, the flame spread is the process of transition from the preheated zone to the pyrolysis zone. Therefore, it is essential to define the boundary between the pyrolysis zone and the preheated zone for the heating of the solid fuel. A thermal thickness is consequently used to define the boundary between the two types of heat transfer in the solid [87]. A solid fuel is thermally thin when the heat conduction time throughout the solid thickness is much shorter than the residence time of the flame in the preheating zone. This property is related to the thickness δ_s of the material

as well as its own thermal conductivity λ_s, so that a thermally thin solid can be defined as follow :

$$\delta_s << (\frac{\lambda_s \, l_h}{V_f})^{1/2} \tag{1.6}$$

where l_h is the characteristic length of preheating zone and V_F is the flame spread rate. In this case, the temperature gradient through the solid's depth is considered negligible. The thermally thick case is the opposite of this, where the temperature gradient presented through the solid's depth is not negligible. This distinction through the thermal thickness of the material can drive the design of microgravity experiments [88]. In most microgravity flame spread experiments, especially in ground-based facilities, thermally thin solids are applied. Because they have a shorter time scale, they are more suitable for experiments with shorter microgravity duration. In addition, thermally thin materials also facilitate the development of models because the heat transfer in a solid will be easier to express as well.
The heat transfer in two different flame spread configurations can be analyzed in the gas phase and in the solid phase, respectively, which is shown in Fig. 1.2. In the gas, phase the heat generated by the reaction can be transported by convection, diffusion, and radiation. In the solid phase, heat is transferred by conduction from the stabilization and pyrolysis zones to the preheated zone to promote flame spread. However, if the solid has high thermal conductivity, the preheated zone may act as a heat sink to dissipate the heat far away. Besides, depending on the nature of the solid itself, it is possible to lose heat through surface radiation and thus slow down the flame spread process. These heat transfer mechanisms can be used to predict the flame spread rate, and related models are always being developed and improved [89–93].
Although the general heat transfer pattern does not change, the dominant heat transfer and the complexity of the model could be different according to the configuration of the flame spread. Since convection is generally more efficient than conduction, the concurrent-flow flame spread is usually faster than opposed-flow flame spread under the same conditions, which causes more issues for the model and the experiment (e.g., more difficult to reach laminar flame). As the opposed-flow flame spread is more stable in general, the past published models and experiments in reduced gravity more focused on opposed-flow flame spread [94]. Considering the stability of flame spread and the available related research, the experiments conducted in this thesis are based on the opposed-flow flame spread. The following discussion will focus on opposed-flow flame spread over a thermally thin solid to analyze the existing various time scales and the dominant heat transfer modes in different cases.

Opposed-flow flame spread in microgravity

From the analysis above, it can be found that flame spread and flammability in opposed-flow are controlled by the feedback between the flame and the fuel surface at the leading edge of the flame. It shows the importance of upstream heat transfer in the gas phase for flame stabilization at the solid fuel surface. In the case of reduced gravity, this upstream heat transfer is governed by the incoming flow relative to the flame because it determines the oxidizer supply. This incoming flow velocity is provided by the spread of flame to the fresh oxidizer:

$$U' = V_f + V_g. \tag{1.7}$$

where V_f is the flame spread rate and V_g is the opposed-flow velocity. In past analyses, three regimes have been identified based on this incoming flow velocity: the blow-off regime, the quenching regime, and the thermal regime. These three regimes help to explain the dominant heat

transfer modes during flame spread or extinction [94].
The blow-off regime is an extinction phenomenon that occurs at a high speed of incoming flow. This regime can be characterized by comparing two time scales. The first time scale is the residence time τ_r of the gas mixture in the flow and is given by the ratio of the characteristic length of the heat conduction of the flame through the gas to the characteristic velocity of the gas flow. It can thus be expressed as:

$$\tau_r = \frac{\alpha_g}{U'^2} \tag{1.8}$$

where α_g is the average thermal diffusivity in the gas phase. The second time scale is the characteristic time of the first-order reaction related to fuel and oxygen, which is called chemical time and can be expressed as:

$$\tau_{ch} = \frac{\rho_g}{Y_F\, Y_O\, p^n\, A_g\, e^{-\frac{E_a}{R T_{fl}}}} \tag{1.9}$$

with mass fractions of fuel and oxygen Y_F and Y_O, pressure p, pre-exponential factor A_g, universal gas constant R, flame temperature T_{fl} and activation energy E_a. Quantifying the relative importance of the residence time and the chemical one leads to the definition of the Damköhler number Da:

$$Da = \frac{\tau_r}{\tau_{ch}} \tag{1.10}$$

The blow-off regime occurs at low Damköhler numbers. In such a case, the extinction is associated with an increase in the incoming flow rate. At the same time, chemical time becomes more important [90]. In this case, the residence time of the fuel in the flame is not enough to complete the exothermic chemical reaction, so the requirement of upstream heat transfer becomes unsustainable and the flame spread is terminated. On the one hand, incomplete chemical reactions reduce the heat release and the overall heat propagation upstream is reduced. On the other hand, an increase in convection velocity inhibits the upstream spread of flame heat [88]. Therefore, extinction or flameless propagation occurs if Da falls below a critical value. In the case of microgravity, this phenomenon is associated with the forced flow. In contrast, if it is in the case of partial gravity, the effect of buoyant flow is also to be taken into account.
The quenching regime is the opposite of the blow-off regime. This regime is found in flames spreading at low incoming flow velocity. In such flames, the relative radiative importance becomes significant due to the decrease in convection [95]. In this radiative heat transfer-dominated mode, it has been demonstrated that the extinction limit occurs when Da becomes large enough [96]. This extinction mode can be interpreted as occurring when the rate of radiation loss from the gas phase exceeds the rate of heat released by combustion. It was predicted theoretically [97] and demonstrated experimentally [33, 98]. At normal gravity, the flow velocity due to natural buoyancy does not satisfy the low flow velocity presented here, so this extinction mode can usually only be observed at reduced gravity. It is worth mentioning that this extinction mode is also observed in partial gravity [47].
The thermal regime is in between the two extinction methods mentioned above. This regime has a moderate Da value thus preventing blow-off and extinction. The focus of this regime is to predict the flame spread rate. As time progressed, many different models were developed. There are two representative theoretical model approaches. The theoretical model proposed by de Ris is constructed by heat transfer mechanisms in the solid and gas phases [87]. This theoretical model can well describe the experimental data away from the blow-off and quenching regimes [99]. Instead of deriving the flame spread rate through various heat transfer mechanisms, Emmons proposed to solve the flame spread problem through a boundary layer type approach [100]. This boundary layer theory demonstrates that the pyrolysis rate of condensed fuels can be expressed

separately as a function of the Spalding mass transfer number. This model relaxes the assumptions of constant flow rate, density, conductivity, specific heat, and diffusivity. Subsequently, this type of analysis was adopted in many applied problems [97, 101–104]. Both types of model bases focus on solving the energy and species concentration distributions in the preheat and pyrolysis zones, yet do not provide relevant results for the stabilization zone [105]. At high incoming flow velocity, it was noted that the volume covered by the preheat and pyrolysis zones is much larger than that of the stabilization zone, thus reducing the importance of the stabilization zone. However, the stabilization zone becomes critical when studying near extinction conditions [106, 107]. It is worth mentioning that none of these two models directly incorporates the effect of radiation. However, it has been reported that the importance of radiation increases with decreasing gravity, in which case thermal radiation should be taken into account.
Although this thesis is mainly experimental, the understanding of the basic theoretical model helps in the subsequent analysis of the experimental data. In addition, the effect of radiation in microgravity can be observed experimentally, which then helps to analyze its role in flame spread. The radiation in the flame is mainly emitted by the hot soot. Therefore, the quantification of soot can be useful for the optimization of theoretical models. Certainly, there are other interests in the study of soot, which will now be described in detail.

1.2.4 Soot particles and smoke emission

For flame spread, radiative heat transfer driven by soot is a key mechanism for flame-sustaining [108, 109]. Meanwhile, in fire safety, soot is associated with two different threats. On the one hand, the high temperature soot radiation is a threat to closed spacecraft. On the other hand, soot emitted by incomplete combustion of the flame becomes a potential suspect for smoke reporting in past fire incidences mentioned in Section 1.1.1. It is worth mentioning that the detection of flames is also dependent on the identification of soot particles that are present in smoke. Therefore, the understanding of soot particles in microgravity is critical, both from the perspective of refinement of the theoretical model and enhancement of practical firefighting strategies. The formation, growth, and oxidation of soot in flames will be described below. The macroscopic and microscopic observation and analysis of the effect of gravity on it will also be presented.

Soot formation, growth, and oxidation processes

Solid fuels usually degrade and release gaseous products when heated. Soot is an ultra-fine particle that is formed by a complex reaction of gaseous molecules released from solid fuels under certain high temperature conditions. This complex process is divided into several steps, including the formation of precursors, soot nucleation, soot surface growth, agglomeration, and soot oxidation, as shown in Fig. 1.3.
Fuel pyrolysis leads to the production of species that are precursors or building blocks of carbon-based soot (especially acetylene) [111, 112]. Soot precursors are considered to be polycyclic aromatic hydrocarbons (PAHs). Soot precursor formation is a competition between the rate of fuel pyrolysis and the rate of precursor oxidation by the hydroxyl radical OH. Both pyrolysis and oxidation rates increase with temperature, but the oxidation rate increases more rapidly [113]. In addition, the quantity of soot precursors depends on the nature of the hydrocarbons in the fuel. The hydrocarbons with high amount of carbon present in the chain or in cycles are more likely to lead to PAH production. The increase in the amount of PAH leads to a greater amount of soot production [114]. This may explain why different materials burn under the same conditions and produce different amounts of soot.

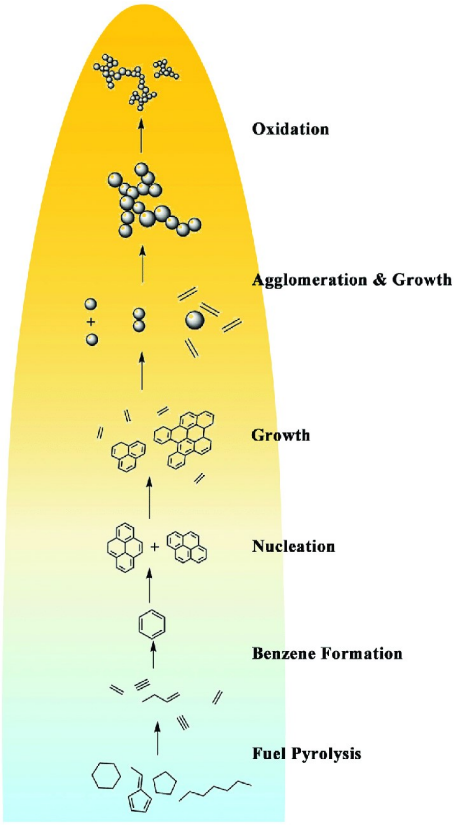

Figure 1.3: Schematic of soot formation, growth, agglomeration, and oxidation process from fuel pyrolysis. Reproduced from Xi et al. (2021) [110].

Nucleation is a very important step that converts the gas phase products into solid particles. The resulting particles are usually referred to as nuclei of soot. Surface growth is the process of adding mass to the surface of the nucleated soot particles[115]. The end of nucleation and the beginning of surface growth occur simultaneously. During this process, the thermally reactive surface of the soot particles readily accepts gas-phase hydrocarbons, which appear to be mainly acetylene. This leads to an increase in soot mass, while the number of particles remains constant [112]. Most of the soot mass is added during the surface growth process, therefore, the residence time of the surface growth process has a significant effect on the total soot mass or soot volume fraction. The surface growth rate of small particles is higher than that of large particles because small particles have more reactive radical sites [116]. The particles resulting from the nucleation process will also collide and coalesce, which reduces the number of particles and keeps the total mass of the two soot particles constant. While this process is occurring, two roughly spherical particles will combine to form a single spherical particle.

Aggregation is the process by which primary soot particles are combined. This process involves individual soot particles or primary soot particles sticking together to form large clusters of primary particles, called aggregate. The primary particles retain their shape, which is usually spherical. The combined soot particles form a chain-like structure or clumping of particles.

In the end, if the local temperature is high enough, the resulting soot aggregates will be oxidized when they are sufficiently exposed to the oxidant. It is worth mentioning that soot oxidation and formation mechanisms can be carried out simultaneously as long as sufficient quantities of reaction chemicals and heat are provided. Thus, the oxidation of PAH and soot particles is in competition with the formation of these species. This also explains why soot particles are formed on the fuel-rich side of the diffusion flame sheet [117].

Macroscopic observations

Soot in a flame can be described via the classic candle flame.
At normal gravity, the candle flame in a quiescent atmosphere is shown on the left side in Fig. 1.4. Flame spread over the candle is considered diffusion flame spread over a solid fuel. Soot forms in the fuel-rich area near the wick and grows within the candle flame envelope. As reactivity increases due to temperature increase [113], primary particles and agglomerates mostly appear near the stoichiometric region where reactivity is highest. This is where the formation and growth of soot aggregates are most important. Primary particles are too large to undergo molecular diffusion [118], so they are first convected by gas velocities and marginally affected by a second-order thermophoretic diffusivity [119]. Formed in a hot buoyant gas, they thus rise in the flame. Furthermore, once soot forms in a flame, its emission in the yellow to red spectral range becomes visible. This is why candle flames are usually observed to be teardrop-shaped under normal gravity. As they migrate, the temperature of the soot particles stabilizes around the temperature of the gas phase [120]. At local thermal equilibrium, primary particles and clumps radiate through Planck's law of blackbody since the low level of light reflection from soot reasonably justifies the application of Kirchhoff's law [121]. These radiative emissions tend to disperse the energy of the flame and thus reduce its temperature [118]. When soot particles encounter a sufficient amount of oxidant, two opposite fates occur: either the local temperature remains high enough to sustain oxidation and the soot is completely consumed, or the local temperature is so low that the soot oxidation reaction becomes inefficient. This radiation-related quenching is known as radiative quenching. In the latter case, soot particles are released into the atmosphere and form a smoke plume.

Figure 1.4: Candle flame at normal gravity in a quiescent atmosphere (left) and candle flame in microgravity with a very low velocity upward air flow (right).
Credits @NASA

In microgravity, the candle flame will gradually fade out in a quiescent atmosphere. In the absence of natural buoyancy, the combustion products increase and accumulate due to the initial high flame temperature, but the diffusion-dominated mass transfer is not sufficient to provide enough oxidant to continue the reaction and the flame is gradually extinguished [122]. Nevertheless, in the " Burning and Suppression of Solids I" (BASS-I) experiment conducted on the International Space Station in 2011, the candle was burned in weightlessness with a very low velocity air flow (as shown on the right side in Fig. 1.4) for simple comparison to the candle flame in a quiescent environment on Earth [123]. The added forced air flow is blown from the bottom. The effect of gravity on the candle flame is evident because of the difference in mass and heat transfer. The most obvious is the uniform oval shape of the flame, due to the lack of free buoyancy and the fact that

diffusion is the dominant mode of transfer. The soot from the burning makes the color yellow, indicating the hottest part of the flame. The maximum amount of soot is found at the opposite end of the candle. The blue color is produced by the chemiluminescence from the burning fuel. Compared to normal gravity, there is a tendency that the yellow part of the flame reduces, while the blue part increases. It is due to the lack of natural buoyancy that affects the mass transfer and thus disrupts the chemical reaction. The accumulation of combustion products and the slow supply of reactants to the flame sheet reduce the reaction rate. In addition, the new spatial distribution of intermediate species in the flame may promote new reaction paths while inhibiting others. If the chemical kinetics decay faster than the flame size, then species spend more time in the heat-rich region of the flame and their residence time increases. This increased time can promote unexpected new chemical reaction pathways. As a result, the chemical and thermal profiles of the flame are fundamentally altered. Such a change also affects the heat transfer, where the natural convective heat transfer disappears and the radiative heat transfer is modified by the temperature and chemical reactions [124]. Therefore, under the same conditions, such as fuel, oxygen content, pressure and fluid velocity, the flame products, including soot particles, will vary in different gravity cases.

Smoke point

The soot formation process of flame spread over a solid fuel configuration has not been investigated much. Instead, burners have been a powerful experimental tool for the study of soot. It can get rid of the influence of solid and liquid phases and control the nature of the gas phase of the inlet fuel, and provide a better understanding of the effect of gravity on laminar diffusion flames. If the solid fuel is axisymmetric, then the burner with coflow can provide a flame appearance similar to that of a steady opposed-flow flame spread over a solid fuel. The soot particle formation process in the flame of the burner can then be used as a reference.
Burners have the ability to change flame characteristics by varying burner diameter, jet exit velocity, fuel and ambient composition, and ambient pressure. Varying these conditions, it is possible to have a transition from a flame with smoke release to a flame without smoke release. This transition is called the smoke point. As shown in Fig. 1.5, it can be observed that the laminar flame in microgravity gradually appears as a smoke point in the co-flow burner under increasing fuel flow. The smoke point appears between the third and fourth flames in Fig. 1.5. The flame becomes longer as the fuel flow increases, the flame tip gets progressively darker and redder and transitions from closed to open. Whether at normal gravity or in microgravity, open-tip flames are common when the smoke point is far exceeded [125]. This is associated with local radiative extinction along the centerline and soot emission from the annular shell.

Smoke points are a common measure of the tendency of fuel sooting tendency in diffusion flames because they are the conditions associated with the initial soot emissions from a flame. For many gaseous, liquid, and solid fuels, smoke points have been measured under normal gravity and are useful in understanding various flame systems. There are four common explanations for the presence of smoke points. For the first one, the smoke point occurs when the soot temperature drops below the critical temperature before the soot is burned out [127, 128]. The second is that the fraction of radiation loss increases with increasing fuel flow thereby causing radiation quenching and the appearance of smoke points [125, 129]. The third explanation is that the ratio of luminous length divided by stoichiometric length increases with increasing flow rate [130, 131]. A fourth common explanation is flame residence time, where an increase in residence time can lead to soot emissions by increasing the time available for soot formation [111, 128, 132]. These explanations

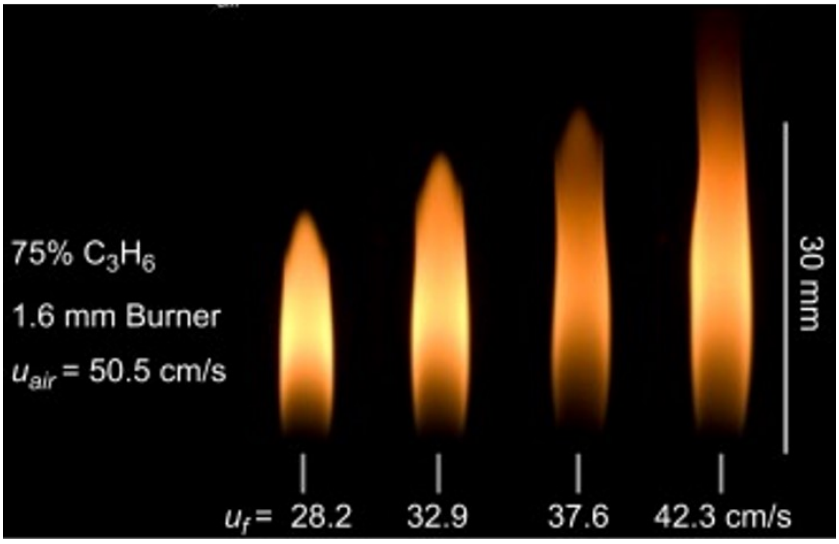

Figure 1.5: Laminar flames established over a co-flow burner in microgravity. Smoke point appears between the third and fourth flames when increasing the fuel flow velocity. Reproduced from Dotson et al. (2011) [126].

are not mutually exclusive and can interact with each other.
Smoke point measurements in microgravity are important for the fire safety of spacecraft. Microgravity can improve control of residence time together with the understanding of the different mechanisms of smoke point in normal gravity and microgravity. In particular, accelerated flow in normal gravity reduces the available time for soot oxidation, while decelerated flow in microgravity leads to radiative quenching of soot reactions. Different entrainment behaviors also lead to different smoke point behaviors in normal and microgravity.
Smoke point measurements in microgravity have given a large amount of valid data in the Smoke Point In Co-flow Experiment (SPICE) on the International Space Station. Using a stable closed laminar diffusion flame provided by a co-flow burner, the experiment was conducted in microgravity between 2009 and 2012. 250 combustion tests were conducted with various fuel mixtures, including propylene, propane and ethylene, and various co-flow rates. 55 smoke points were determined to obtain estimates of soot formation conditions and flame size [126]. It was shown that a decrease in diameter or an increase in co-flow velocity decreases the residence time and radiation loss rate, which in turn leads to a longer visible flame length at the smoke point. The tentative scaling method for residence time did not yield a quantitative correlation of smoke point measurements, but these experimental measurements were added to the smoke point database to understand the effect of fuel on smoke point.

Microscopic observations

From macroscopic observations, the appearance of smoke points is strongly correlated with the soot formation process. Especially, in microgravity, the residence time within non-buoyant flames is significantly longer than that of buoyant flames of the same size, and therefore longer characteristic times for soot nucleation, growth, and oxidation are expected [133]. Thus, the study of soot aggregation and oxidation characteristics through microscopic observations will help further understand the reasons for the appearance of smoke spots. In addition, the knowledge of the properties of non-fully oxidized particles is essential for the development of effective fire detection methods.

The agglomeration phenomenon of open-tip diffusion flames has been documented in experiments using drop towers. Fujita and Ito observed the soot aggregation process in jet diffusion flames using the laser shadowing method to evaluate the soot aggregate diameter and soot volume fraction [134]. Figure 1.6 shows a diffusion flame in normal gravity and in microgravity. The conical flame in normal gravity becomes a larger spherical shape in microgravity. The brightness of the flame is higher in normal gravity than in microgravity due to the adequate air supply to the combustion zone. It is noteworthy that in microgravity, the emission of large soot agglomerates was observed at the top of the flame. Eventually, based on measurements, soot agglomerates were found to be much larger than in normal gravity flames, with a maximum size of more than 100 µm. After aging, the size of soot agglomerates increased naturally with the distance from the burner exit.

This highlights the interaction of a large number of primary soot particles that collect on an

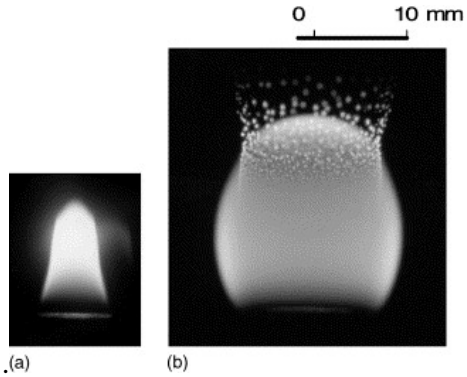

Figure 1.6: Comparison of propane jet diffusion flames at normal gravity (a) and in microgravity (b). Reproduced from Fujita and Ito (2002) [134].

agglomeration line in the rich side of the flame. This is because soot particles are mainly convected at local flow velocities, which change radically in microgravity. Thus, the behavior of soot particles in buoyant and non-buoyant laminar diffusion flames is very different. The accumulation along the agglomeration line is related to the thermophoretic force: primary particles formed in the flame are located in a steep temperature gradient field on the fuel-rich side and therefore have a drift rate toward lower temperatures [134]. The long residence time in the flame, the low local flow rate, and the high oxygen concentration of the surrounding ambient air promote the agglomeration and growth of soot particles. The large agglomerates are uniformly distributed near the flame sheet so that a circular extinction zone is observed in the open-tip flame.

In addition, Ku et al. [135] and Konsur et al. [136] sampled soot particles from a laminar diffusion flame in a drop tower experiment and analyzed the primary particle size and aggregate size by transmission electron microscopy (TEM). Longer residence times in microgravity were found to promote soot formation and growth, and the average primary particle size was twice as large as that observed in normal gravity. Following experiments aboard the space shuttle, Urban et al. [128] also performed soot sampling with the thermophoretic technique for laminar diffusion flame and outlined that soot primary particle size increases with distance from the burner, and that increasing ambient pressure tends to increase particle size.

These microscopic observations of soot particles in diffusion flames established over a gas/gas burner have led to a better understanding of the soot formation process in microgravity. However, it also demonstrates the challenge of detecting soot particles in microgravity that have a different morphology than in normal gravity. After all, all existing smoke detectors on the International Space Station (ISS) today are designed and calibrated based on fire data from normal gravity experiments [5, 6]. So the difference in soot morphology leads to an issue with the accuracy of flame detection. In addition, the research on soot formation has been carried out on burners, and it is necessary to complement the knowledge on soot formation during flame spread over solid fuels. Indeed, there is a high probability that a fire will occur on solid fuels.

1.2.5 Key results in reduced gravity

The investigation of flame spread over solid fuel samples in microgravity has significant implications, both from fire safety and combustion theory point of view. Based on the previous discussion the following advantages can be identified. The ability to study flame spread in a purely buoyancy-free environment is critical to the understanding of the low-velocity quenching regime. In addition, it is easier for the flame to reach laminar form in microgravity, which is crucial for the refinement of simple laminar flame theory. The stabilization zone of flame spread increases in microgravity, and further studies of this region can complete the understanding of flame spread near extinction. In the case of reduced convective heat transfer, the radiative transfer becomes more important and cannot be neglected. The observation of flame radiation under microgravity experiments can help fill this knowledge gap. Eventually, understanding the soot formation mechanism as affected by gravity will further contribute to the comprehension of flame radiative transfer in microgravity. The development of the above knowledge will lead to the enhancement of spacecraft fire safety through fire prevention, detection, and fire control strategies.
Based on this context, relevant experiments have been performed on different microgravity facilities in numerous projects. The applied experimental samples can be different depending on the purpose of the experiment. In order to comply with the available test time and subsequent theoretical model construction, most of the microgravity flame spread experiments have been performed using thermally thin solids [55]. Some key data on flammability and flame spread will be described below to expose the earlier experiments relevant to this thesis.

Flammability

Flammability has received the highest attention from the fire safety community. This attention is driven by the ambition to develop new fire safety standards for materials used in the microgravity environment to avoid repeating the past failures described in Section 1.1.1. Usual tests of fire safety at normal gravity rely on extinction criteria [18]. Since blow-off and quenching conditions are largely influenced by gravity, extinction has been well documented to provide baseline data under varying flow conditions and geometries in microgravity [137].
The key result extracted in the academic configuration is the finding of a U-shaped flammability limit in the flow rate/oxygen content space, presented in Fig. 1.7a and in Fig. 1.7b. The quenching and blow-off regimes are presented in the figures, respectively, proving a decent experimental and theoretical agreement. According to this map, the Minimum Limiting Oxygen Content (MLOC) [1] can be defined as a material property. This result is crucial to define a new standard test for flammability based on the MLOC property.
The new flammability standard test was inspired by the Lateral Ignition and Flame Spread Test (LIFT), an established American Society for Testing and Materials (ASTM) standard test method under normal gravity (No. E 1321) [139]. It consists of a series of experimental ignition delay and lateral flame spread tests performed in still air by irradiating a sample of solid material with a radiation plate to produce a heat flow of known intensity and distribution. The data obtained with the LIFT instrument are used to construct flammability maps of the material, which consist of curves of ignition delay and flame spread rate as a function of externally applied radiation flux.

[1] Minimum Limiting Oxygen Content (MLOC) can be defined as the Minimum LOC in a wide range of external flow velocity.

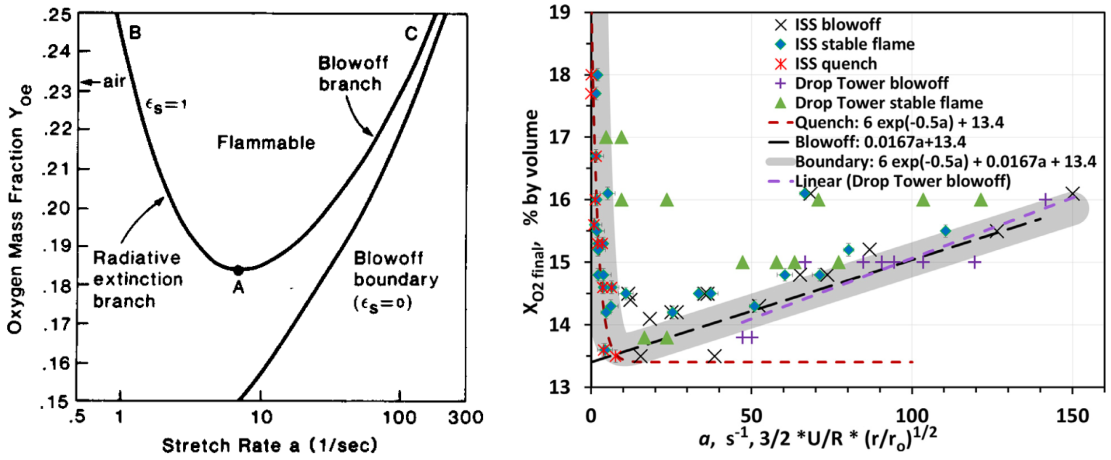

(a) Theory of the existence of the MLOC.

(b) Experimental validation in microgravity.

Figure 1.7: (a) Prediction of the existence of two distinct branches of extinction boundary in microgravity, reproduced from T'ien (1986) [96]. (b) Experimental confirmation over cylindrical samples, with a normalized stretch rate, reproduced from Olson and Ferkul (2017) [138].

These flammability diagrams derive the minimum heat flux for ignition from the flame spread and ignition delay data and can be used to calculate the flammability properties of this material.
However, this test method cannot be applied directly due to the quenching phenomenon that occurs when combustion takes place in quiescent atmospheres under microgravity. Therefore, in the modified LIFT apparatus known as Forced Flow Ignition and Flame Spread Test (FIST), additional flow along the length of the sample and parallel to its surface is provided [140, 141]. This design allows the study of MLOC of different materials. Results obtained on a number of materials in the drop tower, parabolic flight, and space station experiments show that MLOC in microgravity may be smaller than in normal gravity [142]. More than that, some cases highlight that the safety ranking of the material can change between normal and micro-gravity [143, 144].
This difference highlights the variation in flame extinction mechanisms and raises questions about the possibility of similar differences in spread mechanisms. Therefore a series of flame spread experiments were also conducted in microgravity thus studying the flame spread mechanism in microgravity.

Spread over solid fuels

To address the flame spread mechanism over solid fuels, because of the constraints of microgravity experiment duration, the main experiments are performed on the ISS or spacecraft. Corresponding experiments are the Burning and Solid Spreading (BASS) on ISS and the Spacecraft Fire Experiment (Saffire) on the Cygnus resupply vehicle. These two experiments will be briefly described below.
BASS is equipped with a wind tunnel configuration that can apply oxygen/nitrogen flow rates of up to 550 mm/s and oxygen content of up to 21%. It is also equipped with two high-quality cameras to record the experimental process from the front and the side. Thus, the flame appearance, behavior, diffusivity, and extinction dynamics can be captured. In addition, a radiometer allows the radiation emission from the burning system to be recorded. The experiments were divided into two rounds, i.e. BASS I and BASS-II. They contained a total of 141 fuel samples, which can be classified as follows: flat samples, solid spheres, candles within tubes, and stick samples. A brief overview of some of the experiments is given below. First is the effect of flat thickness on

flame spread and extinction [145]. After analysis, a boundary between thin and thick fuels is determined by comparison with thermal regime predictions. Scale arguments are also presented to show that the nature of radiative quenching at low opposed-flow velocity does not depend on fuel thickness but is closely related to the oxygen content [146]. In addition, ignition tests of PMMA rods under an external radiant flux were conducted to investigate the opposed-flow flame spread and quenching limits [147, 148]. The results show that the ignition time of solid combustibles exposed to external radiation flux in low-velocity oxidant flow is shorter in microgravity than in normal gravity, which indicates the loss of natural convective heat flow. Furthermore, the flame spread rate peaks at 17% oxygen content, which is lower than under normal gravity, and this spreading rate decreases with increasing rod diameter. Similar analyses were performed on thin and thick rectangular samples made of SIBAL and PMMA. With the variation of the flow rate, the quenching extinction phenomenon at low velocity and steady flame spread with limiting flame length were easily observed. The diffusivity, flame shape, and flammability limits obtained from these experiments were used to calibrate the detailed 3D transient numerical model. Last, due to concerns about MLOC, flammability tests on PMMA rods in a parallel flow configuration were also included in this experiment. MLOC was found at very low flow rates on the order of diffusion flow ([149]. This minimum occurs where the flow still allows sufficient heat release to sustain the flame but is not so strong as to sweep the fuel out of the hot flame zone before it can react [138].

Saffire conducted five series of experiments [68, 150]. In the Saffire-I and Saffire-III experiments, 40.6 cm by 96 cm SIBAL samples were ignited in a gas stream at atmospheric pressure with airflow velocities of 20 cm/s and 25 cm/s [49]. In both experiments, the samples were first ignited in opposed-flow and then quenched by shutting off the airflow after burning approximately 10 cm of the sample. After that, the ignition in concurrent flow was performed to obtain both propagations under each configuration. These large samples showed short pyrolysis lengths (40-50 mm) and slow propagation with a spread rate of approximately 2 mm/s. The propagation rates were significantly smaller than those previously observed in BASS-II for both configurations (opposed and concurrent flows) and both flow velocities (20 cm/s and 25 cm/s). The explanation comes from the unusually large size of the setup, which allows for better development of the flow boundary layer and limits the forward acceleration of the flow due to thermal expansion, which may affect the flow rate for the smaller BASS experiments. Saffire-II was fitted with nine samples of 50 mm by 290 mm [151]. Two SIBAL samples were ignited under conditions similar to Saffire-I and III in concurrent configuration to observe any size effect. Besides this experiment, the main purpose was to observe the flammability of the flame retardant fabrics material used for spacecraft. The recent Saffire IV and V experiments were conducted with a focus on practical fire safety measures [152]. Materials ignited included PMMA, cotton fabric, and cotton/fiberglass fabric blends. The samples were all 40 cm wide and ranged in length from 18 cm for the PMMA samples to 50 cm for the fabrics. Experiments included post-fire cleanup systems, vehicle interior volume measurements, and transport of acid gases (HCl and HF). In addition to some of the basic measurements of flames mentioned previously, distributed measurements of CO_2 concentration and temperature were performed at six locations in the spacecraft. The remaining relevant measurements are CO_2, CO, O_2, HF, and HCl concentrations, vehicle pressurized volume, and aerosol concentration.

Besides experiments conducted on space stations and spacecraft, shorter duration microgravity experiments also provide critical data on flame spread characteristics in reduced gravity. The main experiments are conducted using drop towers and parabolic flights. As described in Section 1.2.1, these two ground-based facilities can perform experiments frequently, and therefore the experimental data are relatively numerous. However, the duration of the transient regime in microgravity questions the steady-state observations reported in these facilities [49], and the changes in the flammability boundary with increasing microgravity time have been reported accordingly

[36, 153]. Still, conducting these ground-based facility experiments is an effective way to spark insight, develop experiments and conduct preliminary tests prior to any space station experiment design. This approach is currently being used for the Flammability Limits at Reduced Gravity Experiment (FLARE), a project selected by the Japan Aerospace Exploration Agency (JAXA). FLARE has mapped LOC and MLOC for flat and axisymmetric geometries to propose new fire safety criteria for the screening of materials to be used in spacecraft [154]. They have already used the drop tower [36, 142, 153, 155] and parabolic flight [156–159] results to design the appropriate experiment and test matrices for the ISS Kibo module.

Probing flames over electric wire

In addition to the research on flame spread over pure solid fuels, another important aspect that should be taken into account is the flame spread over combinations of solid fuels with other components. After all, the ignition of fire requires a heat source, and from past fire incidents, electrical equipment is the main culprit of fires.
Following reports of electrical hardware fires on space exploration vehicles in the 1970s and 1980s, it prompted the 1992 Wire Insulation Flammability (WIF) experiment [160] in the glove box facility on the space shuttle. This experiment investigated the effects of gravity on Joule heating of electrical wiring in quiescent and low velocity forced flow environments to enhance relevant spacecraft electrical system rating tests. Since the absence of buoyant flow can contribute to the occurrence of electrical overheating, the ignition and spread of flame on overheated wire insulation was observed in microgravity under concurrent and opposed low-velocity flows, and then compared with similar normal gravity results. Nickel-Chrome (NiCr) metallic wire (0.75 mm in diameter, 0.4 mm thick polyethylene coating) was ignited in the air flowing at approximately 10 cm/s under atmospheric pressure and composition. This pragmatic choice of material was considered to provide more realistic results, as this was the ultra-thin sample that was experimented with in parabolic flight and drop towers at that time [33, 46, 98]. To obtain as much information as possible about the elements, a wide range of instruments were included: K-type thermocouples provided temperatures of insulation and gas phase, images of the samples were recorded to obtain spread rates and flame structure, and vacuum flasks were designed to collect the samples of exhaust gases and combustion products, and two Transmission Electron Microscope (TEM) grids were inserted transiently to collect large particles. As expected, the flame spread rate was higher for the concurrent flow configuration than for the opposed-flow configuration. In both flow configurations, the flame spread stabilized around a molten drop of insulation material, in which bubble formation was observed. Since this droplet usually drops under normal gravity, the comparison of these two results becomes difficult [161]. In addition, all tests produced large clusters of soot, especially with the concurrent flow configuration, where strand-like soot structures with a length of about 10 cm were observed downstream of the flame. Microscopic analysis showed that the collected soot particles had a very different morphology than that formed in normal gravity flames, with primary particles three times larger than those obtained in ground-based facilities. These results are consistent with previously reported burner experiments in Section 1.2.4.
Further studies on flame spread over electric wires are available in drop towers and parabolic flight experiments in ground-based facilities. The flame spread characteristics have been investigated in microgravity for various materials such as different metal cores (NiCr, Cu or Fe) and different insulation (Polyethylene or ETFE), under different conditions such as different flow configurations (oxygen content or flow velocity) and atmospheric pressures. The purpose of the investigations are ignition limit [142, 155, 162], flame spread rate [163–166], and extinction limit [159, 167–169].

Due to the short experimental duration, the drop tower is usually used to conduct experiments for ignition limit and extinction limit. For the observation of flame spread which requires a longer experiment duration, it is mostly performed in parabolic flight. The experimental results on ignition limit and extinction limit give valid information for electrical systems safety. While studies on flame spread provide directions for the design of the atmospheric environment inside spacecraft, their axisymmetric geometry of flame spread can also provide some perspectives on combustion theory. The following discussion will focus on flame spread on wires in parabolic flight experiments.

Flame spread over electric wire in parabolic flight

With frequent flight capabilities and few payload limitations, parabolic flight experiments provide an ideal environment for developing tools to observe steady rate flame spread in microgravity. One such parabolic flight experiment setup was developed for observing flame spread on wires and has been upgraded in successive iterations to gain better insight into gas phase observations while maintaining the material limitations typical of spacecraft hardware. The experiments performed in this thesis are also based on this experimental setup, and therefore will be presented in Section 2.1. Past related studies will now be presented thus leading to the main experimental purpose of this thesis.

At the beginning, in order to investigate conditions that reveal how flame spread interactions are influenced by gravity, concomitant concurrent flow flame spread over three parallel electric wires was conducted under both normal and micro-gravity. These wires were 0.5 mm diameter NiCr cores coated with 0.3 mm thick Low-Density PolyEthylene (LDPE). This material was chosen for two reasons. First, it mimics the behavior of the wires identified as potential sources of ignition. Then, polyethylene-based composites are currently being investigated as radiation shielding materials [8, 170].

To track both the flame spread rate and the mass burning rate of the layers, the experiment was set up with a backlighting technique. A 10-bit black-and-white CCD camera recorded the visible flame spread over the wire layers, while another camera facing the backlighting captured the coating profile and the potential flame absorption. The flow conditions were set to a flow velocity of 50 mm/s, an oxygen content of 21% and atmospheric pressure.

This experiment demonstrates that the heat transfer mode can affect the spread rate. The experiment starts with a delayed ignition of the central wire. The steady mass burning rate measured on the central wire has an unambiguous increase compared to the steady burning rate measured on a single wire. As shown in Fig. 1.8, tracking the molten droplets reveals that the flame spreading on the central wire catches up with the other two flames. This spreading interaction that occurs in microgravity cannot be observed at normal gravity. Although the visualization does not provide quantitative data, the significant presence of soot particles in the flame can be inferred from the absorption field. As the soot particles play an important role in radiative heat transfer, it is essential to get more information from the flame luminosity.

Thus further understanding of the effect of radiation and heat flux on flame spread was needed. To this end, a three-CCD color camera replaced later on the black and white CCD camera. The color information provided allows for a better analysis of the radiation from the flame. To understand the potential interaction, the experiment also needed to start with the flame spread away from the quenching or blow-off limits. In addition, a steady rate flame spread with a steady rate is more conducive to the study of heat transfer mechanisms. The tests eventually reveal that a steady rate could be achieved with an opposed flame spread configuration. Then, flame spread in this configuration was systematically performed for different ambient conditions (oxygen content,

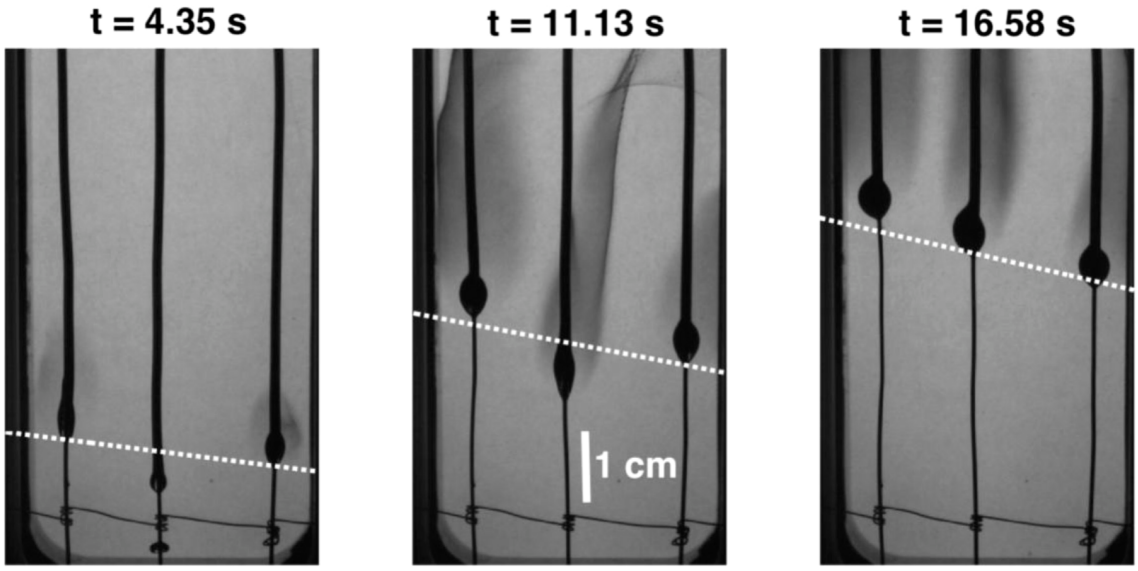

Figure 1.8: Sequence of frames recorded in parabolic flight. The central wire is ignited with a delay of about 4 s compared to the lateral ones. The white dotted lines indicate the location of iso-streamwise coordinate, and highlight the relative acceleration of the central flame. Reproduced from Citerne et al. (2016) [171].

pressure, and flow rate).

For the qualification of steady rate flame spread, the 3-color image is processed using a simple visualization tool that recovers the flame spread rate and pyrolysis rate. A transition period occurs after the wire is ignited, where a molten region forms and retracts, presumably due to surface tension, to form a droplet that recedes over the metallic core. The volume of this droplet, the length of the luminous flame, and the displacement of the luminous flame front are tracked during the microgravity sequence. If the variation in flame length and droplet volume is below the noise level set by the acquisition, and the flame front advances at a steady rate on the parabola, the flame is assumed to have reached a steady spread rate. Figure 1.9 highlights the evolution of these parameters in the opposed-flow configuration. In this set of experimental conditions, with an oxygen content of 19%, a pressure of 101.3 kPa, and a flow rate of 200 mm/s on a 0.5 mm diameter NiCr wire coated with a 0.3 mm LDPE coating, the flame was assumed to spread steadily between 13 s and 19 s after ignition.

In such a configuration where the flame can spread at a steady rate, flame spread experiments are performed under different ambient conditions (oxygen content, pressure, and flow velocity) to study the spread mechanism.

For the effect of oxygen content on the flame spread, experiments were performed at oxygen content from 18% to 21%. To stay away from the quenching limit, the pressure was atmospheric and the flow rate was 150 mm/s. Figure 1.10 shows the variation of the steady rate flame spread profile with oxygen content. The most obvious effect is the transition from a non-smoking flame to a smoking one, the previously mentioned smoke point occurring when the oxygen content increases from 19% to 20%. In addition, the color information shows that the flame is bright orange within the displayed range. Curiously, the flame signal is weaker at higher oxygen content levels, while, intuitively, increasing the oxygen content should promote flame reactivity.

The flame spread at different pressure levels was also studied. The pressure inside the combustion chamber varies from 51 kPa to 142 kPa, while the oxygen content is 19% and the flow rate is 150 mm/s. The flame evolution captured by the three-CCD camera can be observed in Fig. 1.11. It can

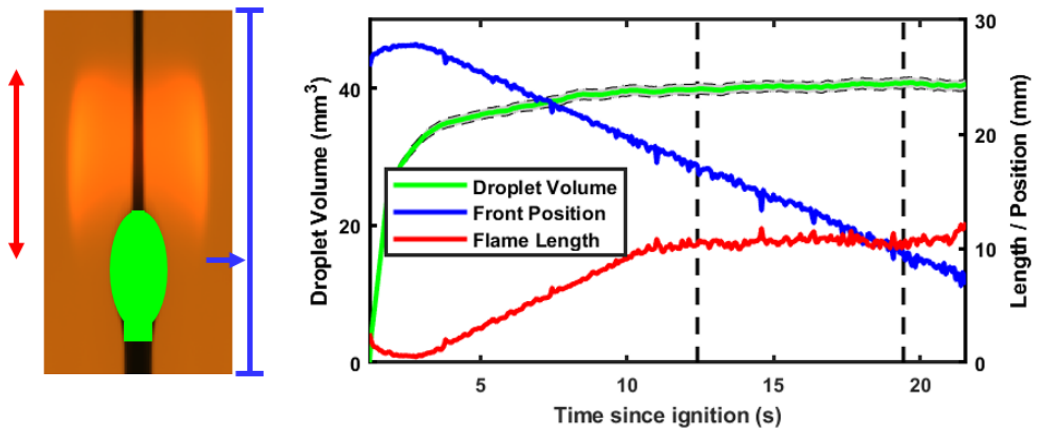

Figure 1.9: Steady state is assessed in parabolic flight by tracking the evolution of the flame front position (blue), flame length (red), and molten droplet volume (green). Between the black dotted lines, the flame length slightly oscillates around a steady value, the droplet volume does not appreciably change and the flame front moves linearly: the flame is assumed to spread at a steady rate. Reproduced from Guibaud (2019) [172].

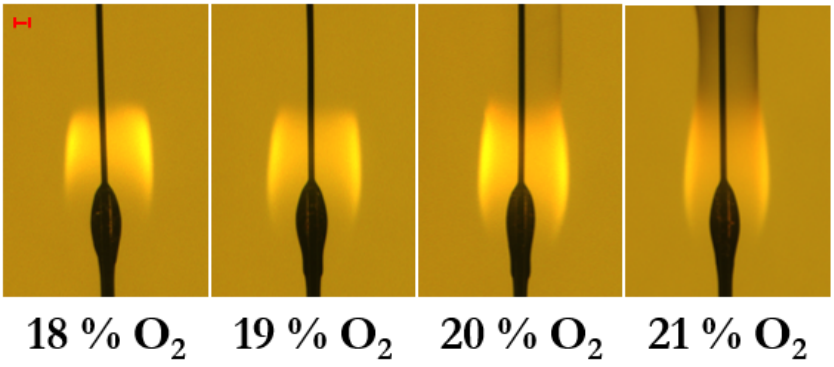

Figure 1.10: Backlighted images of steady rate opposed-flow flame spread in microgravity over a LDPE-coated NiCr wire in varying oxygen content from 18 to 21%. Flow velocity and pressure are 150 mm/s and 101kPa, respectively. A 1mm scale is shown in the upper left corner. Reproduced from Guibaud (2019) [173].

be noticed that the luminosity of the flame is weak at 51 kPa and the flame geometry is not clear. As the pressure increases, the flame geometry becomes more pronounced and the luminosity increases as well. However, at a high pressure of 142 kPa, the luminosity of the flame seems to decrease again. The flame shape also changes, with the oval shape at low pressure gradually opening at the tip as the pressure increases. The flame also gets closer to the wire axis and the visible length of the flame seems to increase with pressure. Moreover, the smoke point appears between 101 kPa and 122 kPa. The broadband emission reported in both cases is typically from soot particles. Since soot particles are involved in radiative heat transfer and radiation is considered to be a leading order mode of heat transfer in microgravity flame extinction, this mode of heat transfer likely leads to variations in spread rates and interactions between the concomitant flame spread. For understanding the role of radiation in the flame spread mechanism, it lead to the development of a finer optical diagnostic method. In this context, a Broadband Modulated Absorption/Emission (B-MAE) technique for measuring soot volume fraction and temperature was thus developed. Then, the local radiative losses could be quantified by calculating the dispersion of the radiative flux at each position of the measured soot volume fraction and temperature. Figure 1.12 shows the soot volume fraction,

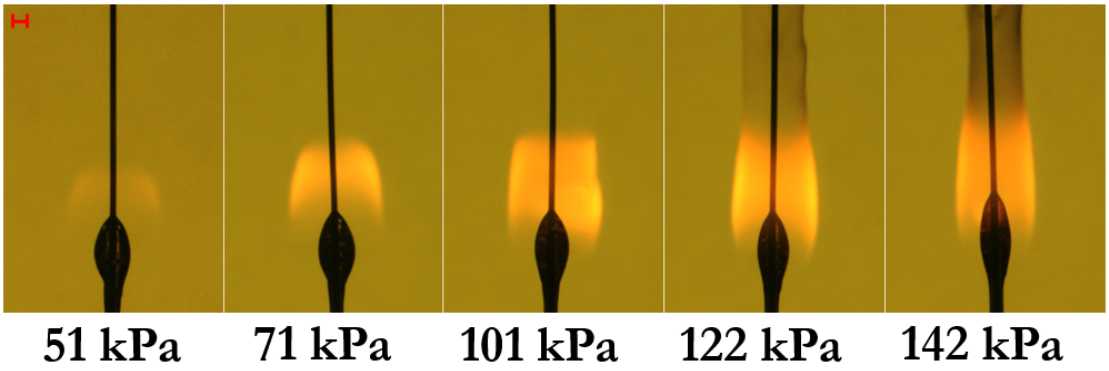

Figure 1.11: Backlighted images of steady rate opposed-flow flame spread in microgravity over a LDPE-coated NiCr wire in varying pressure from 51kPa to 142kPa. Flow velocity is 150 mm/s and oxygen content 19%. A 1mm scale is shown in the upper left corner. Reproduced from Guibaud (2019) [173].

temperature, and radiative losses mapping for a steady rate flame spread with a flow velocity of 200 mm/s, an oxygen content of 19%, and a pressure of 101kPa.
Using this well-established diagnostic method, flame spread under microgravity was observed in the ambient conditions range of oxygen content from 18% to 21%, pressure from 50.4 kPa to 141.8 kPa, and flow velocity from 100 mm/s to 200 mm/s.
It can be found that the flame spread rate is mainly controlled by the oxygen content and the effect of pressure or flow velocity variations is negligible. The pressure and flow rate also have few impacts on the characteristic length scale of soot formation, defined as the distance between the fuel pyrolysis front and the location of the maximum integrated soot volume fraction. It is only influenced by the oxygen content, so the characteristic flow time scale of the soot production process varies with the oxygen content and flow rate.
In addition, all three parameters change the maximum soot volume fraction, although they have different underlying mechanisms. The spread rate increases with increasing oxygen content, which enhances the soot inception rate of the flame. The residence time of soot formation is independent of pressure, while the variation of maximum soot volume fraction with pressure indicates a cubic relationship between soot formation rate and pressure. As for the flow velocity, the reduced radiative losses overcome the effect of lower residence time at higher flow velocities, and the maximum soot volume fraction increases with the flow velocity.
Soot release due to quenching at the trailing edge of the flame is caused by an increase in pressure or oxygen content, which has little impact on the flow velocity. The higher oxygen content leads to an increased spread rate, which results in a higher pyrolysis rate, triggering the transition from non-smoking to smoking flames. When the pressure increases, the same transition is caused by the cubic dependence of the soot formation rate on the pressure. In both cases, the increased soot load raises the radiative losses from the soot and drops the local temperature to a level where the soot oxidation reaction is frozen. The location where soot reaction freezing occurs is determined and local temperatures are reported for a relatively wide range of flow conditions, and a threshold of 1400 K is determined, conforming previous observations in normal gravity and insights from earlier microgravity experiments.
This is the first systematic description of the role of the flow conditions of flame spread over a solid sample on smoke emission. These findings also serve as the basis for quenching and radiative heat feedback analyses, which will support atmospheric selection to limit the threat posed by accidental fires in terms of flame propagation and smoke emissions. In addition, these results have benefited from ongoing observations on the International Space Station [36].

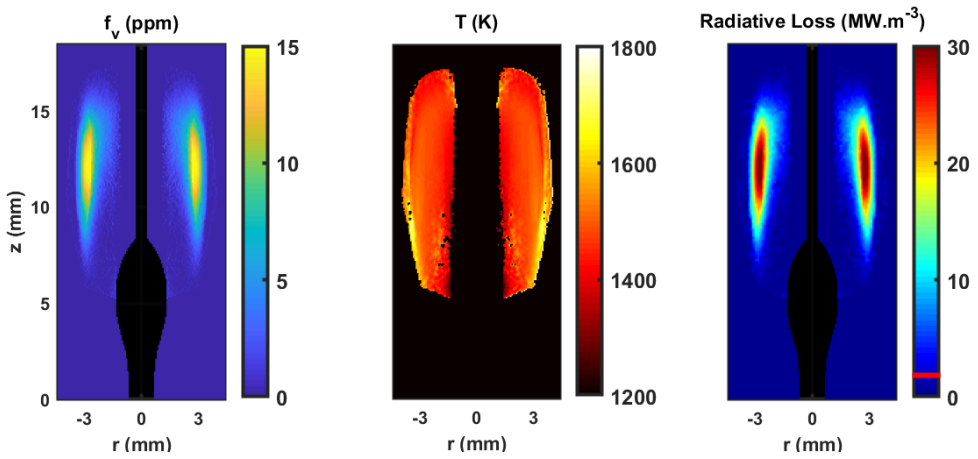

Figure 1.12: Soot volume fraction, temperature, and radiative losses fields obtained in microgravity from the B-MAE technique. The shadow of the burning sample reveals in black. Temperature and hence radiative losses are only evaluated over positions where soot volume fraction levels are above the background noise. Reproduced from Guibaud et al. (2019) [172].

Certainly, such a well-developed diagnostic system for fire safety research will not stop at this point. After all, there are still many fire safety aspects that can be improved, and the understanding of flame spread in reduced gravity still needs to be complemented. The following will discuss the aspects the present thesis focuses on.

1.3 Aim of the present study

The present study continues the observations of flame spread over electric wires carried out under parabolic flight experiments and is developed in the context of the need for fire safety strategies for space exploration. It can be divided into three main aspects. First, to improve the accuracy of flame detection, soot is to be collected from spreading flames over electric wires. Then, to accommodate exploration missions to the Moon and Mars, it is essential to observe the flame spread over electric wires in partial gravity. Finally, the relevance of usual flame retardants needs to be addressed in view of the enhancement of the materials' fire resistance properties. This Section discusses the background of the study according to these three aspects and the feasibility of conducting the experiment in parabolic flight.

1.3.1 Fire detection and soot characteristic in microgarvity

At the heart of the fire safety strategy, detection devices rely heavily on the detection of smoke produced by a fire-like diffusion flame as mentioned in Section 1.1.2. Discrimination from airborne dust is carried out through measurement of the scattering or ionization properties of soot particles, which are aggregates of impure carbon particles resulting from the incomplete combustion of hydrocarbons. However, little is known regarding the effect of reduced buoyancy flows on the soot particle morphology and properties. Consequently, the investigation of smoke generated in a non-premixed flame in microgravity is crucial to prevent false alarms or, worse, the absence of alarm in a fire situation. In addition to these practical considerations, the tracking of soot particle formation, growth, and oxidation in reduced buoyancy presents fundamental benefits as these

mechanisms can be captured with an elongated residence time, creating a new benchmark for numerical and theoretical models.
The lack of data from microgravity experiments has led to detection accuracy difficulties. Trying to capture a fire signature as early as possible, Meyer et al. [7] analyzed particles generated in oxidative pyrolysis in microgravity and found that the particle dimensions were not significantly affected. However, this conclusion on oxidative pyrolysis contrasts with earlier findings regarding the size and morphology of soot particles produced in diffusion flames in microgravity. Due to the increase in residence time, more mature particles are retrieved and this makes the detection of fully-developed fire scenarios increasingly complex [135, 174]. Since the current smoke detectors on the ISS are based on light scattering, an investigation specific to the impact of gravity level on soot optical properties would be particularly relevant.

Optical diagnostic for soot formation

Non-intrusive optical techniques are available to investigate soot particle formation and evolution in situ without disturbing the flame. Such methods as Spectral Soot Emission (SSE) techniques [175], Laser-Induced Incandescence (LII) [176], light extinction [177], and light scattering [178] can lead to the evaluation of soot volume fraction, soot temperature, particle size, and aggregate morphology. Because of constraints in equipment, timing, and volume, these methods can hardly be implemented in microgravity experimental rigs.
Reimann and Will successfully applied the LII method to the study of soot formation in non-buoyant laminar jet diffusion flames in a drop tower experiment [179]. Two-dimensional information on soot concentration and primary particle size in microgravity was obtained simultaneously, and the temperature field was measured by a 2-color emission pyrometer. It was shown that soot formation and oxidation change dramatically in microgravity, with the maximum flame temperature decreasing in the absence of buoyancy and the primary particle size doubling. In addition, as previously described in Section 1.2.4, Fujita and Ito observed the soot aggregation process in a jet diffusion flame at a drop tower using the laser shadowing method to evaluate the diameter and volume fraction [134] of soot aggregates. With the B-MAE technique described above, the measured soot temperature and volume fraction in the flame can also provide certain information about soot formation in a spreading flame.
All of these optical techniques are based on approximations regarding the optical properties of a soot-loaded atmosphere. Among the simplest absorption and diffusion assumptions commonly implemented, the Rayleigh approximation of the Mie theory provides simple calculations if the wavelength of the incoming light source is much larger than the particle size investigated. In typical flame conditions, the young soot particles as primary particles are nearly spherical with a size much smaller than the visible or near-infrared wavelength and they barely interact with each other. Therefore, they can be considered to be in the Rayleigh scattering approximation [180]. However, the mature soot particles as aggregates are usually beyond this limit in terms of dimensions and interactions. Then other theories are better fit to the measurements, such as the Rayleigh-Debye-Gans (RDG) for fractal aggregates (RDG-FA) approximation [180, 181]. In microgravity, mature soot particles acting as microscopic fractal aggregates are more readily produced, casting doubt on the relevance of a Rayleigh approximation and supporting more elaborate assumptions. Nevertheless, RDG and RDG-FA require additional information regarding the size, morphology, and fractal characteristics of the studied soot aggregates. Direct sampling of soot particles to collect data is then required to support the further development of optical diagnostics in reduced buoyancy environments.

Soot sampling

For soot sampling, Dobbins and Megaridis [182] implemented a thermophoretic sampling technique, now widely used to study the evolution of soot morphology and soot volume fraction in laminar diffusion flames [183–185]. In microgravity, Ku et al. [135] and Konsur et al. [136] performed the first thermophoretic sampling on a laminar diffusion flame in a drop tower experiment and analyzed the primary particle size and aggregate dimension with a transmission electron microscope (TEM). It was found that a longer residence time in microgravity enhanced soot formation and growth with an average primary particle size twice as large as that observed for soot formed at normal gravity. As mentioned in Section 1.2.4, with experiments aboard the space shuttle, Urban et al. [128] also performed soot sampling with the thermophoretic technique for laminar diffusion flame and outlined that soot primary particle size increases with distance from the burner, and that increasing ambient pressure tends to increase particle size. Although the results of the study using thermophoretic sampling in microgravity provide important and useful information about the morphology of soot collected in laminar diffusion flames, this sampling method is not fitted to spreading flames where the sampling location might vary, especially if one wants to investigate the effect of ambient conditions in the restricted volume of a combustion chamber.
To address this challenge, the present study develops a novel particle sampling method that uses an electric field to sample soot particles on a brass plate both at normal and micro-gravity from a flame spreading on a cylindrical sample in an opposed-flow configuration. Introducing spatial resolution along the sample's axis, the evolution of soot particle morphology is tracked along the flame height. Combining the ambitions of improving measurements from non-invasive optical diagnostics with the need to qualify the response of fire detection systems to soot particles being emitted at the trailing edge of the flame, the sampled soot particles are observed a posteriori under a TEM and their morphological properties, namely density, particle projected area, radius of gyration, fractal dimension, and primary particles size distribution are extracted.

Spreading flames at normal and micro-gravity

Experiments have been conducted in microgravity and at normal gravity following the procedure detailed in Section 2.2, to highlight the effect of the gravity level on the flame from both macroscopic and microscopic perspectives. The laminar oxidizer flow in the combustion chamber consists of 21% oxygen and 79% nitrogen with a velocity of 150 mm/s and a pressure of 101.3 kPa. Cylindrical wires, which consist of a 0.5 mm diameter Nickel-Chrome (NiCr) core coated with a 0.3 mm thick layer of Low-Density PolyEthylene (LDPE), are ignited under microgravity and normal gravity conditions, respectively. Once the flame is established, it propagates in an opposed-flow configuration, as shown in Fig. 1.13.
It can be seen that the gravity level impacts the condensed phase topology and the flame appearance at a macroscopic scale. In microgravity, the molten LDPE coating forms an axisymmetric bulb that pyrolyses at the flame leading edge upon heating from the flame (see Fig. 1.13 (a)). At normal gravity, this bulb drips away on one side of the wire under its own weight (see Fig. 1.13 (b)), affecting the spread rate, the pyrolysis, and breaking the symmetry of the flow to a certain extent. Furthermore, the flame is more stretched at normal gravity because of natural convection that accelerates the flow in the vicinity of the flame. In turn, this reduces the fuel residence time as compared to microgravity, according to the estimated characteristic flow time scale for the soot production in Section 2.3.1. This also affects soot formation, growth, oxidation, and radiative

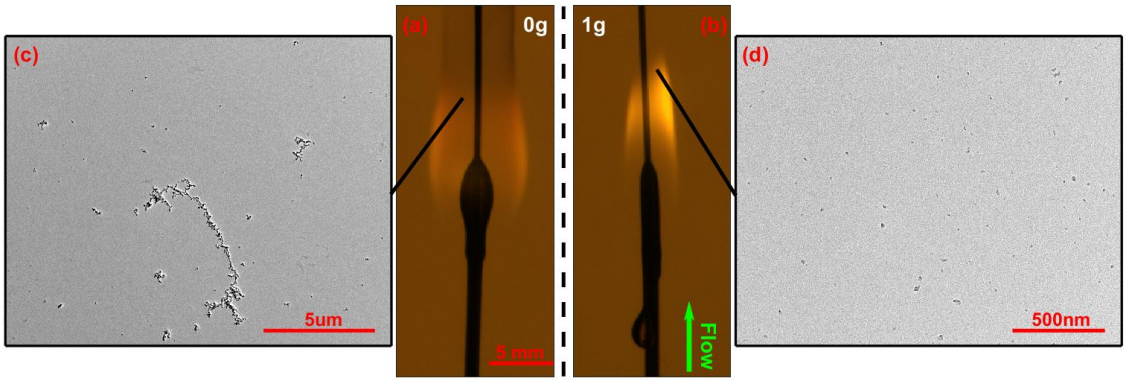

Figure 1.13: Illustration of the gravitational level impact on the flame appearance and the morphology of some soot particles sampled: (a)-(c) in microgravity; and (b)-(d) at normal gravity. The approximate locations of the soot sampling is represented by the end of the straight black solid lines on the imaging of the spreading flames (a) and (b). The smoking flame in microgravity (a) features large mature soot aggregates (c), that cannot be observed on the sampling (d) collected in the brighter flame at normal gravity (b).

properties, and consequently changes the flame temperature and luminosity. The impact is such that the relatively slow flow conditions studied can lead to radiative quenching in microgravity, which is not observed at normal gravity.
These macroscopic observations have been discussed in Section 1.2.5, using optical techniques that yield the fields of soot volume fraction and temperature. Yet, these quantitative measurements rely on a range of hypotheses regarding soot particles' dimensions and morphology to solve the radiative transfer equation across the flame [186]. To further question the validity of these hypotheses, microscopic observations under TEM of particles sampled at the flame trailing edge are displayed for both microgravity and normal gravity in Fig. 1.13 (c) and (d), respectively. The sampling is performed thanks to a novel methodology based on soot particle polarity, which is thoroughly described in Section 2.2. It can be noticed that the longer residence time in microgravity produces soot particles orders of magnitude larger than those sampled at normal gravity, and the more mature aggregates have a richer topology. This discrepancy clearly affects the quantitative results obtained with an optical setup, and also supports evidence of the need to adapt smoke detectors to the particle generated in a reduced-gravity environment.
In Chapter 2, the new sampling methodology is described and its relevance is analyzed before the morphological evolution of soot particles along the flame axis at both gravity levels is presented. Density, soot particle area, the radius of gyration, fractal dimension, and primary soot particle are investigated as key parameters. The influence of gravity on the flame signature can then be documented using the above morphological properties.

1.3.2 Partial gravity experiment in parabolic flight

To date, experiments on flame propagation in partial gravity have only been performed in parabolic flights and drop towers and the relevant experimental data are very scarce, as presented in Section 1.1.3. Solid fuels show lower LOC in partial gravity than in normal gravity, and also flame spread rates on solids show a peak in partial gravity. These experimental results remind the need for further understanding of flame spread mechanisms in partial gravity. Electrical fires are the most likely cause of fires in spacecraft, yet experiments on flame spread over electric wires in partial gravity have never been conducted.

From past experiments in microgravity, the steady flame spread is possible over LDPE coated electric wires. In such a configuration, the flame spread is governed by the conjugated heat transfer from the flame and the metallic core to the virgin solid fuel [187]. The pyrolysis process of LDPE generates a molten droplet that spreads steadily at the same rate of the flame front [172]. A different spread mechanism is observed at normal gravity where downward flame spread was found to be governed by heating due to the dripping flow of hot molten insulation that prevails over the heating by the metallic core [188]. This dripping is a gravity-induced process and evolves through a competition between, on the one hand, gravitational forces and, on the other hand, surface tension and viscous forces [161].
In partial gravity, this naturally raises the question of what mechanisms drive the flame spreading process in such an environment. Therefore, the present study is also conducted to observe the flame spread over electric wires in Lunar and Martian gravity. In Chapter 3, the flame geometry, spread rate, and extinction limits are determined. The effects of different gravity levels are then discussed and compared with data in normal and microgravity.

1.3.3 Material enhancement with flame retardant

The two research aspects above are related to the flame spread over electric wires. To broaden the research aspect, the present study is also conducted on thin cylindrical samples. As described in Section 1.2.5, there is already a lot of data available on flame spread over cylindrical samples in microgravity, and such configurations are also conducive to the development of theoretical models. Based on this consideration, the third aspect is based on a cylindrical sample configuration (which can also be considered as an electric wire without any core) and attempts to modify the combustible material for the enhancement of its flame resistance properties.
Material selection on spacecraft has always been key to fire prevention. However, fire safety has given great limitations to the selection of materials. Because of functional requirements, it is often difficult to avoid using flammable materials on spacecraft. To solve this dilemma, new ideas are needed.
Though leading features of combustion are modified in microgravity, the associated fire safety concerns are not specific to space exploration. As such, inspiration can be found in existing solutions from other industries. For instance, flame resistant or flame retardant materials are commonly employed in construction, transport, cable, or textile industries to improve fire safety, and should be considered in spacecraft design as well. Flame resistant fabrics are made from materials that inherently have low flammability properties, while flame retardant fabrics have been modified by chemical coating or inclusion and thermal treatments to improve on their original behavior.

Flame resistant materials

Concerning flame resistant materials, Orndoff summarized the successful development of several fabrics for space exploration by textile industries since the 1960s, like polybenzimidazole fibers, aromatic polyamide fibers, chlorofluoroethylene fibers, polyimide fibers, and beta fiberglass [189]. These materials could eventually pass flammability tests on the ground to assess their viability in an oxygen-enriched atmosphere (beta fiberglass for instance was designed to be non-flammable in the pure oxygen environment of a spacesuit), and were included in the design of successive spacecraft. However, the tests were not performed in the absence of buoyancy, so it is not known whether these flame retardant fabrics perform in microgravity as well as they do at normal gravity. In

addition, their prohibitive cost and limited range of applications hampers a sustainable production. Investigating the difference caused by buoyancy, Takahashi et al. compared flammability of other more common flame resistant materials, such as NOMEX, Kevlar, Kapton, CARBOGLASS, PEEK, PPSU, silicone resin, and silicone rubber, under both normal and micro-gravity [190, 191]. They found that, among these materials, those with higher pyrolysis temperatures inhibit flame spread in microgravity and can self-extinguish under higher oxygen content than observed at normal gravity. Because they are inherently designed for specific fire needs, flame resistant materials may poorly address other functional requirements vital to space travel [189].

Flame retardant materials

Research on flame retardant materials has also received a special focus to boost the fire properties of existing materials used in spacecraft at a limited development cost. To protect spacecraft and astronauts following the catastrophic 1967 Apollo 1 fire, Parker et al. [192] considered enhancing the fire resistance properties of polymeric materials by adding flame retardant coatings (nitroanailine-sulfonic acids, quinonedioxime-acid mixtures, and nitroanilinosulfones). The nitroanailine-sulfonic acids coating had been tested for its effectiveness in protecting a structure from the fire on the ground and it was shown that the temperature of the coated sample increased five times slower than in the absence of coating. With the same purpose, Kourtides et al. [193] conducted experiments on composite materials loaded with flame retardants (graphite-reinforced composites) on the ground. They found that the loaded samples showed a higher limiting oxygen index (LOI), lower heat release rate, and lower smoke production. These two reports aside, there is a lack of measurements regarding the efficiency of flame retardants in the context of space exploration, amplified by the absence of data in reduced gravity.
In this context, a broad range of flame retardants can be investigated. Intumescent flame retardants, which expand when exposed to external heating while retaining acceptable mechanical properties, are especially relevant in polymer materials increasingly used in spacecraft. In the presence of a flame, an expanded char layer can be formed, inhibiting fire spread by slowing down heat and mass transfer between the gas and condensed phases [194]. Intumescence can be obtained from a series of chemical reactions or using mechanical expansion. Consequently, two flame retardants, Ammonium polyphosphate/Pentaerythritol (AP) and Expandable Graphite (EG), are used to enhance the fire properties of flammable materials in this study, corresponding to the two different ways of obtaining expansion presented above. Once more, the experiments are conducted in microgravity. Chapter 4 will discuss the effect of flame retardants on flame spread characteristics in the absence of gravity.

2 Electric soot sampling in spreading flames

Contents

The second Chapter describes the experimental setup developed before the present thesis to investigate flame spread in parabolic flight, as well as the technique originally designed within the context of the present works to sample soot particles from spreading non-premixed flames and the associated method for the subsequent analysis of sampled particles' morphology.
Section 2.1 tours the experimental device DIAMONDS, which can board the aircraft. Although DIAMONDS was designed before the present work, it has been continuously improved. After reminding the optical diagnostic technique for flame spread, Section 2.2 presents the electric soot sampling technique for spreading flames. The sampling technique is performed both in microgravity and normal gravity and the optimal sampling parameters are analyzed. The collected soot particles are observed a posteriori under Transmission Electron Microscopy (TEM). Eventually, the obtained TEM images are analyzed in Section 2.3. Some image analysis tools have been specifically developed to extract the morphological properties of soot particles, thus enabling the comparison of soot particles collected in microgravity with those collected at normal gravity.

2.1 DIAMONDS experimental rig

To provide a clear framework for the whole microgravity experiment procedure, the hardware elements that constitute the Detection of Ignition And Mitigation On-board for Non-Damaged

Spacecraft (DIAMONDS) are presented in detail. It can be split as the flow system, the optical system, and the fixation of the sample inside the combustion chamber. Then, the experimental procedure in parabolic flight is presented, as well as a description of the post-experimental data management.
A description of the DIAMONDS design, most of which has been done before the present work, can be found in Refs. [171–173]. For clarity, some key elements are reviewed here via Fig. 2.1.

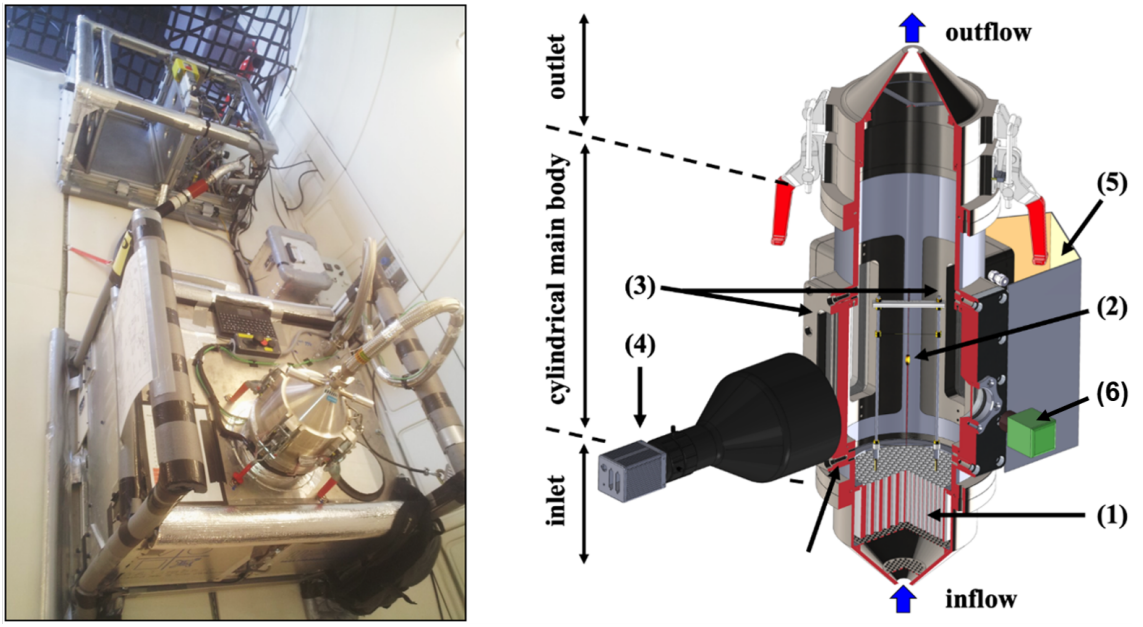

Figure 2.1: Picture of the DIAMONDS rig onboard the Novespace airplane (left), and schematic view of the combustion chamber (right). High pressure cylinders are stored in the top rack, while the combustion chamber, acquisition, and regulation devices are contained in the bottom rack visible in the left picture. Elements of the central combustion chamber can be listed as follows: (1) honeycomb; (2) burning sample (polyethylene coated wire); (3) windows; (4) camera equipped with a telecentric lens; (5) backlighting screen illuminated by red, green, blue, and white LEDs. (6) Infrared camera. The exhaust grid, located in the outlet segment, is not represented for clarity. Reproduced from Guibaud (2019) [173].

2.1.1 Gas flow system

Gas supply

The gas flow system is designed to provide a laminar oxidizer flow to the cylindrical combustion chamber and to ignite the sample in such an environment. Five high-pressure gas cylinders are carried in the aircraft and are supplied by Air Liquide. Three of these cylinders store compressed air, each with a capacity of 21 dm^3 and a pressure of 200 bar, for a total of 6600 nL (normoliters). The synthetic air is composed of an oxygen/nitrogen mixture of up to 99.9999% purity and has an oxygen content of 21.0% $\pm$ 0.2%. The other two high-pressure cylinders store nitrogen gas having the same purity. Each cylinder has 21 dm^3 and 200 bars, for a total of 4200 nL. Thus, the air mixture can be diluted by pure nitrogen so that the oxygen content in the combustion chamber can be adjusted between 0% and 21%. Because plans for future spacecraft include atmospheres at oxygen content higher than 21%, efforts have been done to enable investigations at relatively high oxygen content onboard. However, security concerns in parabolic flight have delayed the potential

for storage and use of higher oxygen content equipment onboard.

Inlet of the combustion chamber

To set in-line mixing of air and nitrogen, these cylinders are connected to high-pressure manifolds. Downstream of the AlphaGaz pressure reducer on each line, a Bronkhorst EL-FLOW mass flow controller adjusts the flow rate between 0 and 250 nL/min before the two flows are mixed. Thereby, both the oxygen content and the velocity of the oxidant flow to the combustion chamber are controlled. To avoid potential fluctuations in ambient temperature and cooling due to gas expansion, a temperature-controlled heating line connects the outlet of the mixing manifold to the inlet of the combustion chamber. Upon entry into the combustion chamber, the flow cascades through a divergent element in which glass beads of 2 mm diameter are stored to homogenize the flow over the cross section of the cylindrical section. In order to obtain a flat oxidant velocity profile at the leading edge of the unburned sample, a stainless-steel honeycomb was placed after the divergent piece.
Above the honeycomb, the body of the combustion chamber is a 600 mm high cylinder with an internal radius of 190 mm. Four N-BK7 windows, each 200 mm high, 40 mm wide and 10 mm thick, provide optical access to the combustion chamber. Since the windows are not curved, they are embedded in four recesses, resulting in two vertical lines of sight. Although they limit the development of the boundary layer at the wall, the 10 mm wide ring at the outlet of the honeycomb and the alcove were proven to maintain the core of the flow. The associated demonstration was obtained from extensive computational fluid dynamics (CFD) simulations and experimental evaluations to assess the quality of the flow field in the combustion chamber. CFD was performed with ANSYS Fluent and included a modest model of gas expansion, i.e., the effect of the flame on the flow. Experimental measurements of a single-component hot wire were performed without any samples. It was found that the flat profile region in the experiments was more restricted than in the numerical simulations and that the actual flow rate was lower than predicted. Hence, it was concluded that uniform flow with a flat velocity profile can be expected over a central cylindrical volume with a diameter of 40 mm and that the relationship between inlet flow and velocity along the central axis of the chamber was experimentally calibrated from 20 to 350 mm/s.

Gas exhaust

After each experiment, the exhaust gases are discharged outside the aircraft through an exhaust duct. They first flow through a metallic mesh grid to trap large soot aggregates. In the exhaust duct, a rotary control valve (RCV) regulates the pressure in the chamber up to 1.5 bar. Measurements with a Keller piezoresistive transmitter show that the valve allows exhaust flow rates of up to 1800 nL/min while keeping the upstream pressure stable. The flow velocity is therefore limited by the capacity of the Bronkhorst inlet flow controllers. Experimental measurements show that due to the airplane's trajectory within a parabola, the pressure downstream of the RCV varies between 32 kPa (top of the parabola) and 38 kPa (bottom of the parabola) in the absence of inlet flow. In the presence of inlet flow, both values increase due to the pressure loss in the exhaust line. Therefore, a pneumatic actuator for the valve was selected and the adjustment of the proportional-integral-derivative controller parameters was given special attention in order to keep the pressure upstream of the RCV constant whatever the variations downstream.

Gas flow restrictions and gas flows of concern

There are three limits that restrict the range of flow rate, oxygen content, and pressure that can be studied. First, there is a limit of 250 nL/min per mass flow controller at the inlet that limits the flow velocity of each line. This limits the high pressure, oxygen content, and flow velocity to be investigated. Additional limitations then occur if the pressure loss in the exhaust line exceeds the pressure in the chamber, which would be expected at lower pressure and higher flow rate. Lastly, the maximum pressure value for the exhaust duct embedded in the aircraft cabin is 85 kPa to avoid dangerous overpressures that may occur during high flow pressure and high flow rate investigations. Therefore, care is to be taken not to exceed these limits when setting the environmental conditions inside the combustion chamber. So far, these flow configurations are available to complete the present study.
The typical gravity-induced flow of a centimeter-scale flame is characterized by a velocity of 200 mm/s [195]. This order of magnitude was retrieved considering a density variation $\Delta\rho/\rho$ of 1 in the flame and neglecting viscous effects. In a centimeter flame on the ground, the flow rate due to buoyancy is:

$$U_{buoyancy} = \sqrt{g_0 \times L} \sim 300 mm/s \tag{2.1}$$

where L is the characteristic flame length. In order to analyze the influence of the flow conditions on the flame spread mechanism in the case of normal gravity usually dominated by buoyancy, the oxidizer velocity in microgravity should therefore be studied from 0 to 200 mm/s, which roughly corresponds to the capacity of this device.

2.1.2 Optical system

An image acquisition system is used to obtain information on flame spread over the wire. As previously described, this system is continuously upgraded between successive parabolic flight campaigns. The optical equipment in use is now presented. The windows on the side of the combustion chamber mentioned above make up two optical axes. One of them has been extensively used for image acquisition in the visible range, while the second one, put into use within the present works, enables the infrared measurements.

Tri-CCD camera and backlight

In the visible range, the flames were imaged with a 12-bit JAI AT-140CL digital tri-CCD camera that imaged the incoming light on three paired matrices of 512 $\times$ 1396 pixels. This matrix is able to discriminate contributions from the red (550 nm $\leqslant \lambda \leqslant$ 680 nm), green (460 nm $\leqslant \lambda \leqslant$ 610 nm) and blue (380 nm $\leqslant \lambda \leqslant$ 510 nm) spectral bands (RGB). The camera is equipped with a telecentric lens that limits the collection of light to a beam parallel to the optical axis. In this arrangement, the spatial resolution of the projected data for each spectral band reaches 73 µm and the images are typically acquired at 39.06 frames per second (fps).
Behind the window opposite the tri-CCD camera, a backlight illumination generated by Cree XLamp MC-E color LEDs was set up. Each LED consists of four adjacent red, green, blue, and white chips (RGBW). Instead of directly illuminating the combustion chamber, the LEDs illuminate a white screen, as shown in Fig. 2.1, facing the window. The purpose is to increase the spatial uniformity of the backlight intensity. For better control of the spectral illumination, the current flowing through each chip of these RGBW LEDs can be adjusted individually. Thus, the spectral

distribution of the backlight can be tuned to be quite similar to the spectral distribution of the flame. This strategy allows for optimizing the utilization of the dynamic range of each CCD. Both devices were carefully calibrated before the first experiments [173].

Infrared camera

Regarding the new infrared measurements, a 640x480 VIM 640 G2 ULC infrared camera has been added along the direction perpendicular to the line-of-sight of the tri-CCD camera and is simultaneously recording the experiment. This additional camera measures the infrared energy emitted from the sample surface through a polished germanium window with a transmissivity spectrum close to 1 between 2µm and 14µm. In addition, a passively thermalized IR lens was installed in order to block the IR signal in the 8 µm to 12 µm spectral band. Thus, the final operating spectral range of this camera is from 8 µm to 14 µm with a resolution of 86 µm and a frame rate of 30 fps. Within the calibration procedure, the infrared camera has been calibrated using the RCN1350 N1 cavity blackbody in a range of 100 to 600 °C. The infrared camera is placed at the closest distance to the blackbody so that the energy emitted by the blackbody is distributed over the entire spatial area captured by the camera. Then, all the signals given by the collecting pixels are averaged to obtain the analog signal of the corresponding temperature at one pixel, as shown in Fig. 2.2. Finally, this information can be used to extract the energy in the infrared range captured by the camera.

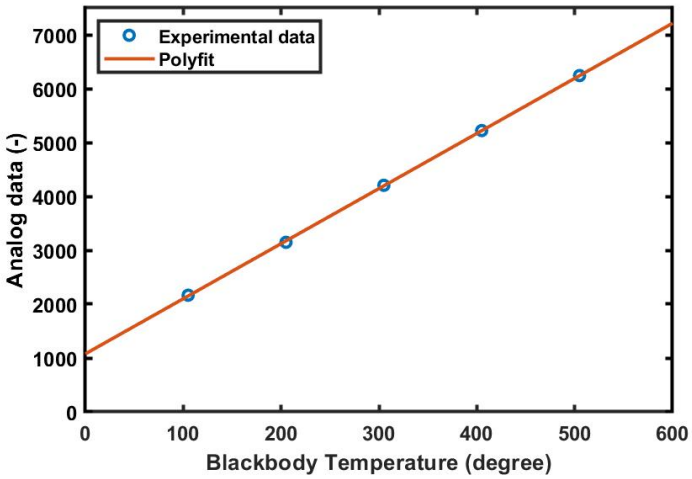

Figure 2.2: Analog data of infrared camera at a single pixel as a function of cavity blackbody temperature. The blue points represent the measured data and the orange line represents a polynomial fit of the data. The analog signal is shown to be a linear function of the blackbody temperature.

2.1.3 Electric wire samples and sample holder

In order to conduct the spread in a region of flat flow velocity, a cylindrical sample is held in the center of the combustion chamber by a sample holder. The axisymmetric geometry allows the development of many powerful image processing tools, and the B-MAE technique is based on this geometry. The sample used in the classical configuration on this experimental rig consists of

a metallic core and polymer insulation. One of the main benefits of this configuration is that the metallic core maintains the sample geometry during the entire flame propagation.

Sample holder

To ensure that the samples are straight and properly aligned with the oxidizer flow, they are mounted on the 210 mm high by 84 mm wide sample holder shown in Fig.2.3. This holder consists of two vertical 4 mm diameter threaded stainless steel rods, with a 1.2 mm diameter horizontal thin stainless-steel rod at the bottom (leading edge) and a 10 mm diameter horizontal thick ceramic rod at the top (trailing edge). One coil of the metallic wire core is wound around the stainless-steel rod, while the other end of the wire is inserted through a hole made through the ceramic rod and held in tension by a stainless-steel spring with a ceramic cap. Since in this configuration the oxidizer flows from bottom to top, hot wire measurements show negligible downstream flow perturbations generated by the leading edge rod over the range of investigated oxidizer velocities.

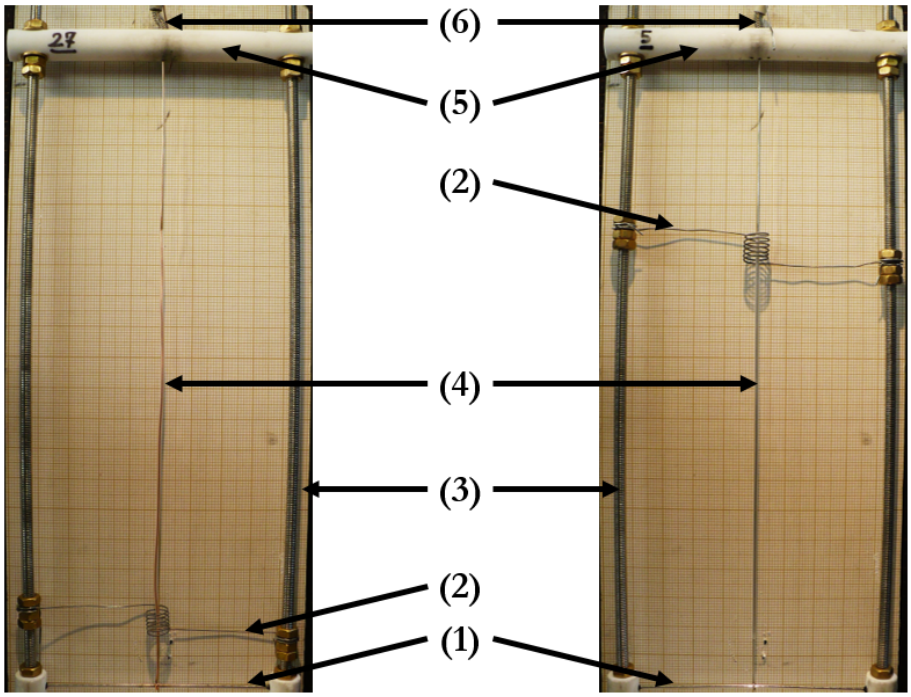

Figure 2.3: Wide-angle pictures of loaded sample holders with graph paper backgrounds. A Cu-core concurrent flow configuration is displayed on the left, while a NiCr-core opposed-flow configuration is displayed on the right. Arrows point to the (1) 1.2 mm diameter stainless steel rod with ceramic holders at both ends; (2) Kanthal wire tightened between brass nuts; (3) 4 mm diameter threaded stainless steel rod; (4) polyethylene coated wire; (5) 10 mm diameter ceramic rod; (6) stainless steel spring and ceramic cap. The Sample on the left is prepared without the wire bending protocol, while the sample on the right is prepared with it. Reproduced from Guibaud (2019) [173].

Electric wire sample preparation

Such wire samples are purchased with large spools of wire and therefore exhibit natural curls. This undesired curl usually exceeds the elastic regime of the wire material and the deformation

is partially maintained when the sample is unwound. The spring is usually not strong enough to overcome the large sample deformation and straighten the wire. To overcome this experimental difficulty, a wire folding device was designed. It consists of a series of 20 mm diameter wheels that bend the wire between two 50 mm diameter elastic drums before forcing the wire to come out of the spool with an elevated torque. The wire coming out of this system proved to be almost straight, forming an arc with a radius of more than 1.4 m (a deviation of 5 mm for a 240 mm long sample). Once the wire was mounted on the sample holder, the connecting spring was stiff enough to reduce the deviation to the size of a camera pixel.

Ignition system

To provide a repeatable ignition procedure, a 0.5 mm diameter Kanthal wire was wrapped around the leading edge of each sample to study concurrent flow flame spread or around the trailing edge of each sample for opposed-flow flame spread. The extremities of this ignition wire were tightened between brass screws to a threaded rod on the side. When the ignition is requested, the power is turned on and current flows in the Kanthal wire. The thread is connected to the power supply by inserting a plug screwed into a slot in the inner wall of the combustion chamber. The ceramic holder electrically isolates the lower metal rod from the threads to prevent short circuits. Early experimental investigations on the effects of the ignition procedure [159] demonstrated that a current of 7.5 A flowing in a 0.5 mm diameter Kanthal coil for 8 s, with 6 turns around the sample and a ring diameter of 8 mm, radiated sufficient heat to systematically ignite the sample in microgravity. Thus, this ignition protocol was applied consistently.

2.1.4 Parabolic flight procedures

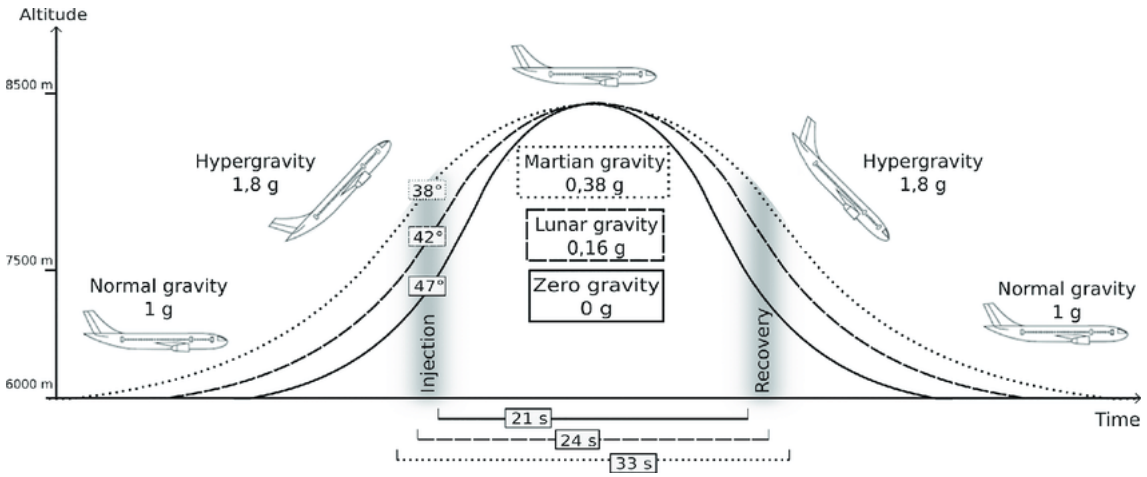

Figure 2.4: Schematic representation of parabolic sequence leading to three different gravity levels onboard. The duration of microgravity, Lunar gravity, and Martian gravity are 21s, 24s, and 33s respectively. Reproduced from Ritzmann (2015). [196]

During a parabolic flight campaign, the DIAMONDS rig is loaded on board the Novespace A310 ZeroG aircraft. A flight campaign consists of three consecutive flight days and 31 parabolas are performed each day. In a typical microgravity parabolic sequence, the aircraft flew steadily for at least three minutes and then pulled up for about 20 seconds before a microgravity sequence of about

21 seconds. At the end of the microgravity sequence, the pilot pulled out of the parabola for approximately 20 seconds to return the aircraft to a steady flight. During the pull-up and pull-out periods, the structure undergoes a peak acceleration of 1.8 g_0. Alternatively, for partial gravity, as shown in Fig. 2.4, the angle of injection is smaller than for microgravity (42° for 0.16 g_0 of Lunar gravity and 38° for 0.38 g_0 of Martian gravity) and the duration of the partial gravity sequence is longer than for microgravity (approximately 24s and 33s for Lunar and Martian gravity levels, respectively). For the flight campaign delivering partial gravity, each gravity level is performed 31 times over three days. Each day, 5 (6 on the very first sequence) consecutive parabolas are performed for each gravity level as a set and then shift to another gravity level. This tight schedule and rapid alternation of hyper/microgravity require delicate preparation of the experiment sequence before each campaign, as well as careful in-flight data management, smooth synchronization between the three DIAMONDS operators on board, and sufficient post-processing tools to provide critical information that may affect same-day measurements. Prior to any campaign, goals are set and flow and sample conditions are defined in a test matrix of 93 predefined parabolas. Potential decision trees with conditions distributed over three flight days to minimize decisions affecting same-day measurements and to comply with oxidizer volume limits.

Prior to any sequence of parabola, two operators open the combustion chamber using the latch

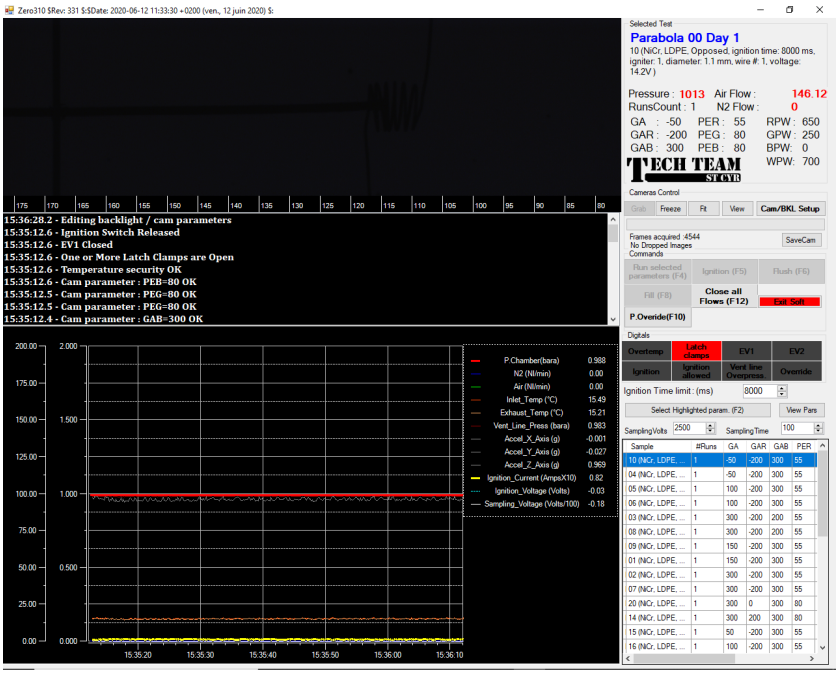

Figure 2.5: Screenshot of the software elaborated by J.-M. Citerne. This software can control the flow and the acquisition system. The flame spread can be observed during the experiment through the window on the top left. All real-time parameters of the flow system are displayed in the graph below. The parameters of the acquisition system for the ongoing experiments are shown at the top right. The list of parameters for the 31 experiments of the day is displayed at the bottom right.

clamps (in red color on Fig. 2.1). A new sample holder is introduced and the combustion chamber is then closed. Except for the sample change, all other operations were managed by a third operator on the command computer through a software elaborated by J.-M. Citerne (engineer at Sorbonne University). As shown in Fig. 2.5, this software controls the flow and acquisition system for control. Exposure time, gain and intensity commands are transmitted to the camera and LED backlight, while flow instructions are passed to the flow meter and RCV. After the introduction of the oxidizer, the pressure in the combustion chamber usually reaches a stable value after 20 seconds. Considering

the overall timing, the flow is initiated before the hypergravity pull-up sequence. Within a parabola, the difference between the set pressure point and the actual combustion chamber pressure is lower than 0.01 bar. As mentioned above, ignition takes about 8s, so the sample starts to be heated 6s before the start of the low gravity period, while both cameras start recording. At the beginning of the low gravity period, the flame usually just starts to form and begins to spread. To obtain the absorption field in the flame, the LED backlight behind the sample was set alternately on and off between each shot of the three CCD camera, so that images were recorded simultaneously with and without the backlight.

2.1.5 Data management

The parabolic trajectory provides low gravity levels of duration from 21s to 33s with a gravity accuracy level of 10^{-2} g_0. As described in Section 1.2.1, the presence of such low gravity accuracy levels and g-jitter has an effect on the flame structure itself, which is difficult to quantify [55, 197]. Although gravity variations at high frequencies have little effect on the flame, variations at low frequencies and high amplitudes can significantly distort the flow field. Accelerometer readings are critical to determine the low gravity level of each parabola. To synchronize the analog data with the camera acquisition, they were also taken at a rate of 39.06 Hz and synchronized at the onset of the sample ignition. After each parabola, the instructions passed to the flow meter, RCV, camera, LED and igniter are saved in a first text file, while the second file contains the measured analog data. A folder is created on the command computer containing these two files as well as all images recorded by the two cameras. In microgravity, the number of pictures recorded by the CCD camera is typically 1200 and the number of pictures by the infrared camera is 775, for a total observation duration of 30.7 s which contains two hypergravity sequences. In Lunar gravity and Martian gravity, the CCD camera recorded 1300 and 1500 pictures, and the infrared camera captured 822 and 969 pictures, with an observation time of 33.3s and 38.4s, respectively. The resulting folder (with a size of 4.6 Gb, 5.0 Gb, and 5.9 Gb in microgravity, lunar gravity, and Martian gravity, respectively) is named using the date and time when the experiment began recording to prevent duplication. It is transferred to Network Attached Storage (NAS) after the flight and duplicated on a large size backup hard disk. The data is then removed from the command computer hard drive to avoid memory overflow on the next flight.

2.2 Soot sampling with electric field

Soot formation in a flame is affected by gravity, as discussed in Section 1.2.4. Since soot particles play an important role in the understanding of flame spread in microgravity (e.g., radiative heat transfer, soot emission, and fire detection), soot sampling from flames is not a new concern. However, soot sampling from spreading flames in microgravity has never been done before. One of the challenges is that microgravity experiments are limited in terms of space and equipment. In addition, it is even more difficult to collect soot particles from a moving flame in microgravity.
To overcome these difficulties, this Section introduces a novel electric soot sampling technique. The equipment required to implement this technique is first described. Then, the sampling process in microgravity and normal gravity is presented, and the corresponding sampling parameters are discussed. In the end, the acquisition of TEM images from the sampled soot particles is also presented.

2.2.1 Electric sampling equipment

This novel sampling method is developed for flame spread over electric wire samples. Since steady spread can be achieved with an opposed-flow flame spread configuration, the present soot sampling is performed for such a configuration. With this premise, the sample holder is modified as shown in Fig. 2.6(a).

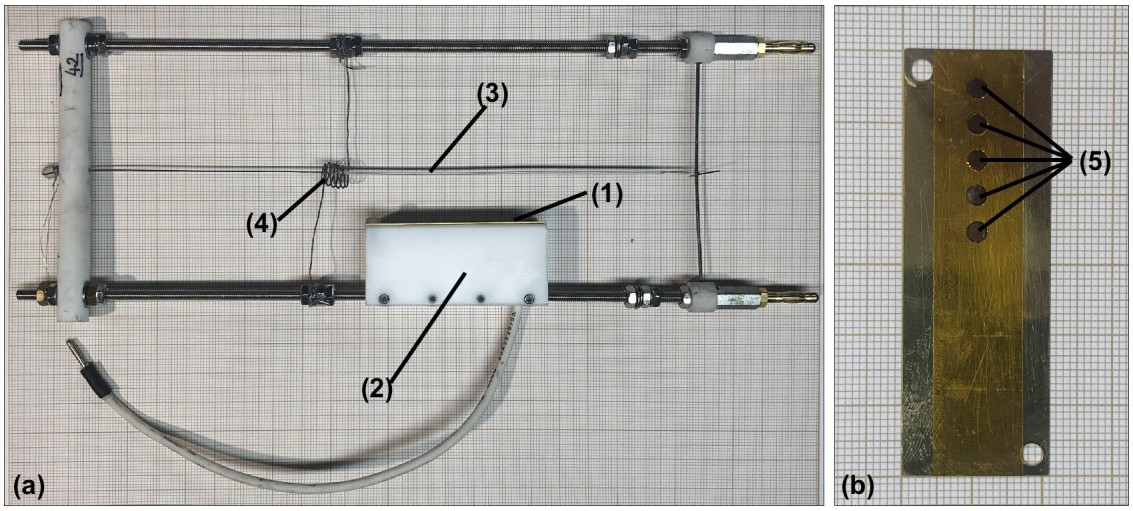

Figure 2.6: (a) Sample holder equipped with a brass plate (1). The brass plate is screwed to a PTFE beam (2) attached along the lower threaded rod of the sample holder. High voltage between the back of the plate and the NiCr core of the LDPE coated wire (3) that is connected to the threaded rod is supplied via a pin plug. The igniting Kanthal wire (4) can be seen. (b) Brass plate with TEM grids (5). The TEM grids are stuck to the plate with high-temperature adhesive tape.

Generation of electric field

The whole sampling process relies on generating a sudden and brief ionic wind under the influence of an electric field. The field of set amplitude and duration is generated between the metallic wire core, and a brass plate embedded into a Polytetrafluoroethylene (PTFE) beam (see (1) and (2) in Fig. 2.6(a)), parallel to the wire and located 20mm away from its axis. The boundary layer generated by the introduction of this additional element in the chamber can affect the flow downstream, but its action on the facing flame is limited. Assuming that the laminar boundary layer flow along the flat plate behaves according to the Blasius solution conditions, the momentum thickness of the layer between the plate and the wire remains below 10mm [198]. This is confirmed by observations of the unperturbed flame geometry. The back of the brass plate is connected via a high voltage wire to an EMCO Q series DC high voltage generator located outside the combustion chamber. This device creates a voltage up to 3kV between the brass plate and the metallic core of the sample, which is electrically connected to the structure of the setup and acts as ground. The tension can be set for a duration prescribed by the operator. As the brass plate is charged by the generator, an electric field orthogonal to the sample's axis is generated between the brass plate, acting as the cathode, and the metallic core, acting as the anode. The negatively charged particles of the flame caught in the field move toward the surface of the brass plate, creating an ionic wind rich in unoxidized soot particles. The particles then impact the surface of the brass plate, creating a shadow of the original flame. Similar to traditional thermophoretic sampling, the surface of the brass plate is cold enough

to freeze the heterogeneous reactions of the sampled particles, and prevents changes in the soot morphology after the particles have impacted upon the cold surface. Once the voltage drops back to zero, the flame retrieves its unperturbed shape.

TEM grid

The particles cannot be directly observed on the brass plate using TEM. To prevent the surface transfer and the associated degradation of the carbonaceous particles, TEM grids with a diameter of 3.05 mm are directly mounted on the central axis of the brass plate using high-temperature adhesive tape as shown in Fig. 2.6 (b). The selected TEM grid is a copper grid with 300 square meshes covered with a film made of 5-6 nm pure carbon deposited on one side of the grid. These mesh grids have specific markers designed for quadrant location, including an asymmetrical mark in the rim and a center mark. It allows to identify their orientation and thus track the morphological evolution of the soot particles at different flame heights. During the electric field activation, the particles are consequently deposited directly on the grids which can be detached with fine reverse action tweezers post-flight and brought to TEM for observation. Following observations from previous experiments in microgravity, five grids are regularly spaced from the top of the brass plate, with an inter-grid distance of 2mm.

Sample and sampling ambient conditions

Using such soot sampling equipment, soot particles have been successfully collected in both microgravity and normal gravity. Within the present study, the conditions were restricted to electric wire of 0.5mm diameter NiCr wire coated with a 0.3mm LDPE coating and the ambient conditions under both gravity levels are 21% oxygen content, 150 mm/s flow velocity, and 101.3kPa pressure.

2.2.2 Sampling procedure and parameters in microgravity

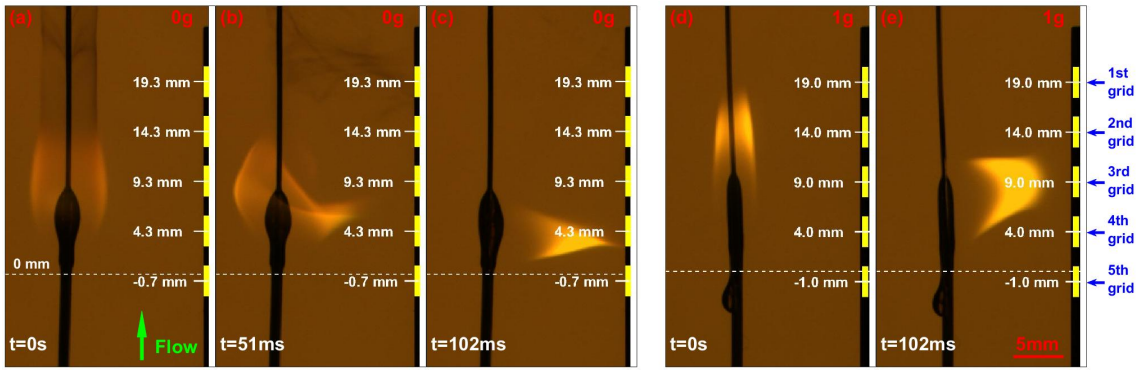

Figure 2.7: Sampling sequence in microgravity and normal gravity. The gravitational level is indicated in the upper right corner of every image and the TEM grid position is represented by the side yellow rectangles. (a) and (d) are the latest images before applying the electric field at t=0. (c) and (e) show maximal flame blending position under an electric field. (b) evidences that soot particles are moving toward the brass plate at the beginning of the sampling.

Sampling in microgravity

To collect the soot particles produced in the flame after the spread at a steady rate is reached in microgravity, sampling is performed at least 20 seconds after the hot wire ignition begins. Here, ignition is initiated before microgravity conditions are attained, to optimize the amount of time available for in-flight observations. Steady rate flame spread is defined as a situation where the flame front position progresses linearly, and the flame length and molten bulb volume are constant [172]. To trap particles from a range of positions within the flame, the electric field is generated once the flame faces the area covered by the TEM grids, which are indicated by horizontal lines on the visualization software to help the operator. Sampling onset is controlled manually because the flame spread rate varies with the ambient conditions.
The sampling sequence in microgravity is recorded in real-time by the tri-CCD camera images as shown in Fig. 2.7 (a, b,c), so the operator can track the evolution of the position of the flame relative to the brass plate. The positions of the five TEM grids are represented in yellow in the figure, and the dotted lines illustrate the upstream deformation position of LDPE, which can be assumed to correspond to the position where the solid fuel begins to pyrolyze and provide gaseous fuel.
During sampling (Fig. 2.7 (b)), it can be noticed that the incandescent soot particles located within the flame and cold soot particles escaping from the trailing edge of the flame accelerate toward the brass plate immediately after the voltage is applied. As long as the electric field is sustained, the flame deforms toward the metal plate, as shown in Fig. 2.7 (c). The flow rate appears to have a limited effect on the geometry of the flame, indicating that the ionic wind dominates the flow locally. The bright yellow aspect of the flame proves that soot particles were still generated when the voltage was on, but it can be expected that these soot particles undergo a very different aging process compared to those to be sampled in the absence of the electric field. It is also worth mentioning that the molten droplets are subjected to ionic forces and start to deform, with some spots of amorphous plastics being recorded on the TEM grids.

Sampling parameters

Voltage value and sampling duration are set in advance before each parabola. For effective sampling, it is necessary to ensure that sufficient soot can be collected on the TEM grids and that the quantity of soot particles is not too high to affect the subsequent TEM observation. From Fig. 2.7 (b), it is found that at 51ms after the application of the electric field, the soot to be sampled is still moving toward the brass plate, and the flame bends to the lowest point at 102ms. Therefore, the sampling time should be at least 100ms, so that the soot particles of interest have enough time to reach the brass plate.
To ensure that enough soot can be sampled onto the TEM grids, different sampling times of 100ms, 300ms, and 500ms were investigated in microgravity under the same ambient conditions. It was observed that the soot particles on the TEM grid were already so dense at 300ms that the amount of overlap prevented a straightforward analysis of the size and properties distribution, with more than 65% of the grid surface being covered by soot particles (versus 30% for a sampling period of 100ms), as shown in Fig. 2.8. A low sampling time of 100ms is also preferred to minimize the amount of soot particles generated and aged within the electric field activation.
To minimize aging as the soot particles transit from their original location to the surface of the TEM grids, the particles should reach the brass plate as fast as possible. Three different voltage levels of 1.8kV, 2.3kV, and 2.8kV were carried out in microgravity with the same ambient conditions. The maximal bending level of the flame was found to be different. The bending angles orthogonal to

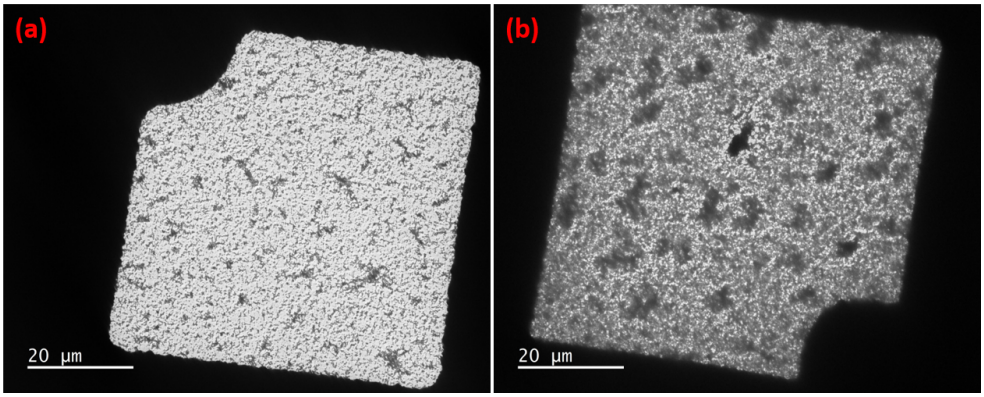

Figure 2.8: TEM images with 100ms (a) and 300ms (b) sampling duration under the same ambient conditions, same sampling voltage parameter, and same observation position. The images are obtained with x400 magnification. The square box in the figure represents one mesh, and the soot particles inside the mesh are in black. At a sampling time of 300ms, the soot particles almost completely cover the entire grid. This results in soot particles overlapping each other and prevents further morphological analysis.

the flow direction were measured to be 18.1°, 7.1° and 4.8°, respectively. From the bending angle of the flame, it can be inferred that the flame bending is affected by both the ionic force generated by the voltage and the momentum attributed to the forced flow momentum. The ionic force increases with the applied voltage and also increases the dominance of the ionic force against the forced flow. Meanwhile, it also appears that the particle trapping could be affected by the forced flow, the particle potentially moving in the downstream direction during the sampling. In order to reduce this effect and let the particles reach the brass plate faster, the sampling voltage used in this paper is 2.8V.

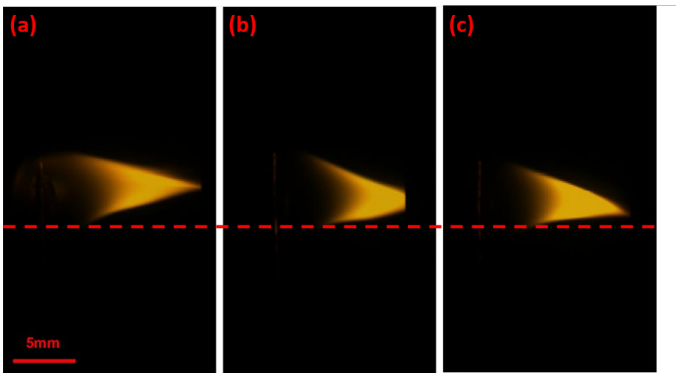

Figure 2.9: Images without backlighting with sampling voltage of 1.8kV (a), 2.3kV (b), and 2.8kV (c) under the same flow conditions and same sampling duration. The images are taken at the moment of maximum flame bending during sampling. It can be noticed that the bending of the flame increases with the sampling voltage.

2.2.3 Sampling at normal gravity

At normal gravity, soot sampling was applied with the same sampling parameters as in microgravity. Here, there is no time constraint imposed by the parabola timing. Still, the flame cannot reach a steady state spread as in microgravity. At the end, the timing of soot sampling is based on using

TEM grids as a reference, triggering the sampling procedure at a position of the flame front as close as possible to that of the flame front during the experiment in microgravity.
As shown in Fig. 2.7 (c) and (d), the spreading flame also bends toward the brass plat under the attracting electric field. However, due to the effect of natural buoyant force, the bending is not as strong as in microgravity. The characteristic velocity overshoot attributed to buoyancy at normal gravity can be provided by the momentum equation as:

$$U_{buoyancy} \approx (\frac{\triangle \rho}{\rho} g L)^{1/2} \tag{2.2}$$

where $\triangle\rho$ and ρ are the density differences and the ambient density, respectively. These can be considered to be of the same order of magnitude [94]. At normal gravity, $g = 9.81\ m/s^2$ and flame length, $L_{f,1g} = 10.53mm$, give a buoyant flow velocity of 321 mm/s. Taking into account the forced flow of 150 mm/s provided in the combustion chamber, the convective flow velocity applied to the flame at normal gravity under the same conditions is three times higher than that in microgravity. This results in a maximum bending angle of 10.5° which is higher than in microgravity. Through the flame bending angle at different gravitational levels, it is possible to roughly infer the applied ionic force during the sampling. With the Boussinesq approximation, the natural buoyancy force can be determined by the following equation:

$$F_{buoyancy} = -g_0 \beta_T \rho_\infty (T - T_\infty) \tag{2.3}$$

With Gay-Lussac's law, the thermal expansion coefficient can be estimated as $\beta_T = 1/T$. T and T_∞ are the adiabatic flame temperature and the ambient temperature, respectively. As the difference in flame bending angle is caused by forced flow, buoyant flow, and electric field, a simple force balance with the known buoyant force allows obtaining the ionic force during the sampling, leading to$10.1N/m^3$.
With the same sampling voltage and duration, the sampling process under normal gravity is affected by natural convection, resulting in soot particles escaping from the flame to the brass plate with a different trajectory than under microgravity. Therefore, to investigate the influence of gravity levels, the following comparison is based on the overall evolution of different soot particle morphological properties along the flame axis, rather than a point-to-point comparison.

2.2.4 TEM images acquisition

The soot particles sampled on the TEM grids are observed under a JEOL JEM 1011 TEM, which is a tungsten hairpin 100kV electron microscope. The bright field images are acquired as tiff files on a 2672x4008 $pixel^2$ CCD camera Gatan Orius SC 1000 A1. During observation, it is noticed that sample modification under electron beam revealed possibly due to soot vibration which limited the time of observation.
As mentioned before, the grid with marks is applied so that it helps to identify the observation location during the TEM observation. For each grid, three locations on it are selected along its central axis for observation under the electron microscope to investigate the morphological evolution of the soot particle along the flame height. These three locations correspond to three meshes on the TEM grid which are located in the central position and the two extreme positions of the central axis. Since the sampled soot particle size is dramatically different depending on the gravitational condition and where they locate on the flame height, the magnification of interest under the TEM observation needs to be varied from x400 to x60 000. As the particle size varies a lot, the choice of

magnification for TEM observation is touchy. If the magnification is too low, the particles sampled at normal gravity might not be observed because their size is too small. If the magnification is too high, the soot aggregates sampled in microgravity cannot be fully displayed in the image due to their excessive size. Based on this challenge, different investigation purposes require analysis at different magnifications.
In TEM, the observation range can be divided into low magnification and high magnification with x1200 magnification as a limit. In the low magnification range, x400 images can show an entire mesh. It can verify whether the mesh has been damaged and whether the mesh is overloaded by the soot particles. Also, it allows for analyzing those huge aggregates. The smallest magnification in the high magnification range, x1200, can provide information about the aggregates that are too large to be fully visualized in the higher magnification images. At x5000 magnification, the particles generated at normal gravity begin to be clearly observed so that the images at this magnification can be applied to extract information on density, aggregate size, and certain large primary particle size, and to analyze the effects of gravity. The magnification between x5000 and x60 000 is intended to extract information on primary particles.

2.3 Morphological properties analysis and discussion

Soot morphological properties are extracted from the obtained TEM images. These properties include soot particle projection density and area, the radius of gyration, fractal dimension, and primary particle size distribution. This Section describes the image processing methods used to obtain each of these properties, and the results obtained are analyzed and compared to document the effect of gravity on soot particle morphology.

2.3.1 Soot particle projected density and area

Image processing

With TEM images, the most intuitive results are the two-dimensional density of soot particles on the image and the projected area of each individual soot particle. To extract this information, it is necessary to accurately identify the soot particles on the TEM images. To this end, T.A. Sipkens' method of soot segmentation [199] is applied, which is built around a k-means clustering algorithm, and involves multiple steps of pre- and post-processing to denoise the images, enhance contrasts, and reconstruct the shapes of particles once the images have been binarized. This segmentation method has proven robust across almost all images, with a few cases of failures where the algorithm is unable to identify particles, due to the image being too noisy (which happened mainly with low magnification 1g-sampling images, where particles sizes rarely exceed a dozen pixels). In these latter cases, binarization was performed manually, while keeping the same image pre- and post-processings. In comparison, the Otsu thresholding method was much less efficient and tended to underestimate the binarization threshold, which led to aggregates being split into multiple parts. The k-means clustering tends on the other hand to overestimate this threshold a little, overestimating the area-equivalent diameter of individual aggregates by 2% on average [199]. With the generated binary masks, the density of soot particles is computed as the ratio of the total area of soot particles to the total area of the image and the individual soot particle projected area can be also obtained easily with the summation of all the detected areas for individual soot particle.

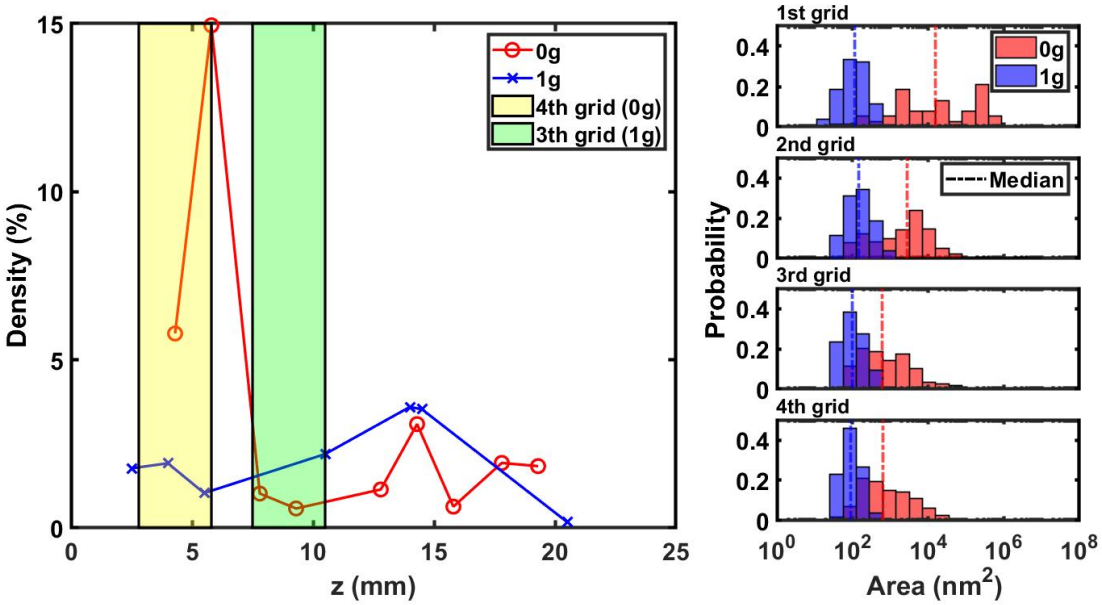

Figure 2.10: Evolution of soot particle density (left) and area distribution (right) along the flame axis. The yellow and the green zones are the 4th grid in microgravity and the 3rd grid in normal gravity, respectively. These two zones represent the positions where the sampling is impacted by the electric field. The corresponding positions of the different grids are shown in Fig. 2.7.

Density

Figure 2.10 shows the evolution of soot particle density and area along the flame axis at both gravity levels. In microgravity, it can be noted that the density of the 4th grid is much higher than that of the other positions. From Fig. 2.7 (c), it can be found that the flame bent and pointed to the 4th grid under the electric field. In addition to the soot particles sampled from the flame in the absence of the electric field, the soot particles produced under the electric field could be sampled, thus affecting the density results on this grid. Nevertheless, some useful information can still be extracted from the particle distribution. Except for this grid, it is observed that from the upstream deformation position of LDPE (z=0mm) to the trailing edge of the flame (from the 4th to the 1st grid, as indicated in Fig. 2.7 (e)), the density tends to increase then decrease, and finally stabilizes from the smoke emission position. At normal gravity, sampling soot particles produced under the effect of the electric field cannot be avoided. But the flame bends and points to the 3rd grid due to the buoyant force (as shown in Fig. 2.7 (e)). However, from the overall view, the soot density shows an increasing trend and then a decreasing one from the LDPE pyrolysis position to the trailing of the flame. At the leading edge of the flame, the soot density is higher than that in microgravity. Interestingly, this trend is reversed at the trailing edge of the flame, which correlates with a heavier smoke release, i.e. a lower soot oxidation efficiency, by the non-buoyant flames.

Area

Regarding the distribution of soot particle projected area, the projected area of the soot particles sampled in microgravity is much larger than those at normal gravity for all positions. In microgravity, a transition from log-normal type distribution to bimodal type one can be observed along the

flame height. On the 4th grid, the soot particles generated under the condition with and without the electric field are all collected. However, according to the TEM images, there are still more young soot particles with a small size that cannot be observed in the downstream flame position and do not yet behave as spherule. Therefore, a log-normal type distribution appears populated mainly by particles of small projected area. Moving to the 3rd grid, the log-normal type distribution is still present, while more of larger particles appear as compared to the 4th grid. This evidences that the particles grow in terms of size along the flame height. On the 2nd grid that faces the trailing edge of the flame, the particles continue to grow and become larger. But the smaller particles are still present, and the projected area distribution gradually divides. From the 2nd grid to the 1st grid, it keeps forming the larger particles and it starts to show two peaks and become bimodal in distribution.

At normal gravity, the distribution does not vary much along the flame axis, and it always shows a log-normal type distribution. However, upon very careful observation, from the median and the maximum value of the particle area, it can be noticed that the particle area tends to increase first and then decrease from the leading to the trailing edge of the flame. The increase in the projected area can be explained by the formation and growth of the soot particles and the decrease is likely due to full oxidation of soot as the flame exhibits a closed tip shape [200, 201]. According to the TEM image observation, most of the particles sampled at normal gravity are young soot particles and close to the spherical primary particles. They are not as mature as the fractal-like aggregates in microgravity. It could be related to the different residence time of soot production at normal and micro-gravity. The characteristic flow time scale for the soot production process can be estimated as:

$$t_{res,s} \sim \frac{L_f}{u_\infty} \tag{2.4}$$

where u_∞ is the flow velocity which includes the buoyant flow velocity and the forced flow velocity and L_f is the visible flame length. The visible flame length in microgravity is $L_{f,0g} = 11.3mm$, hence its flow residence time for soot production is estimated as 75.5 ms. In contrast, at normal gravity, the residence time is 22.3 ms which is three times shorter. With a shorter residence time of soot production, the soot particles sampled at normal gravity do not have enough time to become more mature under high temperatures and lack of oxygen conditions as in microgravity. These young and small soot particles are readily oxidized after contact with oxygen at the trailing edge of the flame [202], hence, it is more difficult to meet smoke emission at normal gravity than in microgravity.

2.3.2 Radius of gyration and fractal dimension

The radius of gyration and fractal dimension are the key properties that allow determining the optical properties from particle morphology, especially for the fractal-like aggregates [180, 203]. Furthermore, they are parameters that can describe the overall size of the particle and its structure. To evaluate these two properties, the binarized image mentioned in the previous Section is first to be produced.

Method

The gyration radius, R_g, is determined using a centroid approach, as described in Ref.[204], where R_g is computed as the root mean square distance of all the mass elements i of aggregate at coordi-

nates r_i to its center of mass r_a :

$$R_g = \sqrt{\frac{1}{N}\sum_i (r_i - r_a)^2} \tag{2.5}$$

The considered mass elements are the pixels composing the binary mask of the aggregate, each having a weight of 1.
The fractal dimension of aggregate, D_f, is computed using the box counting method as:

$$D_f = -\lim_{a\to 0} \frac{\ln(N(a))}{\ln(a)} \tag{2.6}$$

where a represents the box size and $N(a)$ is the number of boxes needed to recover the aggregate binary mask. This method is limited by the resolution of the TEM image, as small borders of aggregate tend to be very pixelated. Thereby, the fractal dimension of aggregates with a size below 1000 pixels is not measured here.

Analysis

Figure 2.11 shows the evolution of the radius of gyration and the fractal dimension distribution, respectively, with some examples of soot particles.
The evolution of the radius of gyration distribution is similar to the evolution of projected area distribution along the flame axis in both gravity levels. The radius of gyration with the soot particles sampled at normal gravity is much smaller than that in microgravity and is basically below 10 nm. In microgravity, the size of soot particles escaping from the leading edge of the flame (on the 3rd and 4th grids) provides a mean value of around 20 nm. At the end of the visible flame (on the 2nd grid), the soot particles grow to an average size of 48 nm. The particles sampled from the smoke emission location (1st grid) have an average size of 143 nm and their maximal size can even reach 695nm. This evolution indicates that the soot particles sampled in microgravity continue to grow until they escape from the trailing edge of the flame.
As mentioned previously, the soot particles sampled are mainly young spherical primary particles at normal gravity. For those fractal-like soot aggregates in microgravity, the evolution of its structure can be tracked by the fractal dimension distribution. Although the mean value of their fractal dimension hardly varies along the flame height and is around 1.86, the evolution of its distribution is significant. In general, a densely packed aggregate has a larger fractal dimension than a chain-like branched aggregate [205] (see the examples in Fig. 2.11), and this trend is also observed in the sampled soot particles and shown in Fig. 2.11. From the leading to the trailing edge of the flame, the median tends to move toward smaller fractal dimensions, which means that more particles transition to the chain-like branched aggregate. It is worth mentioning that the soot particles on the 4th grid, which are affected by the electric field, display a different morphological structure and their distribution is more dispersed than on the 3rd grid and affects their mean value.

2.3.3 Primary particle size distribution

The purpose is now to identify the evolution of the primary particle size along the flame axis. Therefore, this necessarily leads to the development of a specific segmentation algorithm, which aims at identifying a majority of the primary particles, without requiring to identify all the particles. This allowed for faster treatment of a higher number of aggregates, which provided a good statistical

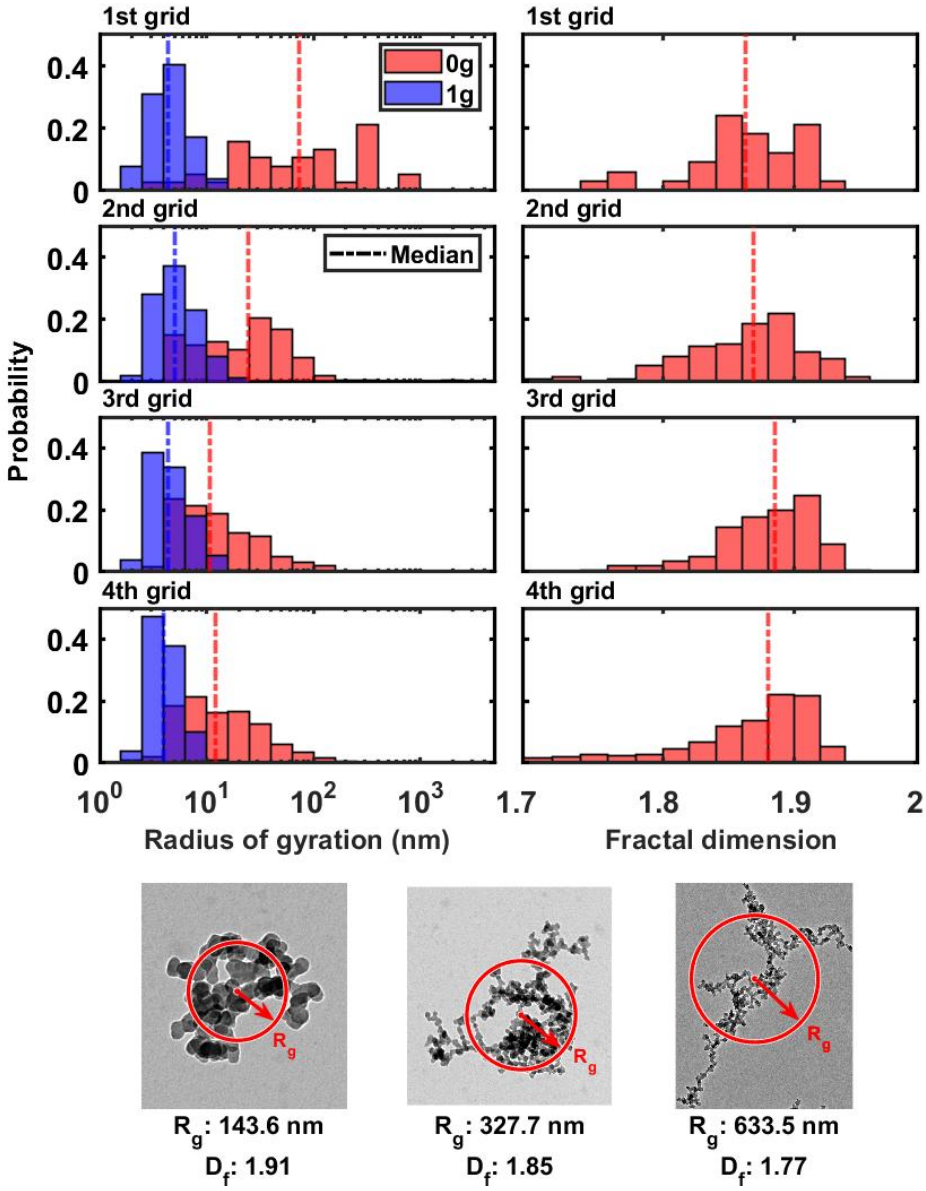

Figure 2.11: Evolution of the radius of gyration distribution (left column) and the fractal dimension distribution (right column), together with three examples of aggregates sampled exhibiting different radii of gyration and fractal dimensions in microgravity (lower line).

correction to compensate for the missing particles.

Semi-automated method for primary particle

This semi-automated method used three different features to segment primary particles. First, it makes use of the Circular Hough Transform (CHT) based algorithm with Matlab, applied to the previously generated binary masks (as shown in Fig. 2.12 (b)), to identify the particles on the contour of the aggregate (yellow circles on Fig. 2.12 (a)). Then, the color gradients of the image are calculated to map all of the uniformly shaded areas of the aggregate which likely correspond to one primary particle (as shown in Fig. 2.12 (c)). The center of each region is then computed and fed to the Center-Selected Edge Scoring (CSES) algorithm [206] which tries and fits a circle on the TEM

image at this approximate location (blue circles in Fig. 2.12 (a)). Finally, an entropy filter is applied to the image to highlight highly-textured areas (as shown in Fig. 2.12 (d)), which are locations where a high number of overlapping particles is likely to be found, and the CSES algorithm is once again applied in this area to identify the primary particles (red circles on Fig. 2.12 (a)).
This method is controlled by a set of operator-defined image-wide parameters, as our progressive know-how showed that the optimal control parameters are the same for all aggregates in one TEM image. These parameters and their subsequent adjustment are as follows:

- The particle radius range has to be adjusted when moving along the flame to accommodate for the evolution of soot maturity.

- The binarization threshold for both the gradient map and the entropy-filtered image mainly depends on the contrast and the overall quality of the image.

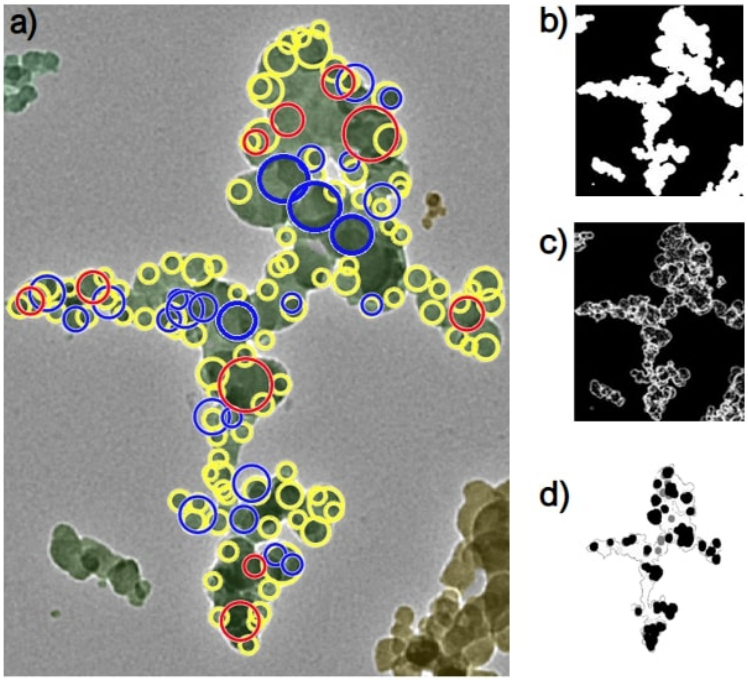

Figure 2.12: Primary particle segmentation process on one aggregate using three different features: (a) result of the primary particle segmentation, (b) binarization, (c) gradient map, and (d) entropy filtering.

This semi-automated method has given satisfying results on all images, both in microgravity and normal gravity, even though the gradient and entropy features require the aggregate to have a certain size to be truly efficient. The number of segmented primary particles was at least 70% of the number of particles identified using an equivalent fully-manual method. The main limitations lie in the difficulty for the CSES algorithm to tell apart particles that overlap with a high number of others and to identify particles in large uniformly-shaded areas. Moreover, as it can be seen in Fig. 2.12, a very small number of the drawn circles are erroneous, which requires manual cleaning. However, their influence on the overall measurements is negligible due to their small number, and this problem is therefore a reasonable concession considering the great gain in efficiency of the method.

Analysis

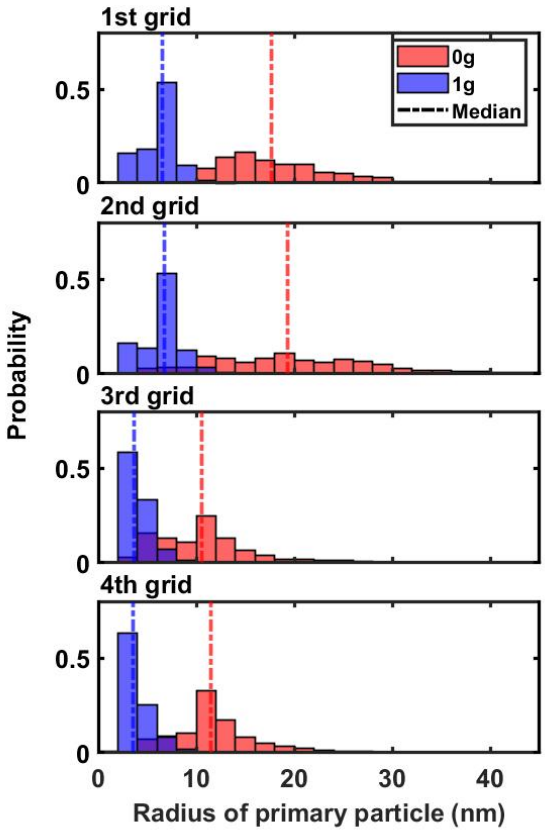

Figure 2.13: Evolution of primary particle radius distribution in microgravity and at normal gravity.

Figure 2.13 shows the evolution of the soot primary particle radius distribution along the flame axis in both gravity levels. Overall, the soot primary particles at normal gravity are smaller than those in microgravity and their radius is mainly lower than 10 nm. As moving away from the LDPE pyrolysis position, the primary particle size distribution at normal gravity shows a trend from power-law type distribution to log-normal type distribution and their size tends to increase first and then decrease slightly. In the beginning, the power-law type distribution is due to the particles nucleating and growing with a radius between 2-4 nm [207]. As these particles continue to grow in the flame, their radius continues to increase between 6-8 nm. In the tailing edge of the flame, the distribution of soot primary particles is slightly skewed toward smaller particles because of the oxidation. In microgravity, the evolution of primary particle size distribution is very different from that in normal gravity and is more dispersed. The log-normal type distribution appears upstream of the flame (see 3rd and 4th grids). Although the 4th grid is affected by the electric field, however, in combination with the information from the 3rd grid, it can be inferred that the particle size distribution is already more dispersed in microgravity than in normal gravity at the locations upstream of the flame. The distributions on the 1st and 2nd grids corresponding to locations downstream of the flame are even more dispersed and the overall particle size is larger than that upstream of the flame. However, from the 2nd grid to the 1st grid, there is a tendency for the size of soot primary particles to decrease due to the oxidation.
Primary particle size data are significant for non-intrusive optical techniques. Because these optical techniques basically require the use of approximation, the primary particle size helps to correctly

choose the appropriate approximation that can be applied. In general, the selection application of approximation needs to be verified by the primary particle size parameter x_p that can be evaluated as follows [180]:

$$x_p = \pi \cdot d_{pp}/\lambda \tag{2.7}$$

where d_{pp} is the diameter of the primary particle and λ is the wavelength of light. In addition, another factor to be taken into account is the dispersity of the primary particle size. Yet it has been shown that the polydispersity of primary particles has a significant effect on the radiative properties of soot [208–210]. Basically, the distribution of primary particle radius has a standard deviation between 15% and 25% of its mean value, which can be largely uniform depending on the particle size [211]. At normal gravity, the largest primary particle radius does not exceed 20 nm, resulting in a $x_p < 0.3$ for the visible or near-infrared wavelength ($\lambda > 500nm$). According to their size, it is reasonable to assume that individual primary particles approximate Rayleigh weakly scattered particles [211]. However, its standard deviation of each grid is above 25% of its mean primary particle radius, still raising questions about the impact of polydispersity. In microgravity, the soot radius produced in the flame can reach a maximum of 40 nm, corresponding to $x_p \approx 0.5$. Then the Rayleigh approximation is there more questionable [180]. Furthermore, its standard deviation is higher than 30% of the mean value of radius for all the grids, and it can even reach 51% for the 2nd grid. Hence, both the primary particle size and polydispersity pose a significant challenge to estimate the associated optical properties [181].

2.4 Summary

The second Chapter presented a novel technique of soot sampling using an attractive electric field for soot collection from an opposed-flow flame spreading over a LDPE coating of NiCr wire both at normal and micro-gravity. The morphological characteristics of the collected soot particles were extracted from TEM images to analyze the effect of gravity on soot particle morphology.

The main parameters of the sampling technique are the sampling duration and voltage. Following the analysis, a shorter sampling time together with a higher sampling voltage lead to an appreciated trade-off between the need for visual discrimination among soot particles observed and the statistical consistency of the features extracted. The differences between microgravity and normal gravity sampling are identified as the experimental setup is operated both in microgravity and at normal gravity.

The sampled soot particles were observed under TEM and the evolution of soot particle morphology along the flame axis was analyzed with known positions in both normal and microgravity conditions. To extract the morphological features of soot particles such as soot particle projected density and area, the radius of gyration, fractal dimension, and primary particle size distribution, corresponding TEM image analysis tools were developed. Using these features, the effects due to gravity can be further characterized.

In microgravity, the density of soot particles sampled at the leading edge of the flame is lower than at normal gravity. This can be correlated with the thermal expansion that is not significantly constrained by the external flow in microgravity. As a result, the flame is locally colder at the flame leading edge and the soot formation rate is believed to be lower.

Interestingly, this trend is reversed at the flame's trailing edge, which correlates with a heavier smoke release by the non-buoyant flames. Overall, soot particles sampled in microgravity are larger than those collected at normal gravity. In addition, the evolution of the soot particle size distribution experiences a transition from log-normal type distribution to a bimodal type one for

microgravity sampling, a trend that cannot be identified at normal gravity.
According to the TEM images, the soot particles sampled in microgravity show up mainly as fractal-like aggregates while at normal gravity they are mainly spherical primary soot particles. The evolution of the soot aggregate structure in microgravity was tracked by its fractal dimension. The mean value of the fractal dimension in microgravity hardly varies along the flame axis and is about 1.86. According to the evolution of its distribution, the closer to the trailing edge of the flame, the more the soot tends to grow as chain-like branched aggregate.
Regarding the soot primary particles, at normal gravity, their radii are not greater than 20 nm, which is consistent with the Rayleigh scattering approximation for wavelength larger than 500 nm. However, their standard deviation is higher than 25% of their mean value for each position, therefore their polydispersity cannot satisfy the assumption of monodispersity. In microgravity, the overall soot primary particles are larger and the distribution in size is still more polydisperse than that at normal gravity. As a result, the trends documented for soot formed in microgravity do not support the monodisperse assumption. This especially poses a challenge for the proper estimation of soot optical characteristics that drive the design of smoke detectors.

3 Flame spread over electric wires in partial gravity

Contents

Moving from a macroscopic scale to a microscopic one it can be observed that flame spread in microgravity is very different from normal gravity, as presented in Chapter 2. To address the ongoing or upcoming Lunar and Martian exploration programs, it is essential to know more about the features of flame spread in partial gravity. This chapter documents the flame spread over metallic wires in partial gravity. Experiments are performed on different types of wire and flow conditions, which are presented in Section 3.1. Section 3.2 first illustrates the flame spread behavior as influenced by gravity, then reports on the extinction limits and flame spread rates for different samples. After having paved an overall understanding of the experimental results, Section 3.3 discusses the flammability of the electric wires. Last, an interesting cyclic spreading phenomenon unveiled at the gravity level of Mars is analyzed in Section 3.4.

3.1 Flow conditions and electric wire samples

DIAMONDS participated for the first time in a partial gravity flight campaign at the end of year 2020. In this flight campaign, the number of parabola at Lunar gravity level and Martian one (0.16 g_0 and 0.38 g_0, respectively) was 33 respectively. The experimental setup was the same as described in Section 2.1. The oxidizer was composed of air potentially mixed with nitrogen, leading to a maximum oxygen content x_{O_2} of 21%. In this study, the forced flow velocity, V_g, was set to 60 or 150 mm/s and the pressure, P , was between 50.7 and 141.9 kPa. The detailed partial gravity experimental procedure is described in Section 2.1.4. The experiments were conducted

equally in microgravity and normal gravity. To compare with the results of steady flame spread in microgravity, the opposed-flow flame spread configuration was chosen.
The selected samples were all electric wires consisting of a metallic core and insulation. Four different configurations were used in this study, as shown in Table 3.1. To investigate the effect of metallic cores with different thermal conductivity on the flame spread, two different metallic cores, i.e. NiCr and Cu, were used. In addition, two different thicknesses of LDPE insulation, i.e. 0.15 mm and 0.3 mm, were used to coat the metallic cores with the purpose of studying the effect of insulation thickness on the flame spread. For convenience, each sample configuration is assigned an ID as shown in Table 3.1, which will be referred to as ID in this Chapter.

ID	Wire dimension		Material	
	Core diameter[mm]	Outer diameter [mm]	Wire core	Insulation
Cu#2	0.5	0.8	Cu	LDPE
NiCr#2	0.5	0.8	NiCr	LDPE
Cu#3	0.5	1.1	Cu	LDPE
NiCr#3	0.5	1.1	NiCr	LDPE

Table 3.1: Configurations of tested wire sample.

3.2 Experimental results

In order to provide an overview of gravitational effects on flame spread over electric wire samples, this section first illustrates and briefly describes the flame spread behavior under different gravity levels. Subsequently, the results of extinction limits and flame spread rates are presented.

3.2.1 Flame spreading behavior at different gravity levels

Figure 3.1 shows representative burning behaviors of Cu#3 and NiCr#3 samples under different gravity levels. Each image was selected when the flame spread process reached a nearly steady rate after ignition. As observed previously, under microgravity, the molten LDPE accumulates in the pyrolysis zone and forms an elliptical shape due to the surface tension of the molten LDPE. Popping flames are sometimes observed around the molten LDPE due to the bursting of bubbles generated in the molten LDPE. The flame along the wire formed a nearly spherical shape in microgravity. Since the soot particles cannot be fully oxidized due to the radiative heat loss, the downstream edge of the flame is open and soot emissions happen.
As the gravitational force increases, both the molten LDPE and the spreading flame take on an axially elongated shape. As shown in Fig. 3.1 (a1) and (b2), the elliptical shape of the molten LDPE is dragged downwards by the gravitational force, and the pyrolysis region is expanded in an axial direction. It should also be noted that during the flame spread process shown in both figures, although molten LDPE dripped along the wire surface, no outflow or separation of molten LDPE from its body enveloped by the visible flame was observed. However, when the size of the molten LDPE accumulated on the wire surface exceeded a certain volume or the gravitational force exceeded a certain level, a molten LDPE droplet without flame appeared upstream of the flame leading edge, as shown in Fig. 3.1 (a3), (a4), (b3), and (b4). This is due to the gravity-induced dropping accompanied by the flow or separation of molten LDPE from its main body.

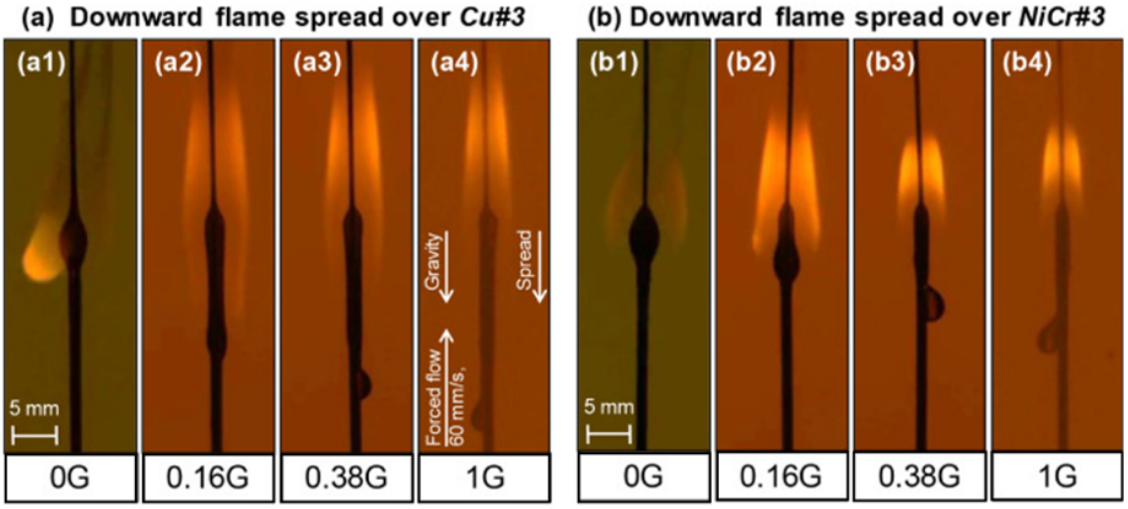

Figure 3.1: Backlighted images of opposed-flow flame spread over the electric wire samples under different gravity levels at 21% oxygen content and 60 mm/s flow velocity. Images on the left are Cu wire samples (Cu#3 configuration) and those on the right are NiCr wire samples (NiCr#3 configuration). [212]

Besides, it can be found that metallic cores with different conductivity have an effect on the flame spread behavior. This difference is even more visible in partial gravity. The Cu core samples with higher conductivity show a more stretched molten LDPE in partial gravity (Fig. 3.1 (a2) and (a3) versus (b2) and (b3)) compared to the NiCr core samples, which means that the pyrolysis zone is enlarged in the axial direction. This leads also to an axial enlargement of gaseous zone and to a longer flame length.

3.2.2 Extinction limits

Figure 3.2 exhibits the flame spread and extinction limits as a function of gravity level for all tested samples at different forced flow conditions with a pressure of 101.3 kPa. To clarify the characteristics of flame spread, the experimental results can be divided into four cases based on the direct observation above. • represents flame spread without any molten LDPE drops (as shown in Fig. 3.1 (a1) and (b1)). ■ represents flame spread with molten LDPE drops, though there is no leakage from its main body (as shown in Fig. 3.1 (a2) and (b2)). ▽ represents the flame spread with molten LDPE drops and leakage from the main body (such as Fig. 3.1 (a3) and (b3)). × represents the extinction condition. The solid line delineates the expected flammability boundary based on the experimental results. Each symbol in the figure corresponds to a single test result. It is important to note that the flames were all systematically observed after the initial ignition procedure, so the extinction limit for this study corresponds to the limiting conditions of flame spread rather than the ignition limit.

From Fig. 3.2, it can be observed that the extinction limit of NiCr samples decreases with gravitational level, while the extinction limit of Cu samples is less affected by gravitational level. In both #2 and #3 samples, the extinction limits of NiCr samples are lower than those of Cu samples in microgravity. However, at higher gravity conditions, the opposite trend is observed. The reason behind such a trend in the extinction limit needs to be analyzed in conjunction with the flame spread rate. Therefore, the relationship between flame spread rates at different gravity levels needs to be presented before further analysis of the observed extinction limits.

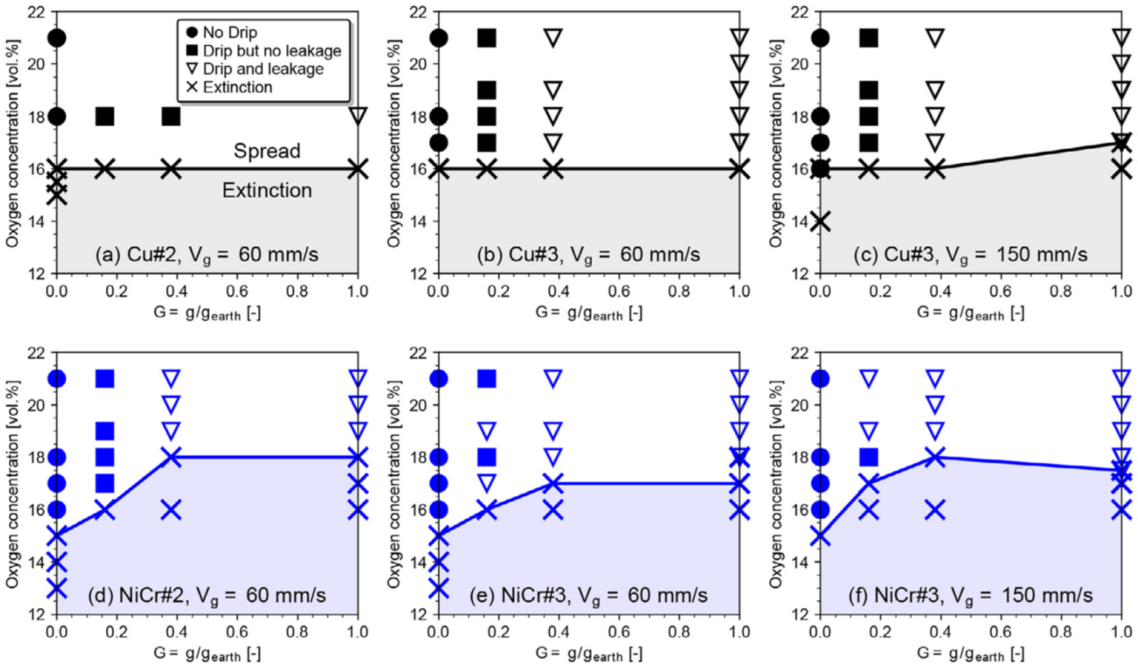

Figure 3.2: Flammability maps as a function of gravity level for different wire samples in different forced flow velocity conditions with a pressure of 101.3 kPa. [212]

3.2.3 Flame spread rates

Except for the NiCr samples in microgravity, where the flame spread is in accordance with the regular steady rate flame spread (as highlighted in Section 1.2.5), the spread on all the remaining samples can only be considered as at nearly steady rate. The main reason for this is that the molten LDPE droplets upstream of the flame are affected by gravity and their observed volume does not reach a steady state, leading to the fact that the gaseous fuel supplied to the flame is not considered constant. Therefore, the definition of flame spread rate needs to be re-emphasized here.

Definition

The leading and trailing edges of the molten LDPE and the visible flame are tracked over time during flame spread to determine the flame spread rate (V_f).
Backlighted and non-backlighted images were used to detect the location of the molten LDPE and visible flame, respectively. Fig. 3.3 shows the four characteristic positions used for motion detection on the burning sample. The leading edge of the molten LDPE is determined by the bottom end of the droplet, regardless of whether it is enveloped by the visible flame (denoted as $x_{PE,front}$ in Fig. 3.3 (a)). The trailing edge of the molten LDPE corresponds to the burning edge of the LDPE (denoted as $x_{PE,tail}$ in Fig. 3.3 (a)). The leading and trailing edges of the diffusion flame are determined from the visible area of the luminous flame (denoted as $x_{Flame,front}$ and $x_{Flame,tail}$ in Fig. 3.3 (b)).

After image analysis, a local least squares polynomial approximation of the data smoothing method (with Savitzky-Gorey filter) was applied to the position history data to calculate the instantaneous velocity of movement at each position. A linear function was chosen to fit the trend and

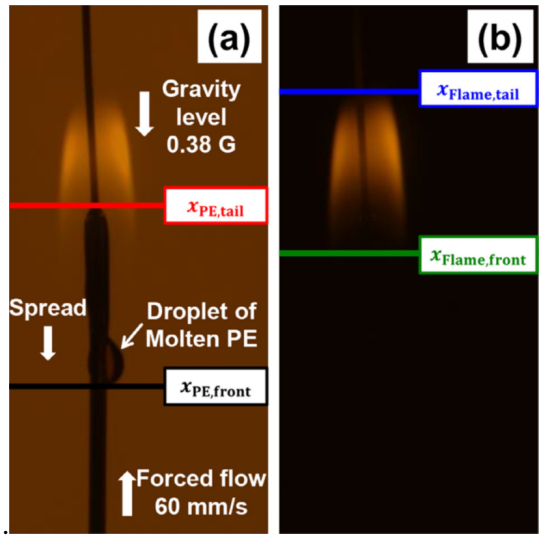

Figure 3.3: Four characteristic positions in the burning wire tracked along time by image processing. (a) backlighted image indicating the positions of the leading edge and trailing edge of the molten LDPE. (b) non-backlighted image indicating the positions of the leading edge and trailing edge of the visible flame. Experimental conditions: NiCr#3, 0.38 g_0, 21% oxygen content, 60 mm/s flow velocity, and 101.3kPa pressure. [212]

its first-order derivative was used to derive the instantaneous travel velocity. The approximate interval of this filter was set to 19 data points, which corresponds to 0.97 seconds in real-time given the frame rate of 19.53 frames/second for both backlighted and non-backlighted images.

Flame spread time history

The results of two representative analyses are shown in Fig. 3.4 along with the time histories of gravity levels recorded within the parabola. The fine solid line and scatter plot represent the raw data from the analysis for the entire period and the high confidence data within a partial gravity period, respectively. The left and right plots represent the results for Cu#3 and NiCr#3, respectively. The experimental conditions were the same for each sample: 0.38 g_0 gravity level, 21% oxygen content, and a flow velocity of 60 mm/s.

In both cases, the leakage of molten LDPE from the burning zone was confirmed during the flame spread, its occurrence being also identified in the figure. As it can be seen in Fig. 3.4, all the travel velocities are accelerating before the end of the partial gravity period of Cu#3, with the same trend in almost all experimental conditions of the Cu sample. In contrast, in the case of NiCr#3, all travel velocities are almost constant except for $\dot{x}_{PE,front}$. These observations are consistent with the theoretical study by Huang et al. [213], who investigated the ignition-to-spread control mechanism for externally heated wire samples and found that achieving ignition was more difficult for higher conductivity wires.

From Fig. 3.4, it can be noted that $\dot{x}_{PE,front}$ is strongly influenced by the motion of the molten LDPE drops and it is difficult to determine V_f using $\dot{x}_{PE,front}$ because its motion is time-dependent, unlike the behavior of the spreading flame. Regarding $\dot{x}_{Flame,front}$ and $\dot{x}_{Flame,tail}$, when the bubble bursting formed in molten LDPE became significant, $\dot{x}_{Flame,front}$ and $\dot{x}_{Flame,tail}$ showed large fluctuations due to the appearance of bursting flames in random directions.

In addition, when the ambient conditions approach the extinction limit, the intensity of the flame emission decreases, and no visible flame can be detected. Based on these observations, $\dot{x}_{PE,tail}$ in the confidence interval was chosen to define V_f because the time history of $\dot{x}_{PE,tail}$ is less influenced by disturbances such as dripping and flame bursting. To minimize the effect of the initial ignition period on the measured V_f, the average of the last three seconds of $\dot{x}_{PE,tail}$ in the confidence interval is defined as V_f in this analysis.

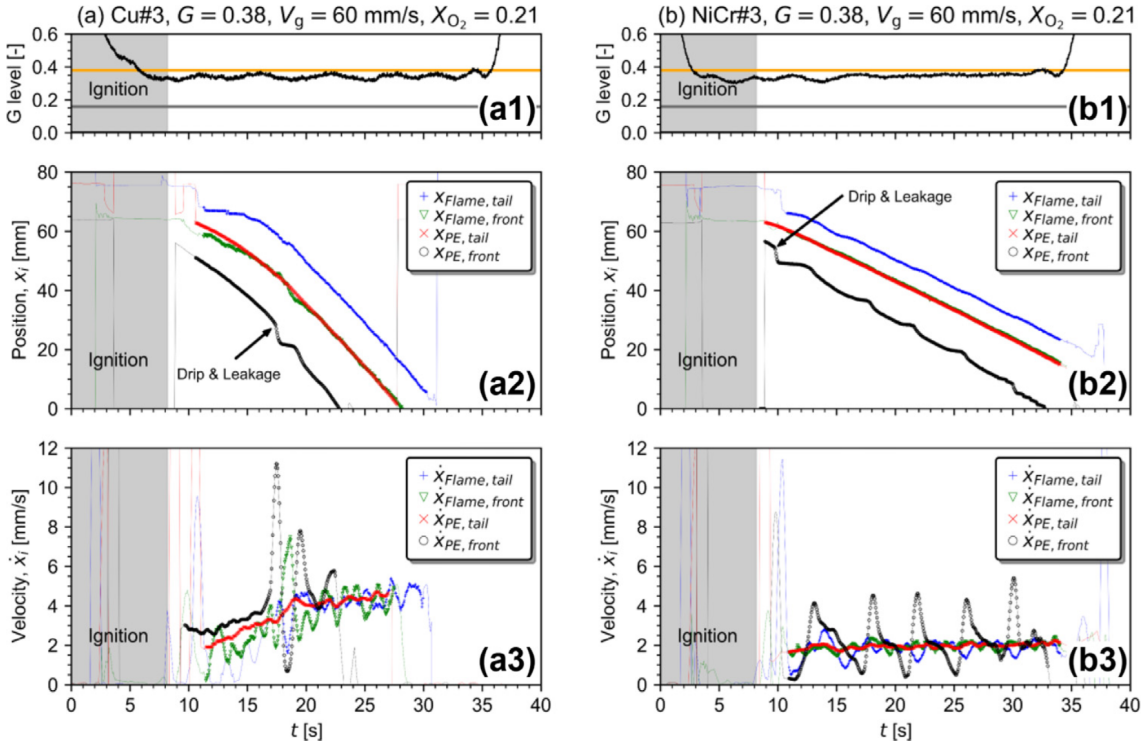

Figure 3.4: From the top to the bottom, evolutions with time of: gravity level during the parabola, four characteristic positions on the burning coating, and the instantaneous traveling velocity of each position. The bolded data in the figures indicate analysis results in the confidence interval. The experimental conditions for each figure are specified on top of the figure. [212]

Flame spread rate results

The measured V_f is plotted in Fig. 3.5 as a function of gravity level with a pressure of 101.3 kPa. Figure 3.5 (a) presents the results of Cu#2 and NiCr#2 samples at flow velocity of 60 mm/s. Figure 3.5 (b) shows the same for Cu#3 and NiCr#3 samples. Figure 3.5 (c) presents the results of Cu#3 and NiCr#3 samples at flow velocity of 150 mm/s. The differences in the dynamic motion of the molten LDPE during flame spread are also indicated by different markers in the same way as in the flammability maps.

It can be seen from the plots that Cu samples always show a larger V_f than NiCr samples under the same experimental conditions. These tendencies are qualitatively consistent with previous studies investigating the effect of core materials on V_f under normal and microgravity [214–216]. It is convinced that for electric wire with high thermal conductivity inner metallic core, the conduction heat supply through the core plays a major role in supporting flame spread.

As for the effect of gravity on V_f, in most cases, V_f tends to increase monotonically with increasing gravity level, but there are some exceptions such as NiCr#2 and NiCr#3 at low oxygen content which shows a peak value at reduced gravity conditions. According to the observation, such a trend is determined by the state of the molten LDPE upstream of the flame. The monotonic increase in flame spread rate with gravity level is due to the fact that the molten fuel is pulled upstream at a faster rate by the increase in gravity. In the case of peak flame spread rate at partial gravity, molten LDPE can be found to drip with irrevocable leakage at higher gravity levels. As the molten LDPE droplet drops and separates from the main body, the separated droplet may begin to cool

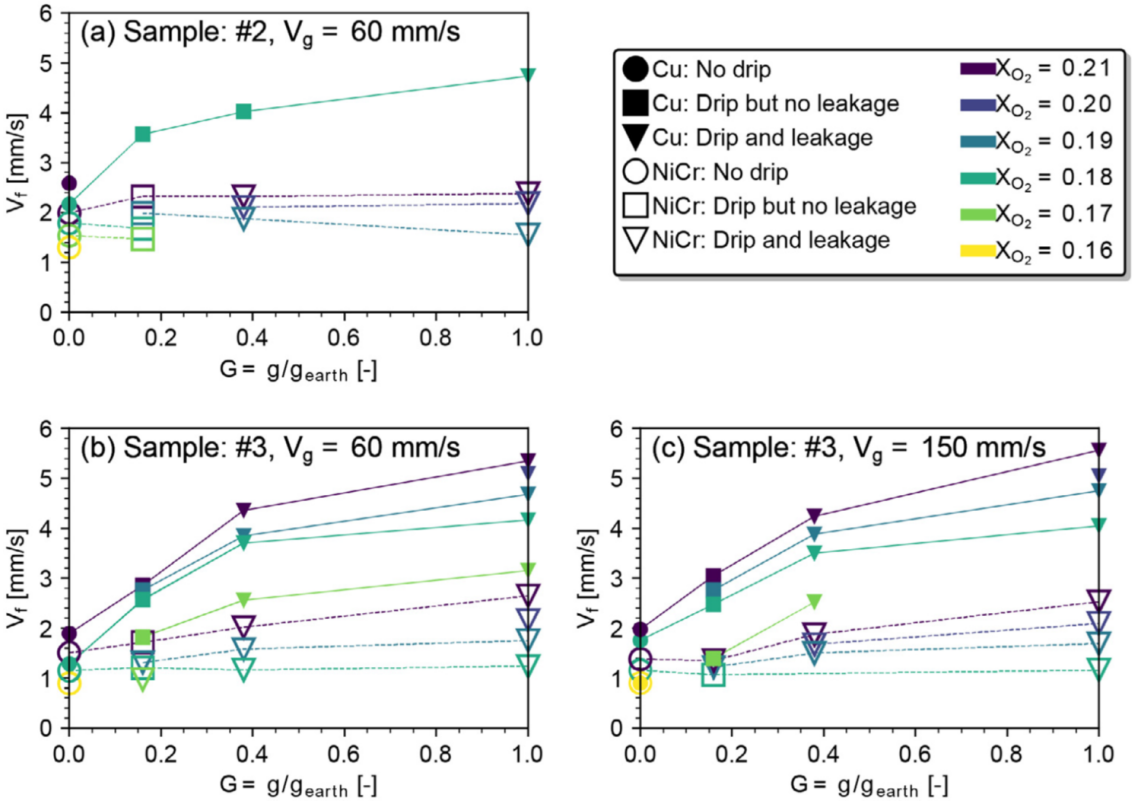

Figure 3.5: Flame spread rate as a function of gravity level with a pressure of 101.3kPa, for different forced flow velocities and oxygen contents. (a) Cu#2 and NiCr#2 in 60 mm/s forced flow, (b) Cu#3 and NiCr#3 in 60 mm/s forced flow, (c) Cu#3 and NiCr#3 in 150 mm/s forced flow. [212]

and slow down upstream due to insufficient heat provided by the flame (e.g., in the case of low oxygen content) or insufficient heat transfer within the metal core (e.g., in the case of the NiCr sample with a lower conductivity). The droplet then accumulates a large amount of fuel upstream of the flame, and when the flame catches up with the droplet, it takes a longer time to pyrolyze it, thus slowing down the flame spread rate. This occurs mainly for NiCr samples with much lower thermal conductivity. From the gaseous zone perspective, it has also been reported that V_f shows a peak value at moderate gravity levels due to the competition between the radiative heat loss from the system and the leakage of reactants due to finite rate chemical reactions [46, 217].
Furthermore, in contrast to extinction limits as a function of gravity level, the variation of V_f to gravity level is more pronounced on Cu samples than on NiCr ones. Further detailed analysis is carried out in the next Section in conjunction with extinction limits and flame spread rates.

3.3 Electric wire sample flammability discussion

Following an overview of the results of flame spread over electric wires at different levels of gravity, in this Section, we will discuss how gravity affects the flammability of the electric wire samples used in the present study. The underlying mechanism of flame spread over solid fuels in different gravitational fields can be consistently explained by the effect of the gas flow velocity under varying gravitational forces as a result of the buoyancy-induced flow nearby the flame. Furthermore, several previous studies [45, 46, 217] reported the well-known U-shaped flammability limit curve for flame spread over solid fuels as a function of gas flow velocity, as discussed in Section 1.2.5. The shape is

driven on one side by the quenching regime at low gravity conditions, where the flame temperature is reduced by radiative heat loss from the gas phase and solid surface, and on the other side by the blow-off regime at high gravity conditions, where the flame temperature is reduced by the leakage of reactant due to the finite rate chemistry (as discussed in Section 1.2.3).

Identification of extinction regime

Similar to the flammability diagrams as a function of the gas flow velocity [167], the extinction limit of the Cu samples is almost constant relative to the gravity level (see Fig. 3.2 (a), (b) and (c)). These trends can be explained by the fact that the observed range is in the overlapping system of the quenching regime and the blow-off regime. In contrast, for the NiCr sample, the extinction limit decreases monotonically with the gravity level, so it can be assumed that the flame spread on the NiCr sample is in the regime of the blow-off branch. Interestingly, the thermal conductivity of the core material is also an important parameter that alters the trend of extinction limits against gravity levels. The reason for this will be explained below in conjunction with the effect of the core material's thermal conductivity on the flame spread rate.

3.3.1 Extinction limits versus flame spread rates

The difference in the extinction limit trend between Cu and NiCr wires versus gravity level can be understood by the difference in V_f between Cu and NiCr wires at the near extinction limit.
It can be seen in Fig. 3.5 that V_f for the spread on Cu samples increases monotonically with the gravity level even at lower oxygen content, while V_f for NiCr samples exhibits a weak dependence on the gravity level at lower oxygen content. Thus, for the Cu sample, more gaseous fuel is supplied to the reaction zone at higher gravity conditions due to the increase in V_f. As a result, the flame spread rate is able to get stable at a shorter residence time of the reactants in the reaction region due to the increased reaction rate supplied by the increased fuel concentration.
The lower extinction limit of the Cu sample as compared to that of the NiCr sample under higher gravity conditions can also be reasonably explained by the difference in V_f controlling the fuel supply to the reaction zone. From another point of view, we can admit that the effect of finite rate chemistry on the flame spread limit is obvious for the NiCr sample because of the smaller amount of vaporized fuel supplying the reaction zone and the smaller V_f.
In microgravity where the flow residence time of the reactants becomes long enough, the Cu sample shows a larger V_f than the NiCr sample, even in the near extinction limits (see Fig. 3.2). This trend is consistent with the theoretical explanation of Konno et al. [218]. These authors argued that the forward heat conduction throughout the wire core can be the dominant mechanism for flame spread over the electric wire because it increases the radiative heat losses from the solid surface and the convective ones from the solid surface in the unburned zone. Furthermore, it has been theoretically demonstrated that flame spread over the wire with high conductivity (e.g., Cu wire) is quenched at a larger V_f as compared to the configuration of low conductive wire (e.g., NiCr wire) due to the increased heat loss in the unburned zone.

3.3.2 Gaseous region

As mentioned above, unlike the trend in the extinction limit, the V_f increases significantly with increasing gravity levels for the Cu samples as compared to the NiCr samples, even at oxygen contents close to the extinction limit. This is probably due to the decrease in the stand-off distance [1] as the buoyancy-induced flow increases (see Fig. 3.1), resulting in an increase in the heat flux from the spreading flame to the solid surface.
In general, highly conductive wires can recirculate more heat from the downstream flame to the upstream unburned insulation [215, 216], so the decrease in flame height acts favorably on the enhancement of flame spread on highly conductive wires. On the other hand, for NiCr samples, the heat recirculation through the wire core is dampened and it leads to a smaller V_f. As previously discussed, the smaller V_f reduces the fuel supply to the reaction zone and, therefore, the flame spread over NiCr samples would be more sensitive to the effect of finite rate chemistry on the flame temperature compared to Cu samples. As a result, blow-off branches appear in the flammability diagram of the NiCr sample, where extinction limit increases with increasing gravity level.

3.3.3 Pyrolysis region

Another important factor affecting the flammability of wire samples in the gravity field is the deformation of the insulation material due to its own weight during flame spread. This deformation occurs mainly in the pyrolysis zone. For thermoplastics, such as LDPE, the deformation of the sample due to gravity becomes more pronounced as its temperature increases and the melted material viscosity decreases [161, 188, 219]. Clarifying whether the deformation of a solid material affects its flammability is arguably an important issue in determining whether the effect of gravity on material flammability can be considered a flow velocity effect.
The three scenarios that molten LDPE can experience are illustrated in both Fig. 3.2 and Fig. 3.5,

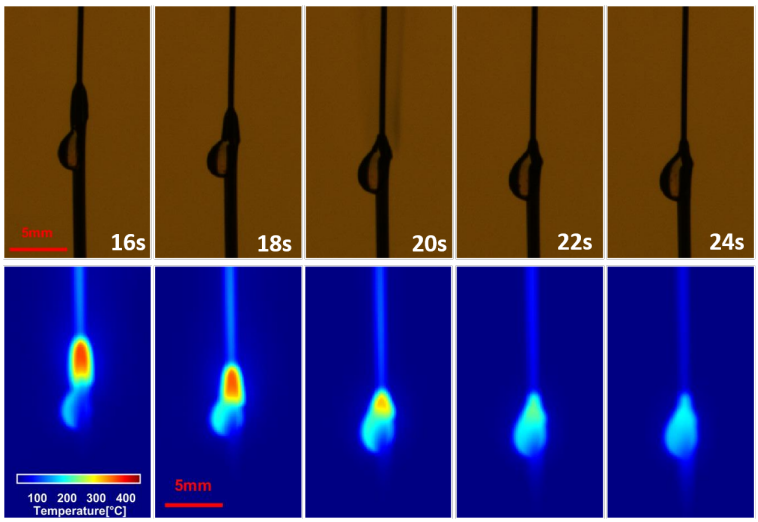

Figure 3.6: Backlighted images captured by the CCD camera (upper row) and infrared images captured by the infrared camera (lower row). Images show the experiment conducted with a NiCr#3 sample at 0.38 g_0 under 18% oxygen content, 150 mm/s flow velocity, and 101.3 kPa pressure. Images are taken from 16s til 24s after the ignition illustrating the extinction process with drip and leakage of molten LDPE. Extinction occurs around time 20s with a release of unburned pyrolysis products.

[1] Stand-off distance is defined as distance of the flame from the solid surface

displaying no drip, drip without leakage, and drip with leakage. It is undeniable that as the gravity level increases, the molten LDPE gradually transitions from no drip to drip without leakage, and finally to drip with leakage.

At higher gravity (0.38 g_0 and 1 g_0), both NiCr#2 and NiCr#3 samples showed drips and separation of the molten LDPE before extinction under conditions near the extinction limit. An example is given in Fig. 3.6, which displays backlighted images captured by a CCD camera together with those obtained by an infrared camera. The infrared images capture the energy emitted from the sample surface, and then the temperature of the sample surface can be estimated assuming that the sample is a gray body with a uniform and constant emissivity of 0.92. This latter evaluation is highly debatable but is extracted from measurements of the emissivity of LDPE within its pyrolysis [220].

The flame is not visible after ignition because of the low oxygen content, but it still starts to spread. The separated droplets accumulated molten fuel upstream and were found to be cooler than the molten LDPE body according to the infrared camera recordings, creating a barrier. The flame downstream provides heat to the main body and thus allows the pyrolysis to be sustained (see Fig 3.6 from 16s til 20s). When the main body is almost consumed, the temperature of the separated droplet upstream rises due to the approach of the flame. However, the heat provided by the flame is not sufficient to feed the pyrolysis process of the separated droplets, thus extinction occurs in Fig. 3.6 (20s), and the unburned pyrolysis products are released from the main body. After extinction, the separated droplets upstream continue to cool down. Since this occurs only at higher gravity levels and leads to the extinction limit at higher oxygen content (e.g., Fig. 3.2 (e) and (f)), such a mechanism seems to facilitate the occurrence of extinction. However, none of the Cu samples showed separation of the molten LDPE from the main body before their extinction under higher gravity levels.

However, at lower gravity levels (0 g_0 or 0.16 g_0) an extinction scenario happens without separation

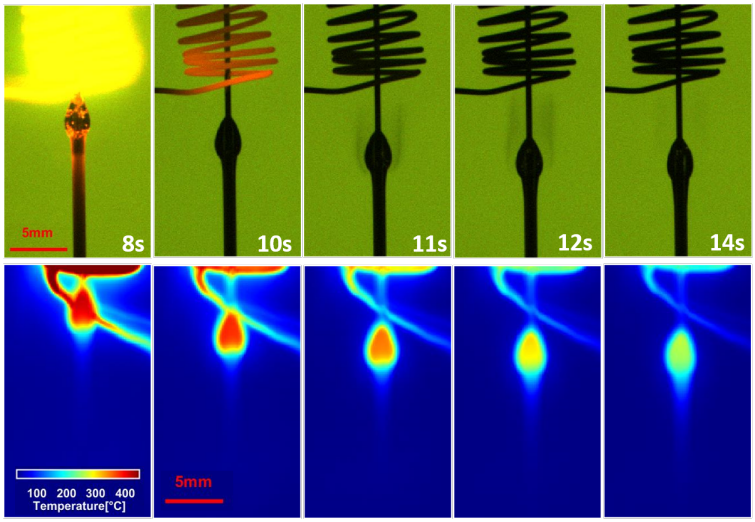

Figure 3.7: Backlighted images captured by the CCD camera (upper row) and infrared images captured by the infrared camera (lower row). Images show the experiment conducted with a NiCr#3 sample at 0.38 g_0 under 16% oxygen content, 60 mm/s flow velocity, and 101.3 kPa pressure. Images are taken from 8s til 14s after the ignition illustrating the extinction process without leakage of molten LDPE. Extinction occurs around time 20s with a release of unburned pyrolysis products.

of the molten LDPE from the main body, as illustrated in Fig. 3.7. In the figure, it can be first observed that a large amount of heat is given by the igniter, which stops applying heat to the sample 8 seconds after the start of the ignition procedure. The regular bulb-shaped molten LDPE is

formed, the flame is not visible due to the low oxygen content, and no leakage of molten LDPE occurs due to the low gravity. The flame heat release rate is too weak to sustain the heat wave to the upstream fuel and the temperature of the molten LDPE started to decrease as can be seen from the infrared camera. The extinction occurred at 11 seconds and the pyrolysis products started to escape from the upstream deformation position of the molten LDPE. The molten LDPE continues to cool down until it reaches ambient temperature.

3.3.4 Leakage of molten LDPE

It follows that leakage of molten LDPE appears to play a key role in an alternative extinction mechanism. The trend and cause of leakage appearance become important for wire flammability understanding. The flame spread at Lunar gravity may provide some useful information.
Under Lunar gravity, some conditions of the NiCr#3 samples showed drips and separation from the main body. However, it was not observed for the Cu#3 samples (including Cu#2). This is attributed to the difference in the thermal conductivity of the metallic wire cores. As mentioned above, the lower thermal conductivity wires (NiCr) lead to less heat recirculation from the downstream flame to the upstream unburned insulation, resulting in a "pear" shape of the accumulated molten LDPE upstream of the flame (see Figure: 3.1 (b2)). In contrast, the molten LDPE of the Cu sample is more stretched in the axial direction (e.g., Fig. 3.1 (a2)). The molten LDPE of NiCr#3 accumulates in such a way that it has an increased local mass and thus appears to be more susceptible to gravity, which triggers dripping and separation from the main body more easily. In addition, the NiCr#2 sample with thinner insulation did not lead to the leakage of molten LDPE, implying that the thicker insulation promoted the separation of the molten LDPE from the main body.
At Lunar gravity, the molten LDPE of NiCr samples dripped at the beginning of the flame spread and the volume of molten LDPE increased continuously. Sometimes the molten LDPE droplets appeared to separate from the main body. The volume of molten LDPE was evaluated based on backlighted images and axisymmetric conjectures. The evaluated volumes revealed that leakage can occur in the case of smaller volumes as well. In contrast, in the case of larger volumes, it is also possible that no leakage occurs. Therefore, no volume threshold for molten LDPE droplet leakage was found. This indicates that its volume is not the only cause of leakage, and its specific causes require further analysis of the complex competition between gravity and droplet surface tension. However, it is evident that the odds of molten LDPE leaking from the main body increase with increasing gravity level. Once leakage occurs, it plays an important role in the extinction mechanism and has a tendency to increase the extinction limit. Therefore, in this case, the effect of gravity on material flammability cannot be considered as a matter of flow rate effect alone. For NiCr samples the trend of molten LDPE leakage can be found in the transition between its non-leakage and leakage at Lunar gravity. In addition, the increase of core conductivity and the decrease of insulation thickness both reduce the occurrence of molten LDPE leakage.

3.4 Cyclic flame spread over LDPE coated NiCr wire at Martian gravity

As discussed in the previous Section, molten LDPE is subject to gravitational effects that can potentially lead to leakage and have an impact on the flammability of the wire samples at higher gravity (0.38 g_0 and 1 g_0). However, molten LDPE leakage affects not only flammability, but also the flame

spread mechanism. An interesting cyclic flame spread mechanism over the NiCr wire samples was discovered. This phenomenon occurs only at Martian gravity (0.38 g_0). This Section begins with a description of cyclic flame spread. This mechanism is then analyzed based on the data obtained from the images. Finally, the effect of oxygen content and pressure on such a spreading mechanism is discussed.

3.4.1 Cyclic flame spread observation

Figure 3.8 illustrates the opposed-flow downward flame spread over a cylindrical sample in both micro- and Martian gravity environments. Ambient conditions of V_g = 60 mm/s, x_{O_2} = 21%, and P = 121.6 kPa illustrate the processes which were systematically observed in all the experiments conducted at Martian gravity. The sets of frames (a) and (b) represent a Martian gravity sequence of backlighted and infrared images, respectively.
These illustrate how the molten droplet accelerates and decelerates upstream of the flame front

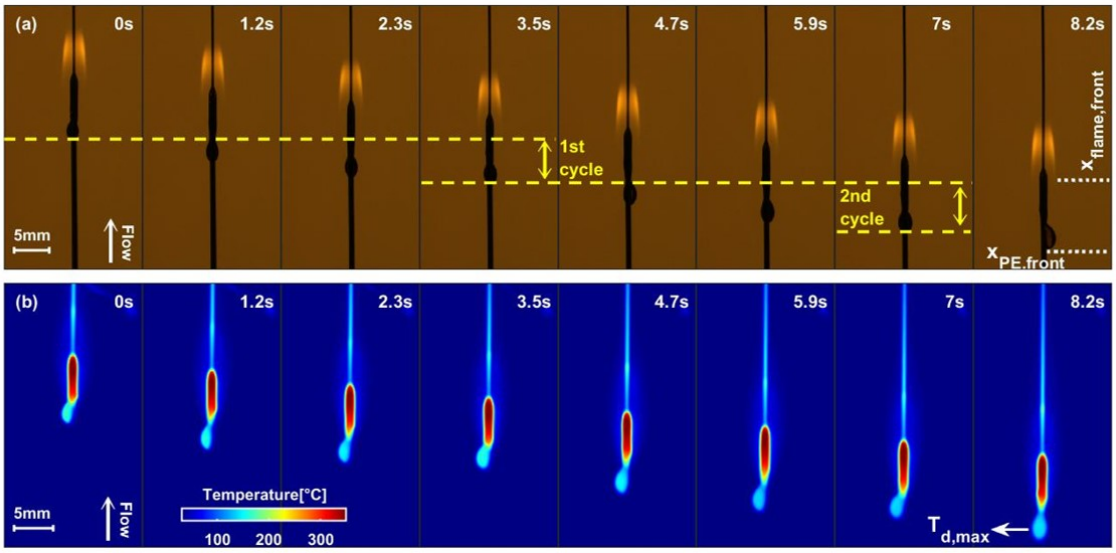

Figure 3.8: (a) Backlighted and (b) infrared frames imaging opposed-flow flame spread over a NiCr#3 wire sample, for V_g = 60 mm/s, x_{O_2} = 21%, and P = 121.6 kPa.

in the course of two successive cycles, with t = 0s corresponding to the beginning of the first cycle. During the second cycle, the droplet accelerates from t = 3.5s til t = 5.9s, and then slows down from t = 5.9s til t = 7s. In the course of this cycle, the luminous flame is shortened during the acceleration stage, reaches a minimum at t = 5.9s, and elongates in the droplet deceleration phase. The infrared camera imaging (see Fig. 3.8(b)) highlights that the droplet progresses only on one side of the wire, and eventually rotates at the end of the second cycle. This calls for a careful evaluation of the quantities of interest, such as the droplet temperature, which can be altered by its position relative to the infrared camera. At the flame leading edge, the pyrolyzing region features surface temperatures above 350°C consistent with the past flame spread observations over LDPE [167]. Upstream of that region, the droplet surface temperature is always much lower, fluctuating in between 150°C and 200°C, yet remains above the 130°C melting point of LDPE. It can then be assumed that the droplet propagates in a liquid state, while vaporization can be neglected. After the droplet starts to slide away from the flame front at t = 3.5s, its surface temperature gradually drops, reaches a minimum at t = 5.9s, and then increases again until the end of the cycle at t = 7s.

Such a cyclic motion of the molten droplet is neither documented at normal gravity, where it detaches from the wire altogether under the dominating effects of gravity, nor in microgravity, where surface tension and viscous forces dominate, allowing the droplet to spread at the same rate of the flame front. In addition, this cyclic spreading was likewise not observed at Lunar gravity of 0.16 g_0. Because the appearance of molten LDPE leakage usually occurs at the end of the flame spreading process, the short microgravity duration is not sufficient to observe the appearance of the complete cyclic spreading.
At the intermediate gravity levels investigated, the competition among the forces induced by the gravitational, the surface tension, and the viscous effects results in this unique pattern. The in-depth analysis of a cycle is performed to evidence the driving mechanisms, before investigating how ambient conditions affect the characteristics of the cyclic propagation.

3.4.2 Mechanisms of cyclic flame spread

To further analyze the experimental configuration presented in Fig. 3.8, Fig. 3.9 presents the evolution with time of the flame front position, $X_{flame,front}$, the droplet front position, $X_{PE,front}$, the advancing contact angle, θ_{Adv}, the receding contact angle, θ_{Rec} (both contact angles are illustrated in Fig.3.15), the maximum surface droplet temperature, $T_{d,max}$. These are defined in Section 3.4.1 and illustrated in Fig. 3.8.
The inflection point of the evolution of the droplet front position is used as a clear marker of the

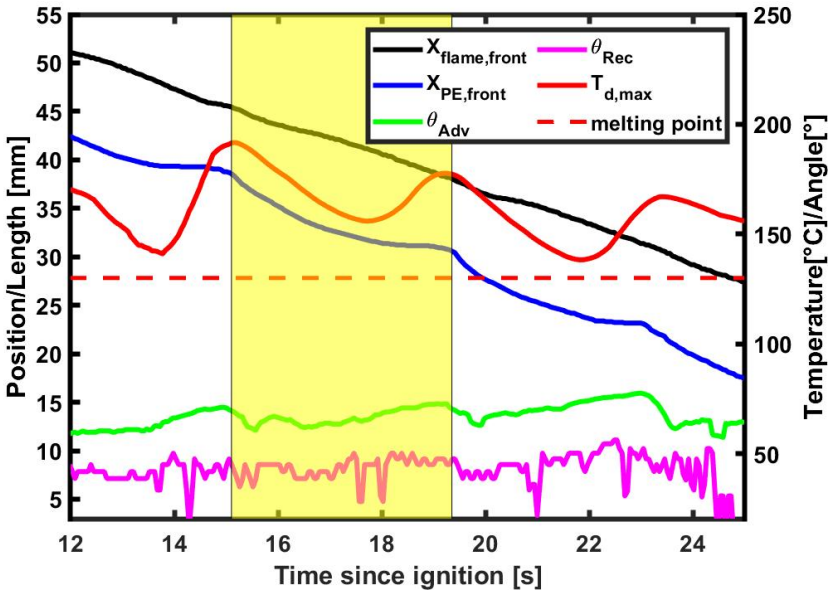

Figure 3.9: Data obtained within a cyclic flame spread at Martian gravity for V_g = 60 mm/s, x_{O_2} = 21%, and P = 121.6 kPa. The evolutions of the flame front position, $X_{flame,front}$ (black), the droplet front position, $X_{PE,front}$ (blue), the advancing contact angle, θ_{Adv} (green), the receding angle, θ_{Rec} (purple), and the maximum droplet temperature, $T_{d,max}$ (red) are reported. The melting point is indicated with a red dotted line, while the highlighted area represents one cycle.

start and end time of the cycle. A cycle that clearly presents the droplet in front of the CCD camera without overlap with the wire, is selected and highlighted in yellow in Fig. 3.9. The purpose is to be able to observe the outline of the leaking droplet for the following analysis. In the course of this cycle, successive snapshots of the shape of the droplet extracted from the backlighted visible frames

are reported in Fig. 3.10. These data allow the formulation of the following theoretical framework.

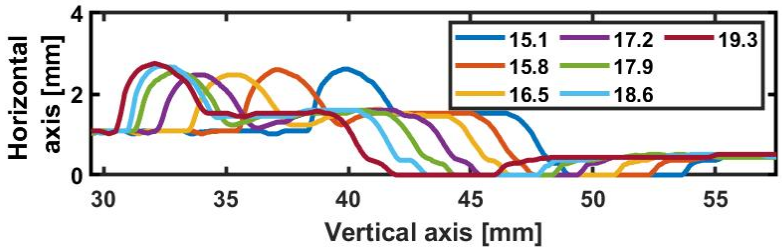

Figure 3.10: Sample profiles extracted from backlighted frames selected along a cycle from 15.1 til 19.3s (period highlighted in yellow in Fig. 3.9). The droplet is here sliding from the right to the left.

Spreading flame

First, Fig. 3.9 shows that the flame front position evolves linearly with time, demonstrating that the flame spreads at a nearly steady rate as discussed in Section 3.2.3. Assuming that the LDPE and the metallic core ahead of the flame front are at thermal equilibrium, the flame spread rate, V_f, which is equal to the flame front velocity, can be estimated as [216]:

$$V_f = \frac{\dot{Q}_{c,fl} + \dot{Q}_{c,s}}{(A_p \rho_p c_p + A_m \rho_m c_m)(T_p - T_\infty)} \tag{3.1}$$

where $\dot{Q}_{c,s}$, A, c, and ρ represent the conductive heat flux from the metallic core to the LDPE, the cross-section area, the specific heat, and the density, respectively. T_p and T_∞ are the pyrolysis and ambient temperatures, respectively, whereas the subscripts p and m refer to the polymer (LDPE) and metallic core, respectively. $\dot{Q}_{c,fl}$ is the conductive heat flux from the flame to the LDPE and can be expressed as follows [216, 221]:

$$\dot{Q}_{c,fl} = \frac{P_p L_g k_g (T_{fl} - T_p)}{r_d \ln(1 + L_g/r_d)} \tag{3.2}$$

where $P_p = 2\pi r_d$ with r_d being the droplet radius. k_g and T_{fl} are the gas-phase heat conductivity and the flame temperature whereas $L_g = \alpha_g / V_g$ is the gas-phase preheat length with V_g being a characteristic velocity of the mixed flow and α_g the gas-phase thermal diffusivity.

Droplet shape

Though the flame front velocity is constant, Fig. 3.9 also shows that $X_{PE,front}$, θ_{Adv}, and $T_{d,max}$ display a periodic behavior.
The following analysis focuses on the dynamics of the leaked droplet in a representative cycle (highlighted in yellow in Fig. 3.9). The evolution of $X_{PE,front}$ over time reveals that the droplet does not travel at a constant velocity. The evolution of its velocity over time can be observed in Fig. 3.11, where the droplet has the highest velocity at the beginning of the cycle. Then, it decelerates during the major part of the cycle and eventually starts to accelerate before the end of the cycle.
During this process, the shape of the droplet also changes and is presented in Fig. 3.10, where the droplet slides from right to left. At the beginning of the cycle, the droplet is in contact with the molten LDPE body and then slides away from the body at high speed, while at the same time

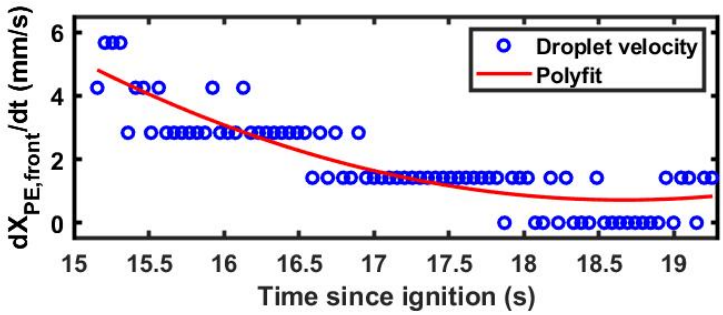

Figure 3.11: Evolution of the leaked droplet velocity with time. This was extracted from $X_{PE,front}$ as a function of time in the discussed cycle (highlighted in yellow in Fig. 3.9). Experimental data are represented in blue. A second order fit is applied and represented in red to illustrate the trend followed.

the droplet height decreases and the velocity continues to slow down. Later in the cycle, the main body of the molten LDPE starts to catch up with the separated droplets, while the droplet height increases.

The capability of the upstream leaked molten LDPE to maintain the droplet shape is related to

Figure 3.12: Comparison of the microdrop (left) and macrodrop (right) shapes (not at scale). Microdrops have the shape of spherical caps, whereas larger drops are flattened by the action of gravity and their height is related to the capillary length. Reproduced from Berthier (2013) [222].

its surface tension and gravity. For example, it is usually observed that large droplets have a flat shape in the solid plane, while small droplets have a spherical shape (as shown in Fig. 3.12). This observation is also related to the balance between gravity and surface tension. The microscopic droplets are controlled by the surface tension, while the shape of the larger droplets is produced by the balance between the two forces. The scale length of this transition is the capillary length [222]:

$$l_c = \sqrt{\frac{\gamma_p}{\rho_p g}} \tag{3.3}$$

where γ is the surface tension, ρ_p is the density, and g is the gravity. When the droplet characteristic length is lower than the capillary length it will be closer to a sphere [223]. The droplet shape provided in Fig. 3.10 allows for a simple analysis. The surface tension of the LDPE droplet is based on the results of Linear polyethylene measured by Roe [224], where the surface tension decreases linearly with increasing its temperature. Also, the density of LDPE decreases with temperature [225]. With the above properties, the capillary length of LDPE droplets can be evaluated and shown in Fig. 3.13. The width of the droplet, w_d, in contact with the wire and the height of the droplet, h_d, during the cycle are also shown.

It can be found that the capillary length is in the same order as the width and height of the droplet during the cycle. Combining Fig. 3.10 and Fig. 3.13, it can be observed that the width of the droplet tends to increase and then decrease during the cycle, while the height of the droplet tends to decrease and then increase. Taking the droplet width w_d as the characteristic length of the droplet, its value close to the capillary length indicates that the shape is not completely controlled by the

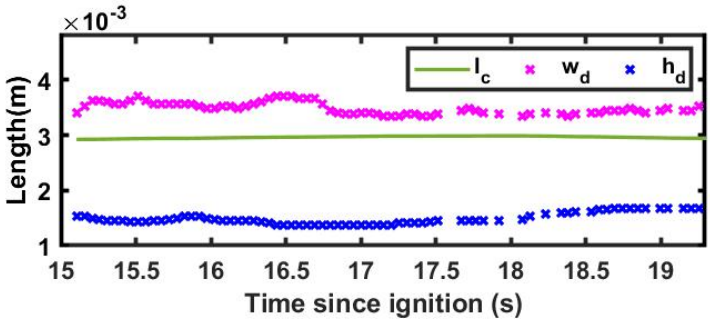

Figure 3.13: Evolution of capillary l_c, width w_d, and height h_d of leaked droplet over time in the discussed cycle (highlighted in yellow in Fig. 3.9). The width and the height of droplet is defined as shown in Fig. 3.15.

surface tension, but it also means that the surface tension still affects the shape of the droplet. Furthermore, the Bond number, which is used to determine the importance of gravitational force compared to surface tension on the droplet front movement, is also used to characterize the shape of the droplet moving in the surrounding fluid [226, 227]. The Bond number can be obtained by the following equation [222]:

$$Bo = \frac{\rho_p g w_d^2}{\gamma_p} \tag{3.4}$$

The evolution of the Bond number with time in the discussed cycle is shown in Fig. 3.9. It can be noticed that its value is close to and greater than 1, which means that the effect of the gravitational force is slightly more prominent compared to surface tension. However, the effect of surface tension cannot be neglected. During the cycle, the Bond number is initially larger and decreases gradually, implying that the importance of surface tension gradually increases. At the end of the cycle, the Bond number tends to increase, which is similar to the evolution of the temperature and velocity of the droplet. The droplet profile also provides the contact angle, which is commonly used to

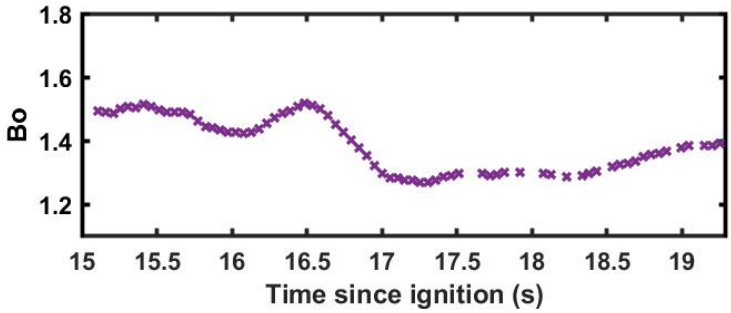

Figure 3.14: Evolution of Bond number Bo of leaked droplet over time in the discussed cycle (highlighted in yellow in Fig. 3.9).

assess the wettability of liquid and solid systems [228]. Young's equation establishes the basis of the wetting behavior by integrating all three components [229]:

$$\cos\theta_Y = (\gamma_{sv} - \gamma_{sl})/\gamma_{vl} \tag{3.5}$$

where γ_{sv}, γ_{sl}, and γ_{vl} represent the solid/vapor, solid/liquid, and vapor/liquid surface tensions, respectively. θ_Y is the so-called Young contact angle. At a given temperature and pressure, a given solid, liquid, and vapor system has a unique equilibrium contact angle [230].
A droplet sliding on a surface always exhibits advancing and receding contact angles. When

different driving forces are applied to the droplet to make it slide at different speeds, the droplet changes its shape to accommodate the new motion. As a result, different advancing/receding contact angles may be observed, resulting in multiple contact angle hysteresis (defined as the discrepancy between the advancing and receding contact angles) on a given surface [230, 231]. The analysis of the droplet profile is given in Fig. 3.15.

For a droplet with a known profile, its width and height can be extracted. Additionally its advancing contact angle θ_{Adv} and its receding one θ_{Rec} can be measured. The evolution of these two contact angles with time can be observed in Fig. 3.9. The droplet advancing contact angle is larger than the receding contact angle during the whole cyclic spreading, and the droplet advancing contact angle exhibits a higher magnitude of cyclic behavior than the receding one. Within the discussed cycle (highlighted in yellow in Fig. 3.9), the advancing angle has a tendency to first decrease and then to increase, as observed with the evolution of the droplet width and temperature in the cycle.

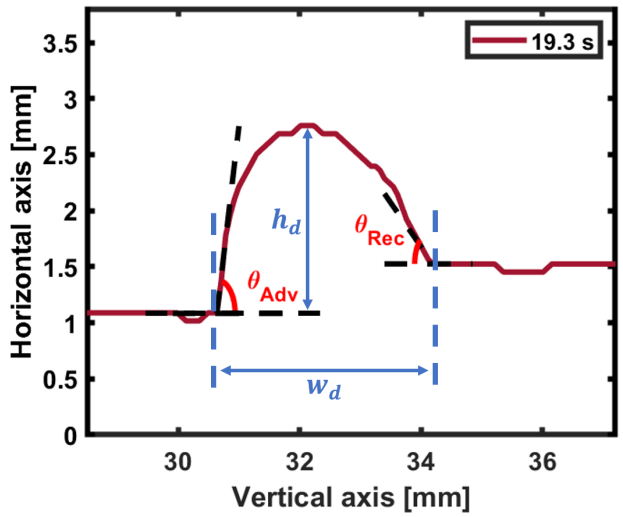

Figure 3.15: Droplet profile at 19.3s in the highlighted cycle as shown in Fig. 3.10 with indicated advancing contact angle, θ_{Adv}, receding contact angle, θ_{Rec}, width w_d and height h_d of the droplet. The droplet is sliding from the right to the left.

The above analysis of droplet shape provides important clues for the following analysis of the droplet dynamics. From the capillary length and Bond number, it can be found that the droplet shape and dynamics are not mainly controlled by surface tension, and other forces need to be taken into account in the system.

Droplet motion

Still focusing on the same cycle (highlighted in yellow in Fig. 3.9), the leaked droplet motion relative to the flame front results from a balance between, on one hand, the gravitational force and, on the other hand, adhesion, F_{ad}, viscous, F_τ, and drag, F_D, forces [232, 233]:

$$\rho_p V_d \frac{d^2 X_{PE,front}}{dt^2} = \rho_p V_d g - F_{ad} - F_\tau - F_D \tag{3.6}$$

where V_d, is the droplet volume. Based on the information provided above regarding the droplet shape (such as the width and height of the droplet), combined with the assumption of treating the droplet as a spherical cap, the droplet volume can be evaluated. The evolution of the discussed cycle is shown in Fig. 3.16, and the gravitational force applied to the droplet can be also inferred from the droplet volume. In the figure, it can be observed that the volume of the droplet shows a

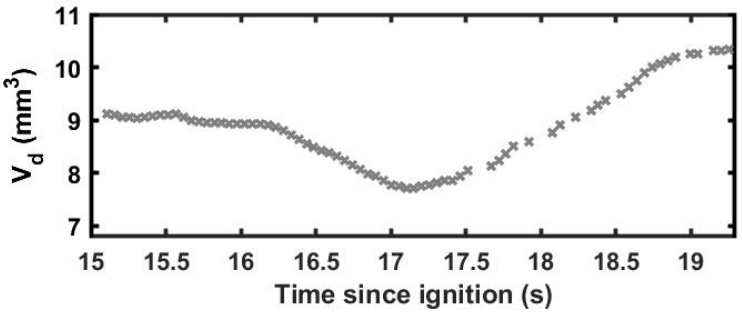

Figure 3.16: Evolution of the leaked droplet volume over time in the discussed cycle (highlighted in yellow in Fig. 3.9).

decrease at the beginning of the cycle and a tendency to increase again until the end of the cycle. Such a trend is consistent with the droplet profile observed in Fig. 3.10. Since the droplet volume is proportional to gravitational force, the evolution of gravitational force has the same trend. It is worth mentioning that the temperature of the droplets during the cycle is less than 200°C, a range much lower than the pyrolysis temperature, which confirms that the droplet mass is lost during the first half of the cycle by a deposit mechanism during the sliding process, rather than by gas-phase pyrolysis. In the second half of the cycle, the approach of the flame allows the molten LDPE to accumulate again in the droplet and increase its volume.
The adhesion force F_{ad} is related to the advancing and receding contact angles and it can be estimated using Furmidge's law [234]:

$$F_{ad} = k\,(\cos\theta_{Rec} - \cos\theta_{Adv})\,\gamma_p\,w_d \tag{3.7}$$

where k is a numerical constant that depends on the shape of the droplet. k can be estimated as follows:

$$k = 0.23 + 1.04\,\beta \tag{3.8}$$

where β_d is the length-to-width aspect ratio of the contact line:

$$\beta_d = L/w \tag{3.9}$$

where L and w are the length and width of the droplet. In the present study, the droplet is assumed as a circular droplet, which means that $\beta_d = 1$.
The viscous force F_τ of the droplet is estimated as [235]:

$$F_\tau \approx A_c\,\mu_p\,\frac{dX_{PE,front}/dt}{h_d} \tag{3.10}$$

where $A_c \approx \pi r_w w_d$ is the contact area of the droplet with the wire [2] and r_w is the radius of the electric wire. Then, μ_p is the dynamic viscosity of the LDPE, which can be defined from the non-Newtonian viscosity η. η depends on shear rate, $\dot{\gamma}$ and temperature [236]. Some typical plots of η as a function of shear rate are given in Fig. 3.17. During the droplet sliding process, the shear rate can be approximated by $1/\dot{\gamma} = \overline{dX_{PE,front}/dt}/\overline{h_d} \approx 1$ [237], where $\overline{dX_{PE,front}/dt}$ and $\overline{h_d}$ are the mean value of droplet velocity and droplet height in the discussed cycle. The droplet temperature is extracted from $T_{d,max}$ and the mean value of droplet temperature in the discussed cycle is applied to define the droplet velocity. According to the above information, the viscosity of the droplet can

[2] recall that droplet is approximated to contact only one side of the wire

be estimated and it is considered a constant to evaluate the viscous force.

The drag force due to the flow resistance when the droplet slides over the electric wire is related to

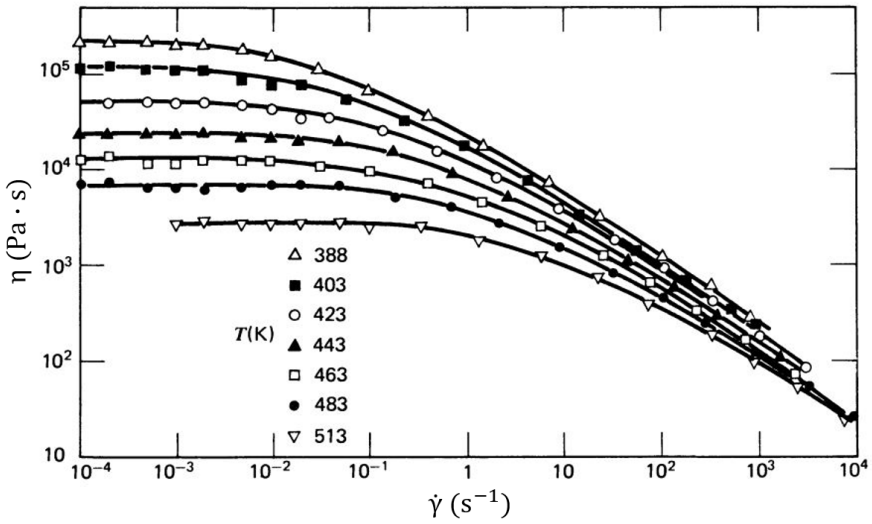

Figure 3.17: Non-Newtonian viscosity η of a LDPE melt at different temperatures. The data taken at shear rates below $5x10^2 s^{-1}$ were obtained with a Weissenberg Rheogoniometer; those at higher shear rates were determined using a capillary viscometer. Reproduced from Bird et al. (1987) [236].

the pressure drag and frictional drag. However, the drag force is related to the Reynolds number and the shape of the droplet. The Reynolds number of flow over the droplet can be defined as follows:

$$Re = (\rho_g V_g h_d)/\mu_{air} \tag{3.11}$$

where ρ_g is the forced flow density and μ_{air} is the dynamic viscosity of the forced flow. The order of magnitude of the calculated Reynolds number is 10 within the discussed cycle. In such a low Reynolds number, the drag force F_D can be estimated with Stokes' law[238]:

$$F_D = 6\pi\mu_{air}(h_d/2)V_g \tag{3.12}$$

The forces acting on the sliding droplet are summarized above and can give a rough analysis of the droplet sliding process. Except for the drag force, the evolution of all the above discussed forces in the highlighted cycle is reported in Fig. 3.18. Since the calculated drag force has a magnitude of 10^{-8} N, which is much smaller than any other force, its effect on the droplet motion is considered negligible.

In the figure, it can be observed that the viscous force is dominant at the beginning of the cycle and is much larger than the gravitational or adhesion ones. Combined with the evolution of the droplet velocity in the cycle (see Fig. 3.11), it can be noticed that the droplet velocity slows down at the beginning of the cycle because of the viscous force. At the same time, the temperature of the droplet is decreasing because the droplet is moving away from the flame (see Fig. 3.9). This significant cooling effect results from the heat exchanges between the droplet and its environment. When the ambient temperature is lower than the droplet temperature, heat is lost to the surrounding gas by convection, at a rate $\dot{q}_g$ that can be evaluated as $\dot{q}_g = hS_g(T_g - T_d)$, where S_g is the surface of the droplet in contact with the gas, and also by conduction through the solid within the condensed phase, $\dot{q}_s$. Assuming that, during this stage, the effect of the variations of the volume on enthalpy

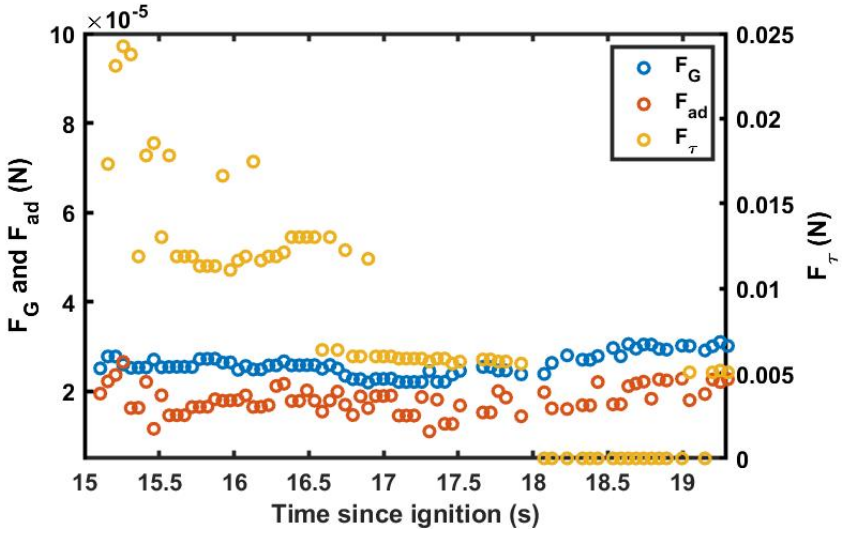

Figure 3.18: Evolution of gravitationnal (F_G), adhesion (F_{ad}), and viscous (F_τ) forces applied on the sliding droplet throughout the discussed cycle (highlighted in yellow in Fig. 3.9).

is secondary, the heat balance equation for the droplet can be written as follows:

$$\rho_p \, V_d \, c_d \, \frac{dT_d}{dt} = \dot{q}_g + \dot{q}_s \tag{3.13}$$

The viscous force is evaluated above at the mean value of $T_{d,max}$ in the cycle. Due to the cooling effect, the actual viscous force is greater when the droplet temperature is below the mean value of $T_{d,max}$ (the viscosity increases as the temperature decreases, see Fig. 3.17). Thus the effect on the droplet velocity reduction is believed to be even more severe. The decrease in droplet velocity combined with the increase in viscosity increases the viscous force acting on the droplet until the droplet velocity becomes zero after 18 seconds. At this point the gravitational force starts to dominate the droplet dynamics, thus allowing the droplet to accelerate later in the cycle and prepare for the next cycle. In addition, the temperature of the droplet increases in the later part of the cycle due to the approach of the flame.
It can be observed in Fig. 3.9 that the maximum surface temperature of the droplet decreases from one cycle to the next one. This can be explained by the fact that the droplet at the beginning of successive cycles becomes heavier, so its thermal inertia increases too, reducing the thermal gains from the flame and the additional molten fuel. This is supported by Fig. 3.10 which shows that the droplet volume is larger at $t = 15.1$ s than at $t = 19.3$s. Such effects should be investigated over a longer observation time to elucidate whether or not the thermal cycles stabilize above the melting point of the LDPE or crystallization of the droplet eventually happens.

3.4.3 Effects of ambient flow conditions

Cyclic flame spread is observed for all the ambient conditions considered in the present study. Yet, the associated period τ_{exp} changes with the ambient conditions depending on the relative motion between the flame front and the droplet. τ_{exp} can be extracted from the experimental measurements by averaging the duration of the cycles. This duration is here evaluated as the time spent between two consecutive inflection points in the evolution with time of the droplet front position. In the following, it is assumed that τ_{exp} is mainly affected by two factors, i.e. the flame

front velocity V_f, and the distance d traveled by the droplet from the moment it is released til the moment it is caught up by the flame front, leading to $d = x_{PE,front}(t = t_0 + \tau_{exp}) - y_{PE,front}(t_0)$. In order to assess the relevance of this hypothesis in the following analysis, a characteristic time τ_c is defined as follows:

$$\tau_c = d/V_f \tag{3.14}$$

τ_c can be interpreted as the time required to the flame front to catch up with the droplet. Because gravity plays a crucial role in the motion of the droplet, additional investigations of the cyclic motion were also conducted at Lunar gravity (0.16 g_0) in parabolic flight. Though the same mechanism of droplet acceleration and deceleration ahead of the flame front was observed, the observation time was too short to observe cyclic behavior. As such, the present results focus on results obtained at Martian gravity.

Effect of oxygen content

Experiments were performed by varying the oxygen content in the oxidizer stream from 18 to 21% at atmospheric pressure and for two levels of flow velocity, i.e. $V_{g,1} = 150$ mm/s and $V_{g,2} = 60$ mm/s. The main characteristics of the spread process are summarized in Tab. 3.2.
Table 3.2 shows that the period of a cycle decreases with the oxygen content for the three contents

	$V_{g,1}$= 150 mm/s				$V_{g,2}$= 60 mm/s			
	x_{O_2}[%]				x_{O_2}[%]			
	18	19	20	21	18	19	20	21
τ_{exp}	x	5.98	3.99	3.57	8.09	4.66	-	4.08
V_f	x	1.38	1.51	1.69	1.22	1.44	-	1.80
d	x	8.75	6.86	6.81	9.87	7.15	-	8.28
τ_c	x	6.34	4.54	4.03	8.09	4.96	-	4.60
x : flame extinction, - : no experiment								

Table 3.2: Cyclic flame spread characteristics as a function of the oxygen content at a pressure of 101.3 kPa.

investigated at $V_{g,1} = 150$ mm/s, backed by the three additional contents investigated at $V_{g,2} = 60$ mm/s. As expected from Eqs. (3.1) and (3.2), increasing the oxygen content increases the heat flux from the flame to the unburnt solid ahead of the pyrolysis front, $\dot{Q}_{c,fl}$, mainly due to an increase in flame temperature. This consequently enhances the flame spread rate, meaning that the droplet has less time to travel ahead of the flame front. As such, the droplet travel distance also naturally decreases with increasing oxygen content. Overall, these two aspects explain the decrease in the experimental period as oxygen content is increased since τ_c shows a trend similar to τ_{exp}.
As the oxygen content is decreased down to 18% at a flow velocity $u_{\infty,1} = 150$ mm/s and a pressure $P = 101.3$ kPa, extinction happens at Martian gravity. This is unexpected since the flame can propagate under the same conditions at normal gravity [239], in spite of the intense dripping that carries fuel away from the flame, as well as in microgravity [186], where the droplet of accumulated molten fuel propagates at the same pace as the flame front. As mentioned in Section 3.3.3, this self-extinction is observed at Martian gravity when the flame catches up with the droplet, and could consequently be triggered by the increased heat losses from the flame to the cooled droplet,

as illustrated in Fig. 3.6.

Effects of pressure

To investigate the effects of pressure on the cyclic flame spread, experiments are performed for pressure levels ranging from 50.7 to 141.8 kPa, at a given oxygen content of 21% and flow velocity of 60 mm/s. As for the analysis of the effects of the oxygen content, similar characteristics are reported in Tab. 3.3.

It can be observed that the period of a cycle decreases when increasing the pressure. According to

	P[kPa]				
	50.7	70.9	101.3	121.6	141.8
τ_{exp}	5.53	5.01	4.08	3.97	4.06
Vf	2.02	1.88	1.91	1.82	1.92
d	10.81	10.09	8.28	8.53	7.60
τ_c	2.02	1.88	1.91	1.82	1.92
dT_d/dt	10.91	10.53	12.03	15.31	18.47
dT_d/dt : droplet temperature drop rate [°C/s]					

Table 3.3: Cyclic flame spread characteristics as a function of the pressure investigated at an oxygen content of 21% and a flow velocity of 60 mm/s.

Eqs. (3.2) and (3.1), the pressure should affect the flame front spread rate mainly through an increase in gas-phase density that, in turn, decreases the gas-phase diffusivity, L_g, hence the conductive heat flux from the flame, $\dot{Q}_{c,fl}$, and eventually the flame spread rate. Nevertheless, this trend does not appear clearly in Tab. 3.3 owing to the moderate range of pressures investigated in the present study and the presence of the metallic core that affects heat transfer in the flame spreading process. Table 3.3 shows that, similarly to the trends observed in our previous studies [186, 240], modifying the pressure has minor effects on spread rate.

On the other hand, Table 3.3 shows that the droplet traveled distance over a cycle, d, decreases as the pressure increases. As discussed in Section 3.4.2, this trend is directly related to heat transfer: increasing the pressure enhances the heat transfer coefficient, h, and, in turn, the rate of cooling of the droplet, $\dot{q}_g$ (see Eq. (3.13)). This process is illustrated in Tab. 3.3 that reports that the rate of cooling of the droplet, dT_d/dt, averaged over a cycle, is enhanced from about 11 °C/s for $P = 50.7$ kPa to about 18.5 °C/s for $P = 141.8$ kPa. A consequence is that the droplet temperature is lower at higher pressure, leading to higher viscosity and, eventually, to a lower traveled distance. As a result, since the flame front velocity is not affected, the flame is able to catch up with the droplet faster. Again, this approach is validated by the good agreement between experimental period measurement τ_{exp} and the characteristic time scale τ_c.

3.5 Summary

In this Chapter, opposed-flow flame spread and extinction of LDPE-insulated wires are studied for the first time at different gravity levels such as the Lunar and Martian levels. The results showed

that the extinction limits of Cu samples exhibit almost constant values with gravity levels, while the extinction limits of NiCr samples decreased with decreasing gravity levels. In addition, the Cu samples showed smaller extinction limits than the NiCr samples at higher gravity conditions, but the opposite trend was confirmed under microgravity conditions. The different behavior of the extinction limits against gravity level for the wire samples can be reasonably understood by the different trends of flame spread rate against gravity level. In the Cu case, the flame spread rate increases significantly with increasing gravity level due to the increase in heat flux from the flame to the solid surface. In contrast, for NiCr, this effect is suppressed due to its small thermal conductivity, thus the flame spread rate shows much smaller values than for the Cu sample. Since the flame spread rate itself controls the fuel supply rate to the reaction zone, the flame spread over low conductivity wires is considered susceptible to finite rate chemistry due to the smaller flame spread rate compared to high conductivity wires.

Although the influence of convection caused by buoyancy on the flame spread phenomenon was reasonably understood, the deformation of the insulation caused by gravity was also an important factor affecting the flammability of the tested wires. The leakage of molten LDPE was found to have a significant effect on the flammability of the wire. Leaked LDPE droplets can form a barrier upstream of the flame, and extinction occurs when the flame does not provide enough heat to pyrolyze them or to keep them advancing upstream. In addition, lower conductivity metallic cores and thicker insulation promote the appearance of molten LDPE leakage. Leaked LDPE droplets not only affect the flammability of the wire but also the flame spread over the wire. Under Martian gravity, the presence of leaked LDPE droplets upstream of the flame leads to the appearance of a unique cyclic flame spread mode. Such a flame spread mode was observed at different levels of oxygen content, pressure, and flow velocity. Although the flame spreads at a constant rate, the leaked molten droplets systematically exhibit a cyclic motion at the flame front. The cycle can be decomposed into a deceleration phase, in which the droplet is decelerating mainly by viscous force and moving away from the flame, and an acceleration phase, in which the flame catches up with the droplet because of its previous deceleration and the gravitational force becomes dominant, allowing the droplet to accelerate. The period of the cycles is influenced by the oxygen content and the pressure in the oxidizer flow. Increasing the oxygen content reduces the period of the cycles primarily by increasing the flame spread rate, meaning that the flame catches up with the droplet faster. As pressure is increased, the flame spread rate is not affected but the period of the cycle is reduced owing to an enhancement in the cooling rate of the droplet when it slides away from the flame front, lowering its velocity and consequently reducing its travel distance. Furthermore, the cyclic behavior unveiled appears as a relevant opportunity especially for the validation of the numerical tools that Prof. Consalvi (from Aix-Marseille University) and his coworkers are currently developing.

4 Material enhancement with flame retardants

Contents

In this Chapter, we report the first experiments conducted with DIAMONDS on cylindrical samples without any metallic core. This configuration is especially relevant to the identification of the effects of flame retardants added to the material investigated. Experiments were conducted in microgravity and normal gravity to observe and analyze the effect of the flame retardant on the flame spread.

Section 4.1 describes the modification of the sample holder to set the samples without metallic cores and investigate the flame spread behavior with this sample configuration. The flame retardant mechanisms of two different intumescent flame retardants (Ammonium polyphosphate/Pentaerythritol (AP) and Expand Graphite (EG)) are explained in Section 4.2. They represent two different ways of obtaining expansion. Subsequently, the home manufacturing process of the flame retardant-loaded samples is presented in Section 4.3. Experiments were conducted on the produced samples, and the flame spread mechanisms of the different types and loading of flame retardant samples are analyzed in Section 4.4 based on the flame morphology and the condensed phase upstream of the flame. With the proposed flame spread mechanism, Section 4.5 presents the extinction limits of the different samples and the potential reasons for the occurrence of extinction. For those conditions with flame spread, Section 4.6 evaluates their average flame spread rate and also analyzes the effect of the altered spread mechanism on the spread rate. Since soot release is also a threat to fire safety inside the spacecraft, Section 4.7 identifies those conditions with soot emissions and indicates the

reasons that may lead to soot release from flames.

4.1 Configuration without metallic core

As previously described, the main kind of sample previously designed for DIAMONDS was the electrical wire configuration, consisting of a metallic core and polymer insulation. Although the metallic core has the essential benefit of stabilizing the flame spread and maintaining its geometry, the presence of a metallic core also makes the flame spread mechanism complex. The heat transferred from the flame to the metallic core can be conducted upstream into the virgin solid fuel to promote spread, but it can also act as a heat sink to distribute heat downstream to the burned zone and inhibit spread. In order to further understand the role of metallic cores in the flame spread mechanism, cores with metals of different thermal conductivity were used for the experiments. As a matter of fact, investigations should be conducted on cylindrical samples that exhibit a fully uniform composition. In addition, sample configurations without metallic cores also facilitate the development of theoretical models, especially the measurement of radiative heat losses using optical diagnostic techniques that can complement the understanding of radiative heat transfer in flame spread mechanisms over cylindrical solid fuels.
Before conducting the experiment, the problem that had to be solved is how to set the sample without a metallic core on the sample holder. This requires a modification of the sample holder designed for wire samples. As described in Section 2.1.3, any electric wire sample can be held at both ends, i.e. at the holder's leading and trailing edges. However, without the presence of the metallic core, the cylindrical sample will not be held at the location of the ignition where the subsequent flame will burn the whole section of the sample. In order to get a new location to hold the sample without any significant change in the experimental procedure, another stainless steel rod identical to the one already presented at the bottom of the holder was added 5 cm above it and fixed to the ceramic holders at both ends. The cylindrical sample is then fixed to these two stainless steel rods by tying two knots using brass wire.
After solving the problem of sample setting, both 1 mm diameter PMMA and 2 mm diameter LDPE cylindrical samples were burned in microgravity under an opposed-flow configuration. These two materials were chosen because the PMMA sample is the most investigated material in microgravity for fire safety research [61], while LDPE is the insulation material used in the classic configuration for the electric wire samples. PMMA samples were tested in the oxygen content range of 15% - 21% with a flow velocity of 150 mm/s and atmospheric pressure, and the extinction limit was found at 15% oxygen content. LDPE samples were conducted under the same ambient conditions and were found to have an extinction limit at 17% oxygen content.
Besides the extinction limit, the potential flame spread should also be documented. As shown in Fig. 4.1, three different samples were conducted in microgravity under the same ambient conditions. It can be noticed that the shape of the molten droplet on the electric wire sample cannot be maintained after the removal of the metallic core. Alternatively, this is replaced by a twin droplet with complex motion. As the flame spreads, these twin droplets merge and separate regularly, with no apparent relation to the residual gravity, proving competing transport mechanisms in the melting phase. Such a motion allows more fuel to be driven upstream of the sample thus resulting in a smaller amount of gaseous fuel being supplied to the flame. Therefore, the flame size also appears to be relatively smaller than that of a classic electric wire sample. Besides, the flame spread over the PMMA sample can be observed as a molten droplet formed upstream of the flame. However, this droplet is not stable during spreading, it keeps shaking and ejecting gas fuel in all directions. The instability of the droplet leads to an unstable supply of gas fuel to the flame, so

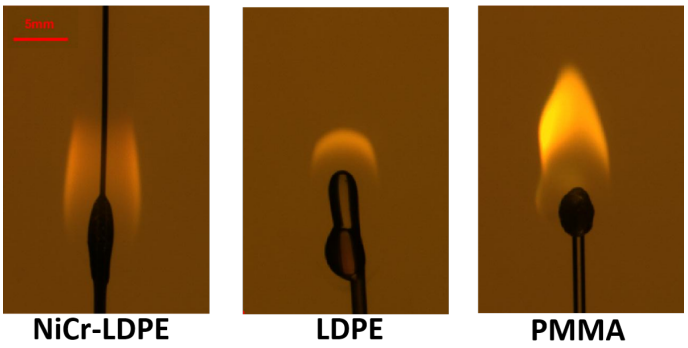

Figure 4.1: Backlighted frames imaging opposed-flow flame spread over NiCr-LDPE electric wire (left), cylindrical LDPE sample (middle), and cylindrical PMMA sample (right) in microgravity. These experiments were performed under the same ambient conditions with an oxygen content of 21%, a flow velocity of 150 mm/s, and atmospheric pressure. As the flame spread with LDPE sample and PMMA sample cannot propagate at a steady rate, the flames are imaged here arbitrarily 15s after ignition, shortly before the end of the flame spread.

the flame flickers continuously during the spreading process and the length of the luminous flame changes constantly.
In the conducted experiments, the flame spread over any of both solid fuels cannot meet the previously established qualifications for steady rate flame spread described in Section 1.2.5, which also leads to additional difficulties in the analysis of their spread mechanisms. This also further demonstrates that metallic cores contribute to steady rate flame spread. Although samples without a metallic core do not provide a completely steady rate flame spread, this sample configuration is more convenient for later theoretical analysis. This configuration allows for a more focused analysis of the effect of flame retardants on flame spread mechanisms before applying the flame retardants to the electric wire samples.

4.2 Intumescent flame retardant

As mentioned in Section 1.3.3, intumescent flame retardants form an intumescent layer upon heating that acts as a barrier to heat and mass transfer and thus slows down the flame spread, while at the same time maintaining the maximum mechanical properties of the material. There are two main ways to obtain intumescent materials, one is through a series of chemical reactions, while the other is through mechanical expansion. Ammonium polyphosphate/pentaerythritol (AP) and Expandable Graphite (EG) flame retardants represent these two different ways of obtaining intumescence, respectively. The mechanism of these two flame retardants is described below.

AP flame retardant

AP flame retardant is a system consisting of ammonium polyphosphate (APP) and PentaERythritol (PER), producing intumescence via a series of chemical reactions. Under the action of external heat flux, APP decomposes and yields acidic phosphates acting as char promoters. Phosphates react with PER to yield char which can expand to a porous char layer, thanks to the evolution of ammonia from APP and the decomposition products of the burning material [241]. Therefore, the post-combustion AP residue is an expanded carbonaceous char, acting as a heat barrier. As shown in Fig. 4.2 (a), its internal structure is foamy with small and large voids. The cohesion of the

structure is relatively high.

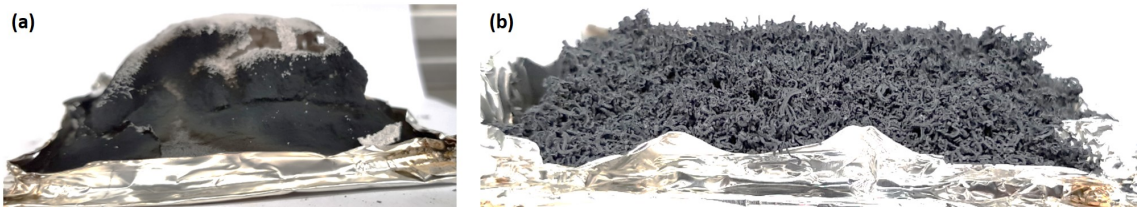

Figure 4.2: Images of LDPE-AP residue (a) and LDPE-EG residue (b) after combustion. For LDPE-AP residue, an expanded carbonaceous char is formed acting as heat barrier. The internal structure is foamy with small and large voids. The cohesion of the structure is relatively high. For LDPE-EG residue, graphite worms can be distinguished at the surface of the residue. Graphite worms make an entangled network acting as physical barrier limiting the combustion of the polymer. Note that the cohesion is enough to provide the protection of interest but it is not strong to resist against fluid flow or other erosion forces. [242]

EG flame retardant

Comparatively, EG flame retardant is a typical example of intumescent flame retardant that follows a mechanical process. Insertion compounds are contained between the graphite layers and upon heating EG expands: the intercalation compound quickly decomposes into gaseous products, thereby exposing the graphite flakes which then form an entangled network of worm-like structures on the surface of the loaded material. This network acts as a protective layer that expands under the rapid sublimation of molecules in the polymeric matrix [243, 244]. It should be noted that the cohesion of the structure is high enough to provide the protection of interest but it is not strong to resist the fluid flow or other erosion forces. The structure difference between AP and EG could lead to a different mass transfer of gaseous fuel to the flame (as shown in Fig. 4.2 (b)).
To investigate the influence of different flame retardants on flame spread in both normal and micro-gravity, the present study is to investigate the consequences of AP and EG addition to standard samples. Many of the results depend on the particular configuration. That being said, the axisymmetric configuration gives access to a relatively simple topology of the flow field and the opposed-flow feature leads to a minimal still relevant interaction between the flame and the condensed phase. As a result, the configuration investigated is believed to offer a fine compromise between applied challenges and fundamental ambitions for the specific study of flame retardants and especially their influence on the condensed phase. Therefore, thin cylindrical samples of LDPE are used as a baseline, to build on the existing literature with uni-directional flame spread. To obtain this sample configuration, the manufacturing process is now described.

4.3 Flame retardant sample manufacturing

These two types of flame retardants, i.e. AP and EG, are added to the LDPE material in order to enhance the fire characteristics of the material. The samples with the flame retardants are also of cylindrical geometry for comparison with the cylindrical pure LDPE samples. The samples were provided by Prof. Bourbigot (from the University of Lille) and the production of the samples is described here.
LDPE was supplied by Sabic (Netherlands) in the commercial grade Sabic® LDPE 2602X1 00900. EG is the commercial grade ES350F5 from Graphitwerk Kropfmühl (Germany) with an average

particle size of 300 µm. Sulfate was used in this grade as an intercalation compound to make graphite bisulfate. APP is the commercial grade of Clariant (Germany) with the brand name Exolit AP422. PER was supplied by Aldrich.
As shown in Fig. 4.3, LDPE was blended with flame retardants in a twin-screw extruder. The total loading of flame retardants in LDPE varied from 2 to 10 wt% of EG and at 5 and 10 wt% for APP/PER with the ratio 3:1 (wt/wt) and hereafter called AP. Compounding was performed using HAAKE Rheomix OS PTW 16 twin-screw extruder. The extruder is a co-rotating intermeshing twin screw with a barrel length of 400 mm and a screw diameter of 16 mm (L/D = 25) with 10 zones. LDPE and flame retardants were incorporated using two gravimetric side feeders into the extruder. The polymer flow rate is fixed to extrude about 500 g/h with a screw speed of 300 rpm.

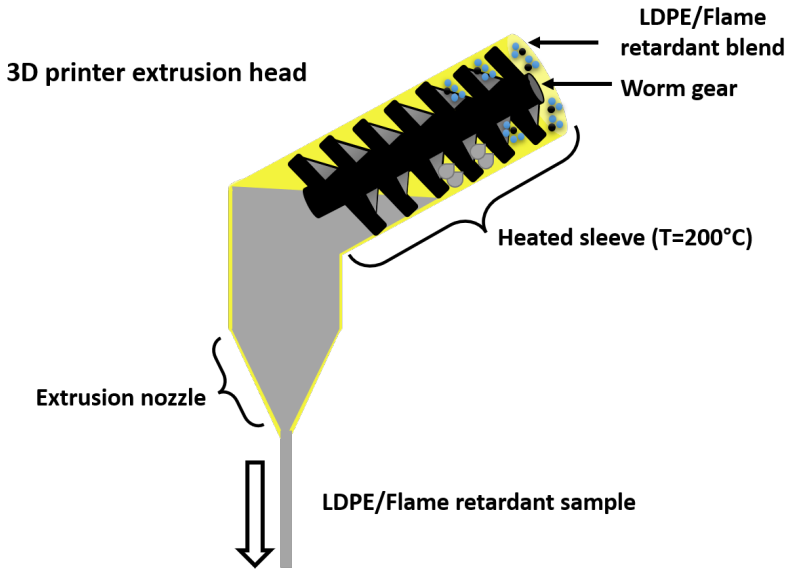

Figure 4.3: Schematic representation of cyclindrical sample production. In a 3D printing extrusion head, the LDPE and flame retardant materials are blended and fused inside a Heated sleeve. In the end, the material is discharged through the extrusion nozzle to form a cylindrical sample. Reproduced from Prof. Bourbigot.

The purpose of the present study is to observe the effect of flame retardants on flame spread at oxygen content from 0% to 21%, a flow rate of 150 mm/s, and a pressure of 101.3 kPa (atmospheric pressure). Thus, the flame retardant loading needs to be adjusted to adapt to the general requirements. The loading of the flame retardant cannot be too high, otherwise, the flame spread cannot be observed and thus the spreading mechanism cannot be studied. At the same time, it cannot be too low, otherwise the effect of the flame retardant cannot be observed. Here, flame retardants are incorporated into the LDPE solid phase, with proportions of 2wt%, 5wt%, and 10wt% for EG, and 5wt%, 10wt% for AP.
Experiments are performed with these samples on the ground and in parabolic flights to study the extinction limit, the average flame spread rate, and smoke emission in the opposed-flow configuration, under varying oxygen content. The experimental procedures in microgravity are described in Section 2.1.4. As the ignition is performed before the microgravity phase, observations are carried out from 15 til 25 seconds after ignition. This allows the flame to spread away from the igniter and reduce undesired interactions while making sure flame spread is analyzed in the steady microgravity phase of the parabola.

4.4 General observation

All sample configurations for flame spread in microgravity and normal gravity are displayed in Fig. 4.4 through the backlighting images to allow overall observation of the flame spread. The samples in the figure are all experiments performed at an oxygen content of 21%. It should be emphasized that such cylindrical samples do not meet the classic steady rate flame spread qualifications presented in Section 1.2.5. Moreover, they do not spread at the same rate and it is possible that the flame spread ends before the microgravity sequence. To extract representative images for the analysis, the images in Fig. 4.4 were taken 15 s after ignition and shortly before the end of the flame spread. In order to analyze the spreading mechanism, a schematic representation of the degradation process is also shown in Fig. 4.4. Based on Fig. 4.4, the intumescence of the two flame retardants under different gravity levels is first analyzed and then compared to the pure LDPE sample. This is followed by the analysis of flame and soot emissions. Finally, the role of intumescence in a flame spread is analyzed with the schematic.

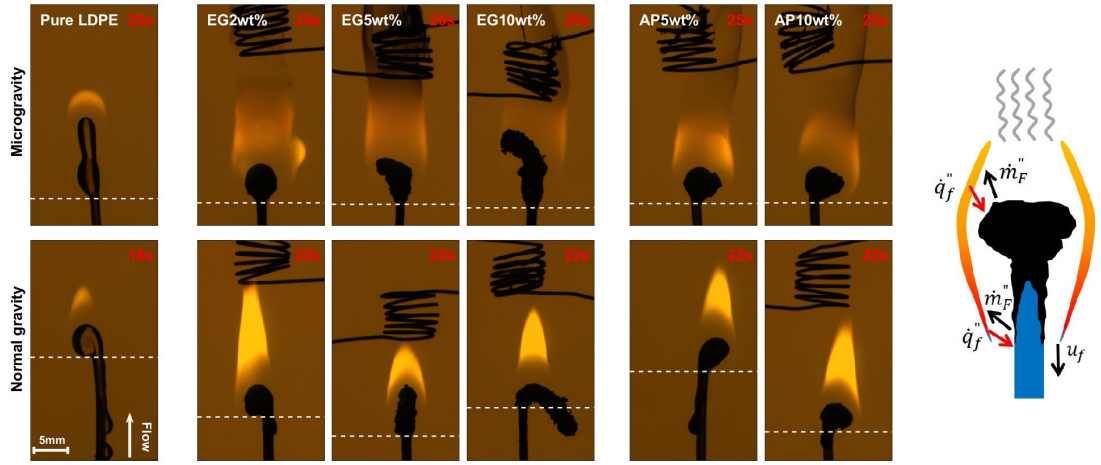

Figure 4.4: Backlighted frames imaging opposed-flow flame spread over cylindrical LDPE samples (left) and schematic of the degradation process (right). All observations are carried out at a pressure of 101.3 kPa, under an oxygen content of 21% and a flow velocity of 150 mm/s, to observe the impact of gravity and both AP and EG flame retardants with varying weight contents. The images are taken 15s after ignition, shortly before the end of the flame spread. The time since ignition is indicated in the upper right corner of every frame. The position of the upstream condensed phase deformation is indicated by a dashed line. [242]

4.4.1 Intumescence

The expansion linked to the intumescent processes is clearly visible in microgravity, as illustrated in Fig. 4.4. AP-loaded samples feature a globally spherical shape in the pyrolyzing region with a size independent of the loading. Yet, this region is larger in microgravity than at normal gravity. In contrast, the intumescent region of EG-loaded samples increases in size with the EG loading, moving from a spherical shape toward a more cylindrical structure. As the expanded carbon layers accumulate, the intumescent region severely bents, and even drops under its own weight at normal gravity, affecting the protection of the unburnt upstream part. Ahead of the intumescent region, dripping is also recorded at normal gravity and increases as the content of flame retardant decreases.

Taking the pure LDPE sample as a basis for comparison, a strong dripping process is observed. At

normal gravity, the intense dripping carries most of the molten fuel away, leading to a short flame length. The dripping occurs due to the effect of gravitational force on the accumulated molten droplet generated by the pyrolysis process of LDPE. It has been observed that the dripping also occurs with a sample at low flame retardant loading (e.g. EG2wt% and AP5wt%), but as the loading continues to increase, the dripping is reduced. In microgravity, a complex motion of twin droplets is observed ahead of the flame. The droplets regularly merge and separate as the flame spreads, with no correlation to the residual gravity, evidencing competing transport mechanisms in the molten phase. This particular transport mechanism disappears after loading the flame retardant.

4.4.2 Flame and smoking situation

Over flame retardant-loaded samples, the luminosity of the flame does not significantly change at a given gravity level, in spite of the severe modifications in the condensed phase with the increased intumescent load. However, as the flame retardant load increases, the flame seems to be more stable, with weaker flickering. At normal gravity, the flame is bright and stretched, while it is wider and less luminous in microgravity. This points to an increased residence time and a lower local soot temperature, which promotes quenching at the flame trailing edge. A dark trail of smoke is systematically observed over flame retardant-loaded samples in microgravity, though it was not reported over the pure LDPE samples. As such, EG and AP seem to promote local quenching earlier along the flame length, which results in increased atmospheric contamination. This illustrates the need for systematic characterization of flame retardant performance in the absence of buoyant flows, as increased smoke production questions their efficiency.

4.4.3 Further mechanism analysis

A schematic is shown in Fig. 4.4 to further analyze the mechanism of flame retardants affecting the flame spread.
The heat flux, $\dot{q}''_f$, from the flame to the sample surface is transferred to the unburned zone at the leading edge of the flame, and the addition of flame retardants slows down the local pyrolysis rate $\dot{m}''_F$ of the solid fuel. This influences the overall pyrolysis rate $\dot{m}_F$, therefore the flame spread rate, V_g, as shown by Eq. (4.1), and potentially stops the flame spreading. In addition, the intumescent region also blocks a part of the heat, $\dot{q}''_f$, which weakens the pyrolysis process and contributes to the mitigation of the flame spread. The gaseous fuel supplied by the pyrolysis needs to flow through the intumescent region to reach the trailing edge of the flame, and this process tends to increase the residence time, which favors soot production in the flame, thus increasing the hazard of smoke emission.

4.5 Extinction limit

Flame spread and self-extinction are investigated first. A perfect example of the self-extinction process is given in Fig. 4.5. Since the igniter provides a large external heat flux in the first few seconds of each experiment, a visible flame appears systematically. During the observation period, if the combustion cannot be self-sustained, the flame becomes smaller and less luminous until the disappearance of the visible flame, as shown in Fig. 4.5 from 20s til 24s. Then, a significant amount of unburnt pyrolysis gases and possibly soot particles are released (as illustrated in Fig. 4.5 at 25s). Such a situation is regarded as extinction [166].

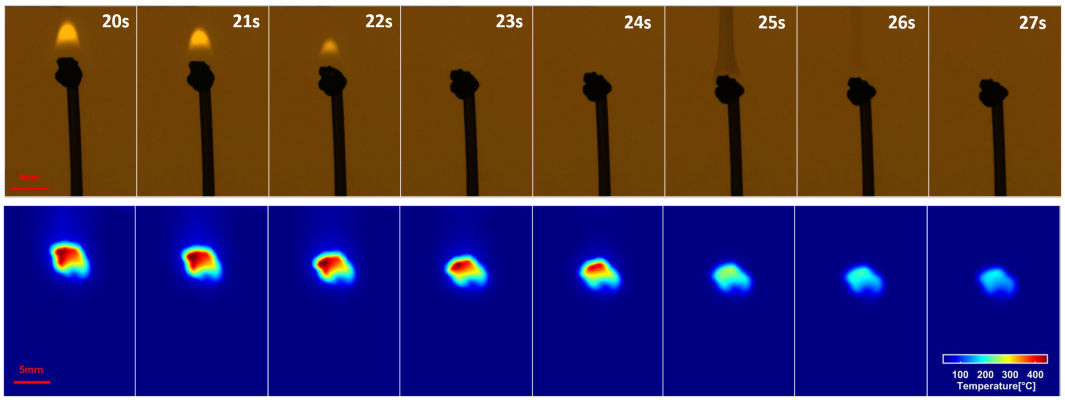

Figure 4.5: Backlighted (upper row) and infrared (lower row) frames imaging a self-extinction sequence on 10wt% EG-loaded sample with an oxygen content of 20%. Under this opposed-flow configuration, the oxidizer flows from the bottom to the top.

The infrared camera provides additional clues regarding the surface temperature evolution. The surface energy emitted by the solid fuel can be collected from the infrared camera as discussed in Section 2.1.2. By assuming a constant sample emissivity of 0.92 (the emissivity of the LDPE material at pyrolysis), the approximate temperature of the solid sample can be deduced from Planck's law. If combustion is sustained at the flame leading edge and the flame spreads, a pyrolysis region of uniform and stable temperature is recorded. In an extinction situation, the infrared signal gradually drops, starting from the upstream preheating region, as heat loss mechanisms dominate in the condensed phase. At the same time, due to the disappearance of the flame, the downstream heat source cannot continuously provide heat to the solid fuel. Between 24s and 25s in Fig. 4.5, the temperature of the pyrolysis zone drops sharply and releases pyrolysis products. It is estimated that the pyrolysis terminates after 25 seconds and the solid fuel end continues to cool down to ambient temperature.
The infrared signal collects quantitative information ahead of the potential visible flame extinction, thus increasing confidence in the discrimination of spread and extinction situations within the limited observation period.
Combining the information from the tri-CCD camera and the infrared camera, the conditions of flame spread and self-extinction can be identified correctly. All conditions for normal gravity and microgravity are reported in Fig. 4.6. Following that, the extinction conditions in both gravity levels are presented and the causes are analyzed.

4.5.1 Normal gravity

Under normal gravity conditions, flame retardants have a noticeable impact on flame extinction. Under the pressure and flow velocity conditions studied, the extinction limit is raised from 18% for the pure LDPE sample to 19% for both EG- and AP-loaded samples, and is even increased to 21% for 10wt% AP-loaded samples.
Increasing the EG load does not show any significant effect on flame extinction. This is interpreted as a consequence of the increase in intumescence volume, which triggers subsequent bending and falling off of the expanded carbon layer under the influence of gravity. As this protective thermal insulation layer is removed, the virgin fuel is exposed to the flame heat flux, which promotes pyrolysis and cancels out the benefits of increased EG loading (as shown in Fig. 4.4 for the 10wt% EG-loaded sample at normal gravity).

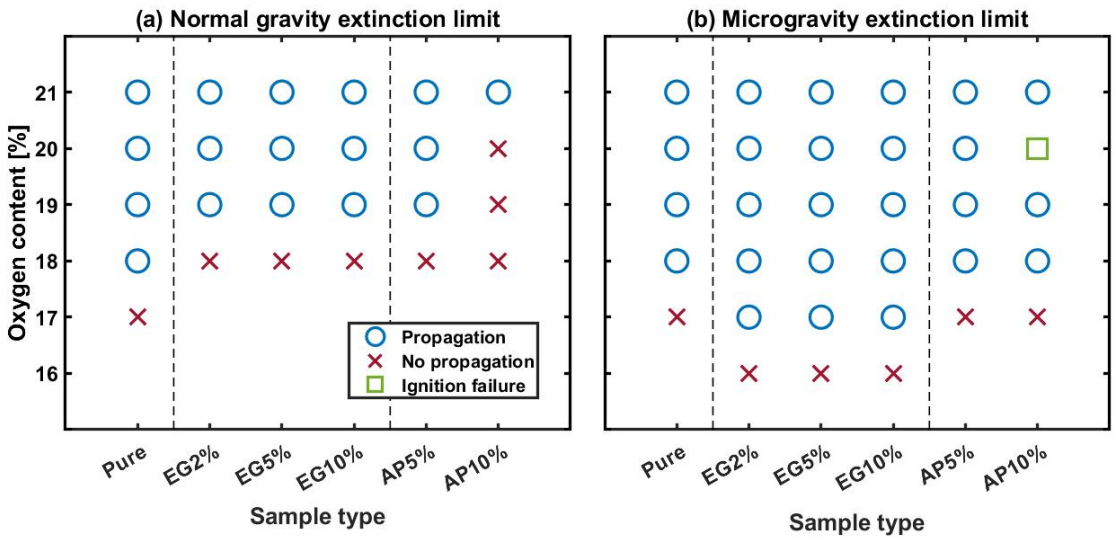

Figure 4.6: Effect of oxygen content on flame spread and extinction over LDPE samples loaded with various flame retardant contents under (a) normal and (b) micro-gravity conditions. The noticeable impact of flame retardants on extinction at normal gravity disappears in microgravity. [242]

On the other hand, the increase in AP loading results in a higher extinction limit since the more compact intumescent volume never detaches from the fuel surface, thus retaining its protective function.

4.5.2 Microgravity

Unlike normal gravity observations, the loading of both flame retardants under microgravity conditions did not raise the extinction limit, regardless of the loading. The flames could spread at 18% oxygen content, the extinction limit for the pure LDPE sample, in spite of the visible intumescence (see Fig. 4.4). As such, the intumescence does not improve on the extinction limit of the studied material under the investigated conditions. Worse still, the EG-loaded samples were even able to spread at 17% oxygen content. In this case, the loading of flame retardants led to lower extinction limits. This completely defeats the original purpose of loading flame retardants. This lack of consistency between normal and micro-gravity observations is particularly problematic as present spacecraft material flammability tests performed on the ground rely on self-extinction criteria [18].
A possible explanation is that the intumescent matrix acts as a porous media in the condensed phase, driving the molten fuel toward the flame through capillarity. This mechanism is likely to be shrouded by dripping at normal gravity but may dominate the viscous flow in microgravity. In addition, the absence of natural convection prevents blow off at the flame leading edge from the increased buoyancy induced air velocity, as the Damköhler number is increased in microgravity [245]. In particular, the EG-loaded sample exhibits a larger volume expansion than the AP-loaded sample under the same conditions and thus is more protective against flame extinction resulting in a lower extinction limit.

4.6 Average flame spread rate

The steadiness of spread rate for a given sample and flow conditions is evaluated based on the steadiness of the flame length, of the droplet volume, and of the velocity of the flame front position over the period of interest, as described in Section 1.2.5. In all studied conditions, the flame length and the droplet volume continuously increase, so no condition can be considered as a steady rate flame spread. An average flame spread rate is then estimated by averaging the displacement of the pyrolysis front over the 10s of observation, with the pyrolysis front being defined as the upstream deformation position of the condensed phase (see Fig. 4.4).
The average flame spread rate at normal gravity and microgravity is plotted as a function of the oxygen content in Fig. 4.7. It should be pointed out that the pure LDPE results at normal gravity under 20 and 21% oxygen content are not reported, because the sample was fully consumed before the end of the observation period. This is attributed to the rapid transfer of the molten solid fuel upstream due to the dripping phenomenon at normal gravity. Still, the average flame spread rate for these two conditions can be considered higher than all the other ones. Therefore, it does not affect the subsequent analysis.

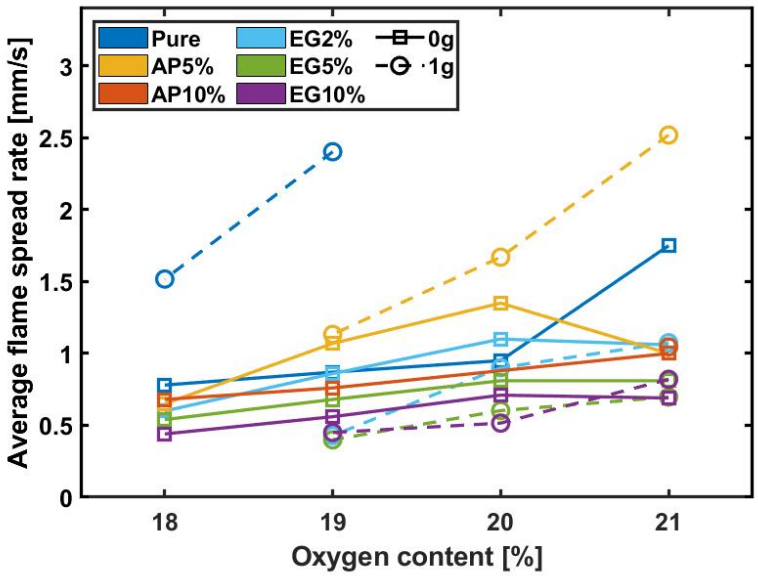

Figure 4.7: Effect of oxygen content on average flame spread rate at normal and micro-gravity. Each color corresponds to a type of sample and two different markers represent two different gravity levels. Flame retardants hinder the spread of flame at both normal and micro-gravity. The associated uncertainties extracted from the measurement of the pyrolysis position and the frame rate of the camera are lower than 2.5% of the average flame spread rate. [242]

Overall, the average flame spread rate increases with the oxygen content, for all flame retardant types and loads, and under both normal and micro-gravity conditions. This is expected as the increased flame temperature enhances the heat transfers to the sample surface.

4.6.1 Normal gravity

At normal gravity and at a set oxygen content, the average flame spread rate decreases when increasing EG and AP flame retardants loads. As introduced previously, the presence of EG and AP

flame retardants slows down the pyrolysis process. At the same time, the expanded condensed phase can block part of the heat transfer from the flame. Moreover, the addition of flame retardants reduces the dripping phenomenon that occurs on pure LDPE samples, thus preventing the molten fuel from being transferred upstream of the sample. It is worth mentioning that the AP-loaded samples perform well in the extinction limit, though the flame spread rate is faster than that of the EG-loaded samples with the same loading. This is probably still related to the dripping phenomenon, since the AP-loaded sample has a more severe dripping phenomenon than the EG-loaded sample at the same loading amount (e.g., at 5 wt% loading). Once the loading amount is reached to inhibit the appearance of dripping phenomenon, the AP loading significantly slows down the flame spread rate and even stops the flame spread by blocking the heat transfer from the flame to the pure sample through the compact expansion structure.

4.6.2 Microgravity

At normal gravity and at a set oxygen content, the average flame spread rate decreases when increasing EG and AP flame retardants loads. In the absence of flame retardant in microgravity, the samples have a tendency to release two droplets upstream of the flame (see Fig. 4.4 upper left), which slows down the propagation as the molten fuel cools down upstream of the flame, thus increasing heat losses. As flame retardant is added, this process is not observed anymore, which increases the flame spread rate for the lowest flame retardant loadings (EG2wt% and AP5wt%) compared to the pure LDPE situation. Yet, as the loading is further increased, a reduction in spread rate is observed. Comparing the amplitude of flame spread rate, higher flame retardant loading is required in microgravity to reduce the spread rate to an extent similar to normal gravity observations, where the slowest spread rates are reported.
It is interesting that the EG-loaded sample tends to provide a higher flame spread rate in microgravity than at normal gravity. The main reason may be associated with the dripping effect. At normal gravity, the increase in EG loading is correlated with a reduced dripping rate. Different effects may contribute to this trend. Among others, the enhanced rugosity associated with the intumescent material, and more specifically the worms formed with EG addition (as discussed in Section 4.2), increases the adherence of the molten droplet at the contact location. As a result, the deceleration of the flame spread with EG loading is significant at normal gravity. In addition, the above trend leads to a certain collapse of the molten droplet formation phenomenology for normal and micro-gravity conditions. However, at normal gravity, the heat of the flame is transferred downstream of the flame especially by the buoyant flow, which reduces the heat transferred upstream, therefore weakening the pyrolysis process. The latest trend can then explain the lower spread rate at normal gravity as compared to that in microgravity as EG loading significantly affects the spread.
Overall, the EG-loaded samples spread more slowly than the AP-loaded samples for the same flame retardant load, under both normal and micro-gravity conditions.

4.7 Smoke emission

In spreading situation where the flame does not quench at the leading edge, local extinction can still take place at the trailing edge, leading to contamination of the surrounding atmosphere. The tendency of the flame to emit smoke can be simply evaluated using the backlighted frames, and results are reported in Fig. 4.8. Smoke-emitting conditions are defined as spreading situations where a continuous flow of broadband absorbing soot particles is reported at the flame trailing edge. On the contrary, smoke-free conditions are defined as spreading situations where the closed-tip flame does not display detectable absorption at the trailing edge (see both pure LDPE conditions in Fig. 4.8 for

instance). It is worth reporting that the flame spread over the EG 10wt% samples is too slow to discriminate the smoking condition, since the flame trailing edge is still intertwined with the igniter.

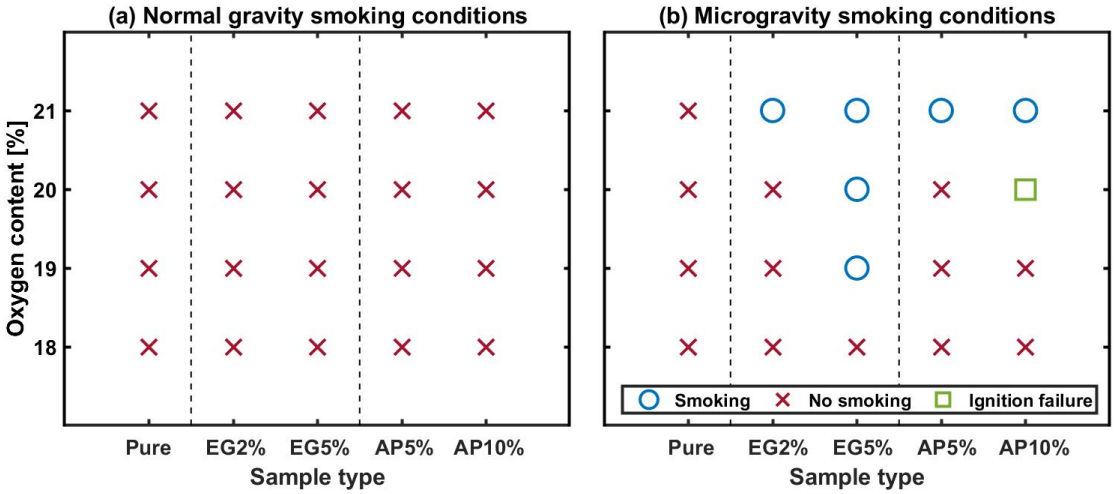

Figure 4.8: Effect of oxygen content on smoke emission over LDPE samples loaded with various flame retardant contents under (a) normal and (b) micro-gravity conditions. Flame retardants globally promote smoke emission in microgravity. [242]

4.7.1 Effects of gravity

At both normal and micro-gravity, no smoke emission was observed over pure LDPE in the studied range of oxygen content. At normal gravity, no smoke emission is also reported for all flame retardant-loaded samples, over the range of oxygen content studied. It should be pointed out that results are affected by significant dripping, which can reduce the fuel supply to the flame, thereby reducing soot production. Besides, it is also worth mentioning that the decrease in soot residence time within buoyant flames also reduces the radiative heat losses, leading to flame temperatures at the trailing edge high enough to support complete soot oxidation.

4.7.2 Effects of flame retardant

Under microgravity conditions, flame retardant-loaded samples show a consistent tendency to emit smoke at an oxygen content of 21% for all flame retardant types and loading. In addition, smoke emission is also observed at an oxygen content as low as 19% for EG-loaded samples of 5 wt%. But, since the nature of EG and AP intumescence is different, the mechanisms leading to smoke emission are different.

EG and AP flame retardant mechanism

EG expansion creates graphite worms through rapid sublimation. As such, it promotes the production of carbonaceous elements which can be released in the flame. Combined with the increase in residence time and hence radiative losses in microgravity, this promotes smoke release. In addition,

higher EG loading leads to an increase in carbon particle production and thus also increases the possibility of smoke emission. AP expansion, on the other hand, is driven by a carbonation mechanism that also promotes smoke emission. When the AP loading increases, the amount of char promoters also increases, thus strengthening the carbonation mechanism. As a result, the smoking also increases with AP loading.

Flame retardant loading

Comparing both flame retardants, the increase in EG loading causes the smoke emission transition to occur at lower oxygen content conditions, while the increase in AP loading has relatively a weaker impact on smoke emission. This is attributed to the different intumescent mechanisms, affecting the pyrolysis processes differently as oxygen content is increased. The gaseous fuel generated from pyrolysis flows through the intumescent region up to the trailing edge. This tends to increase the residence time, favoring soot production, which increases the hazard of smoke emission. As compared to the AP-loaded sample, the EG-loaded one produces a larger intumescent region at similar loading, which leads also to a longer residence time, further promoting the smoke emission. In addition, the cohesion of the EG residue structure is lower than that of the AP residue after combustion. As a result, it can be anticipated that the carbonaceous matter is released at a higher rate from the EG-loaded sample, which also promotes the smoke emission.

4.7.3 Effects of oxygen content

Smoke emission is heavily influenced by oxygen content in microgravity, as the flames spreading over all flame retardant-loaded samples transition from non-smoking to smoking when the oxygen content is increased. Oxygen content has a mixed effect on smoke emission. Higher oxygen content provides higher stoichiometric flame temperature and a higher soot oxidation rate [246], which should block smoke emission. But from the results of the previous Section, it also appears that the flame spread rate, and consequently the pyrolysis rate, increases with oxygen content, which facilitates smoke production [186]. Still the pyrolysis rate is determined as follows:

$$\dot{m}_F = \rho_{pe} \cdot \pi \cdot r_s^2 \cdot V_f \tag{4.1}$$

where ρ_{pe} is the density of LDPE, r_s the cylinder radius, and V_f the spread rate.
To further investigate the role of oxygen content, the relationship between pyrolysis mass flow rate $\dot{m}_F$ and oxygen content x_{O_2} is quantified, following Guibaud et al. [186]. The power law relating pyrolysis mass flow rate to oxygen content is extracted from a least square optimization using logarithmic transform to identify the parameter β, as shown in Eq. (4.2).

$$\dot{m}_F = C\, x_{O_2}^{\beta} \tag{4.2}$$

where C is a constant.
The value of β is then contrasted to a previous investigation by Glassman and Yaccarino at normal gravity [247]. These authors investigated the effect of oxygen content on a coflow diffusion flame at atmospheric pressure, and reported the variation of critical ethylene fuel flow rate $\dot{m}_F^c$ to sustain quenching conditions at the flame tip. Based on the variation of this critical value in the oxygen content range of the present experiment, a critical mass flow rate can be obtained as:

$$\dot{m}_F^c = C\, x_{O_2}^{0.82\pm0.14} \tag{4.3}$$

Any variation above this critical value fosters smoke emission, while any variation below hampers smoke emission. With the present configuration, the fuel is made of a similar chemical structure at the molecular level (polyethylene). Still, it is solid and the fuel pyrolysis rate is especially a function of the oxygen content, therefore cannot be freely adjusted. To understand whether a variation in oxygen content and the subsequent variation in fuel mass flow rate can trigger the release of smoke, a method similar to that of Glassman and Yaccarino is also applied to the present results in microgravity. The values of β extracted for the different sample types (reported in Tab. 4.1) are contrasted with the critical variation reported by Glassman and Yaccarino. All values for β are higher than the critical fuel flow rate variation of Eq. (4.3), so it can be concluded that the pyrolysis mass flow rate of all samples in microgravity increases faster than the critical mass flow rate required to sustain quenching at the flame trailing edge as the oxygen content increases. This means that the increase in pyrolysis mass flow rate with oxygen can be sufficient to justify a transition from non-smoking to smoking conditions. In addition, in the present case and as stated previously, the smoke release is also promoted by the effect of flame retardants on pyrolysis. Consequently, if high flame retardants loadings can further reduce flame spread rate until the increase in pyrolysis rate drops below its critical value, the transition from non-smoking to smoking still needs to be verified.

Pure	EG2%	EG5%	EG10%	AP5%	AP10%
4.84 ± 1.76	3.84 ± 1.16	2.73 ± 0.67	3.11 ± 0.79	3.05 ± 2.35	2.53 ± 0.17

Table 4.1: Flame spread rate exponent β for different samples in microgravity. [242]

4.8 Summary

This Chapter discussed the flame spread characteristics of cylindrical LDPE samples loaded with two intumescent flame retardants (i.e. EG and AP) under normal gravity and microgravity. The samples were ignited at different oxygen content levels under normal and microgravity conditions, and the associated extinction limits, flame spread rates, and smoke emissions were analyzed. The results show significant differences between microgravity and normal gravity conditions, which require careful integration of flame retardants within the context of space exploration.

At normal gravity conditions, extinction limits increased with increasing flame retardant loading. Interestingly, such effects were not reported at microgravity conditions. Worse, the EG-loaded samples presented lower extinction limits than the pure LDPE samples. This situation defeats the original purpose of the loaded flame retardant. The increase in flame retardant loading inhibited flame spread under normal gravity, and this effect was also observed, though less pronounced, when assessing the average rate of spread in microgravity. Under the same ambient conditions and the same loading, the EG-loaded samples showed a reduction in flame spread rate compared to the AP-loaded samples. To confirm that these results stand once the flame spreads at a steady rate, similar long-duration experiments are required. Although flame retardants improve fire safety in microgravity by reducing the flame spread rate, they also promote smoke emissions to an extent not reported in normal gravity. Despite the low flame spread rate, the tendency for enhanced smoke emission was particularly evident on samples loaded with EG, as the production mechanism of expansion in the absence of gravity readily contributes to soot formation.

Overall, it was observed that the combustion characteristics of samples loaded with flame retardants in microgravity differed from those in normal gravity, emphasizing the need for additional experimental observations prior to employing these flame retardants in spacecraft design.

5 Perspectives

Contents

Results in the present study provide useful information and new insights for fire detection and prevention in reduced gravity environments. In the process, new questions have been identified also providing inspiration for future investigations. Section 5.1 presents further developments in fire detection and refinement of released soot particle analysis methods. Then, the next aspects of flame retardant in microgravity and recommendations for the transition from theoretical understanding to the practical application are described in Section 5.2. In Section 5.3, relevant knowledge is presented that needs to be reinforced based on the partial gravity results of the present study.

5.1 Fire dection

As already mentioned in the present study, soot morphological characteristics drive the design of smoke detectors. However, from another perspective, the most straightforward refinement of fire detection leads to directly conduct experiments in microgravity with a detector. To this end, a detector was added to the DIAMONDS experimental setup. The basics of the detector implemented and its first experimental data in microgravity are presented in the following. Meanwhile, the ongoing analysis of soot morphology and the corresponding optimization of the analysis tools will be mentioned in this Section. In this way, the entire process from the formation and emission of soot from the flame to its potential detection can be followed. This provides a global view for fire detection improvement in microgravity.

5.1.1 LOAC Detector

Within the context of the present thesis, the LOAC (Light Optical Aerosol Counter) device has been added to the DIAMONDS experimental setup. LOAC is an original optical aerosol particles counters (OPCs), which measures the scattered part of a laser beam at two scattering angles. The smaller angle, i.e. 12°, leads to a light scattering magnitude that is almost insensitive to the refractive index of the particles. On the contrary, the magnitude of the light scattering at the larger angle, i.e.

60°, is very sensitive to the refractive index of the particles. By combining the measurements at both angles, it is possible to retrieve the size distribution between 0.2 and 100 µm and to identify the nature of the main particles (droplets, carbonaceous, salts, and mineral particles) when the aerosol is relatively homogeneous. This typology is based on calibration maps obtained at LPC2E (Laboratoire de Physique et de Chimie de l'Environnement et de l'Espace, Orléans, France).
A detailed description of LOAC can be found in Ref. [248, 249]. An overview of the basics of LOAC and how its operations on DIAMONDS is presented below.

LOAC basics

The LOAC instrument is shown in Fig. 5.1. The laser chamber of LOAC (see Fig. 5.1(a)) consists mainly of a laser and two detectors. The air being sampled passes through a laser beam of 25 mW operating at a wavelength of 650 nm. The scattered light is recorded by two photodiodes with scattering angles of 12° and 60°. The scattering at the first angle is less sensitive to the imaginary part of the aerosol refractive index and can retrieve the particle size distribution. In contrast, for the second angle, the scattered light is very sensitive to the refractive index of the particles and can therefore be used to assess their type. Instead of using a lens to collect the light, the photons reach the photodiode directly through the duct, providing a field of view of several degrees. The collection area of the photodiode is larger than the diameter of the pipe. This system prevents optical misalignment problems in case of vibrations and strong temperature changes.
The calibration procedure is performed for the 12° channel. The 60° channel is used as a compari-

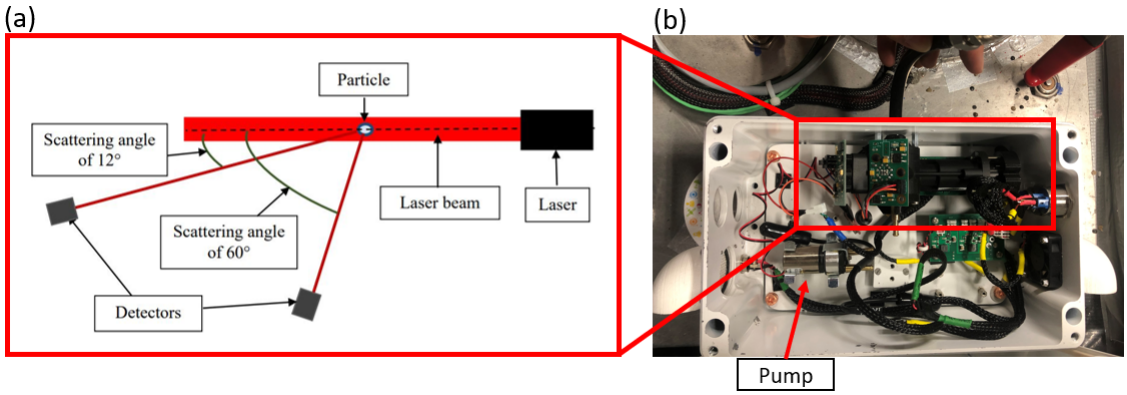

Figure 5.1: The LOAC instrument: (a) principle of measurement in LOAC's laser chamber (Reproduced from Renard et al. (2016) [248]); (b) picture of the instrument as implemented on DIAMONDS.

son with the 12° channel measurement to determine the type of aerosol. According to the range of particle diameters detected, the calibration procedure uses monodisperse latex beads (perfectly transparent spheres) and irregular particles of different natures (e.g. carbon particles, various types of dust, sand, ash, and salts). Considering the field of view of the LOAC, Mie theoretical calculations are performed and compared with the actual measurements. Based on the calibration, the output voltage recorded by the detectors allows the evaluation of the particle size. Overall, a total of 19 size classes between 0.2 and 100 µm diameter are defined. However, the upper limit can be lower, depending on the sampling collection cutoff of the inlet.
The counting is performed as the particles pass through the laser beam one by one and are classified into different size classes according to the scattering intensity. The measurements over the

configured time span are converted into number densities or particles cm^{-3}. The detectors of the two channels (12° and 60°) work asynchronously, thus enabling concentration measurements for different particle sizes.

As mentioned above, the scattered light recorded at a scattering angle of about 60° is very sen-

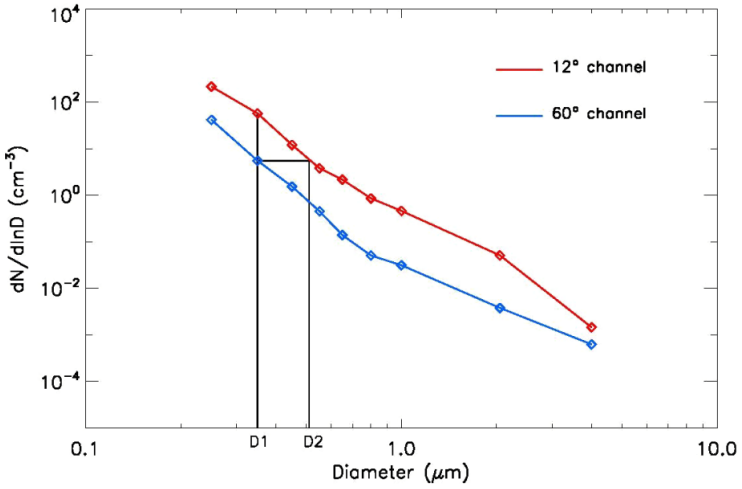

Figure 5.2: Principle of the determination of the "speciation index" D_2/D_1 (reproduced from Renard et al. (2016) [248]).

sitive to the refractive index of the particles and therefore to their nature. The more absorbing the particles, the lower the scattered light is. Hence, the refractive index dependence of the 60° channel response is used to diagnose the nature of the particles. This channel uses the same output voltage threshold (in mV) as the 12° channel to allow a direct comparison of the counts detected by the two channels. For a given size class and for a given particle concentration recorded in the 12° channel, the concentration detected in the 60° channel is reduced. An underestimation of the actual particle size also occurs, thus creating a diameter bias in the size distribution (diameter and concentration) of the 60° channel relative to the 12° channel. For a given particle size (denoted D1) in the 12° channel, the concentration value of the 60° channel is then evaluated, as shown in Fig. 5.2. With this concentration value, the corresponding diameter (D2) is then determined. Finally, the so-called "species formation index" is defined as the ratio D2 /D1. The more absorbing the particles, the higher this ratio is. Different types of particles have been tested in the laboratory to assess the magnitude of the species formation index over the whole measured size range: organic carbon, black carbon, desert dust or sand from different sources (except black sand), volcanic ash, gypsum, salt (NaCl), water droplets, droplets of a mixture of water and sulfuric acid. They can be divided into four categories: carbonaceous particles, minerals, salts, and droplets.

Overall, LOAC can provide three main pieces of information: particle size, concentration, and refractive index of the particles. If the morphological characteristics of the particle products emitted by the flame can be carefully defined, combined with the performance of LOAC for particle detection, the fire signature can be accurately documented.

LOAC implementation on DIAMONDS

LOAC is a modular instrument, some parts of which can be modified according to the measurement conditions (e.g. pump, inlet, and outlet of LOAC). Therefore, to adapt it to the DIAMONDS setup and the experimental environment in microgravity, some changes have been made but the main

principle remains the same. Figure 5.3 shows the position of LOAC on DIAMONDS. As shown in Fig. 5.1, LOAC contains a Rotary Vane pump (G 02-4-EB). The maximum flow that it can provide is 3.7 L/min. The flow into the LOAC is extracted from a port located close to the upstream end of the combustion chamber exhaust line. The extracted flow passes through the laser chamber of the LOAC as described above and is then discharged to a port located further downstream the aforementioned exhaust line. The material of the tube connecting LOAC to DIAMONDS is PFA (perfluoroalkoxy), as the semi-transparent plastic tube shown in Fig. 5.3. This material is chosen mainly because it is tough and flexible with a low coefficient of friction and its non-stick surface property. The external and internal diameters of the tube are 6.35mm and 3.97mm, respectively. The length of the inlet tube is 840mm, while the length of the outlet tube is 760mm. The tubes are laid out in such a way that they are not bent as much as possible, thus avoiding the loss of particles during the transport process.

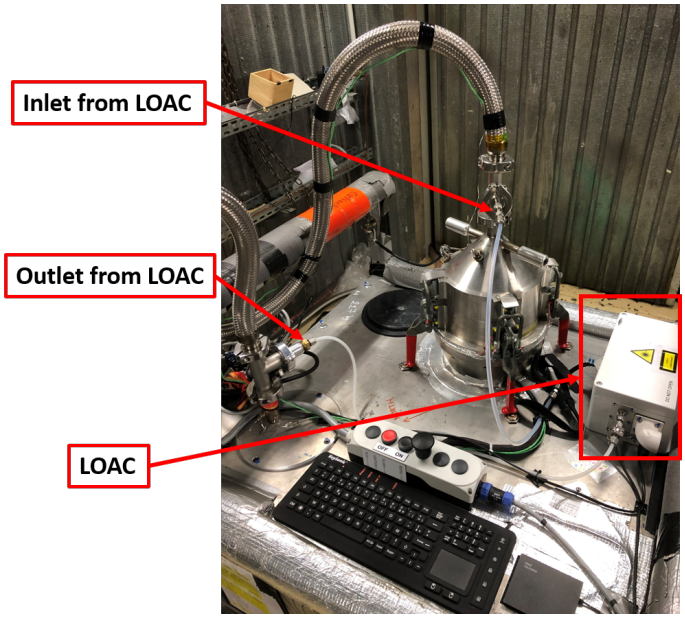

Figure 5.3: Picture of the LOAC incorporated onto DIAMONDS. LOAC is connected to DIAMONDS from an upstream port on the exhaust line and to a downstream one with the PFA tubes.

LOAC in parabolic flight

LOAC on DIAMONDS has recently been operated for the first time in microgravity. Since LOAC requires a minimum of five minutes of auto-calibration time for the startup, it needs to be run well in advance of each first parabolic flight in the day. During the flight, LOAC runs continuously until the end of the flight. Therefore, the whole day's data is stored in the same file. In addition, LOAC is automatically calibrated every ten minutes, and the duration of the calibration is one minute. Hence, when designing the experimental tests matrix of the day, it is important to note that LOAC may be in autocalibration during the microgravity phase. The time span for data acquisition of LOAC has been enhanced specifically for the present works by J.-M. Citerne and is now 3 seconds. In this context, there would be about 6 measurement points in a single microgravity experiment. Each experimental point corresponds to 3 seconds of integrated information about the particles collected by LOAC. The raw data are analyzed using the software that comes with LOAC. The concentrations and the speciation index of different particle sizes can be extracted directly.

First results in microgravity

The sample investigated in these experiments in microgravity is a classical electric wire sample with a 0.5 mm diameter NiCr metal core coated with a 0.3 mm thickness of LDPE insulation. Opposed flow flame spread is investigated. Such a configuration can provide a steady rate flame spread. In addition, this is the configuration with the most experiments performed on DIAMONDS, and the previous experimental data and studies can support further data analysis. Regarding the oxidizer flow conditions, the oxygen content and pressure are varied from 18 to 21%, and from 60.7 to 141.6 kPa, respectively, with a fixed flow velocity of 150 mm/s. The objective is to observe whether LOAC can detect the difference in flame spread products released at different levels of oxygen content and pressure. The same experiments are performed at normal gravity to compare the results in microgravity.
As described above, the LOAC works continuously during a full-day mission, so it collects all data during the mission. In order to extract representative data, it is necessary to identify the data collected during the steady rate flame spread. This requires the analysis of three parameters, i.e. flame spread rate, flame length, and molten LDPE droplet volume to determine the phase at a steady rate of the flame spread during each experiment. In addition, several data are likely to be collected during this phase. In this case, the data is taken near the end of the microgravity phase so that it would allow enough time for the flame to reach a completely steady spread rate.
An additional consideration is a time required for the particles to be transported from the flame to the LOAC. The flame spreads about 400 mm from the exhaust of the combustion chamber. In a microgravity environment, the forced flow governs the particle transport. With a flow velocity of 150 mm/s, it takes about 2.6s to transport the particles from the flame to the exhaust of the combustion chamber. If the pump can provide a maximum flow of 3.7 L/min, the time required for the particle to pass through the tube connected from the exhaust of the combustion chamber to LOAC with a length of 840mm and an internal diameter of 3.97mm is about 0.17s. In this experiment, the steady flame spread duration for all tests is at least 5s. This further justifies the selection of data near the end of the microgravity phase for the subsequent analysis.
Under normal gravity, however, the flame cannot achieve a completely steady rate spread as in microgravity. Nevertheless, the experiment at normal gravity is carried out according to the duration of the experiment performed in microgravity. Similarly, the data just before the end of the experiment is selected for analysis.
Figure 5.4 shows the concentration of different particle sizes (normalized with particle size) for experiments performed in microgravity and normal gravity. It provides an overall view of the first experiment. In microgravity, the concentration of the detected particles increases with the pressure. In addition, the maximum particle size also has a tendency to increase with the pressure. However, the effect of oxygen content on the concentration and size of particles is difficult to determine. At normal gravity, the effects of pressure and oxygen content on particle concentration and size follow a similar trend as in microgravity. Comparing the results between the two gravity levels, it can be found that the particle concentrations detected in microgravity are much higher than those in normal gravity under the same conditions. Furthermore, the maximum particle size is larger in microgravity than at normal gravity under the same conditions.
Figure 5.5 shows the speciation index for different particle sizes detected in microgravity and normal gravity. As mentioned before, LOAC uses different particles for calibration and can be divided into four main categories, i.e. carbonaceous particles, minerals, salts, and liquid droplets. These correspond to absorbent solid, semi-transparent solid, transparent solid, and droplets, respectively, which can be used to roughly determine the sensitivity of the scattered light to the refractive index of the particles. In microgravity, the scattered light is more sensitive to the refractive index

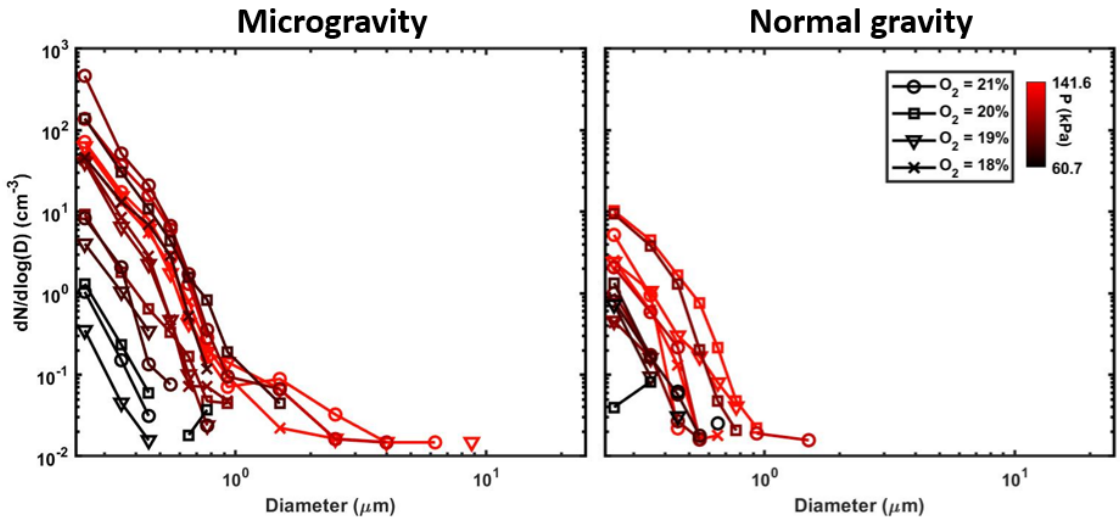

Figure 5.4: Evolution of particle concentration as a function of particle size under different oxygen content (represented with different symbols) and different pressure levels (represented with different colors) for a fixed flow velocity of 150 mm/s.

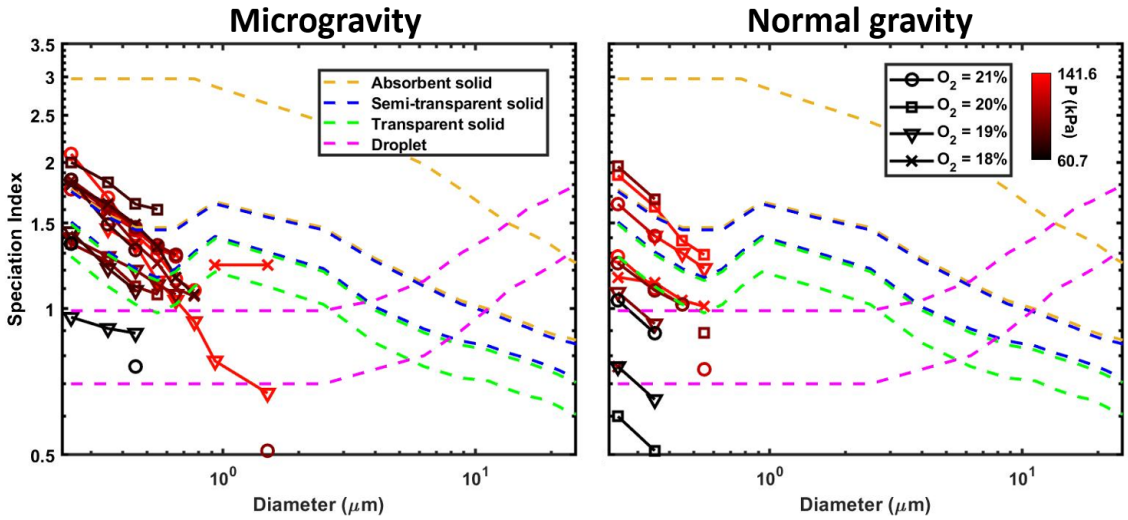

Figure 5.5: Evolution of speciation index as a function of particle size under different oxygen content (represented with different symbols) and different pressure levels (represented with different colors) for a fixed flow velocity of 150 mm/s. Four different zones are delineated in between couples of dashed lines, i.e. absorbent solid, semi-transparent solid, transparent solid, and droplet.

of the particles emitted by the flame at higher pressure. However, the effect of oxygen content is difficult to clarify. The same trend is observed in normal gravity. Overall, the scattered light is more sensitive to the refractive index of the particles in microgravity than at normal gravity.

Some next envioned steps

The experimental data presented above reveals that LOAC detects the effect of gravity and pressure on the particles emitted by the flame. Although it is only a preliminary observation, these data are still encouraging. From past macroscopic observations, it has been found that the reduction of gravity contributes to the emission of soot particles at the trailing end of the flame for the opposed

flame spread configuration. Besides, from the soot morphological analysis, the particle size is larger in microgravity than at normal gravity. These findings are consistent with those detected by LOAC. To further validate the LOAC data, an understanding of the reproducibility of the LOAC detection needs to be carried out. The experiment described above was repeated at least twice in microgravity and normal gravity. The next priority is to analyze the difference in data between the repeated experiments.
In addition, the above analysis only shows the evolution of the detected particles with the pressure and oxygen content in terms of the overall trend. More careful data analysis and presentation methods need to be developed to further clarify the differences in the detected particles under different ambient conditions.
Since LOAC provides the sensitivity of scattered light to the refractive index of the particles, the next step is to combine the study presented in chapter 2 to extract the refractive index of the collected soot particles by their morphology and then compare it with the LOAC data.
Besides the analysis of data, it is important to take into account that particles can be lost in the

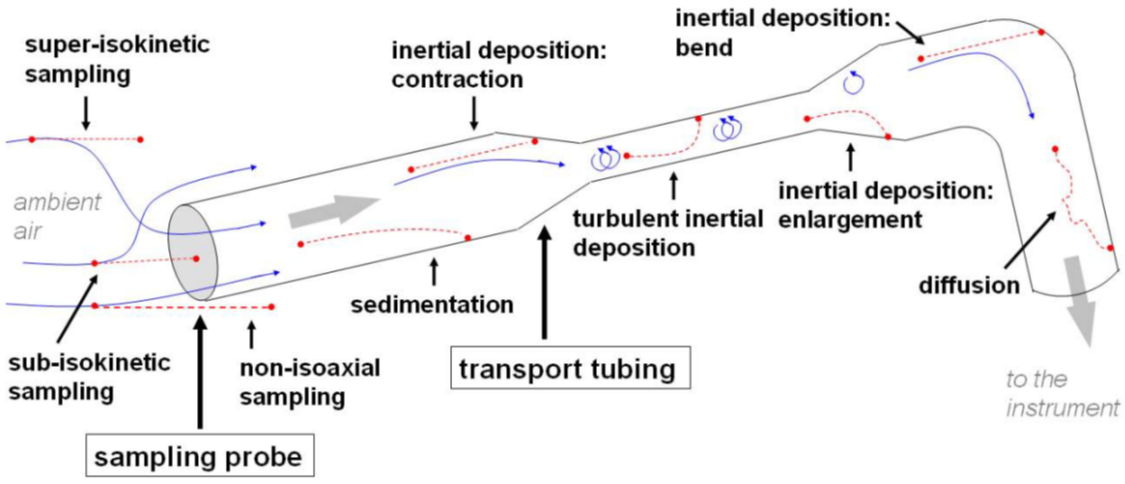

Figure 5.6: Mechanisms occurring during particle sampling and transport in a sampling probe and a transport tube. Reproduced from Von der Weiden et al. (2009) [250].

transport process from the flame emission up to the LOAC. Figure 5.6 shows the mechanisms of the particle sampling and transport processes. Using these mechanisms, combined with the actual situation of LOAC on DIAMONDS, the particle losses can be evaluated. The evaluated particle losses will contribute to more accurate detection data.

5.1.2 Effect of oxydizer flow conditions on soot formation in microgravity

Preliminary data from LOAC reveal that differences in soot particles are detected and certain trends can be observed at different pressure levels. In addition, as also found in previous works, the flames show different morphologies under macroscopic observation as the pressure and oxygen content varies (as described in Section 1.2.5). All these factors point to the fact that the morphology of soot particles emitted by the flame is likely to be different under different oxidizer flow conditions.
In this context, soot sampling was performed in this study for flame spread at different levels of pressure and oxygen. The sampling process is described in detail in Chapter 2. In studying the effect of pressure, the oxygen content and the flow velocity were set to 21% and 150 mm/s, respectively. The variation in pressure was from 60.7 to 141.8 kPa. While studying the effect of

oxygen content, the pressure and the flow velocity were set to 101.3 kPa and 150 mm/s, respectively. The variation in oxygen content was from 18 to 21%.
This whole process takes more time due to the TEM observation and the acquisition of TEM images after the sampling, and then the analysis of the TEM images for all different conditions. The collected soot particles are being analyzed and the results obtained will be combined with the previously obtained macroscopic observations and the LOAC detection results.

5.1.3 Soot morphology characterization

Chapter 2 describes the procedure to evaluate the morphological characteristics of the sampled soot particles. Whether using the classical thermophoretic sampling technique or the electric field sampling technique introduced in this study, the process of soot sampling transforms three-dimensional (3D) information into two-dimensional (2D) information. However, it is not easy to extract the original 3D information from the acquired 2D information through post-processing. With these challenges clear, it is important to clarify that the objective here is to extract essential information under limited conditions. Then, this information is then used to identify the evolution of soot morphological characteristics with ambient conditions. It is worth mentioning that the optical detector also extracts the 2D characteristics of the particles for the detection of particles.
The same challenge arises for the TEM image analysis. The soot morphological features extracted from the images also have only 2D characteristics. The following discussion is to optimize the approach of TEM observation and image analysis in order to extract as much as possible of the 3D morphological information of soot particles.

TEM image

Before discussing TEM image optimization, it is necessary to understand the principle of TEM image production, which uses an electron beam to resolve the image. The electron beam is generated by heating a tungsten filament and focusing it using a magnetic field. A high level of vacuum is required to prevent collisions between energetic electrons and air molecules, and air analysis absorbs energy from the electrons [251]. To obtain TEM images, the prepared thin sample is irradiated by a high-energy electron beam. The electron beam is guided using an electromagnetic lens. The electrons are scattered elastically or inelastically as they penetrate the sample. Either transmitted or scattered electrons can be imaged, called dark-field and light-field imaging, respectively. Imaging depends on the contrast, which can come from three processes, i.e. mass-thickness contrast, diffraction contrast, and phase contrast [252].
This imaging process is different from regular photo imaging, which means that the intensity information in the image cannot be directly applied as the third dimensional information (z-direction) for extracting soot morphology. This poses a significant difficulty in identifying primary soot particles. The difference in intensity on the same soot particle does not simply imply an overlap between primary soot particles. Electrons are scattered elastically in the process of penetrating soot particles, thus affecting the imaging of TEM images and their intensity information.

STEM image

This problem may be solved with STEM (Scanning Transmission Electron Microscopy), which is similar to TEM. In TEM, the parallel electron beam is focused perpendicular to the sample plane, while in STEM, the beam is focused at a large angle and converges to a focal point. The emission signal is collected as a function of the beam position as it is rasterized on the sample [253].
STEM imaging has several detectors: BF (Bright Field) detector, ADF (Annular Dark Field) detector, and HAADF (High Angle Annular Dark Field) detector. The difference between these detectors lies in their detection angles. The HAADF image with the largest detection angle allows for enhanced contrast. No elastically scattered electrons reach the detector, so it can only image from inelastically scattered electrons. This is also called Z-contrast imaging because there is a direct correlation between the local contrast and the local mass thickness.
In this case, the intensity of the images obtained by STEM is directly linked to the thickness of the soot particles. This provides the possibility to extract a more accurate number and size information of primary particles.

Recently, the sampled soot particles were attempted to obtain images by STEM, as shown in Fig. 5.7. However, due to the time constraints of the present study, no further analysis has been performed. Further analysis of the STEM images can be attempted and compared with the data obtained from the TEM images to determine if the STEM images can bring more information than the TEM ones.

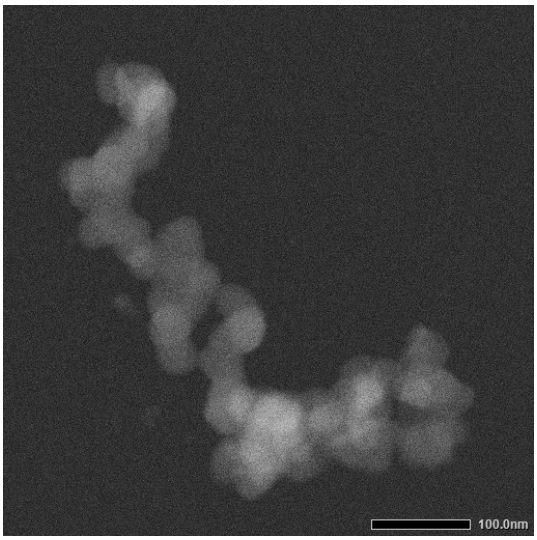

Figure 5.7: STEM image (with HAADF detector) of Soot particle sampled in microgravity with an oxygen content of 21%, a pressure of 101.3 kPa, and a flow velocity of 150 mm/s.

Electron tomography

Electron Tomography (ET) is a technique that can obtain the 3D morphological properties of objects with dimensions ranging from tens of nanometers to a few micrometers. It combines a series of TEM images obtained in different viewing directions to obtain the 3D morphology of an object. This technique has been applied in different fields such as biology [254, 255], materials science [256], and aerosol science[257]. ET is also used to determine the 3D morphology of individual soot particles [258].

Adachi et al. [259] obtained bright-field images by tilting the soot particle sample in the electron beam (typically in 1° increment from -70° to 70°) and recording images at each tilt step. Subsequent 3D reconstructions (Fig. 5.8 (b) and (d)) are calculated from this tilt series using a sequential iterative

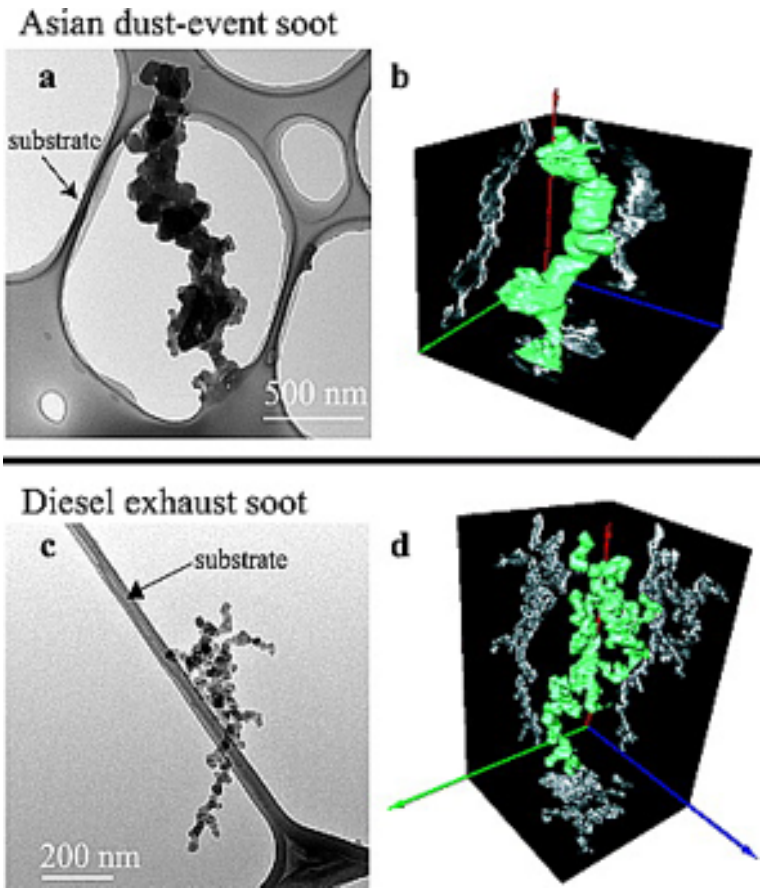

Figure 5.8: Two- and three-dimensional images of soot particles. (a) and (c) TEM images of particles and their supporting substrates. (b) and (d) 3D images of soot together with their projections along three orthogonal directions in shadow boxes. Reproduced from Adachi et al. (2007) [259].

reconstruction technique (SIRT) algorithm with 15 iterations. Based on the information on the 3D morphology, they developed methods to calculate the fractal dimension (D_f), radius of gyration (R_g), volume (V), surface area (A_s), and structure coefficients (k_a) of soot particles. Since this procedure allows the determination of structural parameters directly from the reconstructed 3D data, it eliminates the effect of pores and particle overlap that are not detected in 2D images.
Baldelli et al. [260], on the other hand, used this technique to evaluate the effect of variation in projection angle on 2D soot particle morphology results. They found that primary particle size varied by less than 16% as the projection angle changed, while projected area-equivalent diameter varied by only 6% across projection angles. This implies that the soot characteristics evaluated by the classical 2D projection results are equally representative.
Obviously, the ET technique provides more information in the third dimension than the regular TEM images. However, each analysis requires a significant amount of time to analyze a single soot particle sample. In the context of the present study, a large number of soot particles after sampling need to be analyzed to provide as much information as possible. It is not practical to analyze all collected soot particles using the ET technique. Therefore, for the application of the ET technique in the present study, a few representative soot particles need to be identified first. Then, more specific 3D morphological characteristics can be extracted for the soot particles.

5.2 Material enhancement

The cylindrical samples loaded with flame retardants showed unexpected performances in microgravity. This also demonstrates that further understanding is needed before applying flame retardant to a manned spacecraft in a microgravity environment. Since the ambient conditions inside the manned spacecraft are controllable, the present study observed the effect of oxygen content on the flame spread on the samples loaded with flame retardants and also analyzed their flame spread mechanisms (see Chapter 4). High oxygen content and lower pressure are usually combined from a spacecraft engineering standpoint. For example, it can reduce the pressure difference applied to the spacecraft enclosure. At the same time, the weight of the structure can be reduced, which in turn reduces the fuel and price needed to send the spacecraft into orbit or further away. Unfortunately because of today's parabolic flight restrictions, the oxygen content must not exceed 21%. However, in addition to the study of the oxygen content effects, the performance of flame retardants in low-pressure environments is equally promising. With the understanding of the effects of flame retardants on flame spread in microgravity, it is also expected that flame retardants will be applied to wire samples and subjected to microgravity experiments.

5.2.1 Low pressure environment

The performance of flame retardants in low-pressure environments has rarely been studied because fire scenarios in low-pressure environments are not common on the ground. This has highlighted the need to understand the role of flame retardants in low-pressure environments. Recently, experiments were conducted in microgravity to investigate the effect of low-pressure environments on opposed-flow flame spread over cylindrical samples loaded with flame retardants.
The same sample configuration as that used to study the effect of oxygen content was applied (described in detail in Chapter 4). The samples were pure LDPE samples, 2 to 10 wt% EG loaded samples, and 5 to 10 wt% AP loaded samples. The pressure varied between 50.6 and 101.3 kPa at an oxygen content of 21% and a flow velocity of 150 mm/s.
The obtained experimental results will be analyzed for flame extinction limit, flame spread rate, and smoke emission. In addition, the mechanism of intumescence formation from flame retardant upon heating will be observed. Since the intumescence is formed by local pressure difference, lower ambient pressure may have an effect on the intumescence formation.

5.2.2 Flame retardant loaded electric wire

Besides fundamental studies, it is equally important to study the application of flame retardants. Recently, experiments have been conducted on wire samples loaded with flame retardants in microgravity and normal gravity.
The manufacturing of the wire samples loaded with flame retardants is similar to that of flame retardant loaded cylindrical samples. As shown in Fig. 5.9, the fabrication is performed using HAAKE Rheomix OS PTW 16 twin-screw extruder. The extruder is a co-rotating intermeshing twin screw with a barrel length of 400 mm and a screw diameter of 16 mm (L/D = 25) with 10 zones. LDPE and flame retardants were incorporated using two gravimetric side feeders into the extruder. The material is discharged through the extrusion nozzle. At the same time, the metallic core passes through the extrusion nozzle and produces a flame retardant loaded electric wire sample.
The wire samples are configured with a 0.5 mm diameter NiCr core coated with a 0.4 mm thick

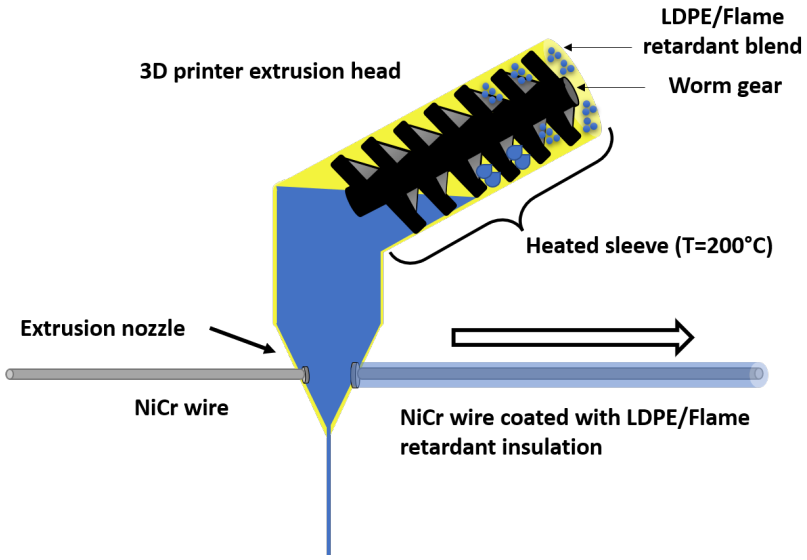

Figure 5.9: Schematic representation of flame retardant loaded electric wire production. In a 3D printing extrusion head, the LDPE and flame retardant materials are blended and fused inside a Heated sleeve. In the end, the material is discharged through the extrusion nozzle. At the same time, the metallic core passes (from the left to the right side) through the extrusion nozzle and produces a flame retardant loaded electric wire sample. Reproduced from Prof. Bourbigot.

LDPE insulation loaded with flame retardant. Since the EG-loaded samples showed lower extinction limits than the pure LDPE samples in the previous microgravity experiments investigating the effect of oxygen content, this time the flame retardant loading is mainly AP with 10 wt% and 20 wt% loadings, respectively. In addition, three other different flame retardants are studied (10wt% loading), namely phosphorus-based flame retardant, Adeka (halogen-free flame retardant), and FlameOff flame retardant. The objective is to find the most suitable flame retardant formulation for use in the microgravity environment.
Experiments conducted with these samples are carried out under different oxidizer flow conditions. To investigate the effect of oxygen content and pressure on opposed flame spread over flame retardant loaded electric wire sample, the oxygen content and pressure were varied from 16 to 21% and from 50.6 to 101.3 kPa, respectively, with a fixed flow velocity of 150 mm/s. These recent incoming data are being processed.

5.3 Partial gravity

The DIAMONDS experimental setup was successfully operated in a partial gravity environment, as described in detail in Chapter 3. The flame spread data in this particular environment were successfully obtained. While the data from 33 lunar gravity and 33 Mars gravity experiments provide valid information, more experiments are needed to have a complete understanding of flame spread in partial gravity.
In particular, past experiments have shown that materials in partial gravity provide different flammability than normal gravity and microgravity [44–47], suggesting that testing of materials in partial gravity is still needed.
In addition, many results are determined with the sample configuration. In the past, most experiments conducted in microgravity have been on flat samples [61]. To use these data as references, the

DIAMONDS rig can probably be extended for experiments on other configurations than cylindrical samples. The sample holder could be improved, perhaps to embed flat samples. Thus, it would be possible to perform experiments on flat samples under partial gravity.

In the present experiments investigating convective flame spread, it was found that dripping and leakage of molten droplets may have an effect on both the extinction limit and flame spread at partial gravity. However, it has been observed in the past that the dropping phenomenon of concurrent flow flame spread is more severe under normal gravity compared to opposed-flow flame spread. A counter-intuitive observation emerged from concurrent flow flame spread experiments conducted under normal gravity and is detailed in Appendix A. The purpose of the experiment is to evaluate the extinction limit for concurrent flow flame spread under normal gravity in varying oxygen content. Upward vertical flame spread and self-extinction over electric wire samples are systematically evaluated at different oxygen levels with the expectation that lowering the oxygen content would lead to a transition from flame propagation to self-extinction. However, the results show that flames can propagate in the range of 13-15% of oxygen content, below the onset of self-extinction at 16-18%. These observations are replicated at different levels of pressure and flow velocity. It is proposed that, at high oxygen content, the combined effect of increasing dripping and flame instability can reduce the pre-heating of the original fuel and act as a heat sink, respectively, to trigger self-extinction. As the oxygen content decreases, these instabilities are reduced to the point where flame spread can be sustained again. Such configuration-related observations need to be carefully understood to support the development of reliable fire safety standards. Partial gravity experiments may provide an opportunity to clarify this observation. The frequency of dripping might be reduced with the reduction of gravity, and thus identify whether this unusual phenomenon is dominated by the dripping effect.

Conclusion

The present works constitute the second PhD completed in the context of the DIAMONDS project. The above research is an expansion of the first PhD and provides valuable data for practical fire safety applications while taking into account the scientific research aspects. Furthermore, during this PhD, different ambitious research directions were initiated and established.
To improve the fire safety of spacecraft, special attention has been paid to the detection and mitigation prerequisites to study flame and soot properties in a reduced gravity environment. The experiments of opposed-flow flame spread over cylindrical samples under reduced gravity were conducted on DIAMONDS parabolic flight setup.
From a practical point of view, the present PhD thesis contributes to a database for fire detection in microgravity. The soot particles were successfully collected in microgravity through a novel soot sampling technique using electric fields. The collected soot particles were then observed under TEM. The morphological characteristics of the soot particles released from the flame were analyzed using the developed TEM image analysis tools. Their morphological characteristics will allow inferring the optical properties of soot particles and thus optimizing the accuracy of fire detection. In addition, for the first time, flame retardant loaded materials were subjected to experiments in microgravity. Two types of flame retardant with different expansion mechanisms are considered, namely Expanded Graphite (EG) and Ammonium polyphosphate/ Pentaerythritol (AP). Under normal gravity, increasing flame retardant loading increased the extinction limit of the samples and slowed down the flame spread rate. However, in microgravity, increasing flame retardant loading did not improve the extinction limit of the samples. Even worse, EG loading led to lower extinction limits. Although flame retardants could improve fire safety in microgravity by reducing flame spread rates, they also promoted smoke emissions to an extent not reported in normal gravity. These results show significant differences at different gravity levels and highlight the need for additional experimental observations before employing these flame retardants in spacecraft design.
From a scientific point of view, the soot sampling at normal gravity and microgravity allows the study of soot formation processes at different gravity levels. The differences can be determined by the morphological properties of soot particles, projected density and area of soot particles, the radius of gyration, fractal dimension, and primary particle size distribution. The evolution of these morphological properties along the flame axis was analyzed. Overall, soot particles sampled in microgravity are larger than those collected in normal gravity. In addition, soot particles sampled under microgravity are mainly fractal aggregates, while under normal gravity they are mainly spherical primary soot particles. According to the evolution of their distribution, the closer to the trailing edge of the flame, the more the soot tends to grow as chain-like branching aggregates. In microgravity, the soot primary particles are larger and the size distribution remains more polydisperse than in normal gravity. Therefore, the soot particles formed in microgravity do not support the monodisperse assumption. The understanding of the soot morphological properties can be used to improve the non-intrusive optical techniques and thus better study the flame spread behaviors in microgravity. Besides, for the first time, experiments on flame spread over electric wires were

conducted under partial gravity and the effect of gravity on the characteristics of flame spread was analyzed. Different configurations of LDPE coated electric wire were tested with an oxygen content ranging from 0 to 21%. The effect of gravity on the extinction limit and flame spread rate was found to show different trends depending on the thermal conductivity of the wire core. As the gravity increases, molten LDPE upstream of the flame drips or even leaks. The leaked molten LDPE droplets have an effect on both the extinction limit and flame spread. In Martian gravity, the presence of leaked LDPE droplets upstream of the flame leads to the appearance of a unique cyclic flame spread mode. The mechanism of this unique flame spread is analyzed and supported by associated theoretical considerations. Furthermore, the revealed cyclic behavior seems to be a relevant opportunity, especially for the validation of the numerical tools currently under development.

Appendices

A Multiple flame spread domains

Contents

In view of the technical difficulties in collecting results in reduced buoyancy flows, methods have been developed to extrapolate low-gravity data from normal gravity measurements [261, 262]. Any perturbation in the normal gravity results can thus have dramatic consequences for fire safety provisions in the microgravity environment. Therefore, the observations at normal gravity should be carefully understood before applying them to support the development of reliable fire safety in microgravity. The following highlights counter-intuitive low-oxygen flame spread observations related to the experimental assessment of extinction limit in varying oxygen content for concurrent flow flame spread over an electric wire under normal gravity. DIAMONDS was used in previous publications to assess the extinction limit in this very configuration, by running flame spread experiments at gradually lower oxygen content. The flame spreads at high oxygen content, and extinction is reported below a certain oxygen threshold taken as the value at extinction. Here, unexpected behaviors are reported where the flame can spread again at oxygen contents below the extinction value, creating a discontinuous domain of flame spread.

A.1 Inital observation

The discontinuous domain of flame spread is illustrated in Fig. A.1 for three different oxygen content values. Vertical concurrent flow flame spread is established over an electric wire with a NiCr core diameter of 0.5 mm and a 0.3 mm thick LDPE coating. 8 s later, the hot Khandal wire igniter is switched off. The three experiments are carried out at a pressure of 101.3 kPa with a set upward forced flow of 60 mm/s for three different oxygen content,namely 14, 17 and 21%.

At x_{O_2}=21%, a bright flame spreads over the entire length of the wire as shown in Fig. A.1 (a). After a few seconds, the coating is either consumed or drips away from the flame as the droplets formed by the molten LDPE fall under their weight. Reducing the ambient oxygen content in the same configuration, a new sample is ignited at x_{O_2} = 17%, as shown in Fig. A.1 (b). As in the previous case, a visible flame is established and dripping is recorded, but this time extinction occurs 4 s after the end of ignition and a large part of the virgin coating remains. This would conventionally point to the existence of an extinction limit between these two values in the configuration studied, suggesting that no sustained propagation can occur below x_{O_2} = 17%. However, further reducing the oxygen content to x_{O_2} = 14%, the sample is ignited and a less bright flame is established, as shown in Fig. A.1 (c). Contrary to predictions, self-extinction does not occur and the flame is able

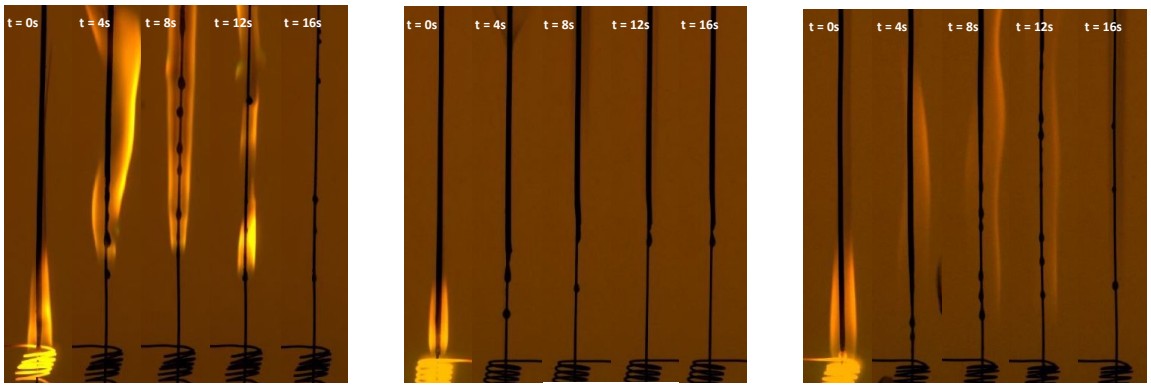

(a) x_{O_2} = 21% **(b)** x_{O_2} = 17% **(c)** x_{O_2} = 14%

Figure A.1: Backlighted images of flame spread over LDPE-coated NiCr wire at atmospheric pressure (101.3 kPa) and a set concurrent flow velocity (60 mm/s) for different oxygen contents. Images captured every 4 seconds evidence the degradation of the coating and flame propagation. Flame spread is sustained at oxygen contents of (a) 21% and (b) 14% but not (c) 17%, highlighting the existence of multiple flame spread domains. The igniter is switched off at t=0s.

to spread again until the coating is consumed.
With all parameters set, this experiment illustrates that there exists a configuration in which reducing the oxygen content in turn raises the risk of flame propagation. Following this initial observation, it was first hypothesized that this unusual phenomenon could be related to the dripping rate of molten LDPE along the metallic wire core. Dripping seemed to increase with oxygen content, acting as an additional heat sink mechanism which could lead to two domains of existence of the flame: one with high flame temperature and high dripping rate at high oxygen content, and a second at low temperature and low dripping rate at low oxygen content. This hypothesis was tested by repeating tests at normal gravity to assess the potential for re-ignition at low oxygen content and the associated dripping level.

A.2 Methodology

The experiments are carried out in the DIAMONDS experimental rig. The sample used is a wire sample, made of a 0.5 mm cylindrical core of NiCr coated with a 0.3 mm thick LDPE insulation. Ignition is performed using a Kanthal coil-shaped wire through which provides a tension of 14.2 volts is applied for 8s. Since a concurrent flow flame spread configuration is studied, the igniter is set below the sample holder as shown in Fig. 2.3. The pressure, flow velocity, and oxygen content of oxidizer flow are adjusted. The oxygen content varies from 12 to 21%. Three levels of flow velocities, namely 60, 100, and 150 mm/s, and three levels of pressure, namely 50.7, 101.3, and 141.8 kPa, are investigated. Concurrent flow flame spread systematically results in the existence of two discontinuous oxygen content domains allowing flame spread. This discontinuity is reported at different pressures and flow velocities. Each experiment has been performed twice to enhance confidence in the results.
The igniter systematically heats the wire until a flame appears, and extinction always occurs when the flame spreads to the end of the sample. Therefore a systematic post-treatment is implemented to distinguish between self-quenching and quenching caused by sample edge effects. For this purpose, the burn length L_b is defined as the length from the igniter to the visible upper position of the wire's exposed NiCr core. This means that L_b is the length at which the combustible coating is

completely consumed at the end of the experiment. A critical length of 7.5 cm (half of the sample length) is used to distinguish between self-extinction ($L_b < 7.5$ cm) and propagation situations ($L_b > 7.5$ cm). Overall, the measurement uncertainty of 1 mm is an order of magnitude lower than the uncertainty associated with experimental repeatability, so it is neglected.
During each experiment, molten LDPE is systematically observed to drip along the metal core as the solid fuel degrades. In order to extract the dripping rate for each condition, the profile of the molten coating is evaluated from backlighted images. In the studied configuration, the pyrolysis front does not displace with a steady state. It is assumed that the first upstream LDPE deformation position corresponds to the limit between the burnt zone and pyrolysis zone, thus providing a reference position for tracking the droplet movement. The motion of the droplet is then captured by tracking the deformation at three different locations located downstream of the defined reference point. Each location is correspondingly isolated by 2cm to achieve redundancy. Given that the backlighted image was recorded with a frame rate of 15 fps, this approach reasonably assumes a drop velocity of less than 30 cm/s near the pyrolysis front, where the initial velocity of droplet formation is 0 cm/s. The drop velocity is eventually obtained at each marked location and averaged to obtain the average drop velocity and associated standard deviation for each test.
In addition, the average position of the visible flame and its deviation from the wire axis are analyzed to qualify the heat transfer from the flame to the solid fuel. To optimize the contrast, the flame position is evaluated with non-backlighted images. A larger deviation means that the flame sheet is further away from the fuel surface, or that the flame is flickering. In both cases, the heat transfer from the flame to the solid fuel is reduced.

A.3 Multiple flame spread domains in different ambient conditions

Figure A.2 shows the measured burn lengths at different oxygen contents and flow rates, at pressures of 50.6, 101.3, and 141.8 kPa. The critical length of 7.5 cm is plotted as a dashed line on each graph to distinguish between the flame spread case and the self-extinction case.
Under a pressure of 101.3 and 141.8 kPa (see Fig. A.2 (b) and (c)), starting at $x_{O_2} = 21\%$, extinction is first reached before a secondary domain of oxygen content allowing flame spread is crossed for every flow velocity investigated. Though a limiting oxygen content of $x_{O_2} = 18\%$ or $x_{O_2} = 19\%$ is identified, subsequent experiments at lower oxygen content reveal that flames spread again over a domain spanning approximately from $x_{O_2} = 12\%$ to $x_{O_2} = 15\%$. If the arbitrary definition of the threshold value questions the exact boundaries of the secondary domains, the results obtained at 150 mm/s stress that, at both pressures, the fuel is totally consumed at $x_{O_2} = 14\%$ and $x_{O_2} = 19\%$ while self-extinction occurs at $x_{O_2} = 16\%$ even though more than two-third of the sample length is left unburnt. The secondary flame spread domain is less pronounced at lower flow rates, but the overall trend can still be clearly identified at both pressures.
As pressure is decreased to 50.6kPa in Fig. A.2 (a), the situation is less clear and the error bar increases dramatically. Still, all three velocities display at least one intermediate oxygen content value at which self-extinction clearly occurs, separating two domains where the sample is totally consumed for at least one oxygen content value.
Overall, pressure widens the gap between the two domains, and the burnout lengths in the secondary flame spread domain increase with the flow velocity. This suggests that the mechanism responsible for self-extinction at intermediate oxygen content values is amplified at high pressure, and at low flow velocity.

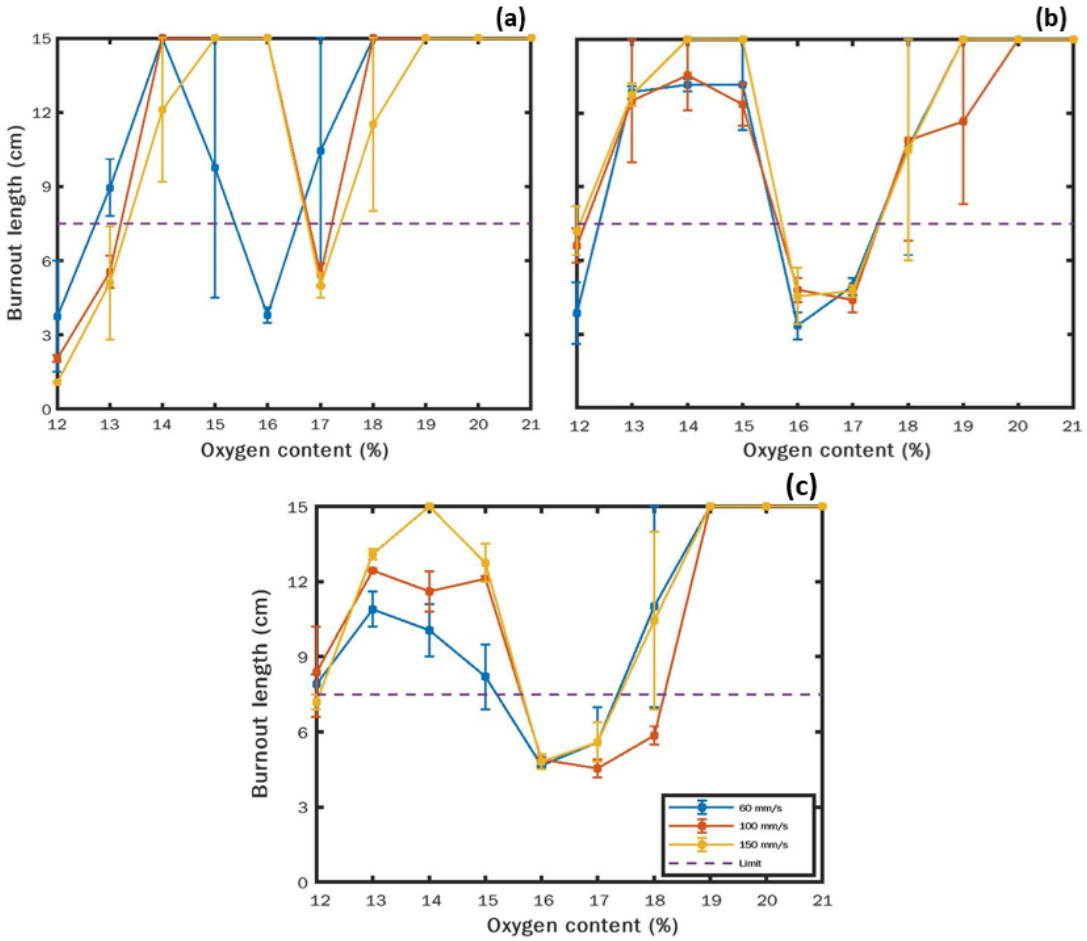

Figure A.2: Burnout length for experimented electric wires under a pressure of 50.7 (a), 101.3 (b), and 141.8 kPa for 3 velocities. The dashed line indicates the conceptual separation between an extinction case (below) and a spreading case (above) for each figure.

A.4 Effect of dripping and flame instability

To investigate the effect of dripping and flame instability, the following analysis concentrates on experimental data at a pressure of 101.3 kPa. The data selected are from the same set of experiments as in Fig. A.2 (b), i.e., three different flow rates at ambient pressure.

Figure A.3 (a) indicates the dripping frequency for each experiment. Because of the observed variations in spread rate and ultimate burnout lengths, the number of droplets reported is normalized by the length of the burnt wire. As a result, this number provides an illustration of the amount of fuel per unit length that is lost to dripping. At this stage, the size of the droplets is not considered, assuming that dripping occurs once a critical mass is attained in the molten phase, independently of any other parameter. For the maximum and minimum flow velocities (in yellow and blue, respectively), the number of droplets released is higher at low oxygen content than at high oxygen content, meaning that additional dripping heat loss is reported at low oxygen content. At high oxygen contents, the amount of droplets at the end of all the experiments lies between 4 and 6 droplets per cm, except for the condition under 60 mm/s flow velocity at 19% oxygen content. In the low oxygen content region, the amount of droplets is around 6 to 8 droplets per cm.

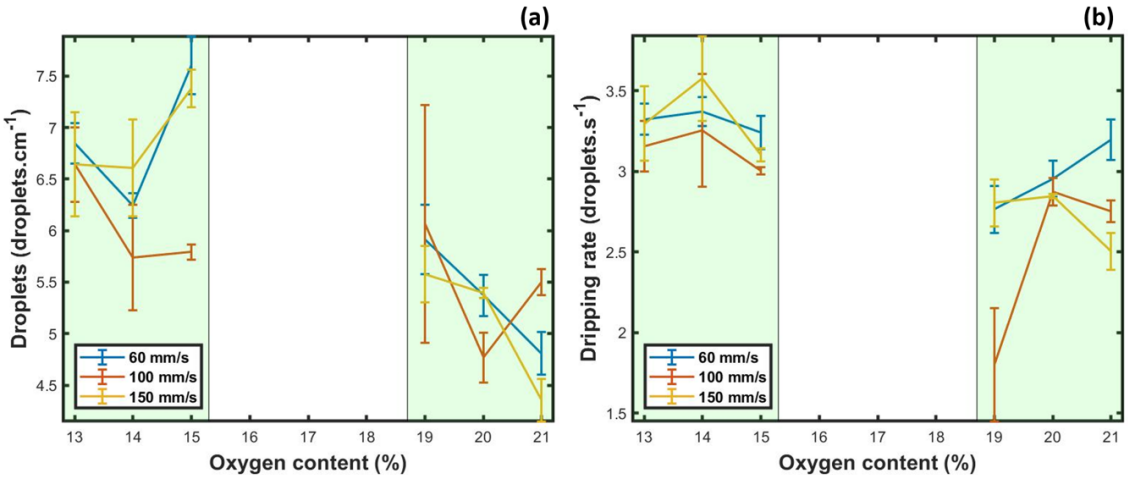

Figure A.3: Burnout length for experimented electric wires under a pressure of 50.7 (a), 101.3 (b), and 141.8 kPa for 3 velocities. The dashed line indicates the threshold between an extinction case (below) and a spreading case (above).

Similar conclusions can be drawn from the 100 mm/s experiments if only the averaging curve is considered, without the error bars.
The dripping rate (or frequency) presented in Fig. A.3 can be obtained for the same experiments. It is evaluated as the ratio between the number of droplets emitted and the time interval between the first and the last droplet. Results seem to indicate again that dripping is more pronounced at low oxygen levels, which goes against the initial assumptions.

A.5 Conclusion

The extinction limit of concurrent flame spread over the electric wire was assessed by varying the oxygen content under normal gravity. In the process, multiple flame spread domains were discovered. This phenomenon occurs equally at different flow velocities and pressures. The number of dripping droplets and the dripping rate were extracted, however the obsevations invalidate the initial hypothesis regarding the role of dripping. Beyond the question of standard tests, this issue raises an important question regarding fire safety at intermediate gravity levels, where dripping can become increasingly complex.
Following this first analysis, a new hypothesis was made that the appearance of this phenomenon could be due to the presence of the igniter upstream, acting as an anchor for the flame at low oxygen content thus preventing blowoff. To clarify the role of the igniter in this phenomenon, the current igniter needs to be modified to move away from the sample axis after ignition. Because these developments could not be carried out yet, this section has been moved to the Appendix.
If the occurrence of this phenomenon were to be attributed to the presence of the igniter, it means that interactions can dramatically change extinction limits, which must be considered when designing fire strategies that rely on oxygen depletion. On the other hand, if similar observations of disjointed flame spread domains are reported in the absence of flame anchoring on the igniter, then additional investigations are required to evaluate the relevance of existing standard tests.

Bibliography

[1] E. Seedhouse. *Lunar outpost*. Springer, 2009. (Cited on page 1.)

[2] C. Zhou, R. Chen, J. Xu, L. Ding, H. Luo, J. Fan, E. J. Chen, L. Cai, and B. Tang. In-situ construction method for lunar habitation: Chinese super mason. *Automation in Construction*, 104:66–79, 2019. (Cited on page 1.)

[3] J. Crusan. Habitation module. In *NASA Advisory Council, Human Exploration and Operations Committ*, 2016. (Cited on page 1.)

[4] A. Guibaud, G. Legros, J.-L. Consalvi, and J. Torero. Fire safety in spacecraft: Past incidents and deep space challenges. *Acta Astronautica*, 2022. (Cited on pages 1, 4, 5, and 6.)

[5] R. W. Bukowski and G. W. Mulholland. Smoke detector design and smoke properties. final report. Technical report, NBS Technical Note 973, National Bureau of Standards, Gaithersburg, MD, 1978. (Cited on pages 1 and 27.)

[6] R. W. Bukowski, R. D. Peacock, J. D. Averill, T. G. Cleary, N. P. Bryner, P. A. Reneke, et al. Performance of home smoke alarms, analysis of the response of several available technologies in residential fire settings. *Technical Note (NIST TN), National Institute of Standards and Technology, Gaithersburg, MD*, 2003. (Cited on pages 1 and 27.)

[7] M. E. Meyer, D. L. Urban, G. W. Mulholland, V. Bryg, Z. G. Yuan, G. A. Ruff, T. Cleary, and J. Yang. Evaluation of spacecraft smoke detector performance in the low-gravity environment. *Fire safety journal*, 98:74–81, 2018. (Cited on pages 1 and 37.)

[8] C. Harrison, S. Weaver, C. Bertelsen, E. Burgett, N. Hertel, and E. Grulke. Polyethylene/boron nitride composites for space radiation shielding. *Journal of Applied Polymer Science*, 109:2529–2538, 2008. (Cited on pages 4 and 32.)

[9] G. E. Apostolakis, I. Catton, T. Paulos, K. Paxton, and S. Jones. Findings of a review of spacecraft fire safety needs. Technical report, National Aeronautics and Space Administration, 1992. (Cited on page 4.)

[10] T. D. Swanson and G. C. Birur. Nasa thermal control technologies for robotic spacecraft. *Applied Thermal Engineering*, 23(9):1055 – 1065, 2003. ISSN 1359-4311. 12th International Heat Pipe Conference, 2002. (Cited on page 4.)

[11] H. R. Greider and J. R. Barton. Criteria for design of the mercury environmental control system, method of operation and results of manned system operation. *J Aviat Med*, 32:839–43, 1961. (Cited on page 5.)

[12] F. L. Thompson et al. National aeronautics and space administration, report of apollo 204 review board, washington, usa, 1967. (Cited on page 5.)

[13] R. W. Bricker. *Apollo Command Module Mockup Flammability Tests*. National Aeronautics and Space Administration, 1970. (Cited on page 7.)

[14] E. M. Roth. Space cabin atmospheres. In *Proceedings of the Fourth National Conference on the Peaceful Uses of Space*, 1964. (Cited on page 7.)

[15] J. R. Davis, R. Johnson, and J. Stepanek. *Fundamentals of aerospace medicine*. Lippincott Williams & Wilkins, 2008. (Cited on page 7.)

[16] Odour Flammability. Offgassing requirements and test procedures for materials in environments that support combustion, nasa specification, nasa handbook 8060.1, rev, 1974. (Cited on page 7.)

[17] R. Friedman, B. Jackson, and S. Olson. Testing and selection of fire-resistant materials for spacecraft use. Technical report, National Aeronautics and Space Administration, 2000. (Cited on page 7.)

[18] D. Mulville. Nasa std 6001: Flammability, odor, offgassing, and compatibility requirements and test procedures for materials in environments that support combustion. Technical report, National Aeronautics and Space Administration, 1998. (Cited on pages 7, 9, 28, and 99.)

[19] Y.M. Volynkin and V.I. Yazdovskiy. The first manned space flights, nasa technical note (translated) (n63-15658). Technical report, National Aeronautics and Space Administration, 1962. (Cited on page 7.)

[20] J. E. Brooker, D. L. Urban, and G. A Ruff. Iss destiny laboratory smoke detection model. Technical report, SAE Technical Paper, 2007. (Cited on page 8.)

[21] D. Urban, D. Griffin, G. Ruff, T. Cleary, J. Yang, G. Mulholland, and Z. G. Yuan. Detection of smoke from microgravity fires. *SAE Transactions*, 114:375–384, 2005. (Cited on page 8.)

[22] R. Friedman and K. R. Sacksteder. Fire behavior and risk analysis in spacecraft. In *Winter Annual Meeting of the American Society of Mechanical Engineers*, number E-4232, 1988. (Cited on page 8.)

[23] R. Friedman. Fire safety in the low-gravity spacecraft environment. Technical report, National Aeronautics and Space Administration, 1999. (Cited on page 8.)

[24] B. J. Bluth and M. Helppie. Soviet space stations as analogs. Technical report, National Aeronautics and Space Administration, 1986. (Cited on page 8.)

[25] G.M. Grechko. Speech at the national technical university of ukraine, May, 13th, 2011. (Cited on page 8.)

[26] Y. Batullin. Speech at the national technical university of ukraine. *Lyudi, RTSoft*, page 281, 2005. (Cited on page 8.)

[27] R. Friedman and D. L. Dietrich. Fire suppression in human-crew spacecraft. Technical report, National Aeronautics and Space Administration, 1991. (Cited on page 8.)

[28] P. O. Wieland. Designing for human presence in space: an introduction to environmental control and life support systems (eclss). Technical report, National Aeronautics and Space Administration, 2005. (Cited on pages 8 and 10.)

[29] P. Baker. *The Story of Manned Space Stations: An Introduction*. Springer Science & Business Media, 2007. (Cited on page 9.)

[30] K. Skinner and M. Emery. Fire in space-what do you do? Technical report, National Aeronautics and Space Administration, 2002. (Cited on page 9.)

[31] M. Darrach, A. Chutjian, B. Bornstein, A. Croonquist, V. Garkanian, V. Haemmerle, W. Heinrichs, J. Hofman, D. Karmon, J. Kenny, et al. On-orbit measurements of the iss atmosphere by the vehicle cabin atmosphere monitor. In *41st International Conference on Environmental Systems*, page 5214, 2011. (Cited on page 9.)

[32] NASA Exploration Atmospheres Working Group et al. Recommendations for exploration spacecraft internal atmospheres: the final report of the nasa exploration atmospheres working group. Technical report, National Aeronautics and Space Administration, 2010. (Cited on page 9.)

[33] S. L. Olson, P. V. Ferkul, and J. S. Tien. Near-limit flame spread over a thin solid fuel in microgravity. In *Symposium (International) on Combustion*, volume 22, pages 1213–1222. Elsevier, 1989. (Cited on pages 10, 21, and 31.)

[34] D. Thelen, N. Packham, and B. Wood. Significant incidents and close calls in human spaceflight. Technical report, Flight Safety Office, February 2009. (Cited on page 10.)

[35] P. Mudgett. Nasa johnson space center. Technical report, Personal Communication, April 2015. (Cited on page 10.)

[36] M. Kikuchi, O. Fujita, S. Takahashi, A. Ito, H. Torikai, Y. Nakamura, and S. L. Olson. Overview of the "solid combustion" experiment in the japanese experiment module "kibo" on the international space station. In *45th International Conference on Environmental Systems*, 2015. (Cited on pages 10, 31, and 35.)

[37] K. R. Daues. A history of spacecraft environmental control and life support systems. Technical report, National Aeronautics and Space Administration, 2006. (Cited on page 10.)

[38] D. Urban, G. Ruff, J. Brooker, T. Cleary, J. Yang, G. Mulholland, and Z. Yuan. Spacecraft fire detection: Smoke properties and transport in low-gravity. In *46th AIAA Aerospace Sciences Meeting and Exhibit*, page 806, 2008. (Cited on page 10.)

[39] A. R. Donnarumma and T. Hoppenbrouwers. Operation training for ground support personnel: Fire, strategy and hardware. Technical report, European Space Agency, 2019. (Cited on page 10.)

[40] T. S Limero, S. W. Beck, and J. T. James. The portable monitor for measuring combustion products aboard the international space station. Technical report, SAE Technical Paper, 2002. (Cited on page 10.)

[41] X. Wang, H. Zhou, W. P. Arnott, M. E. Meyer, S. Taylor, H. Firouzkouhi, H. Moosmüller, J. C. Chow, and J. G. Watson. Characterization of smoke for spacecraft fire safety. *Journal of Aerosol Science*, 136:36–47, 2019. (Cited on page 10.)

[42] S. Kopylov, N. V. Smirnov, and L. T. Tanklevsky. Fire extinguishers for manned spacecraft. *Acta Astronautica*, 109:225–230, 2015. (Cited on page 10.)

[43] D. El Sherif and J. C. Knox. International space station carbon dioxide removal assembly (iss cdra) concepts and advancements. Technical report, SAE Technical Paper, 2005. (Cited on page 11.)

[44] P. V. Ferkul and S. L. Olson. Zero-gravity centrifuge used for the evaluation of material flammability in lunar gravity. *Journal of Thermophysics and Heat Transfer*, 25:457–461, 2011. (Cited on pages 11, 13, and 116.)

[45] SL Olson and P. Ferkul. Evaluating material flammability in microgravity and martian gravity compared to the nasa standard normal gravity test. In *42nd International Conference on Environmental Systems*, page 3492, 2012. (Cited on pages 11, 13, and 73.)

[46] K. R. Sacksteder and J. S. Tien. Buoyant downward diffusion flame spread and extinction in partial-gravity accelerations. In *Symposium (International) on Combustion*, volume 25, pages 1685–1692. Elsevier, 1994. (Cited on pages 12, 14, 31, and 73.)

[47] I. I. Feier, H. Y. Shih, K. R. Sacksteder, and J. S. Tien. Upward flame spread over thin solids in partial gravity. *Proceedings of the Combustion Institute*, 29:2569–2577, 2002. (Cited on pages 12, 21, and 116.)

[48] R. Schaezler, A. Ghariani, A. Cook, and D. Leonard. Trending of overboard leakage of iss cabin atmosphere. In *41st International Conference on Environmental Systems*, page 5149, 2011. (Cited on page 12.)

[49] D. L. Urban, P. Ferkul, S. Olson, G. A. Ruff, J. Easton, J. S. T'ien, Y. T. Liao, C. Li, C. Fernandez-Pello, J. L. Torero, G. Legros, C. Eigenbrod, N. Smirnov, O. Fujita, S. Rouvreau, B. Toth, and G. Jomaas. Flame spread: Effects of microgravity and scale. *Combustion and Flame*, 199:168 – 182, 2019. ISSN 0010-2180. (Cited on pages 12 and 30.)

[50] W. Liu, Z. Liu, J. Chen, and Y. Peng. Selection of spacecraft atmospheric pressure regime for manned lunar exploration mission. *Manned Spaceflight*, 22:687–693, 2016. (Cited on page 12.)

[51] R. English, R. Benson, V. Bailey, and C. Barnes. Apollo experience report: Protection against radiation. Technical report, National Aeronautics and Space Administration, 1973. (Cited on page 12.)

[52] A. Sandinge, P. Blomqvist, A. Dederichs, and F. Markert. The necessity of accelerated ageing in fire performance assessments of composite materials. *Safety science*, 141:105358, 2021. (Cited on page 12.)

[53] J. Lekan. Microgravity research in nasa ground-based facilities. In *27th Aerospace Sciences Meeting*, page 236, 1989. (Cited on page 13.)

[54] X. Zhang, L. Yuan, W. Wu, L. Tian, and K. Yao. Some key technics of drop tower experiment device of national microgravity laboratory (china)(nmlc). *Science in China Ser. E Engineering & Materials Science*, 48:305–316, 2005. (Cited on page 13.)

[55] H. D. Ross. *Microgravity combustion: fire in free fall*. Elsevier, 2001. (Cited on pages 13, 14, 16, 18, 19, 28, and 51.)

[56] W. R. Corliss. *NASA sounding rockets, 1958-1968: A historical summary*. NASA History Series, 1971. (Cited on page 14.)

[57] C. K. Law and G. M. Faeth. Opportunities and challenges of combustion in microgravity. *Progress in Energy and Combustion Science*, 20(1):65–113, 1994. (Cited on page 14.)

[58] S. Olson, U. Hegde, S. Bhattacharjee, J.L. Deering, L. Tang, and R. A Altenkirch. Sounding rocket microgravity experiments elucidating diffusive and radiative transport effects on flame spread over thermally thick solids. *Combustion science and technology*, 176(4):557–584, 2004. (Cited on page 14.)

[59] T. Vietoris, J. L. Ellzey, P. Joulain, S. N. Mehta, and J. L. Torero. Laminar diffusion flame in microgravity: the results of the minitexus 6 sounding rocket experiment. *Proceedings of the Combustion Institute*, 28:2883–2889, 2000. (Cited on page 14.)

[60] W. Hu and Q. Kang. *Physical Science Under Microgravity: Experiments on Board the SJ-10 Recoverable Satellite*. Springer, 2019. (Cited on page 15.)

[61] R. Ulises and J. Grunde. A historical overview of experimental solid combustion research in microgravity. *Acta Astronautica*, 2022. (Cited on pages 15, 92, and 116.)

[62] W. Kong, K. Wang, W. Xia, and S. Xue. Ignition and combustion characteristics of overloaded wire insulations under weakly buoyancy or microgravity environments. In *Physical Science Under Microgravity: Experiments on Board the SJ-10 Recoverable Satellite*, pages 191–235. Springer, 2019. (Cited on page 15.)

[63] F. Zhu, Z. Lu, S. Wang, and Y. Yin. Microgravity diffusion flame spread over a thick solid in step-changed low-velocity opposed flows. *Combustion and Flame*, 205:55–67, 2019. (Cited on page 15.)

[64] S. Wang and Y. Yin. Microgravity smoldering combustion experiments aboard the china recoverable satellite sj-8. *Journal of Space Science*, 28(20080105):22, 2008. (Cited on page 15.)

[65] L. Johnson and M. Herrmann. International space station electrodynamic tether reboost. In *AIP Conference Proceedings*, volume 458, pages 490–495. AIP, 1999. (Cited on page 15.)

[66] R. DeLombard, K. Hrovat, E. Kelly, and K. McPherson. Microgravity environment on the international space station. In *42nd AIAA Aerospace Sciences Meeting and Exhibit*, page 125, 2004. (Cited on page 15.)

[67] K. Jules, K. McPherson, K. Hrovat, E. Kelly, and T. Reckart. A status report on the characterization of the microgravity environment of the international space station. *Acta astronautica*, 55(3-9):335–364, 2004. (Cited on page 15.)

[68] G. Jomaas, J. L. Torero, C. Eigenbrod, J. Niehaus, S. L Olson, P. V. Ferkul, G. Legros, A. C. Fernandez-Pello, A. J. Cowlard, and S. Rouvreau. Fire safety in space–beyond flammability testing of small samples. *Acta Astronautica*, 109:208–216, 2015. (Cited on pages 15 and 30.)

[69] M. J. Hurley, D. T. Gottuk, J. R. Hall Jr, K. Harada, E. D. Kuligowski, M. Puchovsky, J. M. Watts Jr, and C. J. Wieczorek. *SFPE handbook of fire protection engineering*. Springer, 2015. (Cited on page 16.)

[70] G. M. Faeth. Current status of droplet and liquid combustion. In *Energy and combustion science*, pages 149–182. Elsevier, 1979. (Cited on page 16.)

[71] S. P. Burke and T. Schumann. Diffusion flames. *Industrial & Engineering Chemistry*, 20(10): 998–1004, 1928. (Cited on page 16.)

[72] C. K. Law. *Combustion physics*. Cambridge university press, 2010. (Cited on page 16.)

[73] N. Peters. Laminar diffusion flamelet models in non-premixed turbulent combustion. *Progress in energy and combustion science*, 10(3):319–339, 1984. (Cited on page 16.)

[74] R. W. Bilger. Turbulent jet diffusion flames. In *Energy and Combustion Science*, pages 109–131. Elsevier, 1979. (Cited on page 16.)

[75] W. R. Hawthorne, D. S. Weddell, and H. C. Hottel. Third symposium on combustion and flame and explosion phenomena. *The Williams and Wilkins Co., Baltimore, Maryland*, pages 266–288, 1949. (Cited on page 16.)

[76] D. B. Spalding. *Combustion and mass transfer*. Pergamon Press, 1979. (Cited on page 17.)

[77] S. Ostrach. Natural convection in enclosures. *Journal of Heat Transfer*, 110(4b):1175–1190, 1988. (Cited on page 17.)

[78] E. M. Purcell. Life at low reynolds number. *American journal of physics*, 45(1):3–11, 1977. (Cited on page 17.)

[79] T. J. Ohlemiller. Smoldering combustion. *SFPE handbook of fire protection engineering*, 3, 2002. (Cited on page 18.)

[80] G. Rein. Smouldering combustion phenomena in science and technology. In *International Review of Chemical Engineering IRECHE-Praise Worthy Prize*, 2009. (Cited on page 18.)

[81] L. M. McKenzie, W. M. Hao, G. N. Richards, and D. E. Ward. Measurement and modeling of air toxins from smoldering combustion of biomass. *Environmental Science & Technology*, 29(8): 2047–2054, 1995. (Cited on page 18.)

[82] T. Yamazaki, T. Matsuoka, Y. Li, and Y. Nakamura. Applicability of a low-pressure environment to investigate smoldering behavior under microgravity. *Fire Technology*, 56(1):209–228, 2020. (Cited on page 18.)

[83] J. L. Torero, A. C. Fernandez-Pello, and D. Urban. Experimental observations of the effect of gravity changes on smoldering combustion. *AIAA journal*, 32:991–996, 1994. (Cited on page 18.)

[84] S. L. Olson, H. R. Baum, and T. Kashiwagi. Finger-like smoldering over thin cellulosic sheets in microgravity. In *Symposium (International) on Combustion*, pages 2525–2533. Elsevier, 1998. (Cited on page 18.)

[85] T. Faravelli, G. Bozzano, C. Scassa, M. Perego, S. Fabini, E. Ranzi, and M. Dente. Gas product distribution from polyethylene pyrolysis. *Journal of Analytical and Applied Pyrolysis*, 52(1): 87–103, 1999. (Cited on page 18.)

[86] J. S.T'ien, H. Shih, C. B. Jiang, H. D.Ross, F. J. Miller, C. Fernandez-Pello, J. L. Torero, and D. Walther. Mechanisms of flame spread and smolder wave propagation. *Microgravity Combustion: Fire in Free Fall*, page 299, 2001. (Cited on page 19.)

[87] J. N. De Ris. Spread of a laminar diffusion flame. In *Symposium (International) on Combustion*, volume 12, pages 241–252. Elsevier, 1969. (Cited on pages 19 and 21.)

[88] A. C. Fernandez-Pello and T. Hirano. Controlling mechanisms of flame spread. *Combustion Science and Technology*, 32(1-4):1–31, 1983. (Cited on pages 20 and 21.)

[89] I. S. Wichman. Theory of opposed-flow flame spread. *Progress in Energy and Combustion Science*, 18:553–593, 1992. (Cited on page 20.)

[90] A. C. Fernandez-Pello, S. R. Ray, and I. Glassman. Flame spread in an opposed forced flow: the effect of ambient oxygen concentration. In *symposium (international) on combustion*, volume 18, pages 579–589. Elsevier, 1981. (Cited on page 21.)

[91] M. A. Delichatsios. Exact solution for the rate of creeping flame spread over thermally thin materials. *Combustion Science and Technology*, 44(5-6):257–267, 1986. (Cited with the first apparition of previous citation.)

[92] S. Bhattacharjee, J. West, and R. A. Altenkirch. Determination of the spread rate in opposed-flow flame spread over thick solid fuels in the thermal regime. In *Symposium (International) on Combustion*, volume 26, pages 1477–1485. Elsevier, 1996. (Cited with the first apparition of previous citation.)

[93] S. Bhattacharjee, R. Ayala, K. Wakai, and S. Takahashi. Opposed-flow flame spread in microgravity-theoretical prediction of spread rate and flammability map. *Proceedings of the Combustion Institute*, 30(2):2279–2286, 2005. (Cited on page 20.)

[94] K. R. Sacksteder. The implications of experimentally controlled gravitational accelerations for combustion science. In *Proc. Combust. Inst*, volume 23, page 1589. Elsevier, 1990. (Cited on pages 20, 21, and 56.)

[95] H. Bedir, J. S. T'ien, and H. S. Lee. Comparison of different radiation treatments for a one-dimensional diffusion flame. *Combustion Theory and Modelling*, 1:395–404, 1997. (Cited on page 21.)

[96] J. S. Tien. Diffusion flame extinction at small stretch rates: the mechanism of radiative loss. *Combustion and flame*, 65(1):31–34, 1986. (Cited on pages 21 and 29.)

[97] C. H. Chen and J. S. T'ien. Diffusion flame stabilization at the leading edge of a fuel plate. *Combustion Science and Technology*, 50(4-6):283–306, 1986. (Cited on pages 21 and 22.)

[98] S. L. Olson. Mechanisms of microgravity flame spread over a thin solid fuel: oxygen and opposed flow effects. *Combustion Science and Technology*, 76:233–249, 1991. (Cited on pages 21 and 31.)

[99] F. A. Lastrina, R. S. Magee, and R. F. McAlevy III. Flame spread over fuel beds: solid-phase energy considerations. In *Symposium (International) on Combustion*, volume 13, pages 935–948. Elsevier, 1971. (Cited on page 21.)

[100] H. W. Emmons. The film combustion of liquid fuel. *ZAMM-Journal of Applied Mathematics and Mechanics/Zeitschrift für Angewandte Mathematik und Mechanik*, 36(1-2):60–71, 1956. (Cited on page 21.)

[101] T. M. Shih and P. J. Pagni. Laminar mixed-mode, forced and free, diffusion flames. *Journal of Heat Transfer*, 100:253–259, 1978. (Cited on page 22.)

[102] J. L. Torero, T. Vietoris, G. Legros, and P. Joulain. Estimation of a total mass transfer number from the standoff distance of a spreading flame. *Combustion Science and Technology*, 174: 187–203, 2002. (Cited with the first apparition of previous citation.)

[103] A. S. Rangwala, S. G. Buckley, and J. L. Torero. Analysis of the constant b-number assumption while modeling flame spread. *Combustion and Flame*, 152(3):401–414, 2008. (Cited with the first apparition of previous citation.)

[104] Y. Pizzo, J. L. Consalvi, and B. Porterie. A transient pyrolysis model based on the b-number for gravity-assisted flame spread over thick pmma slabs. *Combustion and Flame*, 156(9): 1856–1859, 2009. (Cited on page 22.)

[105] A. C. Fernandez-Pello. Flame spread in a forward forced flow. *Combustion and Flame*, 36: 63–78, 1979. (Cited on page 22.)

[106] A. E. Frey Jr and J. S. Tien. A theory of flame spread over a solid fuel including finite-rate chemical kinetics. *Combustion and Flame*, 36:263–289, 1979. (Cited on page 22.)

[107] C. Di Blasi, S. Crescitelli, and G. Russo. Near limit flame spread over thick fuels in a concurrent forced flow. *Combustion and flame*, 72(2):205–215, 1988. (Cited on page 22.)

[108] M. A. Delichatsios. Flame heights in turbulent wall fires with significant flame radiation. *Combustion Science and Technology*, 39(1-6):195–214, 1984. (Cited on page 22.)

[109] J. L. De Ris, P. K. Wu, and G. Heskestad. Radiation fire modeling. *Proceedings of the Combustion Institute*, 28:2751–2759, 2000. (Cited on page 22.)

[110] J. Xi, G. Yang, J. Cai, and Z. Gu. A review of recent research results on soot: The formation of a kind of carbon-based material in flames. *Frontiers in Materials*, 8:695485, 2021. (Cited on page 23.)

[111] I. Glassman. Soot formation in combustion processes. In *Symposium (international) on combustion*, volume 22, pages 295–311. Elsevier, 1989. (Cited on pages 22 and 25.)

[112] M. Frenklach. Reaction mechanism of soot formation in flames. *Physical chemistry chemical Physics*, 4(11):2028–2037, 2002. (Cited on pages 22 and 23.)

[113] D. R. Tree and K. I. Svensson. Soot processes in compression ignition engines. *Progress in Energy and Combustion Science*, 33:272–309, 2007. (Cited on pages 22 and 24.)

[114] S. C. Graham, J. B. Homer, and J. L. Rosenfeld. The formation and coagulation of soot aerosols generated by the pyrolysis of aromatic hydrocarbons. *Proceedings of the Royal Society of London. A. Mathematical and Physical Sciences*, 344(1637):259–285, 1975. (Cited on page 22.)

[115] B. S. Haynes and H. G. Wagner. Soot formation. *Progress in energy and combustion science*, 7: 229–273, 1981. (Cited on page 23.)

[116] William Bartok and Adel F Sarofim. Fossil fuel combustion: a source book. 1991. (Cited on page 23.)

[117] M. D. Smooke, M. B. Long, B. C. Connelly, M. B. Colket, and R. J. Hall. Soot formation in laminar diffusion flames. *Combustion and Flame*, 143(4):613–628, 2005. (Cited on page 23.)

[118] P. B. Sunderland, S. Mortazavi, G. M. Faeth, and D. L. Urban. Laminar smoke points of nonbuoyant jet diffusion flames. *Combustion and Flame*, 96:97–103, 1994. (Cited on page 24.)

[119] A. D. Eisner and D. E. Rosner. Experimental studies of soot particle thermophoresis in nonisothermal combustion gases using thermocouple response techniques. *Combustion and Flame*, 61(2):153–166, 1985. (Cited on page 24.)

[120] P. E. Best, P. L. Chien, R. M. Carangelo, P. R. Solomon, M. Danchak, and I. Ilovici. Tomographic reconstruction of ft-ir emission and transmission spectra in a sooting laminar diffusion flame: species concentrations and temperatures. *Combustion and Flame*, 85(3-4):309–318, 1991. (Cited on page 24.)

[121] P. M. Robitaille. Blackbody radiation and the carbon particle. *Progress in Physics*, 3:36, 2008. (Cited on page 24.)

[122] W. Y. Chan and J. S. T'ien. An experiment on spontaneous flame oscillation prior to extinction. *Combustion Science and Technology*, 18(3-4):139–143, 1978. (Cited on page 24.)

[123] I. S. Wichman, S. L. Olson, F. J. Miller, and A. Hariharan. Fire in microgravity. *Amer. Sci*, 104: 44–51, 2016. (Cited on page 24.)

[124] F. B. Carleton and F. J. Weinberg. Electric field-induced flame convection in the absence of gravity. *Nature*, 330(6149):635, 1987. (Cited on page 25.)

[125] D. L. Urban, Z. G. Yuan, P. B. Sunderland, K. C. Lin, Z. Dai, and G. M. Faeth. Smoke-point properties of non-buoyant round laminar jet diffusion flames. *Proceedings of the Combustion Institute*, 28:1965–1972, 2000. (Cited on page 25.)

[126] K. T. Dotson, P. B. Sunderland, Z. G. Yuan, and D. L. Urban. Laminar smoke points of coflowing flames in microgravity. *Fire Safety Journal*, 46(8):550 – 555, 2011. ISSN 0379-7112. (Cited on page 26.)

[127] J. H. Kent and H. G. Wagner. Who do diffusion flames emit smoke. *Combustion science and technology*, 41(5-6):245–269, 1984. (Cited on page 25.)

[128] D. L. Urban, Z. G. Yuan, P. B. Sunderland, G. T. Linteris, J. E. Voss, K. C. Lin, Z. Dai, K. Sun, and G. M. Faeth. Structure and soot properties of nonbuoyant ethylene/air laminar jet diffusion flames. *AIAA journal*, 36:1346–1360, 1998. (Cited on pages 25, 27, and 38.)

[129] G. H. Markstein. Relationship between smoke point and radiant emission from buoyant turbulent and laminar diffusion flames. In *Symposium (International) on Combustion*, pages 1055–1061. Elsevier, 1985. (Cited on page 25.)

[130] F. G. Roper and C. Smith. Soot escape from laminar air-starved hydrocarbon flames. *Combustion and Flame*, 36:125–138, 1979. (Cited on page 25.)

[131] K. C. Lin, G. M. Faeth, P. B. Sunderland, D. L. Urban, and Z. G. Yuan. Shapes of nonbuoyant round luminous hydrocarbon/air laminar jet diffusion flames. *Combustion and Flame*, 116:415 – 431, 1999. ISSN 0010-2180. (Cited on page 25.)

[132] Y. R. Sivathanu and G. M. Faeth. Soot volume fractions in the overfire region of turbulent diffusion flames. *Combustion and Flame*, 81(2):133–149, 1990. (Cited on page 25.)

[133] O. A. Ezekoye and Z. Zhang. Soot oxidation and agglomeration modeling in a microgravity diffusion flame. *Combustion and Flame*, 110(1-2):127–139, 1997. (Cited on page 26.)

[134] O. Fujita and K. Ito. Observation of soot agglomeration process with aid of thermophoretic force in a microgravity jet diffusion flame. *Experimental Thermal and Fluid Science*, 26(2-4): 305–311, 2002. (Cited on pages 27 and 37.)

[135] J. C. Ku, D. W. Griffin, P. S. Greenberg, and J. Roma. Brief communication: Buoyancy-induced differences in soot morphology. *Combustion and Flame*, 110:216–218, 1995. (Cited on pages 27, 37, and 38.)

[136] B. Konsur, Co. M. Megaridis, and D. W. Griffin. Fuel preheat effects on soot-field structure in laminar gas jet diffusion flames burning in 0-g and 1-g. *Combustion and flame*, 116(3):334–347, 1999. (Cited on pages 27 and 38.)

[137] D. B. Hirsch, J. H. Williams, S. A. Harper, H. Beeson, and M. D. Pedley. Oxygen concentration flammability thresholds of selected aerospace materials considered for the constellation program. *2nd IAASS Conference Space Safety in Global World*, 2, 2007. (Cited on page 28.)

[138] S. L. Olson and P. V. Ferkul. Microgravity flammability boundary for pmma rods in axial stagnation flow: experimental results and energy balance analyses. *Combustion and Flame*, 180:217–229, 2017. (Cited on pages 29 and 30.)

[139] J. L. Cordova, J. Ceamanos, and A. C. Fernandez-Pello. Piloted ignition of a radiatively heated solid combustible material in a forced oxidizer flow. Technical report, American Society of Mechanical Engineers, 1998. (Cited on page 28.)

[140] J. L. Cordova, J. Ceamanos, A. C. Fernandez-Pello, R. T. Long, J. L. Torero, and J. G. Quintiere. Flow effects on the flammability diagrams of solid fuels. In *International Microgravity Combustion Workshop*, volume 4, pages 405–410, 1997. (Cited on page 29.)

[141] S. M. Olenick. *Validation of the Forced Flow Ignition and Flame Spread Test (FIST), A Reduced Scale Test Apparatus, to Assess Material Flammability for Micro-Gravity Environments*. PhD thesis, University of Maryland, College Park, 1999. (Cited on page 29.)

[142] O. Fujita, T. Kyono, Y. Kido, H. Ito, and Y. Nakamura. Ignition of electrical wire insulation with short-term excess electric current in microgravity. *Proceedings of the Combustion Institute*, 33(2):2617–2623, 2011. (Cited on pages 29 and 31.)

[143] J. S. Tien. The possibility of a reversal of material flammability ranking from normal gravity to microgravity. *Combustion and Flame*, 80(3):355–357, 1990. (Cited on page 29.)

[144] S. L. Olson, G. A. Ruff, and J. M. Fletcher. Microgravity flame spread in exploration atmospheres: pressure, oxygen, and velocity effects on opposed and concurrent flame spread. In *38th International Conference on Environmental Systems*, 2008. (Cited on page 29.)

[145] S. Bhattacharjee, M. Laue, L. Carmignani, P. Ferkul, and S. Olson. Opposed-flow flame spread: a comparison of microgravity and normal gravity experiments to establish the thermal regime. *Fire Safety Journal*, 79:111–118, 2016. (Cited on page 30.)

[146] S. Bhattacharjee, A. Simsek, S. Olson, and P. Ferkul. The critical flow velocity for radiative extinction in opposed-flow flame spread in a microgravity environment: A comparison of experimental, computational, and theoretical results. *Combustion and Flame*, 163:472–477, 2016. (Cited on page 30.)

[147] C. Fernandez-Pello. Material ignition and suppression test (mist) in space exploration atmospheres, summary of research. Technical report, National Aeronautics and Space Administration, 2013. (Cited on page 30.)

[148] S. Link, X. Huang, C. Fernandez-Pello, S. Olson, and P. Ferkul. The effect of gravity on flame spread over pmma cylinders. *Scientific reports*, 8:120, 2018. (Cited on page 30.)

[149] S. L. Olson and P. V. Ferkul. Microgravity flammability of pmma rods in concurrent flow. In *U.S. National Combustion Meeting*, volume 9, 2015. (Cited on page 30.)

[150] G. A. Ruff, D. L. Urban, A. C. Fernandez-Pello, J. S. T'ien, J. L. Torero, G. Legros, C. Eigenbrod, N. Smirnov, O. Fujita, and A. J. Cowlard. Spacecraft fire experiment (saffire) development status. In *44th International Conference on Environmental Systems*. Texas Tech University Libraries, 2014. (Cited on page 30.)

[151] W. Schoren, G. A. Ruff, and D. L. Urban. The spacecraft fire experiment (saffire)-objectives, development and status. In *International Association for the Advancement of Space Safety Conference*, volume 8, 2016. (Cited on page 30.)

[152] David Urban, Gary Ruff, Paul Ferkul, John Easton, Jay Owens, Sandra Olson, Marit Meyer, Claire Fortenberry, John Brooker, John Graf, Michael Casteel, Grunde Jomaas, Balazs Toth, C. Eigenbrod, James T'ien, Ya-Ting Liao, A. Fernandez-Pello, Florian Meyer, Guillaume Legros, and Osamu Fujita. Fire safety implications of preliminary results from saffire iv and v experiments on large scale spacecraft fires. In *50th Int. Conf. Environ. Syst*, 07 2021. (Cited on page 30.)

[153] N. Shigeta, H. Ito, and O. Fujita. Ignition limit of electric wire insulation with continuous excess current in several microgravity periods. In *43rd International Conference on Environmental Systems*, page 3387, 2013. (Cited on page 31.)

[154] O. Fujita. Introduction of jaxa priority project flare utilizing iss/" kibo". *International Journal of Microgravity Science and Application*, 32(4):3204021–5, 2015. (Cited on page 31.)

[155] Y. Takano, O. Fujita, N. Shigeta, Y. Nakamura, and H. Ito. Ignition limits of short-term overloaded electric wires in microgravity. *Proceedings of the Combustion Institute*, 34(2):2665–2673, 2013. (Cited on page 31.)

[156] M. Kikuchi, M. Nokura, T. Suzuki, A. Hosogai, M. Katsuta, H. Saruwatari, Y. Nakamura, S. Yamamoto, Y. Goto, and Y. Sakaino. Development status of the solid combustion experiment module for material flammability experiments on the iss/kibo. In *46th International Conference on Environmental Systems*, 2016. (Cited on page 31.)

[157] S. Takahashi and K. Maruta. Prediction of limiting oxygen concentration of thin materials in microgravity. *Transactions of the Japan Society for Aeronautical and Space Sciences, Aerospace Technology Japan*, 16(1):28–34, 2018. (Cited with the first apparition of previous citation.)

[158] M. Nagachi, F. Mitsui, J. M. Citerne, H. Dutilleul, A. Guibaud, G. Jomaas, G. Legros, N. Hashimoto, and O. Fujita. Can a spreading flame over electric wire insulation in concurrent flow achieve steady propagation in microgravity? *Proceedings of the Combustion Institute*, 37:4155–4162, 2019. (Cited with the first apparition of previous citation.)

[159] M. Nagachi, F. Mitsui, J. M. Citerne, H. Dutilleul, A. Guibaud, G. Jomaas, G. Legros, N. Hashimoto, and O. Fujita. Effect of ignition condition on the extinction limit for opposed flame spread over electrical wires in microgravity. *Fire Technology*, pages 1–20, 2019. (Cited on pages 31 and 49.)

[160] P. S. Greenberg, K. R. Sacksteder, and T. Kashiwagi. Wire insulation flammability experiment: Usml-1 one year post mission summary. *Joint Launch, One Year Science Review of USML-1 and USMP-1 with the Microgravity Measurement Group*, 2:631–656, 1994. (Cited on page 31.)

[161] Y. Kobayashi, X. Huang, S. Nakaya, M. Tsue, and C. Fernandez-Pello. Flame spread over horizontal and vertical wires: The role of dripping and core. *Fire Safety Journal*, 91:112–122, 2017. (Cited on pages 31, 40, and 75.)

[162] K. Shimizu, M. Kikuchi, N. Hashimoto, and O. Fujita. A numerical and experimental study of the ignition of insulated electric wire with long-term excess current supply under microgravity. *Proceedings of the Combustion Institute*, 36(2):3063–3071, 2017. (Cited on page 31.)

[163] O. Fujita, M. Kikuchi, K. Ito, and K. Nishizawa. Effective mechanisms to determine flame spread rate over ethylene-tetrafluoroethylene wire insulation: discussion on dilution gas effect based on temperature measurements. *Proceedings of the Combustion Institute*, 28(2): 2905–2911, 2000. (Cited on page 31.)

[164] O. Fujita, K. Nishizawa, and K. Ito. Effect of low external flow on flame spread over polyethylene-insulated wire in microgravity. *Proceedings of the Combustion Institute*, 29(2): 2545–2552, 2002. (Cited with the first apparition of previous citation.)

[165] M. K. Kim, S. H. Chung, and O. Fujita. Effect of ac electric fields on flame spread over electrical wire. *Proceedings of the Combustion Institute*, 33(1):1145–1151, 2011. (Cited with the first apparition of previous citation.)

[166] M. Nagachi, J. M. Citerne, H. Dutilleul, A. Guibaud, G. Jomaas, G. Legros, N. Hashimoto, and O. Fujita. Effect of ambient pressure on the extinction limit for opposed flame spread over an electrical wire in microgravity. *Proceedings of the Combustion Institute*, 38(3):4767–4774, 2021. (Cited on pages 31 and 97.)

[167] S. Takahashi, H. Ito, Y. Nakamura, and O. Fujita. Extinction limits of spreading flames over wires in microgravity. *Combustion and Flame*, 160(9):1900–1902, 2013. (Cited on pages 31, 74, and 78.)

[168] K. Mizutani, K. Miyamoto, N. Hashimoto, Y. Konno, and O. Fujita. Limiting oxygen concentration trend of etfe-insulated wires under microgravity. *Int J Microgravity Sci Appl*, 35:350104, 2018. (Cited with the first apparition of previous citation.)

[169] A. F. Osorio, K. Mizutani, C. Fernandez-Pello, and O. Fujita. Microgravity flammability limits of etfe insulated wires exposed to external radiation. *Proceedings of the Combustion Institute*, 35(3):2683–2689, 2015. (Cited on page 31.)

[170] J. W. Shin, J. W. Lee, S. Yu, B. K. Baek, J. P. Hong, Y. Seo, W. N. Kim, S. M. Hong, and C. M. Koo. Polyethylene/boron-containing composites for radiation shielding. *Thermochimica acta*, 585:5–9, 2014. (Cited on page 32.)

[171] J. M. Citerne, H. Dutilleul, K. Kizawa, M. Nagachi, O. Fujita, M. Kikuchi, G. Jomaas, S. Rouvreau, J. L. Torero, and G. Legros. Fire safety in space–investigating flame spread interaction over wires. *Acta Astronautica*, 126:500–509, 2016. (Cited on pages 33 and 44.)

[172] A. Guibaud, J. M. Citerne, J. L. Consalvi, O. Fujita, J. L. Torero, and G. Legros. Experimental evaluation of flame radiative feedback: methodology and application to opposed flame

spread over coated wires in microgravity. *Fire Technology*, pages 1–23, 2019. (Cited on pages 34, 36, 40, and 54.)

[173] A. Guibaud. *Flame spread in microgravity environment: influence of ambient flow conditions*. PhD thesis, Sorbonne université, 2019. (Cited on pages 34, 35, 44, 47, and 48.)

[174] H. Ito, O. Fujita, and K. Ito. Agglomeration of soot particles in diffusion flames under microgravity. *Combustion and Flame*, 99(2):363–370, 1994. (Cited on page 37.)

[175] M. Y. Choi, A. Hamins, G. W. Mulholland, and T. Kashiwagi. Simultaneous optical measurement of soot volume fraction and temperature in premixed flames. *Combustion and flame*, 99 (1):174–186, 1994. (Cited on page 37.)

[176] H. A. Michelsen, C. Schulz, G. J. Smallwood, and S. Will. Laser-induced incandescence: Particulate diagnostics for combustion, atmospheric, and industrial applications. *Progress in Energy and Combustion Science*, 51:2–48, 2015. (Cited on page 37.)

[177] M. Y. Choi, G. W. Mulholland, A. Hamins, and T. Kashiwagi. Comparisons of the soot volume fraction using gravimetric and light extinction techniques. *Combustion and Flame*, 102(1-2): 161–169, 1995. (Cited on page 37.)

[178] C. M. Sorensen. Light scattering by fractal aggregates: a review. *Aerosol Science & Technology*, 35(2):648–687, 2001. (Cited on page 37.)

[179] J. Reimann and S. Will. Optical diagnostics on sooting laminar diffusion flames in microgravity. *Microgravity-Science and Technology*, 16(1-4):333–337, 2005. (Cited on page 37.)

[180] U. O. Koylu and G. M. Faeth. Radiative properties of flame-generated soot. *Journal of heat transfer*, 115(2):409–417, 1993. (Cited on pages 37, 59, and 64.)

[181] T. L. Farias, U. O. Köylü, and M. G. Carvalho. Range of validity of the rayleigh–debye–gans theory for optics of fractal aggregates. *Applied Optics*, 35(33):6560–6567, 1996. (Cited on pages 37 and 64.)

[182] R. A. Dobbins and C. M. Megaridis. Morphology of flame-generated soot as determined by thermophoretic sampling. *Langmuir*, 3(2):254–259, 1987. (Cited on page 38.)

[183] U. O. Koylu, C. S. McEnally, D. E. Rosner, and L. D. Pfefferle. Simultaneous measurements of soot volume fraction and particle size/microstructure in flames using a thermophoretic sampling technique. *Combustion and Flame*, 110(4):494–507, 1997. (Cited on page 38.)

[184] M. Kholghy, M. Saffaripour, C. Yip, and M. J. Thomson. The evolution of soot morphology in a laminar coflow diffusion flame of a surrogate for jet a-1. *Combustion and Flame*, 160(10): 2119–2130, 2013. (Cited with the first apparition of previous citation.)

[185] M. L. Botero, N. Eaves, J. A. Dreyer, Y. Sheng, J. Akroyd, W. Yang, and M. Kraft. Experimental and numerical study of the evolution of soot primary particles in a diffusion flame. *Proceedings of the Combustion Institute*, 37(2):2047–2055, 2019. (Cited on page 38.)

[186] A. Guibaud, J. M. Citerne, J. L. Consalvi, and G. Legros. On the effects of opposed flow conditions on non-buoyant flames spreading over polyethylene-coated wires–part i: Spread rate and soot production. *Combustion and Flame*, 221:530–543, 2020. (Cited on pages 39, 87, 88, and 103.)

[187] A. Umemura, M. Uchida, T. Hirata, and J. Sato. Physical model analysis of flame spreading along an electrical wire in microgravity. *Proc. Combust. Inst.*, 29:2535–2543, 2002. (Cited on page 40.)

[188] Y. Kobayashi, Y. Konno, X. Huang, S. Nakaya, M. Tsue, N. Hashimoto, O. Fujita, and C. Fernandez-Pello. Effect of insulation melting and dripping on opposed flame spread over laboratory simulated electrical wires. *Fire Safety Journal*, 95:1–10, 2018. (Cited on pages 40 and 75.)

[189] E. Orndoff. Flame retardant fibers for human space exploration-past, present, and future. *Dornbirn Man-Made Fibers Congress*, 2017. (Cited on pages 40 and 41.)

[190] S. Takahashi, M. A. F. bin Borhan, K. Terashima, A. Hosogai, and Y. Kobayashi. Flammability limit of thin flame retardant materials in microgravity environments. *Proc. Combust. Inst.*, 37 (3):4257–4265, 2019. (Cited on page 41.)

[191] S. Takahashi, K. Terashima, M. A. F. bin Borhan, and Y. Kobayashi. Relationship between blow-off behavior and limiting oxygen concentration in microgravity environments of flame retardant materials. *Fire Technology*, 56(1):169–183, 2020. (Cited on page 41.)

[192] G.M. Fohlen, J.A. Parker, S.R. Riccitiello, and P.M. Sawko. Intumescence: an in situ approach to thermal protection. *WESRAC-Fireproofing and Safety Symposium*, 1972. (Cited on page 41.)

[193] D. A. Kourtides. *Flame-retardant composite materials*, volume 3109. Technology 2000: Proceedings of a Conference, 1991. (Cited on page 41.)

[194] J. Alongi, Z. Han, and S. Bourbigot. Intumescence: Tradition versus novelty. a comprehensive review. *Progress in Polymer Science*, 51:28–73, 2015. (Cited on page 41.)

[195] T. Hirano, S. E. Noreikis, and T. E. Waterman. Measured velocity and temperature profiles near flames spreading over a thin combustible solid. *Combustion and Flame*, 23:83–96, 1974. (Cited on page 46.)

[196] Ramona Ritzmann, Kathrin Freyler, Elmar Weltin, Anne Krause, and Albert Gollhofer. Load dependency of postural control-kinematic and neuromuscular changes in response to over and under load conditions. *PloS one*, 10(6):e0128400, 2015. (Cited on page 49.)

[197] S. Rouvreau, P. Cordeiro, J. L. Torero, and P. Joulain. Influence of g-jitter on a laminar boundary layer type diffusion flame. *Proceedings of the Combustion Institute*, 30(1):519–526, 2005. (Cited on page 51.)

[198] H. Schlichting and J. Kestin. *Boundary layer theory*, volume 121. Springer, 1961. (Cited on page 52.)

[199] T.A. Sipkens and S.N. Rogak. Technical note: Using k-means to identify soot aggregates in transmission electron microscopy images. *Journal of Aerosol Science*, 152:105699, 2021. ISSN 0021-8502. (Cited on page 57.)

[200] Z. Li, L. Qiu, X. Cheng, Y. Li, and H. Wu. The evolution of soot morphology and nanostructure in laminar diffusion flame of surrogate fuels for diesel. *Fuel*, 211:517–528, 2018. (Cited on page 59.)

[201] M. L. Botero, Y. Sheng, J. Akroyd, Jv Martin, J. A. H. Dreyer, W. Yang, and M. Kraft. Internal structure of soot particles in a diffusion flame. *Carbon*, 141:635–642, 2019. (Cited on page 59.)

[202] B. R. Stanmore, J. F. Brilhac, and P. Gilot. The oxidation of soot: a review of experiments, mechanisms and models. *carbon*, 39(15):2247–2268, 2001. (Cited on page 59.)

[203] U. O. Koylu and G. M. Faeth. Optical properties of soot in buoyant laminar diffusion flames. *Journal of heat transfer*, 116(4):971–979, 1994. (Cited on page 59.)

[204] M. Altenhoff, S. . Aßmann, C. Teige, F. J. T. Huber, and S. Will. An optimized evaluation strategy for a comprehensive morphological soot nanoparticle aggregate characterization by electron microscopy. *Journal of Aerosol Science*, 139:105470, 2020. (Cited on page 59.)

[205] L. Liu, M. I. Mishchenko, and W. P. Arnott. A study of radiative properties of fractal soot aggregates using the superposition t-matrix method. *Journal of Quantitative Spectroscopy and Radiative Transfer*, 109(15):2656–2663, 2008. (Cited on page 60.)

[206] P. M. Anderson, H. Guo, and P. B. Sunderland. Repeatability and reproducibility of tem soot primary particle size measurements and comparison of automated methods. *Journal of Aerosol Science*, 114:317–326, 2017. (Cited on page 61.)

[207] B. Zhao, Z. Yang, J. Wang, M. V Johnston, and H. Wang. Analysis of soot nanoparticles in a laminar premixed ethylene flame by scanning mobility particle sizer. *Aerosol Science & Technology*, 37(8):611–620, 2003. (Cited on page 63.)

[208] G. Bushell, R. Amal, and J. Raper. The effect of polydispersity in primary particle size on measurement of the fractal dimension of aggregates. *Particle & Particle Systems Characterization: Measurement and Description of Particle Properties and Behavior in Powders and Other Disperse Systems*, 15(1):3–8, 1998. (Cited on page 64.)

[209] J. Y. Yin and L. H. Liu. Influence of complex component and particle polydispersity on radiative properties of soot aggregate in atmosphere. *Journal of Quantitative Spectroscopy and Radiative Transfer*, 111(14):2115–2126, 2010. (Cited with the first apparition of previous citation.)

[210] N. Doner and F. Liu. Impact of morphology on the radiative properties of fractal soot aggregates. *Journal of Quantitative Spectroscopy and Radiative Transfer*, 187:10–19, 2017. (Cited on page 64.)

[211] U. O. Koylu, G. M. Faeth, T. L. Farias, and M. G. Carvalho. Fractal and projected structure properties of soot aggregates. *Combustion and Flame*, 100(4):621–633, 1995. (Cited on page 64.)

[212] Y. Konno, Y. Li, J. M. Citerne, G. Legros, A. Guibaud, N. Hashimoto, and O. Fujita. Experimental study on downward/opposed flame spread and extinction over electric wires in partial gravity environments. *Proceedings of the Combustion Institute*, 2022. (Cited on pages 69, 70, 71, 72, and 73.)

[213] X. Huang, Y. Nakamura, and F. A. Williams. Ignition-to-spread transition of externally heated electrical wire. *Proceedings of the Combustion Institute*, 34(2):2505–2512, 2013. (Cited on page 71.)

[214] Y. Nakamura, N. Yoshimura, T. Matsumura, H. Ito, and O. Fujita. Opposed-wind effect on flame spread of electric wire in sub-atmospheric pressure. *Journal of thermal science and technology*, 3(3):430–441, 2008. (Cited on page 72.)

[215] L. Hu, Y. Zhang, K. Yoshioka, H. Izumo, and O. Fujita. Flame spread over electric wire with high thermal conductivity metal core at different inclinations. *Proceedings of the Combustion Institute*, 35(3):2607–2614, 2015. (Cited on page 75.)

[216] Y. Konno, N. Hashimoto, and O. Fujita. Downward flame spreading over electric wire under various oxygen concentrations. *Proceedings of the Combustion Institute*, 37:3817–3824, 2019. (Cited on pages 72, 75, and 80.)

[217] C. H. Chen and M. C. Cheng. Gas-phase radiative effects on downward flame spread in low gravity. *Combustion science and technology*, 97(1-3):63–83, 1994. (Cited on page 73.)

[218] Y. Konno, N. Hashimoto, and O. Fujita. Role of wire core in extinction of opposed flame spread over thin electric wires. *Combustion and Flame*, 220:7–15, 2020. (Cited on page 74.)

[219] Y. Nakamura, K. Kizawa, S. Mizuguchi, A. Hosogai, and K. Wakatsuki. Experimental study on near-limiting burning behavior of thermoplastic materials with various thicknesses under candle-like burning configuration. *Fire Technology*, 52(4):1107–1131, 2016. (Cited on page 75.)

[220] R. Sonnier, L. Ferry, B. Gallard, A. Boudenne, and F. çois Lavaud. Controlled emissivity coatings to delay ignition of polyethylene. *Materials*, 8(10):6935–6949, 2015. (Cited on page 76.)

[221] M. A. Delichatsios, R. A. Altenkirch, M. F. Bundy, S. Bhattacharjee, L. Tang, and K. Sacksteder. Creeping flame spread along fuel cylinders in forced and natural flows and microgravity. *Proceedings of the Combustion Institute*, 28(2):2835–2842, 2000. (Cited on page 80.)

[222] J. Berthier. Chapter 3 - the physics of droplets**this chapter was written with the collaboration of kenneth a. brakke (mathematics department, susquehanna university, selinsgrove, pa). In Jean Berthier, editor, *Micro-Drops and Digital Microfluidics (Second Edition)*, Micro and Nano Technologies, pages 75–160. William Andrew Publishing, second edition edition, 2013. (Cited on pages 81 and 82.)

[223] E. Lorenceau and D. Quéré. Drops on a conical wire. *Journal of Fluid Mechanics*, 510:29–45, 2004. (Cited on page 81.)

[224] R. J. Roe. Surface tension of polymer liquids. *The Journal of Physical Chemistry*, 72(6):2013–2017, 1968. (Cited on page 81.)

[225] S. Takahashi, H. Takeuchi, H. Ito, Y. Nakamura, and O. Fujita. Study on unsteady molten insulation volume change during flame spreading over wire insulation in microgravity. *Proceedings of the Combustion Institute*, 34(2):2657–2664, 2013. (Cited on page 81.)

[226] P. Dimitrakopoulos. Gravitational effects on the deformation of a droplet adhering to a horizontal solid surface in shear flow. *Physics of Fluids*, 19(12):122105, 2007. (Cited on page 82.)

[227] T. Gilet, D. Terwagne, and N. Vandewalle. Droplets sliding on fibres. *The European Physical Journal E*, 31(3):253–262, 2010. (Cited on page 82.)

[228] T. Tanaka, J. Lee, and P. R. Scheller. Chapter 1.5 - interfacial free energy and wettability. In Seshadri Seetharaman, editor, *Treatise on Process Metallurgy*, pages 61–77. Elsevier, Boston, 2014. (Cited on page 82.)

[229] T. Young. An essay on the cohesion of fluids. In *Abstracts of the Papers Printed in the Philosophical Transactions of the Royal Society of London*, number 1, pages 171–172. The Royal Society London, 1832. (Cited on page 82.)

[230] D. Briggs, D. G. Rance, and B. J. Briscoe. 23 - surface properties. In Geoffrey Allen and John C. Bevington, editors, *Comprehensive Polymer Science and Supplements*, pages 707–732. Pergamon, Amsterdam, 1989. (Cited on pages 82 and 83.)

[231] Y. Wang, J. Zhao, D. Zhang, M. Jian, H. Liu, and X. Zhang. Droplet sliding: The numerical observation of multiple contact angle hysteresis. *Langmuir*, 35(30):9970–9978, 2019. (Cited on page 83.)

[232] B. S. Yilbas, A. Al-Sharafi, H. Ali, and N. Al-Aqeeli. Dynamics of a water droplet on a hydrophobic inclined surface: influence of droplet size and surface inclination angle on droplet rolling. *Rsc Advances*, 7(77):48806–48818, 2017. (Cited on page 83.)

[233] N. G. Kowalski and J. B. Boreyko. Dynamics of fog droplets on a harp wire. *Soft Matter*, 2022. (Cited on page 83.)

[234] C. W. Extrand and Y. Kumagai. Liquid drops on an inclined plane: the relation between contact angles, drop shape, and retentive force. *Journal of colloid and interface science*, 170(2): 515–521, 1995. (Cited on page 84.)

[235] A. Keiser, L. Keiser, C. Clanet, and D. Quéré. Drop friction on liquid-infused materials. *Soft Matter*, 13(39):6981–6987, 2017. (Cited on page 84.)

[236] R. B. Bird, R. C. Armstrong, and O. Hassager. Dynamics of polymeric liquids. vol. 1: Fluid mechanics. 1987. (Cited on pages 84 and 85.)

[237] D. Bartolo, A. Boudaoud, G. Narcy, and D. Bonn. Dynamics of non-newtonian droplets. *Physical review letters*, 99(17):174502, 2007. (Cited on page 84.)

[238] J. Xie, J. Xu, W. Shang, and K. Zhang. Mode selection between sliding and rolling for droplet on inclined surface: Effect of surface wettability. *International Journal of Heat and Mass Transfer*, 122:45–58, 2018. (Cited on page 85.)

[239] F. Mitsui, M. Nagachi, J. M. Citerne, H. Dutilleul, A. Guibaud, G. Jomaas, G. Legros, N. Hashimoto, and O. Fujita. Effect of the ignition method on the extinction limit for a flame spreading over electric wire insulation. *International Conference on Environmental Systems*, 47:1–5, 2017. (Cited on page 87.)

[240] A. Guibaud, J. M. Citerne, J. L. Consalvi, and G. Legros. On the effects of opposed flow conditions on non-buoyant flames spreading over polyethylene-coated wires–part ii: Soot oxidation quenching and smoke release. *Combustion and Flame*, 221:544–551, 2020. (Cited on page 88.)

[241] S. Bourbigot, M. Le Bras, and R. Delobel. Carbonization mechanisms resulting from intumescence association with the ammonium polyphosphate-pentaerythritol fire retardant system. *Carbon*, 31(8):1219–1230, 1993. (Cited on page 93.)

[242] Y. Li, A. Guibaud, J. M. Citerne, J. L. Consalvi, A. Coimbra, J. Sarazin, S. Bourbigot, J. L. Torero, and G. Legros. Effects of flame retardants on extinction limits, spread rate, and smoke release in opposed-flow flame spread over thin cylindrical polyethylene samples in

microgravity. *Proceedings of the Combustion Institute*, 2022. (Cited on pages 94, 96, 99, 100, 102, and 104.)

[243] S. Bourbigot, J. Sarazin, T. Bensabath, F. Samyn, and M. Jimenez. Intumescent polypropylene: reaction to fire and mechanistic aspects. *Fire Safety Journal*, 105:261–269, 2019. (Cited on page 94.)

[244] T. Bensabath, J. Sarazin, M. Jimenez, F. Samyn, and S. Bourbigot. Intumescent polypropylene: Interactions between physical and chemical expansion. *Fire and Materials*, 45(3):387–395, 2021. (Cited on page 94.)

[245] M. C. Johnston, S. James, D. E. Muff, X. Zhao, S. L. Olson, and P. V. Ferkul. Self induced buoyant blow off in upward flame spread on thin solid fuels. *Fire safety journal*, 71:279–286, 2015. (Cited on page 99.)

[246] J. L. Consalvi, A. Guibaud, A. Coimbra, J. M. Citerne, and G. Legros. Effects of oxygen depletion on soot production, emission and radiative heat transfer in opposed-flow flame spreading over insulated wire in microgravity. *Combustion and Flame*, 230:111447, 2021. (Cited on page 103.)

[247] I. Glassman and P. Yaccarino. The effect of oxygen concentration on sooting diffusion flames. *Combustion Science and Technology*, 24(3-4):107–114, 1980. (Cited on page 103.)

[248] J. B. Renard, F. Dulac, G. Berthet, T. Lurton, D. Vignelles, F. Jégou, T. Tonnelier, M. Jeannot, B. Couté, R. Akiki, et al. Loac: a small aerosol optical counter/sizer for ground-based and balloon measurements of the size distribution and nature of atmospheric particles–part 1: Principle of measurements and instrument evaluation. *Atmospheric Measurement Techniques*, 9 (4):1721–1742, 2016. (Cited on pages 106 and 107.)

[249] J. B. Renard, F. Dulac, G. Berthet, T. Lurton, D. Vignelles, F. Jégou, T. Tonnelier, M. Jeannot, B. Couté, R. Akiki, et al. Loac: a small aerosol optical counter/sizer for ground-based and balloon measurements of the size distribution and nature of atmospheric particles–part 2: First results from balloon and unmanned aerial vehicle flights. *Atmospheric Measurement Techniques*, 9(8):3673–3686, 2016. (Cited on page 106.)

[250] S. L. Von der Weiden, F. Drewnick, and S. Borrmann. Particle loss calculator–a new software tool for the assessment of the performance of aerosol inlet systems. *Atmospheric Measurement Techniques*, 2(2):479–494, 2009. (Cited on page 111.)

[251] L. E. Smart and E. A. Moore. *Solid state chemistry: an introduction*. CRC press, 2012. (Cited on page 112.)

[252] W. D. Pyrz and D. J. Buttrey. Particle size determination using tem: a discussion of image acquisition and analysis for the novice microscopist. *Langmuir*, 24(20):11350–11360, 2008. (Cited on page 112.)

[253] S. G. Wolf and M. Elbaum. Cryostem tomography in biology. *Methods in Cell Biology*, 152: 197–215, 2019. (Cited on page 113.)

[254] J. Frank. *Electron tomography: methods for three-dimensional visualization of structures in the cell*. Springer Science & Business Media, 2008. (Cited on page 113.)

[255] R. McIntosh, D. Nicastro, and D. Mastronarde. New views of cells in 3d: an introduction to electron tomography. *Trends in cell biology*, 15(1):43–51, 2005. (Cited on page 113.)

[256] M. Weyland and P. A. Midgley. Electron tomography. *Materials Today*, 7(12):32–40, 2004. (Cited on page 113.)

[257] L. H. Van Poppel, H. Friedrich, J. Spinsby, S. H. Chung, J. H. Seinfeld, and P. R. Buseck. Electron tomography of nanoparticle clusters: Implications for atmospheric lifetimes and radiative forcing of soot. *Geophysical research letters*, 32(24), 2005. (Cited on page 113.)

[258] H. Friedrich, M. R. McCartney, and P. R. Buseck. Comparison of intensity distributions in tomograms from bf tem, adf stem, haadf stem, and calculated tilt series. *Ultramicroscopy*, 106 (1):18–27, 2005. (Cited on page 113.)

[259] K. Adachi, S. H. Chung, H. Friedrich, and P. R. Buseck. Fractal parameters of individual soot particles determined using electron tomography: Implications for optical properties. *Journal of Geophysical Research: Atmospheres*, 112(D14), 2007. (Cited on pages 113 and 114.)

[260] A. Baldelli, U. Trivanovic, and S. N. Rogak. Electron tomography of soot for validation of 2d image processing and observation of new structural features. *Aerosol Science and Technology*, 53(5):575–582, 2019. (Cited on page 114.)

[261] J. W. Marcum, S. L. Olson, and P. V. Ferkul. Correlation of normal gravity mixed convection blowoff limits with microgravity forced flow blowoff limits. In *2016 Spring Technical Meeting of the Central States Section of The Combustion Institute*, number GRC-E-DAA-TN30478, 2016. (Cited on page 123.)

[262] G. A. Ruff, D. L. Urban, and D. Dietrich. Demonstration experiments to advance spacecraft fire safety technology. *A Safer Space for Safer World*, 699:81, 2012. (Cited on page 123.)